
FORMATION AND PHYSICAL PROPERTIES
OF CENTRAL STRUCTURES IN
BARRED GALAXIES



Adrian Bittner
Munich 2021

Formation and Physical Properties of Central Structures in Barred Galaxies

Dissertation

at the

Faculty of Physics

of the

**Ludwig Maximilians University
Munich**

submitted by

Adrian Bittner

born on 15th of February 1994 in Kronach

Munich, 17th of March 2021

Entstehung und Eigenschaften von Zentralen Strukturen in Balkengalaxien

Dissertation

an der

Fakultät für Physik

der

Ludwig Maximilians Universität
München

vorgelegt von

Adrian Bittner

geboren am 15. Februar 1994 in Kronach

München, den 17. März 2021

Erstgutacher: PD Dr. Klaus Dolag
Zweitgutachter: Prof. Dr. Joseph Mohr
Tag der mündlichen Prüfung: 30. April 2021

ESO Betreuer: Dr. Dimitri A. Gadotti

People ask me, “What is the use of climbing Mount Everest?” and my answer must at once be, “It is of no use. There is not the slightest prospect of any gain whatsoever.” [...]

If you cannot understand that there is something in man which responds to the challenge of this mountain and goes out to meet it, that the struggle is the struggle of life itself upward and forever upward, then you won't see why we go.

What we get from this adventure is just sheer joy. And joy is, after all, the end of life. We do not live to eat and make money. We eat and make money to be able to live. That is what life means and what life is for.

— GEORGE MALLORY

Chapter
Contents

Abstract	1
1 Introduction	5
1.1 Galaxy Formation and Evolution	5
1.1.1 Cosmology and Galaxy Formation	5
1.1.2 Galaxy Evolution	6
1.1.3 Galaxy Morphology	7
1.2 Bars in Disc Galaxies	8
1.2.1 Bar Formation and Disc Instabilities	8
1.2.2 Orbital Structure of Bars	10
1.2.3 Spectroscopic Properties of Bars	11
1.2.4 The Frequency of Bars	12
1.3 Secular Evolution in Disc Galaxies	13
1.3.1 Outward Angular Momentum Transport	13
1.3.2 Bars, Star Formation, and AGN Activity	13
1.3.3 Inner and Outer Rings	15
1.3.4 Disc Breaks	16
1.4 Central Substructures in Disc Galaxies	16
1.4.1 Bulges in Disc Galaxies	17
1.4.2 Nuclear Discs and Nuclear Rings	19
1.4.3 Box/Peanut Structures	21
1.4.4 Inner Bars	22
1.4.5 Classical Bulges	23
1.5 Constraints on Global Galaxy Evolution	25
1.5.1 Measuring the Age of Bars	25
1.5.2 Internal versus External Evolution of Disc Galaxies	25
1.6 Goals of this Thesis	26
2 The GIST Pipeline	29
2.1 Introduction	29
2.2 Pipeline Implementation	31
2.2.1 Core Design Principles	31
2.2.2 Code Architecture and Workflow	33
2.2.3 Implementation of the Framework	36
2.3 Application to MUSE Data	44
2.3.1 Observations and Data Reduction	44
2.3.2 Data Analysis Set-up	45
2.3.3 Stellar Kinematics	46
2.3.4 Emission-line Kinematics and Fluxes	48
2.3.5 Absorption-line Strength Analysis	50
2.3.6 Stellar Population Properties	50
2.4 Summary and Conclusions	52

3	Kinematic Signatures of Nuclear Discs	55
3.1	Introduction	55
3.2	The TIMER Survey	58
3.3	Stellar Kinematics of Nuclear Discs	59
3.3.1	Data Analysis	59
3.3.2	Systemic Velocities and Central Velocity Dispersions	60
3.3.3	Maps of the Stellar Kinematics	62
3.3.4	Previous Observations with Integral-field Spectrographs	71
3.4	Comparison with Results from Photometric Decompositions	72
3.4.1	Kim et al. 2014	73
3.4.2	Salo et al. 2015	74
3.4.3	Exponential Photometric Bulges are Nuclear Discs	74
3.5	The Origin of Nuclear Discs	76
3.6	Discussion and Conclusions	80
4	Stellar Populations of Nuclear Discs	85
4.1	Introduction	85
4.2	The TIMER Survey	88
4.3	Data Analysis	88
4.4	Stability and Errors of the Measurements	92
4.4.1	Population Properties with and without $[\alpha/\text{Fe}]$ Modelling	92
4.4.2	Population Properties from pPXF and STECMAP	94
4.4.3	Error Estimates on Stellar Population Properties	95
4.5	Results	96
4.5.1	Maps of Dust-corrected $\text{H}\alpha$ Emission-line Fluxes	96
4.5.2	Maps of Mean Stellar Population Properties	99
4.5.3	Radial Profiles of Mean Stellar Population Properties	101
4.5.4	Stellar Population Content in Nuclear Discs and Nuclear Rings	102
4.6	Discussion	103
4.6.1	The Connection between Nuclear Rings and Nuclear Discs	103
4.6.2	Nuclear Discs in the Global Context of Secular Evolution	105
4.6.3	The Simultaneous Growth of Nuclear Discs and Bars	106
4.6.4	The Absence of Kinematically Hot Spheroids	109
4.6.5	Rejuvenation of an old Nuclear Disc in NGC 1097	113
4.7	Summary and Conclusions	114
5	Stellar Populations of Inner Bars	117
5.1	Introduction	117
5.2	Sample, Observations, and Data Analysis	119
5.2.1	Double-barred Galaxies in TIMER	119
5.2.2	Observations and Data Reduction	120
5.2.3	Data Analysis	121
5.3	Results	124
5.3.1	Mean Stellar Population Properties in Inner Bars	124
5.3.2	Profiles along the Inner Bar Major and Minor Axis	127
5.4	Discussion	130
5.4.1	Stellar Populations in Bars, Inner Bars, and their Star Formation Deserts	130
5.4.2	Flat Population Gradients along Inner Bars: Orbital Mixing	131
5.4.3	Young Ends of Inner Bars: Orbital Age Separation	132
5.5	Summary and Conclusions	133

6	Summary and Conclusions	137
7	Outlook	141
7.1	The BANG Survey: Bulge Assembly in Nearby Galaxies	141
7.2	Kinematic Decompositions of Galaxies	144
7.3	Extending the Efforts of the TIMER Survey	146
A	Appendices of “Kinematic Signatures of Nuclear Discs”	149
A.1	Kinematic Maps and Discussion of Exceptional Cases	149
A.1.1	Nuclear Discs	149
A.1.2	Bars	152
A.1.3	Box/Peanuts	153
A.2	Analysis of Trends between Kinematic Radii and Bar Properties	153
B	Appendices of “Stellar Populations of Nuclear Discs”	157
B.1	Descriptions of Individual Galaxies	157
B.2	Maps of Dust-corrected H α Fluxes	160
B.3	Maps and Radial Profiles of Stellar Population Properties	160
	Bibliography	171
	Acknowledgements	185

Abstract

The evolution of disc galaxies is governed not only by violent and external processes, but also by slow and continuous, internal evolution. One of the main drivers of this secular evolution are bars: these strongly non-axisymmetric stellar structures are present in 2/3 of all massive disc galaxies in the local Universe and have a substantial impact on their evolution. Amongst many other effects, they efficiently facilitate the inflow of gas from the main galaxy disc to their central regions, where this gas settles and eventually new stellar structures, such as nuclear discs, nuclear rings, and inner bars, are built. In this thesis, we aim to better characterise the properties of these central stellar structures and constrain their formation and evolutionary history.

To this end, we employ integral-field spectroscopic observations from MUSE, obtained as part of the TIMER survey. The sample consists of 21 barred disc galaxies in the local Universe exhibiting a variety of central structures, and about 100 000 science-ready spectra are available for each galaxy. In order to facilitate the exploitation of this massive data set, we develop the sophisticated software framework **GIST** for the analysis and visualisation of spectroscopic data. Using this tool, we derive stellar kinematics and mean population properties in the central regions of these galaxies at an unprecedented spatial resolution.

We find that nuclear discs are characterised by high rotational velocities, low velocity dispersions, and near-circular orbits, while consisting of stellar populations that are significantly younger, more metal-rich, and less $[\alpha/\text{Fe}]$ enhanced, as compared to their direct surroundings. These properties of nuclear discs are consistent with the bar-driven formation scenario. Based on our radial population profiles in the nuclear discs, in particular stellar ages decreasing from the galaxy centre to their outer edge, and a correlation between the radii of (gaseous) nuclear rings and the bar length, we propose a new inside-out formation scenario for nuclear discs: in this picture, (stellar) nuclear discs are formed from a series of star-forming nuclear rings that grow in radius as the bar evolves. Combining measurements of both kinematics and stellar population properties, we find only little evidence for the presence of large, classical bulges in these galaxies. Although the galaxy sample is biased towards barred galaxies, the absence of classical bulges in such massive galaxies is surprising.

Investigating the stellar population content of the three inner bars in TIMER, we find that these structures are characterised by high metallicities and low $[\alpha/\text{Fe}]$ abundances, similar to main bars. Moreover, inner bars exhibit slightly younger stellar ages at their outer ends, an effect known from studies on main bars as orbital age separation. In addition, radial profiles of metallicities and $[\alpha/\text{Fe}]$ enhancements are flat along the inner bar major axis, but show significantly steeper slopes along their minor axis, again analogous to previous findings in the context of main bars. These results suggest that inner and main bars are dynamically similar structures that differ only in the spatial scale on which they exist.

Zusammenfassung

Die Entwicklung von Scheibengalaxien wird nicht nur durch externe Prozesse beeinflusst, sondern auch durch langsame, interne Vorgänge. Einer der wichtigsten Einflussfaktoren bei dieser internen Entwicklung sind Balken: Diese nicht axialsymmetrischen, stellaren Strukturen sind in 2/3 aller massiven Scheibengalaxien im lokalen Universum vorhanden und haben erheblichen Einfluss auf deren Entwicklung. Zum Beispiel ermöglichen sie den Transport von Gas von der Hauptscheibe zum Zentrum der Galaxien. Dort sammelt sich das Gas an und formt neue stellare Strukturen, insbesondere Nukleare Scheiben, Nukleare Ringe und Innere Balken. In dieser Arbeit beabsichtigen wir diese Strukturen genauer zu charakterisieren, um ihre Entstehungs- und Entwicklungsgeschichte besser zu verstehen.

Dazu verwenden wir spektroskopische Beobachtungen mit MUSE, die im Rahmen des TIMER Projektes durchgeführt wurden. Der Datensatz enthält 21 Balkengalaxien im lokalen Universum, die eine Vielzahl von zentralen Strukturen aufweisen, und besteht dabei aus ca. 100 000 Spektren pro Galaxie. Um die Auswertung dieser Datenmenge zu vereinfachen, entwickeln wir die Software GIST für die Analyse von spektroskopischen Beobachtungen. Mit dieser Software messen wir die stellare Kinematik und die Sternpopulationen in den Zentren dieser Galaxien mit hoher räumlicher Auflösung.

Unsere Messungen ergeben, dass Nukleare Scheiben – im Gegensatz zu ihrer direkten Umgebung – hohe Rotationsgeschwindigkeiten, eine niedrige Geschwindigkeitsdispersion und Sterne auf ungefähr kreisförmigen Orbits aufweisen, wobei die Sternpopulationen erheblich jünger sind, und außerdem hohe Metallizitäten und niedrige $[\alpha/\text{Fe}]$ Verhältnisse haben. Diese Eigenschaften sind konsistent mit ihrer Entstehung durch den durch Balken ausgelösten Gasfluss zum Galaxienzentrum. Basierend auf radialen Profilen der Sternpopulationen in Nuklearen Scheiben, insbesondere der Verjüngung der Populationen nach außen, und einer Korrelation zwischen dem Radius von (gasförmigen) Nuklearen Ringen und der Balkenlänge, schließen wir, dass Nukleare Scheiben von innen nach außen wachsen. Dabei entstehen die (stellaren) Nuklearen Scheiben aus einer Serie von Nuklearen Ringen mit Sternentstehung, die zusammen mit dem Balken im Radius wachsen. Darüber hinaus finden wir in den Messungen der stellaren Kinematik und Sternpopulationen kaum Charakteristika von Klassischen Bulges. Obwohl unsere Stichprobe von Galaxien nicht repräsentativ ist, ist das Fehlen von Klassischen Bulges in massiven Galaxien überraschend.

Bei der Untersuchung der Sternpopulationen in den drei Inneren Balken in TIMER zeigt sich, dass diese Strukturen durch hohe Metallizitäten und niedrige $[\alpha/\text{Fe}]$ Verhältnisse charakterisiert sind, ähnlich zu den Hauptbalken in Galaxien. Außerdem haben Innere Balken etwas jüngere Sternpopulationen an ihren Enden, ein Effekt der von Studien zu Hauptbalken als Orbital Age Separation bekannt ist. Darüber hinaus zeigen radiale Profile der Metallizitäten und $[\alpha/\text{Fe}]$ Verhältnisse, dass diese entlang der Hauptachse der Inneren Balken flach verlaufen, aber deutlich höhere Gradienten entlang der kleinen Halbachse aufweisen. Auch dieser Effekt ist bereits von Studien an Hauptbalken bekannt. Daher legen die Ergebnisse nahe, dass Innere Balken und Hauptbalken dynamisch ähnliche Strukturen sind, die sich hauptsächlich durch ihre Größe unterscheiden.

The majestic view of the night sky has fascinated humans for thousands of years, making astronomy the probably first natural science developed by humanity. From the presumably oldest representation of the night sky, the Nebra sky disk, over the early observations in Babylonia and ancient Egypt that employed astronomy as a practical tool to measure time, to the first star catalogue compiled by a Greek philosopher, the night sky always inspired the curiosity of humans. But it was only with the invention of the telescope at the beginning of the 17th century that humanity started to understand its place in the cosmos. With the revolutionary observations of Kepler (1609) and Galilei (1610), and eventually the emerging understanding of the physical laws of nature (Newton 1687), a scientific revolution took over and paved the way for modern natural sciences. Thereafter, it still took hundreds of years until galaxies, one of the most fundamental building blocks of the Universe, were identified as such. The Great Debate of Shapley & Curtis (1921) was questioning whether spiral nebulae are small and relatively close objects within the Milky Way itself, or much larger and further away representing distinct galaxies just as the Milky Way, so-called “island universes”, as first speculated by Kant (1755). The debate was finally resolved by Hubble (1925) who determined distances based on Cepheid variables and provided evidence that these objects are of extragalactic origin – making the Milky Way only one of many galaxies in the Universe and therewith marking the emergence of extragalactic astronomy itself. In the past century since Hubble’s discovery, many details about the nature of these structures was revealed, but it is only now that unprecedented spectroscopic instruments at the world’s largest observatories allow us to explore the foundations of galaxy evolution.

1.1 Galaxy Formation and Evolution

Galaxies are without any doubt some of the most beautiful objects in the Universe. Generally understood as gravitationally bound systems of baryonic matter, in particular stars, gas and dust, which presumably are embedded in massive halos consisting of dark matter, galaxies exhibit a large variety of appearances, fundamental properties, and cover orders of magnitude in their total mass.

1.1.1 Cosmology and Galaxy Formation

The foundation of galaxy formation and evolution was already laid shortly after the emergence of our Universe itself in a Hot Big Bang (Gamow 1946) approximately 13.8 billion years ago (Planck Collaboration et al. 2016). The cosmic microwave background (CMB; Alpher & Herman 1948; Penzias & Wilson 1965), which consists of residual radiation from a time approximately 360 000 years after the Big Bang when the Universe first became transparent to photons, allows probing the initial conditions for galaxy formation. Observations of the CMB with the COBE, WMAP, and Planck satellites (Smoot et al. 1992; Bennett et al. 2003; Planck Collaboration et al. 2011) provided conclusive evidence that the Universe is very homogeneous on large scales, but also detected anisotropies in the temperature T of the microwave background at the order of $\Delta T/T \approx 10^{-5}$.

These anisotropies in the CMB are the observational signature of density fluctuations in the young Universe and ever since gravity facilitates the continuous growth of these structures. Over-dense regions exert a gravitational pull to the surrounding matter, grow in mass until they become unstable, and eventually collapse to form a gravitationally bound halo. Baryonic matter is forced to follow this clustering process, shocks and cools during its infall into the potential, and eventually forms the baryonic component of galaxies that are observed throughout the Universe (White & Rees 1978; Fall & Efstathiou 1980). In this picture, disc galaxies are formed from gas falling into dark matter halos while conserving its angular momentum, whereas elliptical galaxies are a result of mergers (Toomre & Toomre 1972; Fall & Efstathiou 1980; Mo et al. 1998; Cole et al. 2000).

A fundamental ingredient in this process of structure formation is the presence of dark matter. Without this additional gravitating component that is not interacting with its surroundings via electromagnetic radiation, the subtle density fluctuations observed in the early Universe could not evolve into the large-scale structure evident at the present day (see e.g. Mo et al. 2010). After first observational signatures of dark matter based on the kinematic structure of the Coma Cluster (Zwicky 1933), more evidence was found, for instance based on the rotation curves of galaxies, the orbits of their satellites, or gravitational lensing effects (Roberts & Rots 1973; Ostriker et al. 1974; Einasto et al. 1974; Bosma 1978; Rubin et al. 1978; Bosma & van der Kruit 1979; Walsh et al. 1979; Rubin et al. 1980; Bosma 1981).

Understanding the physical nature of dark matter is still an ongoing effort, but so far no particle could be associated with it. However, the thermal velocities of possible dark matter particles could be well constrained, based on the observed galaxy clustering on large scales. Today, dark matter is generally assumed to be thermally cold (so-called “cold dark matter”) and together with a cosmological constant Λ to assure a flat topology of the Universe, the Λ CDM cosmological model provides the best physical description of our Universe, in particular on large scales (see e.g. Mo et al. 2010, for a review). However, several challenges remain for the Λ CDM paradigm, in particular at small scales (Bullock & Boylan-Kolchin 2017). Alternative models that do not require the existence of an unseen dark matter component have also been proposed. Instead, a modification of Newtonian dynamics at cosmological scales is suggested (e.g. “Modified Newtonian Dynamics” Milgrom 1983), but to date, the Λ CDM cosmological model remains the accepted paradigm.

1.1.2 Galaxy Evolution

The main mechanism facilitating the growth of halos in this Λ CDM cosmology is hierarchical clustering. In this picture, initially low-mass halos that developed through the gravitational collapse of primordial overdensities grow via mergers with other halos (White & Rees 1978). In this way, all larger structures in the Universe, ranging from galaxies and groups of galaxies to the largest galaxy clusters, are assembled. In this picture, mergers of galaxies are frequent events (see e.g. Maller et al. 2006; Stewart et al. 2008) and not only represent the main channel for the growth of halos, but also a fundamental process in galaxy evolution. More specifically, elliptical galaxies are thought to be formed in merger-driven processes. While in dissipationless simulations of galaxy mergers the violent relaxation of stars can produce remnants that resemble elliptical galaxies (Barnes 1988; Hernquist 1992), in more realistic models their formation requires a mixture of both minor and major mergers with a range of gas fractions (Oser et al. 2012; Porter et al. 2014, but see also Brooks & Christensen 2016 for a review). The formation of dispersion-dominated

spheroids in the centres of disc galaxies (so-called classical bulges) is as well expected to be a merger-driven process, although these structures are thought to form predominantly via minor mergers (see e.g. Bournaud et al. 2005b; Brooks & Christensen 2016).

As the expansion of the Universe accelerates (Riess et al. 1998; Perlmutter et al. 1999) and galaxy mergers become less frequent, at later cosmic epochs other processes start to play a more important role in galaxy evolution (see Kormendy & Kennicutt 2004; Sellwood 2014, for reviews). These processes depend not only on the internal properties of galaxies but also on the environment in which they reside. While in high-density environments in and around galaxy clusters the evolution of galaxies is still governed by violent and external processes, for instance ram-pressure stripping, harassment, and starvation (see e.g. Gunn & Gott 1972; Moore et al. 1996), in low-density regions of the Universe slow, internal processes become the most important mechanism.

This more gentle mode of galaxy evolution driven by internal processes is typically referred to as “secular evolution”. Although these mechanisms are sometimes overlooked in light of the various external effects on galaxies, they can have a tremendous influence on their structure and evolution. In particular, they facilitate the re-distribution of angular momentum throughout galaxy discs, a mechanism often driven via non-axisymmetric disturbances such as bars (see e.g. Kormendy & Kennicutt 2004; Sellwood 2014; Laurikainen et al. 2016, for reviews). We detail the effect of bars and secular evolution on disc galaxies in the remainder of this thesis.

1.1.3 Galaxy Morphology

The many processes that partake in galaxy formation and evolution and the fact that galaxy formation is still a currently ongoing process result in a large diversity of galaxies. This diversity of the galaxy population in the Universe becomes evident in a large number of morphological structures of galaxies, their dynamical properties, as well as stellar population content.

On the most basic level, galaxies can be distinguished into those showing significant rotation and flattening, that is disc galaxies, and those exhibiting a more spheroidal structure and being dynamically supported by random motions, in particular elliptical galaxies. These galaxies show a great variety of structural and physical properties resulting in the large diversity observed in the Universe. A first attempt to classify this diversity of galaxies was made by Hubble (1926, 1936) and later, with increasing observational capabilities and a growing understanding of their physical nature, further refined (see e.g. de Vaucouleurs 1959; Sandage 1961; Buta et al. 2015). The original classification scheme of Hubble (1926) is widely known as “Hubble sequence” or “Hubble tuning-fork”.

Elliptical galaxies exhibit elliptical isophotes with little internal substructure and are generally referred to as “early-type” galaxies. As a result of their very old stellar component, elliptical galaxies exhibit mostly red colours. They are kinematically characterised by low rotational velocities and elevated velocity dispersions, a natural result of their merger-driven formation scenario (Mo et al. 2010). In contrast to disc galaxies, these ellipticals contain only little volumes of cold gas but exhibit significant amounts of hot gas that constitutes their interstellar medium (Fabbiano et al. 1989; Roberts et al. 1991).

On the contrary, disc galaxies are characterised by thin and regularly rotating discs consisting of stars, gas, and dust. These galaxies typically contain substantially larger amounts of cold gas than ellipticals and often show signs of ongoing star-formation. As a result, disc galaxies show bluer colours and younger stellar populations at a given luminosity, as compared to ellipticals (Mo et al. 2010). Nonetheless, disc galaxies can exhibit very old stellar components, with ages well above 10 Gyr (see e.g. Gadotti et al. 2015). Moreover, they contain a wealth of substructures: the discs often feature spiral arms, bars, and multiple rings, as well as a variety of additional components in their centre (see Sect. 1.4 for a detailed account). The Milky Way is a poster child example of such a disc galaxy hosting a wealth of substructures (Bland-Hawthorn & Gerhard 2016).

Lenticular galaxies were originally introduced in the Hubble sequence as an intermediate type between ellipticals and spirals (Hubble 1936). Galaxies classified as lenticular typically exhibit a pronounced central spheroid surrounded by a disc in which bars are frequently observed. However, these discs usually do not exhibit any spiral structure. Moreover, there is typically little gas and no ongoing star formation in these galaxies, while significant amounts of dust remain within them (see e.g. Aguerri 2012). Recently, the SAURON and ATLAS^{3D} surveys conclude that, in this picture, there is frequent misclassification between ellipticals and lenticulars. Based on the kinematic properties of early-type galaxies, they instead distinguish them in fast and slow rotators. As a result, they propose a new classification scheme in which disc and lenticular galaxies represent parallel sequences of fast rotating galaxies, while elliptical galaxies are identified as slow rotators (Emsellem et al. 2007; Cappellari et al. 2011b; Krajnović et al. 2011).

1.2 Bars in Disc Galaxies

The bars of galaxies are undoubtedly one of the most prominent and fascinating features of disc galaxies (see Fig. 1.1). These strongly elongated stellar structures are found in the centres of many massive disc galaxies, are rigidly rotating, and a result of dynamical instabilities in the discs. Bars exhibit typical radii of a few kiloparsecs, depending on the size of the host galaxy disc (Gadotti 2011) and exist in the majority of all disc galaxies in the local Universe (Eskridge et al. 2000). In the following, we briefly summarise the formation and physical structure of bars, while their effect on the evolution of disc galaxies is detailed in Sects. 1.3 and 1.4.

1.2.1 Bar Formation and Disc Instabilities

Rotationally supported, self-gravitating stellar discs are typically globally unstable (Hohl 1971; Kalnajs 1972; Ostriker & Peebles 1973; Kalnajs 1978; Jalali 2007). In a first approximation, this can be described in terms of the local stability criterion of Toomre (1964)

$$Q = \frac{\sigma_R \kappa}{3.36 G \Sigma} > 1 \quad (1.1)$$

with the radial velocity dispersion σ_R , the epicyclic frequency κ , the gravitational constant G , the disc surface density Σ , and the Toomre parameter Q . This relation can be understood with rotation and random motions stabilising discs on large and small scales, respectively, while increased surface densities support their fragmentation. A system is considered globally unstable if the Toomre parameter is below unity and, in fact, this seems to be the case for most realistic models of rotationally supported stellar discs (see e.g. Sellwood 2014). The result of this disc instability is initially the formation of a bi-symmetric, two-armed



Figure 1.1: Hubble Space Telescope image of the galaxy NGC 1300 which hosts a prominent and particularly strong bar. Gas inflows along the leading edges of the bar are highlighted by two dust lanes which end at a nuclear disc in its very centre. In the outer parts, two bi-symmetric spiral arms extend from the outer ends of the bar. Credit: NASA, ESA, and the Hubble Heritage Team (STScI/AURA).

spiral pattern. However, while its inner part is straightened and eventually transformed into a bar, the outer part of this spiral structure winds up and subsequently vanishes (Toomre 1981; Sellwood 2014). The result is the formation of a bar that can also be understood as an attempt of the galaxy disc to minimize its internal energy.

It is important to note that this process of bar formation does proceed without the need for in-situ star formation in the bar. In other words, the bar is formed from stars that already existed in the galaxy disc before a dynamical instability triggered the formation of the bar. Therefore, the stars in the bar can be considerably older than the bar itself. As a result, measurements of bar ages based on the stellar population content within them are very challenging (Gadotti et al. 2015, Sect. 1.5.1).

In an alternative scenario, the formation of bars can also be triggered by external effects, in particular via tidal interactions (see e.g. Gerin et al. 1990; Peschken & Łokas 2019). However, it remains debated if tidally induced bars are identical to spontaneously formed bars or if they systematically differ in their properties, for instance by rotating slower, exhibiting flatter surface brightness profiles, or showing a shorter radial extent (Noguchi 1996; Miwa & Noguchi 1998; Berentzen et al. 2004). Interestingly, while some observational studies conclude that bars are more frequently found in galaxy pairs or show some environmental clustering, other studies find no dependence of the bar fraction on environment (Elmegreen et al. 1990; Aguerri et al. 2009; Li et al. 2009; Skibba et al. 2012; Lin et al. 2014). Although galaxy interaction can trigger the formation of bars, the same processes might also be able to prevent bar formation through dynamical heating of the galaxy disc or even destroy existing bars (Berentzen et al. 2003; Debattista et al. 2006). As a result, the combined effect of galaxy interactions triggering and destroying bars might be negligible.

However, realistic disc galaxies are influenced by several other factors that have a substantial impact on the formation and evolution of bars. In particular, elevated stellar velocity dispersions, large fractions of gas, and low surface densities of galaxy discs can hinder the formation of bars (see e.g. Athanassoula & Sellwood 1986; Athanassoula et al. 2013;

Berrier & Sellwood 2016). The presence of a massive, dispersion-dominated spheroid, for instance a classical bulge or halo component that is unresponsive to the evolution of the disc, can also prevent bar formation (see e.g Ostriker & Peebles 1973; Sellwood & Evans 2001; Athanassoula 2002) or only delay its formation and eventually lead to the emergence of stronger bars (Athanassoula 2013). However, given the large fraction of bars in the local Universe and the common global instability of galaxy discs, it is often more challenging to understand why a particular galaxy does not form a bar rather than why a bar formed (Sellwood et al. 2019).

In principle, tidal interactions, extremely gas-rich galaxy discs, or substantial central mass concentrations could lead to the dissolution of bars. However, recent numerical studies typically indicate that bars are persistent, long-lived structures that can hardly be destroyed (Berentzen et al. 2003; Athanassoula 2005; Bournaud et al. 2005a; Debattista et al. 2006; Berentzen et al. 2007; Kraljic et al. 2012). During their typical lifetime of several Gyr, bars efficiently facilitate the re-distribution of angular momentum throughout galaxy discs and into the halo. As a consequence, bars grow longer and stronger, their pattern speeds decrease, and they are one of the main drivers of secular evolution in disc galaxies (Athanassoula & Misiriotis 2002; Athanassoula 2003; Martinez-Valpuesta et al. 2006; Gadotti 2011, as detailed in Sects. 1.3 and 1.4). Eventually, further dynamical instabilities affect the structure of bars, most importantly the buckling instability that leads to their thickening vertical to the galaxy disc. The resulting structures are observed as box/peanuts (in edge-on configurations) and barlenses (in face-on configurations) in the inner parts of bars (Combes & Sanders 1981, as detailed in Sect. 1.4.3).

1.2.2 Orbital Structure of Bars

Bars exhibit a complicated orbital structure and are dynamically supported by stars on various families of resonant orbits (also referred to as periodic orbits). Given a bar that is rigidly rotating with a constant angular frequency Ω_p (i.e. its pattern speed), a star with radial frequency Ω_R and angular frequency Ω_ϕ orbits in resonance with the bar if

$$\Omega_p = \Omega_\phi + \frac{l}{m} \Omega_R \quad (1.2)$$

with the signed integer l and the integer m representing an m -fold rotational symmetry (Binney & Tremaine 1987; Sellwood 2014).

Various solutions to Eq. 1.2 are relevant in barred galaxies. Firstly, if $l = 0$ the angular frequency of the star equals the pattern speed of the bar. In other words, the star orbits synchronously with the bar, a configuration typically referred to as ‘‘corotation resonance’’ or simply ‘‘corotation’’ (CR). Secondly, with $l = \pm 1$ above relationship reduces to

$$\Omega_R = m |\Omega_\phi - \Omega_p| \quad (1.3)$$

and, hence, the frequency of the radial oscillation of the star equals the frequency at which the star encounters the bar. In particular, the cases of $m = 2$ and $l = \pm 1$ are relevant in barred galaxies. More precisely, $l = -1$ defines the ‘‘Inner Lindblad Resonance’’ (ILR) that is located within the corotation resonance where the angular frequency of the star is higher than the pattern speed of the bar. At $l = +1$ the pattern speed of the bar is higher than the angular frequency of the star and the corresponding ‘‘Outer Lindblad Resonance’’ (OLR) is located well outside of corotation. Resonances associated with higher values of l are typically not dynamically relevant. Finally, the ‘‘ultraharmonic resonances’’ (UHR) defined by $l = \pm 1$ and $m = 4$ are located relatively close to corotation are relevant

in the context of bar-driven secular evolution and are associated with the location of inner rings (Sellwood 2014, see also Sect. 1.3.3 for a more detailed discussion on inner and outer rings).

Moreover, bars are supported by families of periodic orbits, most importantly the x_1 orbit family. These orbits are elongated along the bar major axis and are radially extending close to corotation. In contrast, the x_2 orbits are oriented along the bar minor axis and their appearance is tightly connected to the ILR of the bar (Contopoulos & Papayannopoulos 1980; Contopoulos 1980; Athanassoula et al. 1983). Moreover, stars can be trapped in quasi-periodic orbits around these stable orbital families, further supporting the bar (Contopoulos 1980; but see also Sellwood 2014 for a review).

1.2.3 Spectroscopic Properties of Bars

This orbital structure of bars can not only be inferred via numerical simulations but also leaves a significant imprint in its observable properties. In particular, integral-field spectroscopic observations are well suited to uncover signatures of bar dynamics by measuring the kinematic and stellar population properties of bars.

In kinematic maps of disc galaxies, bars are often associated with a correlation between the radial velocity v and the higher-order moment h_3 of the line-of-sight velocity distribution (LOSVD). This v - h_3 correlation is a result of stars moving on highly elongated x_1 orbits along the major axis of the bar. More precisely, stars on such strongly elongated orbits exhibit higher velocities at a given radius than the velocity corresponding to a circular orbit at the same radius. The resulting LOSVD then exhibits a tail towards higher velocities and, hence, a correlation between v and h_3 (Bender et al. 1994; Bureau & Athanassoula 2005; Iannuzzi & Athanassoula 2015; Li et al. 2018).

Studies focussing on the stellar population content in bars do also detect signatures of their dynamical structure. The radial profiles of mean stellar population properties along the bar major axis are the topic of numerous observational studies (Pérez et al. 2007, 2009; Sánchez-Blázquez et al. 2011; Seidel et al. 2016; Fraser-McKelvie et al. 2019; Neumann et al. 2020). Although the earlier studies come to somewhat ambiguous results, more recently there is growing evidence that radial metallicity profiles along the bar major axis are flat. This is typically interpreted as a result of “radial mixing”: along the strongly elongated bar x_1 orbits different stellar populations on different orbits spatially approach each other (Binney & Tremaine 1987; Contopoulos & Grosbol 1989; Athanassoula 1992b). As a result, the mean stellar metallicities derived from the integrated light appear flat along the radial extent of the bar.

A related effect connecting the stellar dynamics of bars to their observed stellar population content is known as “orbital age separation” or “kinematic fractionation” (Pérez et al. 2007; Wozniak 2007; Fragkoudi et al. 2017b, 2018; Athanassoula et al. 2017; Debattista et al. 2017). This effect is a result of distinct components of the galaxy disc responding differently to the formation of the bar. While kinematically cold stars with low radial velocity dispersions contribute to the most elongated bar x_1 orbits, kinematically hotter stars form the less eccentric part of the same orbit family. Therefore, stars originating in the kinematically cold component of the galaxy disc dominate the outer ends of the bar and are more closely aligned with the bar major axis. In a realistic galaxy, these hot and cold disc components can be associated with the thin and thick disc (Fragkoudi et al. 2017b; Debattista et al. 2017; Athanassoula et al. 2017). Since the thin disc exhibits lower

velocity dispersion and younger ages (Prochaska et al. 2000; Cheng et al. 2012; Pinna et al. 2019), the outer ends of bars are often characterised by younger stellar populations compared to their inner parts. In line with the above theoretical expectations, Neumann et al. (2020) find that the youngest stellar populations in bars are found closest to their major axis.

1.2.4 The Frequency of Bars

Bars are very frequent structures in disc galaxies. In the local Universe, approximately 70% of all disc galaxies host bars (Eskridge et al. 2000; Menéndez-Delmestre et al. 2007; Aguéri et al. 2009). However, the frequency of bars is steeply declining with increasing redshift and at a redshift of $z \sim 1$ only 10% to 15% of all disc galaxies are observed to be barred (Sheth et al. 2008, 2012; Melvin et al. 2014). Nonetheless, the oldest bars are detected at redshifts as high as $z \sim 2$, based on direct observations with the *Hubble Space Telescope* (Simmons et al. 2014). Moreover, Gadotti et al. (2015) and Pérez et al. (2017) infer the formation time of bars in the local Universe and identify two bars that formed as early as $z \sim 1.7$ (NGC 6032) and $z \sim 1.8$ (NGC 4371).

The detection of bars based on direct observations of high-redshift galaxies is challenging. Firstly, at such distances the spatial resolution of the observations becomes a limiting factor that biases possible detections to the strongest and longest bars. Moreover, as bars are mostly stellar components that suppress star formation within them, they are often more prominent in the near-infrared than at optical wavelengths (Eskridge et al. 2000). Since observations in the optical wavelength range correspond to shorter wavelengths at the rest-frame of galaxies at high-redshifts, the detection of bars is further hindered.

Nonetheless, the studies mentioned above take these biases into account and consistently report a decrease of the bar fraction with increasing redshift. This seems to be a natural result of the distinct kinematic structure of galaxy discs at high redshifts and the necessary conditions for bar formation. As high-redshift galaxies are often more turbulent and kinematically hot while bars require a sufficiently cold and rotation-dominated disc for their formation, the bar fraction decreases with redshift (Sheth et al. 2012).

Interestingly, the decrease in bar fraction with increasing redshift appears to be a strong function of the galaxy mass. Sheth et al. (2008) find only little evolution of the bar fraction in the most massive galaxies between $z \sim 0.1$ and $z \sim 0.8$, but a significant decrease in the bar fraction of lower mass galaxies (see also Melvin et al. 2014). This supports the picture of the “downsizing-scenario” (Cowie et al. 1996; Thomas et al. 2010) in which more massive galaxies form and mature earlier, resulting in the earlier formation of a bar (Sheth et al. 2012; Kraljic et al. 2012). Besides this, bars are thought to be persistent, long-lived structures (Athanasoula 2005; Bournaud et al. 2005a; Berentzen et al. 2007; Kraljic et al. 2012), in line with the constant bar fraction observed between redshift $z \sim 1$ and $z \sim 2$ (Simmons et al. 2014).

The requirement of kinematically cold galaxy discs for bar formation together with their longevity is distinguishing bars as a tracer of the kinematic structure of galaxy discs. More precisely, a thorough understanding of the bar frequency as a function of galaxy mass, redshift, and environment could help to constrain the dynamical evolution of disc galaxies in greater detail (see Sect. 1.5.1).

1.3 Secular Evolution in Disc Galaxies

Bars are one of the main drivers of secular evolution in disc galaxies. Their strongly non-axisymmetric structure facilitates the re-distribution of angular momentum throughout the galaxy disc and into the halo and therewith plays a fundamental role in shaping these galaxies. In the following, we provide an overview of some of the main effects bars have on disc galaxies, specifically focussing on the processes that influence the global evolution of galaxies. Mechanisms that lead to the formation of central substructures, in particular the bar-driven gas inflow to the galaxy centre and the buckling instability of bars, are detailed in Sect. 1.4.

1.3.1 Outward Angular Momentum Transport

The most fundamental mechanism that triggers secular evolution processes in disc galaxies is based on the attempt of physical systems to minimize their energy. However, in a rotationally supported disc, the minimization of energy is constrained by the conservation of the angular momentum of the disc material. Therefore, rotationally supported galaxy discs need to minimize their energy at fixed angular momentum (Kormendy 2013).

As first summarised by Lynden-Bell & Kalnajs (1972) and Lynden-Bell & Pringle (1974) in the context of extragalactic astronomy, this can be achieved by transporting angular momentum outward (see also Tremaine 1989). In other words, the energy of a rotationally supported disc is minimized if the outer parts of discs expand while their centres become more compact. In this picture, it is energetically favourable if mass moves outwards after gaining angular momentum from masses at smaller radii (Kormendy 2013).

This spreading/contraction as a result of angular momentum exchange is not only taking place in galaxy discs but also in many other astrophysical systems. In contrast to galaxy discs, globular clusters and nuclear star clusters are dynamically supported by random motions but they undergo similar processes. Two-body relaxation between stars within them facilitate an outwards energy transport resulting in the densification of their core and the evaporation of their outer parts (see e.g. Kormendy 2013). Similar processes also take place in other systems, such as protoplanetary discs and accretion discs.

Naturally, bars are efficiently supporting this exchange of angular momentum. The strongly non-axisymmetric potential they impose on the galaxy disc facilitates the transport of angular momentum outwards. In this way, bars exchange angular momentum with the outer discs and halos of galaxies (see e.g. Athanassoula 2003), exert significant torques and tangential forces on gas in the main galaxy disc, and are the main driver of secular evolution in disc galaxies.

1.3.2 Bars, Star Formation, and AGN Activity

The colours and global star-formation rate of galaxies show a clear bimodality: one group of galaxies represents a star-forming “blue sequence” while another group exhibits low star-formation rates and constitutes the “red sequence”. While a part of this bimodality could be explained by the different morphologies of galaxies, in particular the significant differences between ellipticals and disc galaxies, this bimodality also suggests the presence of processes that are capable of suppressing star formation in galaxies at global scales. Various mechanisms in galaxy evolution could be responsible for the global cessation of

star formation, for instance mergers, ram-pressure stripping, harassment, starvation, and strong feedback processes, but also bars do have a significant effect on the star formation in disc galaxies (see e.g. Mo et al. 2010).

Bars do influence star formation in a variety of ways. On the one hand, bars re-distribute gas throughout galaxy discs, leading to the accumulation of gas in nuclear rings (see Sect. 1.4.2) as well as inner and outer rings (see Sect. 1.3.3). For instance, Sakamoto et al. (1999) find that barred galaxies exhibit elevated concentrations of molecular gas in their centres, as compared to unbarred galaxies (see also Sheth et al. 2005), resulting from a bar-driven gas inflow to the galaxy centres. As a result, star formation in the innermost regions of barred galaxies is often enhanced (see e.g. Heckman 1980; Ho et al. 1997; Alonso-Herrero & Knapen 2001; Regan et al. 2006; Ellison et al. 2011; Lin et al. 2017). This acceleration of star-formation in certain regions of the galaxy could support the more rapid exhaustion of the galaxy’s gas supply.

While bars are increasing star formation in some parts of disc galaxies, in other regions bars produce the opposite effect. For instance, the shear forces induced by the bar, in particular onto gas that flows along the bar to the galaxy centre, efficiently suppresses star formation in the bar itself (see e.g. Verley et al. 2007; Emsellem et al. 2015). Similarly, as bars are efficiently promoting the inflow of gas to the galaxy centre, the regions within the radial extent of the bar but outside of the bar itself (a region typically referred to as “star formation desert”; see the left-hand image of Fig. 1.2) is rapidly depleted of gas soon after bar formation (James et al. 2009; James & Percival 2016, 2018; Donohoe-Keyes et al. 2019). As a result, star formation is suppressed in these regions and observations even indicate a reduced stellar surface density (see e.g. Gadotti & de Souza 2003; Gadotti 2008; Kim et al. 2016). Although the effect of bars on the star-formation in disc galaxies are multifaceted, bars tend to increase star formation in some regions, leading to rapid consumption of the available gas. In this way, bars contribute to quenching the cessation of star formation in galaxies (see e.g. Haywood et al. 2016; Newnham et al. 2020).

Bars do not only affect the star-formation activity but have also been proposed to provide a possible feeding mechanism of active galactic nuclei (AGN; Shlosman et al. 1989, 1990). Since bars are an efficient driver of gas inflows from the main discs of galaxies to their central regions, they might facilitate the accumulation of gas in the vicinity of central supermassive black holes and its subsequent accretion. While the bar-driven gas inflow is a well-understood process (see Sect. 1.4.2), its capability to feed AGN remains debated. To date, there is no clear evidence if bars are more frequent in active galaxies (or vice versa) or that there is a connection between the strength of AGN activity and the presence of bars (see e.g. Ho et al. 1997; Knapen et al. 2000; Coelho & Gadotti 2011; Cisternas et al. 2013; Galloway et al. 2015; Cheung et al. 2015; Alonso et al. 2018). In fact, the very short timescales of AGN variability in the context of a typical lifetime of bars of multiple Gyr make statistical studies on their connection challenging.

Moreover, the bar-driven gas inflow is typically halted a few hundred parsecs from the galaxy centre (see Sect. 1.4.2). These distances are well beyond the sphere of influence of the central black hole and additional processes might be required to transport the gas to radii at which it can be accreted. Inner bars have been proposed as a possible mechanism to enable this subsequent gas inflow (Shlosman et al. 1989), however, more studies are needed to better constrain gas flows along inner bars (see also Sect. 1.4.4).

1.3.3 Inner and Outer Rings

Barred galaxies often harbour a set of rings throughout their discs: nuclear rings, inner rings, and outer rings (Buta 1986a). Nuclear rings are structures with typical sizes of a few hundred parsecs located in the centres of disc galaxies and thought to be built via bar-driven gas inflows (see Sect. 1.4.2 for a review of these structures and their formation mechanism). In contrast, inner and outer rings are found at much larger radii. Inner rings have typical radii of a few kiloparsecs and virtually always coincide with the ends of the bars. Outer rings are found at even larger radii of approximately twice the bar length (Kormendy 2013; Buta et al. 2015). Comerón et al. (2014) detect inner rings in approximately 35% of all disc galaxies while outer rings are less common with a frequency of 16%. An example of a galaxy hosting both inner and outer rings is displayed in the left-hand image of Fig. 1.2.

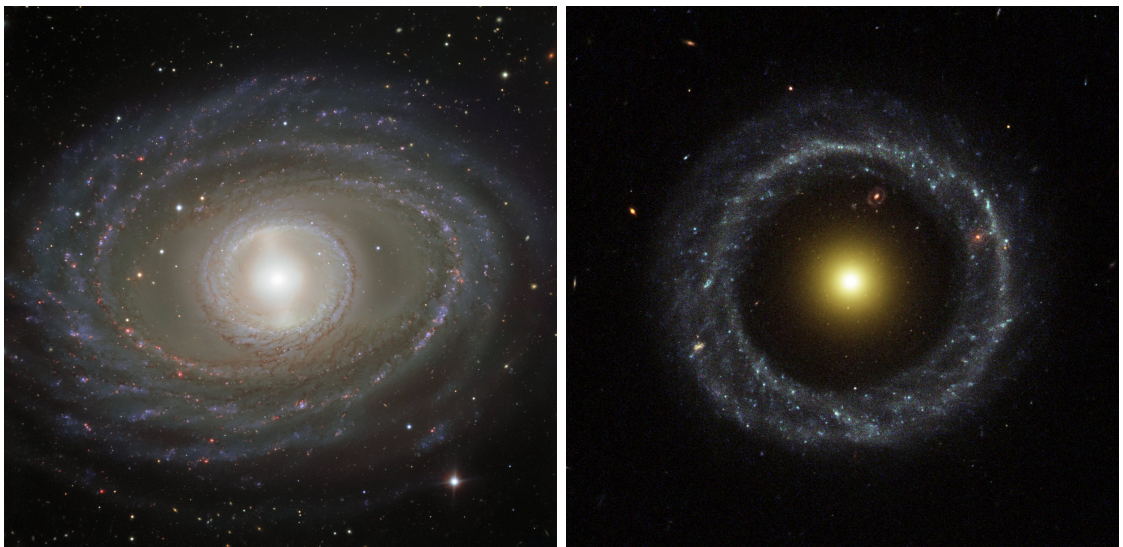


Figure 1.2: *Left:* Optical image of the galaxy NGC 1398 which is a prominent example of a disc galaxy hosting a strong bar and various rings. An inner ring directly connecting to the ends of the bar is clearly visible and encompassed by an outer ring at larger radii. The star formation deserts, i.e. two regions inside of the inner ring but outside of the bar, are also visible and characterised by lower surface brightnesses and redder colours. Credit: ESO. *Right:* Hubble observation of a galaxy known as Hoag's object (Hoag 1950), a prominent example of a galaxy exhibiting a collisional ring. Credit: NASA/ESA and The Hubble Heritage Team (STScI/AURA).

These structures are thought to arise via a continuous aggregation of gas at bar resonances. The bar exerts tangential forces on the gas in the galaxy disc, unless this gas is located close to a bar resonance. Inside of corotation resonance, the gas loses angular momentum and streams inwards, while outside of corotation the gas is pushed outwards. These slow gas movements are stopped at the OLR and the Ultra Harmonic Resonance (inner 4/1 resonance) of the bar where the tangential forces vanish and the gas accumulates. Subsequent star formation transforms this gas into stars and the resulting morphological structures are detectable as inner and outer rings (see e.g. Buta & Combes 1996; Kormendy & Kennicutt 2004). This process is well reproduced by a set of hydrodynamical simulations of barred galaxies (see e.g. Athanassoula 1992a; Rautiainen & Salo 2000; Kim et al. 2012b; Li et al. 2015).

However, not all rings in disc galaxies at sizes of several kiloparsecs are generated by secular evolution. Some external effects can cause the emergence of rings in disc galaxies as well, in particular encounters between galaxies. Polar rings are rings of stars and gas inclined with respect to the main disc of galaxies. These rings reach out over the pole

of the main galaxy (e.g. Sparke et al. 2008) and are typically thought to form from gas stripped from a companion galaxy, either during a close encounter or, under specific orbital configurations, a minor merger (Schweizer et al. 1983). Another interesting class of objects are the so-called ring galaxies, with the probably most famous example being Hoag’s object (Hoag 1950, see the right-hand image of Fig. 1.2). This object exhibits a central spheroid, but the galaxy disc appears to be confined to a detached ring structure. Lynds & Toomre (1976) argue that such objects are a result of high-velocity, face-on collisions with smaller galaxies. In this picture, the companion galaxy causes a significant, ring-like density wave in the galaxy while the smaller companion itself simply flies through it.

1.3.4 Disc Breaks

The radial surface brightness profiles of galaxies have originally been described as single-exponential profiles (Freeman 1970). However, already Freeman (1970) and later van der Kruit (1979) realised that some galaxy discs show significant breaks in their surface brightness profiles and, hence, require two exponential profiles to be properly modelled. While some galaxies exhibit steeper slopes in their outer parts (so-called down-bending discs) others have shallower surface brightness gradients beyond the break (so-called up-bending discs) or even multiple breaks throughout the disc. Numerous recent observations corroborate their findings and conclude that a substantial fraction of all galaxy discs show breaks in their radial surface brightness profiles (see e.g. Pohlen et al. 2002; Erwin et al. 2005; Gutiérrez et al. 2011; Comerón et al. 2012; Muñoz-Mateos et al. 2013; Kim et al. 2014), although their fraction of the total population of disc galaxies remain debated (Hunter & Elmegreen 2006; Pohlen & Trujillo 2006; Erwin et al. 2008).

The existence of such disc breaks is now known for more than half a century, however, their formation mechanism is still not fully understood. It has been proposed that disc breaks are a result of the angular momentum distribution during galaxy formation (van der Kruit 1987). Other studies propose that the emergence of disc breaks is related to the gas density in the disc or other constraints on the star formation efficiency like different phases of the interstellar medium (Kennicutt 1989; Elmegreen & Parravano 1994; Schaye 2004; Elmegreen & Hunter 2006). Today, bars are thought to play a major role in the formation of down-bending disc breaks. Based on numerical simulations, Foyle et al. (2008) conclude that initially single-exponential profiles easily develop down-bending disc breaks. In this picture, the formation of the disc break and flatter inner profile is connected to the development of the bar, while the outer surface brightness profile remains unaltered. Bittner et al. (2017) corroborate this connection between bars and down-bending disc breaks, at least for grand-design galaxies, by showing that the bar-interbar luminosity contrast correlates with the disc break radius.

1.4 Central Substructures in Disc Galaxies

The central regions of disc galaxies can host a large variety of stellar and gaseous substructures. Some of these components, in particular nuclear discs and nuclear rings, are thought to be formed through bar-driven secular evolution processes, while classical bulges are a result of more rapid, external processes. Box/peanuts and barlenses are simply the inner part of the bar itself that thickened through the bar’s buckling instability. The origin and physical nature of inner bars remains debated, but it is remarkable how closely they resemble the appearance and physical properties of main bars in the main discs of galaxies. In the following, we review these central structures in disc galaxies in detail.

1.4.1 Bulges in Disc Galaxies

The centres of disc galaxies often show a substantially different appearance compared to their outer parts. In the case of the Milky Way, this distinct central structure can already be recognized with the unaided eye on the night sky, but these structures have also long been observed in other galaxies. After initially being referred to with very ambiguous names, such as “amorphous central region”, “unresolved nuclear region”, and “central nucleus”, nowadays the morphologically distinct centres of disc galaxies are typically referred to as “bulges” (Madore 2016). This term is still highly ambiguous, as it has been used to refer to numerous central components found in disc galaxies that have vastly different formation mechanisms and physical properties.

For this reason, it is challenging to find a general definition of a bulge. Often a galaxy bulge is understood as a central component with an excess surface brightness above the inward extrapolation of the exponential surface brightness profile of the galaxy disc. Alternative approaches understand a galaxy bulge as a component that geometrically extends out of the plane of the galaxy disc (in the case of edge-on orientations) or other morphological constraints based on the analysis of isophotes (see e.g. Gadotti 2012; Fisher & Drory 2016). Nonetheless, such definitions of galaxy bulges remain highly ambiguous, unless the physical nature of these structures is understood. This is particularly important as the centres of disc galaxies host many different components with quite different physical properties that have historically been hard to distinguish and, hence, were misleadingly summarised with the term “bulge”.

Key to a better understanding of galaxy centres is numerous photometric studies that exploit multi-component decompositions of the galaxy light distribution. Such photometric decompositions are necessary as in disc galaxies, and in particular in their centres, the light of many distinct structural components overlap. In the past decades, a set of sophisticated fitting routines has been developed, both for one- and two-dimensional, multi-component decompositions (de Souza et al. 2004; Méndez-Abreu et al. 2008a; Peng et al. 2010; Erwin et al. 2015). These routines are not only capable of modelling the radial surface brightness profiles of discs and spheroids, but also other components, such as bars.

The surface brightness profiles of galaxy discs are typically described as exponential profiles

$$I(r) = I_0 e^{-r/r_0}, \quad (1.4)$$

with the surface brightness I , the radius r , the central surface brightness I_0 (at $r = 0$), and the scale length r_0 (Freeman 1970). While this exponential profile is well suited to model galaxy discs, elliptical galaxies (and some bulges of disc galaxies) typically show a stronger central light concentration that is better represented by a de Vaucouleurs profile (de Vaucouleurs 1948)

$$I(r) = I_0 e^{(-r/r_0)^{1/4}} \quad (1.5)$$

or more generally with a Sérsic profile (Sérsic 1963; Sérsic 1968)

$$I(r) = I_0 e^{(-r/r_0)^{1/n}} \quad (1.6)$$

with the Sérsic index n . This index describes the central light concentration of the radial profile, with high Sérsic indices being associated with high central light concentrations, as observed in the case of elliptical galaxies. In contrast, low values for the Sérsic index, when $n \sim 1$, correspond to an exponential profile and are again associated with disc-like structures (see e.g. Gadotti 2009).

Applying these photometric decompositions to the central regions of disc galaxies shows that there are structures that exhibit a range of different Sérsic indices. High central light concentrations are linked to the presence of dispersion-dominated spheroids, that is classical bulges, while Sérsic indices around unity are understood as a sign of so-called “pseudo-bulges” (Kormendy & Kennicutt 2004; Gadotti 2009; Méndez-Abreu et al. 2014).

Again, using the term pseudo-bulge to identify central structures with approximately exponential light profiles is highly ambiguous, as several physical components are showing this behaviour. This includes nuclear discs, nuclear rings and inner bars (which are thought to form from gas funnelled to the galaxy centre), as well as box/peanut structures (which are a result of the dynamical evolution of bars). Therefore, Athanassoula (2005) uses the term “disc-like bulge” to refer to nuclear discs and nuclear rings with the intention of more clearly distinguishing them from box/peanut structures.

As unclear as the nomenclature of the central stellar structure in disc galaxies are the metrics to photometrically distinguish between them. In some cases, the morphological structures are easily distinguishable by eye in photometric observations, for instance in the case of some box/peanut structures in edge-on galaxies or inner bars in face-on discs (see Figs. 1.4 and 1.5). Nonetheless, observationally distinguishing nuclear discs from classical bulges remains challenging, in particular when only photometric decompositions can be employed.

It has been proposed that a Sérsic index of $n = 2$ can be used as a threshold to distinguish between classical bulges and nuclear discs based on their central light concentration (see e.g. Fisher & Drory 2008; Gadotti 2009). However, there is no physical justification for this threshold and the typical measurement error of the Sérsic index is large compared to this value (see also Gadotti 2008, 2009; Fisher & Drory 2016; Neumann et al. 2017). In addition, the results of photometric decompositions fundamentally depend on the number of galaxy components included in the fit which typically is a subjective choice. Finally, the spatial resolution of the data constitutes another limitation to the accuracy of such studies (see also Section 7.1). To date, it remains challenging to distinguish nuclear discs and classical bulges solely based on photometric decompositions, resulting in significant observational uncertainties about their relative frequency, that is their number density and stellar mass distribution, in the Universe (Weinzirl et al. 2009; Kormendy et al. 2010; Sachdeva & Saha 2016; Kormendy 2016, but see also Sect. 7.1).

In summary, the large amount of ambiguities related to central stellar structures in disc galaxies, in particular the confusing nomenclature and the difficulties in photometrically distinguishing between them, highlight how complicated the central regions of disc galaxies are. This is further complicated by the fact that these structures are spatially overlapping, although exhibiting very distinct physical properties and formation scenarios. Eventually, thanks to spectroscopic observations of galaxies, the central components in disc galaxies can be better distinguished, their physical properties deciphered, and formation mechanisms constrained.

Below we review the current understanding of the formation, physical nature, and observational signatures of the central structures in disc galaxies. In particular, we summarise the properties of bar-built structures, such as nuclear rings, nuclear discs, and inner bars, as well as box/peanuts structures as the inner parts of bars, and violently-built classical bulges.

1.4.2 Nuclear Discs and Nuclear Rings

One of the most prominent effects bars have on disc galaxies is the bar-driven inflow of gas from the main galaxy disc to its centre. The non-axisymmetric potential of the bar exerts strong tangential forces onto the gas in the main disc of the galaxy which subsequently shocks and loses angular momentum. As a result, the gas streams inwards, in particular along the leading edges of the bar. The precise shape of these gaseous streamlines is determined by the bar's orbital configuration (Athanasoula 1992b). While the overall process of bar-driven gas inflow is well reproduced in numerous hydrodynamical simulations (see e.g. Piner et al. 1995; Kim et al. 2012b; Cole et al. 2014; Emsellem et al. 2015; Sormani et al. 2015; Fragkoudi et al. 2016), the gas inflow can also be observed in galaxies, in particular as prominent dust lanes extending along the bar (see e.g. Sheth et al. 2002; Gadotti et al. 2019). This is further illustrated in Fig. 1.3 in which these striking dust lanes can be seen.



Figure 1.3: Images of two poster child examples of strongly barred galaxies hosting a prominent nuclear disc (left-hand panel; NGC 1433) and star-forming nuclear ring (right-hand panel; NGC 1097). The striking dust lanes along the leading edges of the bars clearly highlight the bar-driven gas inflow from the main disc. Credit: ESA/Hubble & NASA, D. Calzetti (UMass) and the LEGUS Team – NGC 1433; ESO – NGC 1097.

However, this gas inflow does not directly continue to the centres of the galaxies. Instead, the flow is halted in the central regions, typically at radii of a few hundred parsecs from the galaxy centre where the gas accumulates in nuclear rings. Although the bar-driven gas inflow is a well-understood process, to date it remains somewhat debated which physical mechanism determines the radius at which this inflow is halted. Often the radius of nuclear rings is associated with bar resonances, in particular to the location of the ILR of the bar. In this picture, the gas inflow is constrained by the radial extent of the x_2 orbit family of the bar (see e.g. Combes & Gerin 1985; Athanasoula 1992a,b; Knapen 2005; Comerón et al. 2010, and references therein). However, based on hydrodynamical simulations, Kim et al. (2012a) argue that the radius of nuclear rings is simply a result of the residual angular momentum of the inflowing gas while more recently Sormani et al. (2018) discuss the effect of viscous shear forces on the properties and sizes of nuclear rings. Interestingly, Seo et al. (2019) conclude that nuclear rings are formed with small radii and later grow in radius simultaneously with the bar. In fact, observations suggest that the sizes of nuclear rings and bars are correlated (Knapen 2005; Comerón et al. 2010).

Regardless of the physical mechanism that constrains the radial gas inflow, the gas settles in the galaxy centre and, due to the collisional nature of gas, eventually cools and then proceeds to form stars. The result is the formation of new stellar components in the galaxy

centre, in particular nuclear discs and nuclear rings. While nuclear rings show both an inner and outer edge, nuclear discs appear to be continuous components from an outer edge throughout the galaxy centre (Buta et al. 2015). The morphological difference between both structures is further illustrated in Fig. 1.3. To date, it remains unclear why some galaxies appear to host nuclear discs while the centres of others are dominated by nuclear rings, although both structures are thought to form via the same bar-driven mechanism.

The resulting nuclear discs and nuclear rings are frequent structures in barred galaxies and approximately 20 % of all disc galaxies host nuclear rings (Comerón et al. 2010). The majority of nuclear rings in this study exhibit radii of a few hundred parsecs, although the largest nuclear rings have radii up to ~ 2 kpc. Interestingly, de Sá-Freitas et al. (in prep.) detects nuclear rings that are as small as ~ 70 pc in radius.

If these nuclear discs are indeed bar-built structures, then nuclear discs should almost solely be observed in barred galaxies. However, to date, it remains debated if nuclear discs sometimes exist in unbarred galaxies and, if they do, what fraction of nuclear discs exist in these peculiar circumstances. Comerón et al. (2010) compiles an atlas of rings in a total of 107 galaxies and concludes that 19 % of all nuclear discs exist in unbarred galaxies. However, they argue that at least some of these galaxies show non-axisymmetric features in their discs that could, in principle, facilitate the formation of a nuclear ring analogous to the bar-driven scenario. In our own visual inspections of these galaxies we corroborate this picture, find signatures of previously undetected bars, and conclude that, at least in some cases, the limited spatial resolution prevents a reliable detection of bars and nuclear discs. In summary, from an observational perspective, there is convincing evidence that barred galaxies frequently host nuclear discs (Comerón et al. 2010; Buta et al. 2015), but it remains unclear how rare nuclear discs are in unbarred disc galaxies.

In an alternative scenario, the formation of a nuclear disc could have been triggered by a bar via the inflow of gas from the main galaxy disc but if the bar dissolved after this process, one would detect a bar-built nuclear disc located in an unbarred galaxy. However, bars are thought to be long-lived and dynamically stable structures that are difficult to destroy once they have formed, except in the case of significant mergers or a very gas-rich disc (Bournaud et al. 2005a; Berentzen et al. 2007; Kraljic et al. 2012). In this context, it is also unclear if a nuclear disc would survive a dynamical disturbance strong enough to dissolve a stable bar.

Scenarios for a merger-induced build-up of nuclear discs – independently from bars – have also been explored. For instance, Mayer et al. (2008) and Chapon et al. (2013) argue based on hydrodynamical simulations that the tidal torques in galaxy mergers can cause gas inflows resulting in the formation of a nuclear disc in the centre of the merger remnant. However, the nuclear discs in their models are typically one order of magnitude smaller than those observed in the local Universe. Eliche-Moral et al. (2011) claim that nuclear discs can even be reproduced in collisionless N-body simulations of minor galaxy mergers, at least under specific circumstances. Nonetheless, the kinematic properties of their simulated nuclear discs are inconsistent with the conclusions of recent observational studies (Gadotti et al. 2019) and the results presented in this thesis (Chapters 3 and 4).

1.4.3 Box/Peanut Structures

While nuclear discs and nuclear rings are formed via in-situ star formation in the galaxy centre, other prominent inner structures are a result of dynamical processes concerning the stellar component of the bar. The so-called box/peanuts (sometimes also referred to as X-shaped bulges) are generally thought to be a result of a second instability after the formation of the bar, in particular its buckling instability. In summary, the vertically thickened part of the bar arises as a result of dynamical instabilities and resonant heating (Combes & Sanders 1981; Combes et al. 1990; Pfenniger & Friedli 1991; Raha et al. 1991; Martínez-Valpuesta et al. 2006). Interestingly, this buckling instability leading to the formation of box/peanuts is observed to affect not only main bars but also inner bars (Méndez-Abreu et al. 2019, see also Sect. 1.4.4).

As a result of this instability, the inner part of the bar thickens vertically out of the disc plane, but also within the disc plane perpendicular to the major axis of the bar. The vertical thickening can be easily observed in edge-on galaxies as box/peanut or X-shaped structures in their centre (see Fig. 1.4). In galaxies with a face-on orientation, the same structure becomes detectable as a so-called barlens, that is a structure shorter and less eccentric than the bar itself (Athanasoula et al. 2015; Gonzalez & Gadotti 2016; Laurikainen & Salo 2017).

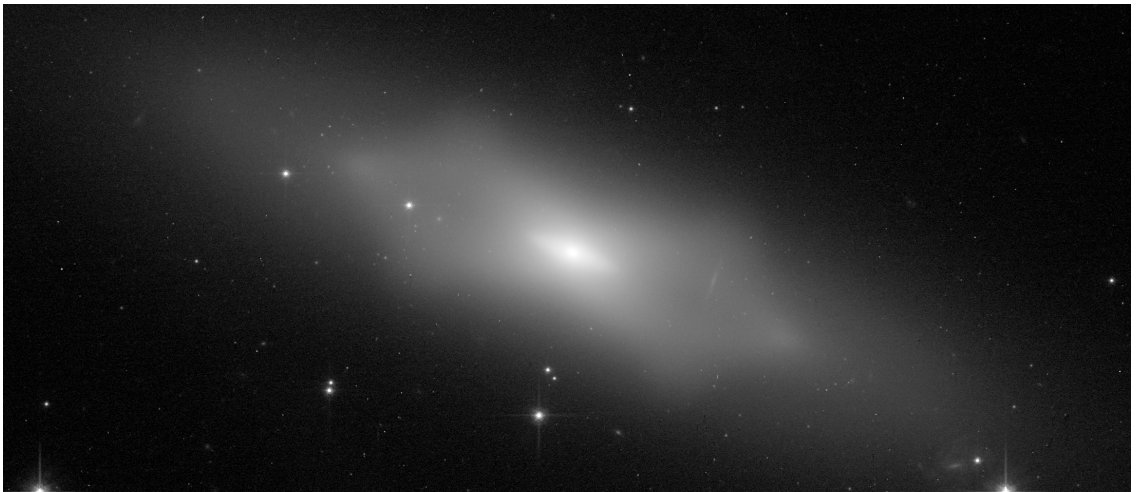


Figure 1.4: Hubble image of the edge-on galaxy NGC 1175 hosting a pronounced box/peanut (X-shaped) structure. Credit: NASA/ESA Hubble Space Telescope and William Keel (University of Alabama) and the Galaxy Zoo team.

While box/peanuts in edge-on galaxies are easy to identify, their detection in only mildly inclined or even face-on galaxies is more challenging. Nonetheless, a set of signatures to identify box/peanuts in these cases have been developed, based on both photometric and spectroscopic arguments (Debattista et al. 2005; Méndez-Abreu et al. 2008b; Erwin & Debattista 2013; Łokas 2019; Fragkoudi et al. 2020). For instance, box/peanuts can be detected in spatially resolved maps of stellar kinematics as bi-symmetric minima of the higher-order moment h_4 of the LOSVD along the major axis of the bar.

Generally, box/peanuts are frequent structures in barred galaxies. Recent studies indicate that between 50 % (Méndez-Abreu et al. 2014) and 79 % (Erwin & Debattista 2017) of barred galaxies exhibit signatures of box/peanut structures. Their frequency is decreasing with increasing redshift and also a strong function of stellar mass, with box/peanuts being

found most often in massive barred galaxies (Kruk et al. 2019). In fact, the Milky Way is also known to host a box/peanut bulge in its centre (see e.g. Shen et al. 2010; Li & Shen 2012; Gerhard & Martinez-Valpuesta 2012; Vásquez et al. 2013; Fragkoudi et al. 2018).

1.4.4 Inner Bars

Main bars located in the main discs of galaxies are very frequent structures, however, some galaxies host more than only one bar at a time. In addition to the main bar, these double-barred galaxies also host a smaller, inner bar in their centres that closely resemble the morphological appearance of main bars (see Fig. 1.5). After the discovery of the first double-barred galaxy in the 1970s (NGC 1291; de Vaucouleurs 1974, 1975), today numerous galaxies hosting inner bars are known. While previous estimates concluded that approximately 30% of all barred galaxies host two bars (Erwin & Sparke 2002; Laine et al. 2002; Erwin 2004; Buta et al. 2015), more recently Hildebrandt et al. (2020) claim that only 12% of all barred galaxies are indeed double-barred. To date, these measurements provide only lower limits on the frequency of inner bars. The small physical sizes of inner bars (0.3 kpc to 2.5 kpc; de Lorenzo-Cáceres et al. 2020), the limited spatial resolution of large photometric surveys, the many spatially co-existing stellar components in galaxy centres, and the influence of gas and dust in late-type disc galaxies make their detection a challenging task.



Figure 1.5: Image of the galaxy NGC 7098 hosting a prominent main and inner bar, both oriented towards the upper-left of the image. Credit: ESO.

The most extensive set of spectroscopic studies on inner bars is the one conducted by de Lorenzo-Cáceres et al. (2008, 2012, 2013). Using long-slit and integral-field spectroscopic observations, they explore the stellar kinematics, population properties, and ionized gas content of inner bars. They discover a striking spectroscopic characteristic of inner bars, typically referred to as “ σ -hollows”. More precisely, the outer ends of inner bars are prominently highlighted as regions of low velocity dispersion. To date, these σ -hollows have been detected in all spectroscopic observations of inner bars (see also Méndez-Abreu et al. 2019). de Lorenzo-Cáceres et al. (2008) suggest that these σ -hollows are a result of kinematically distinct components (e.g. a dispersion-dominated spheroid and the comparably cold inner bar) dominating the stellar light at different spatial locations. Based on numerical simulations, Du et al. (2017) claim that such σ -hollows might also exist in the main bars of single-barred galaxies, but observationally their existence is not well established (see also Chapter 3).

The physical nature and formation mechanism of inner bars remain debated, but so far two scenarios have been proposed. Firstly, inner bars might form directly from gas brought to the galaxy centre that gets trapped in the elongated x_2 orbits of the main bar. Subsequent star formation transforms this initially gaseous component into a stellar inner bar. However, an inner bar formed via this scenario is not dynamically stable and, given the short dynamical timescales in the centres of disc galaxies, should rapidly mix and vanish (Friedli & Martinet 1993; Heller et al. 2001; Shlosman & Heller 2002; Englmaier & Shlosman 2004). Alternatively, it has been suggested that inner bars could form from a dynamical instability in the nuclear disc, analogous to the formation of main bars in main galaxy discs. In this picture, the main difference between inner and main bars is not their dynamical nature or formation mechanism, but only the spatial scale on which they develop. Such a purely dynamical origin of inner bars without the requirement of star formation is reproduced in N-body simulations (Rautiainen et al. 2002; Debattista & Shen 2007; Shen & Debattista 2009; Du et al. 2015; Wozniak 2015). Inner bars formed this way are expected to evolve similarly to main bars and are persistent, long-lived structures. The recent numerical simulations of Wozniak (2015) produce inner bars that are stable for as long as 7 Gyr.

Recent observational studies aimed to better characterise the stellar kinematics and population content in inner bars to shed further light on their formation processes. Méndez-Abreu et al. (2019) explored the stellar kinematics of the galaxy NGC 1291 and discovered a box/peanut structure related to the inner bar in this galaxy. This suggests that inner bars undergo the same buckling instability as main bars what strongly supports the idea that both structures form via similar disc instabilities. Moreover, de Lorenzo-Cáceres et al. (2019b) combined detailed, multi-component photometric decompositions with integral-field spectroscopic observations of two double-barred galaxies. The derived star formation histories suggest that the inner bars are 4.5 Gyr and 6.5 Gyr old, reinforcing the idea that inner bars are dynamically stable structures.

If inner bars are indeed long-lived structures, they might represent an important clue to galaxy evolution, in particular as a mechanism to feed AGN. Main bars are known to efficiently transport gas from the main galaxy disc to its central regions. However, this gas inflow is typically halted a few hundred parsecs from the centre where the gas accumulates in a nuclear ring. At this point, the non-axisymmetric potential of the inner bar might enable further gas inflow to the direct vicinity of the central black hole (Shlosman et al. 1989, 1990) where it eventually can be accreted.

1.4.5 Classical Bulges

Although the formation of nuclear discs, nuclear rings, box/peanuts, and inner bars is ultimately a result of secular evolution processes, not all central stellar components in disc galaxies are formed in this way. In fact, the formation of classical bulges is based on more rapid and violent processes (see Fig. 1.6).

Classical bulges are generally thought to be a result of the early and violent phases of galaxy evolution. Minor mergers of galaxies with mass ratios between 1:4 and 1:10 are expected to often result in disc galaxies with compact classical bulges in their centres (Bournaud et al. 2005b, but see also Brooks & Christensen 2016 for a review). In this picture, the build-up of the classical bulge is not driven by the violent relaxation of the existing stellar components but instead facilitated by the chaotic, merger-driven gas inflow to the merger remnant and subsequent star formation. As a result, this mechanism depends on the gas fraction of



Figure 1.6: Image of the early-type disc galaxy NGC 4594 (also known as Sombrero Galaxy) which hosts a striking classical bulge. Credit: ESO/P. Barthel, Mark Neuser (Kapteyn Institute, Groningen) and Richard Hook (ST/ECF, Garching, Germany).

the merging galaxies (Hopkins et al. 2009b), and the resulting classical bulges are formed in-situ of the merger remnant, consistent with the results of cosmological simulations (see Brooks & Christensen 2016, and references therein).

In an alternative scenario, classical bulges could as well be formed via fragmentation and clump migration in high-redshift disc galaxies. Massive galaxy discs at high-redshifts are globally unstable and naturally fragment into giant clumps. As a result of gravitational torques and dynamical friction, these clumps consisting of gas and stars lose angular momentum and sink towards the galaxy centre where they contribute to the assembly of a classical bulge. Apart from the clumps originating in the galaxy disc itself, this process proceeds analogous to the accretion of a satellite galaxy in a minor merger (see e.g. Shlosman & Noguchi 1993; Noguchi 1999; Elmegreen et al. 2008; Bournaud 2016; Brooks & Christensen 2016).

As a result of their violent formation process, classical bulges are expected to typically be dispersion dominated components, that is exhibit high velocity dispersions and little rotational support. As they are typically formed at early cosmic epochs, classical bulges are characterised by old stellar populations and, as a result of their rapid formation process, elevated $[\alpha/\text{Fe}]$ enhancements (see e.g. Fisher & Drory 2016).

In the picture of hierarchical structure formation, the fundamental process that facilitates the growth of structures is the merging of smaller halos (White & Rees 1978). Therefore mergers, and in particular minor mergers that should result in the formation of classical bulges, are expected to be very common (see e.g. Maller et al. 2006; Stewart et al. 2008; Fakhouri et al. 2010). As a result, classical bulges should be ubiquitously present in the centres of disc galaxies and, at least in the local Universe, easy to identify. However, current observational constraints on their abundance often indicate the contrary. A large fraction of disc galaxies in the local Universe seem to not host a classical bulge (see e.g. Weinzirl et al. 2009; Kormendy et al. 2010; Fisher & Drory 2011; Sachdeva & Saha 2016). We discuss the implications of this apparent discrepancy in greater detail in Sect. 7.1 (but see also Brooks & Christensen 2016; Kormendy 2016, for reviews).

1.5 Constraints on Global Galaxy Evolution

Studying the nature of central substructures, such as nuclear discs, not only helps to better understand their formation in the context of bar-driven secular evolution but also allows constraining the evolutionary history of their host galaxies in a more global context.

1.5.1 Measuring the Age of Bars

Early in cosmic history, the evolution of galaxies is mostly driven by fast and violent processes, that is galaxy mergers in the context of hierarchical structuring, while in the local Universe, at least outside of dense environments, galaxy evolution often is a slow process driven through mechanisms internal to the galaxy (Kormendy & Kennicutt 2004). Understanding when this transition from external to internal evolution occurred in individual disc galaxies is an important aspect of extragalactic astrophysics.

One clear signature of this transition from turbulent and kinematically hot galaxy discs at high redshifts to the kinematically cold and rotationally dominated galaxies in the local Universe is the first occurrence of bars. Once a galaxy disc is dynamically mature and subject to self-gravity, bars are known to form very rapidly within them (Kraljic et al. 2012). Therefore, the time in cosmic history when a galaxy disc first became dynamically mature can be determined by measuring the age of its bar.

But estimating the age of bars is not straightforward: as bars are a result of dynamical instabilities in the galaxy disc, they consist of stars that formed in this disc long before the bar came into existence itself. However, nuclear discs in the centres of these galaxies open an opportunity to constrain the bar ages. As the stellar populations in a nuclear disc are thought to be formed from gas brought to the galaxy centre shortly after the emergence by the bar itself, the star formation histories of these nuclear discs can be used to constrain the ages of bars. More precisely, the oldest episode of star formation unique to the nuclear disc signifies the time of the first bar-driven gas inflow and, hence, provides a lower limit on the age of the bar. In this way, the effects of bar-driven secular evolution in the central regions of disc galaxies allow constraining the development of galaxies in a more global context.

Determining the age of bars from the star formation histories in nuclear discs is the main question posed by the TIMER survey (Time Inference with MUSE in Extragalactic Rings; Gadotti et al. 2019). Recent studies of the collaboration, including the results presented in this thesis, lay out the basis for a detailed understanding of star formation histories in nuclear discs that will be used to derive bar ages.

1.5.2 Internal versus External Evolution of Disc Galaxies

The formation scenarios of nuclear discs and classical in the centres of disc galaxies are substantially different (see Chapter 1.4). While nuclear discs are the results of internal, bar-driven evolution, the formation of classical bulges is typically thought to be a result of violent and external processes, in particular minor mergers.

Therefore, the relative frequency of nuclear discs and classical bulges, in particular their number density and stellar mass distribution, might be an indicator of the relative importance of their formation processes. In other words, the central regions of disc galaxies might hold clues on whether the evolution of a particular galaxy was dominated by exter-

nal or internal processes. This might offer new possibilities to investigate this aspect of galaxy evolution as a function of galaxy mass and environment and provide fundamental constraints to large-scale cosmological simulations (see Sect. 7.1).

1.6 Goals of this Thesis

The main goal of this thesis is to better understand the effects of bar-driven secular evolution on the centres of disc galaxies. We aim to characterise the properties of central stellar structures, such as nuclear discs, nuclear rings, and inner bars, in more detail by simultaneously investigating their stellar kinematics and mean stellar population content together with their morphology. These measurements will help to decipher their formation processes and evolutionary history, in particular in the picture of bar-driven secular evolution. In this context, we will specifically address the following questions:

- How are nuclear discs and nuclear rings characterised by their stellar kinematics and mean population properties? Are these properties consistent with their bar-driven formation scenario? Can merger-driven formation mechanisms be ruled out?
- Why do the centres of some galaxies appear to be dominated by nuclear rings, while others appear to host nuclear discs? What is the precise difference between these structures, or are these simply distinct parts of the same physical component?
- How exactly do nuclear discs and nuclear rings form in the picture of bar-driven secular evolution? Do nuclear discs and nuclear rings grow with time or is their spatial extent set during their initial formation?
- Are the spectroscopically identified nuclear discs indeed the exponential, disc-like bulges known for decades from photometric decompositions of disc galaxies?
- What is the physical nature of inner bars? Are these structures (dynamically) similar to main bars and only a scaled-down version of them? Or are inner bars only transient features in nuclear discs that rapidly disappear due to orbital mixing?
- Can these bar-built stellar structures help to constrain galaxy formation and evolution in a more global context, or even provide some constraints to cosmological models?

To address these questions, we exploit integral-field spectroscopic observations from the Multi Unit Spectroscopic Explorer (MUSE; Bacon et al. 2010) at ESO’s Very Large Telescope, obtained as part of the TIMER survey (Gadotti et al. 2019). The TIMER sample consists of a total of 24 galaxies of which, to date, 21 have been observed, amounting to almost two million spectra. The sample has been drawn from the *Spitzer* Survey of Stellar Structures in Galaxies (S⁴G; Sheth et al. 2010) and, hence, is restricted to bright ($m_B < 15.5$ mag) and large ($D_{25} > 1$ arcmin) galaxies in the local Universe ($d < 40$ Mpc). Moreover, the sample was selected to show significant signatures of bar-built central substructures, as determined by Buta et al. (2015), exhibit relatively face-on inclinations ($i < 60$ deg), and eventually samples a stellar mass range from $2.0 \times 10^{10} M_\odot$ to $17.4 \times 10^{10} M_\odot$. Thanks to the superb spatial sampling of the MUSE spectrograph of 0.2 arcsec, a typical seeing during the observations of 0.8 arcsec to 0.9 arcsec, together with the fact that only nearby galaxies are observed, the TIMER survey provides a unique data set sampling the central regions of disc galaxies at unprecedented physical spatial resolution.

This thesis is structured as follows: in the next chapter, we detail the development of a software framework for the analysis and visualisation of (integral-field) spectroscopic data that was fundamental to the swift and robust exploration of the TIMER observations. In

Chapter 3 we investigate the stellar kinematic properties of nuclear discs, before discussing their mean stellar population content in Chapter 4. A thorough analysis of the stellar population content of inner bars leading to new constraints on their dynamical structure is presented in Chapter 5. We summarise the results of this thesis in Chapter 6. Finally, we provide an outlook on possible future studies and review the motivation for the forthcoming BANG survey in Chapter 7.

The GIST Pipeline

A Multi-Purpose Tool for the Analysis and Visualisation of (Integral-field) Spectroscopic Data

We present a convenient, all-in-one framework for the scientific analysis of fully reduced, (integral-field) spectroscopic data. The Galaxy IFU Spectroscopy Tool (GIST) is entirely written in Python 3 and conducts all the steps from the preparation of input data to the scientific analysis and to the production of publication-quality plots. In its basic set-up, it extracts stellar kinematics, performs an emission-line analysis, and derives stellar population properties from full spectral fitting and via the measurement of absorption line-strength indices by exploiting the well-known pPXF and GandALF routines, where the latter has now been implemented in Python. The pipeline is not specific to any instrument or analysis technique and provides easy means of modification and further development, thanks to its modular code architecture. An elaborate, Python-native parallelisation is implemented and tested on various machines. The software further features a dedicated visualisation routine with a sophisticated graphical user interface. This allows an easy, fully interactive plotting of all measurements, spectra, fits, and residuals, as well as star formation histories and the weight distribution of the models. The pipeline has been successfully applied to both low- and high-redshift data from MUSE, PPAK (CALIFA), and SINFONI, and to simulated data for HARMONI and WEAVE and is currently being used by the TIMER, Fornax3D, and PHANGS collaborations. We demonstrate its capabilities by applying it to MUSE TIMER observations of NGC 1433.

2.1 Introduction

Over the past decades, spectroscopic observations have provided significant insights into the fundamental properties of galaxies. In particular, the measurement of stellar and gaseous motions as well as the inference of stellar population properties have made substantial contributions to our understanding of the formation and evolution of galaxies.

With the introduction of the first integral-field spectrographs (IFS, see e.g. Bacon et al. 1995), it became feasible to perform such observations in a spatially resolved manner and for larger samples of galaxies. The SAURON survey (Bacon et al. 2001; de Zeeuw et al. 2002) was one of the first projects to make extensive use of this technology. Based on their representative sample of 72 nearby early-type galaxies, the project investigated stellar and gaseous kinematics (Emsellem et al. 2004; Sarzi et al. 2006; Falcón-Barroso et al. 2006; Ganda et al. 2006) and stellar population properties (Peletier et al. 2007; Kuntschner et al. 2010), and distinguished between fast and slow rotating early-type galaxies (Emsellem et al. 2007). Subsequently, the ATLAS^{3D} project (Cappellari et al. 2011a) continued this endeavour by further investigating kinematic properties, for instance the global specific angular momentum (Emsellem et al. 2011), based on a volume complete sample of 260 early-type galaxies. The CALIFA survey (Sánchez et al. 2012) advanced these previous

studies towards a morphologically unbiased sample of 667 galaxies. In addition, it provides a unique combination of a large spatial coverage of a few effective radii and high spatial sampling (see also García-Benito et al. 2015). Other surveys observe even larger samples: while the SAMI survey (Croom et al. 2012; Bryant et al. 2015) includes ~ 3000 galaxies across different environments, MaNGA (Bundy et al. 2015) will contain approximately 10 000 nearby galaxies. Most recently, these projects are being complemented by IFS studies of local galaxies in unprecedented spatial resolution (e.g. MUSE, Bacon et al. 2010). For instance, the TIMER project (Gadotti et al. 2019) analyses the central structures of 24 barred local disc galaxies in order to study the formation histories of these structures and infer constraints on the related secular evolution processes. Fornax3D (Sarzi et al. 2018; Iodice et al. 2019) investigates mostly early-type galaxies in the Fornax cluster environment, spatially covering galaxies up to four effective radii. The PHANGS survey (Leroy et al.,¹ in prep.) aims to connect the physics of gas and star formation with the large-scale galactic structure by complementing IFS data from MUSE with interferometric data from ALMA.

Spatially resolved spectroscopic data contain an outstanding amount of information. It is not only possible to measure the stellar motions and perform an emission-line analysis, but also to infer star formation histories. However, the extraction of these quantities from the science-ready IFS data is very complex, and sophisticated analysis techniques are indispensable. Over time a set of commonly used and well-tested techniques for this analysis has emerged. After various pioneering works on the measurement of stellar kinematics since the early 1970s (see e.g. Simkin 1974; Sargent et al. 1977; Tonry & Davis 1979; Franx et al. 1989; Bender 1990; Rix & White 1992; Kuijken & Merrifield 1993; van der Marel & Franx 1993; Statler 1995; Merritt 1997), the vast majority of recent studies exploit the penalised pixel-fitting code `pPXF` (Cappellari & Emsellem 2004; Cappellari 2017) to infer a stellar line-of-sight velocity distribution (LOSVD). Similarly, the Gas and Absorption Line Fitting (`GandALF`) software (Sarzi et al. 2006; Falcón-Barroso et al. 2006) as well as the `pyPARADISE` tool (Walcher et al. 2015; Husemann et al. 2016) are methods widely used to conduct a thorough emission-line analysis. Non-parametric star formation histories can, for instance, be extracted with `MOPED` (Heavens et al. 2000), `pPXF`, `STARLIGHT` (Cid Fernandes et al. 2005), `STECKMAP` (Ocvirk et al. 2006a,b), `VESPA` (Tojeiro et al. 2007), as well as `ULySS` (Koleva et al. 2009).

Such a well-established set of sophisticated techniques provides a good base for the analysis of spectroscopic data. Moreover, the application of these techniques to actual data is, in principle, not difficult, as implementations of these codes are widely available. However, in practice this task soon becomes very tedious; the use of different IFS instruments, spectral template libraries, and analysis set-ups in the context of different scientific objectives and surveys add some inconvenience to the day-to-day usage of these techniques. Further complications arise if a very large sample of galaxies makes use of an automated pipeline necessary, especially in light of the tremendous amount of spectra provided by state-of-the-art instruments (e.g. MUSE) and therefore the inevitable requirement of parallelised software.

We aim to overcome these inconveniences by introducing the Galaxy IFU Spectroscopy Tool (`GIST`), which is modular and general enough to be easily applied to data from all existing IFS instruments and in the context of different scientific objectives and surveys. In particular, the code architecture provides easy means of modification and expansion, while being a convenient all-in-one framework for the scientific analysis of fully reduced

¹<http://www.phangs.org/>

IFS data. In addition, the software package features sophisticated visualisation routines and employs a well-tested parallelisation. While this is not the first time a pipeline of this sort has been developed (e.g. `Pipe3D`, Sánchez et al. 2016; LZIFU, Ho et al. 2016 or the MaNGA pipeline, Westfall et al. 2019), it is the first time one has been offered publicly with a wide range of built-in configurations for several instruments and surveys. The large scientific community that is in need of such a multi-purpose IFS analysis tool is highlighted by the fact that the `GIST` pipeline is already being employed by the `TIMER`, `Fornax3D`, and `PHANGS` collaborations. In addition, various researchers are applying the code to both low- and high-redshift data from `MUSE`, `PPAK` (`CALIFA`), and `SINFONI` (Eisenhauer et al. 2003), and to simulated data for `HARMONI` (Thatte et al. 2010a) and `WEAVE IFU` modes (Dalton et al. 2012).

This paper is organised as follows. In Sect. 2.2 we introduce the core design principles of the pipeline, its code architecture and workflow, and the most important aspects of the implementations. In Sect. 2.3 we apply the pipeline to `TIMER` data of NGC 1433 obtained with the `MUSE` spectrograph. We finish with a summary of this work in Sect. 2.4.

2.2 Pipeline Implementation

In this section we summarise the core principles we followed in the design of the `GIST` pipeline. We further detail the architecture of the code and its general workflow, before presenting the details of the implementation of all modules included in this framework.

2.2.1 Core Design Principles

The pipeline architecture is designed in such a way that the following high-level objectives are achieved.

Convenience: Our aim is to provide a convenient, all-in-one framework for the scientific analysis of fully reduced (integral-field) spectroscopic data. This includes all steps from the read-in and preparation of input data over the several analysis steps to the production of well-structured output tables and publication-quality plots. Such a framework not only accelerates and simplifies the analysis, but also assures the consistency of the analysis throughout large data samples.

Extensive Functionality: The basic version of the `GIST` pipeline extracts stellar kinematics and non-parametric star formation histories by exploiting the `pPXF` routine (Cappellari & Emsellem 2004; Cappellari 2017), determines gaseous kinematics and emission-line fluxes with the `GandALF` procedure (Sarzi et al. 2006; Falcón-Barroso et al. 2006), and measures line strength indices, as well as the corresponding single-stellar population equivalent population properties (SSP; Kuntschner et al. 2006; Martín-Navarro et al. 2018). These methods can be executed in a multitude of different flavours and configurations (see Sect. 2.2.3).

Flexibility: This code is not specific to any instrument, fitting procedure, or scientific project. Instead, the implementation features a high level of flexibility, as we aim to provide an analysis framework that suits the needs of a variety of scientific objectives across various collaborations. This flexibility is evident given that the pipeline is

capable of handling data from different instruments and its execution can be tailored to reflect a variety of different flavours in either interactive or non-interactive batch processing manner.

Modifiability/Expandability: Regardless of how extensive and flexible an analysis pipeline is, it is virtually impossible for one particular design to satisfy all conceivable scientific requirements. Thus, it is necessary to provide easy means of modification of the code that will allow it to tackle specific problems. This can be achieved by using a modular architecture while keeping the source code as clean and readable as possible. Moreover, this makes it straightforward for the user to expand the pipeline by adding user-defined modules.

Visualisation: The GIST pipeline outputs various high-level data products. However, while visualisation routines for input IFS cubes are widely available (e.g. QFitsView²), the software capable of displaying the data products is still limited (e.g. E3D³, PINGSOFT⁴, MARVIN⁵), and it is often specific for an instrument or project. These visualisation routines are important in order to simplify the inspection of the output and facilitate the immediate monitoring of observed spectra, their best fits, and residuals. Thus, in this software package we provide the dedicated visualisation routine `Mapviewer`, specifically designed to access all data products of this pipeline. To this end, it exploits a sophisticated graphical user interface with fully interactive plots. For instance, the spectra, their corresponding fits and residuals, the star formation histories, and the weight distribution of the models in a particular bin can be plotted by only a simple mouse-click on the given bin in the map. The `Mapviewer` is highly performance optimised and thus capable of handling the bulk of data products without noticeable interruption.

Performance: State-of-the-art IFS instruments output an enormous number of spectra per pointing. This implies significant computational expense for the analysis of the data, in particular when larger samples of galaxies are considered. This necessitates the use of parallelised software and large, cluster-scale computing resources. In particular, a Python-native parallelisation, based on its `multiprocessing` module, is implemented to conduct the analysis on multiple spectra simultaneously. This parallelisation has been successfully tested with up to 40 processors on various machines and scales linearly.

The code is publicly available through a dedicated webpage⁶. Additional analysis modules, for instance the inclusion of `STECKMAP` and `pyPARADISE`, will be done in the future. We encourage the community to put forward their own input on the future development of the code, in particular by creating their own specific modules.

This paper intends to give an overview of the extensive capabilities of the code and is complemented by online documentation⁶, which includes detailed information on the practical use of the pipeline. Therefore we describe its download and installation, and provide a dedicated tutorial. In addition, the documentation gives various examples of the pipeline usage and instructions on its modification.

²<http://www.mpe.mpg.de/~ott/dpuser/qfitsview.html>

³<http://www.caha.es/sanchez/euro3d/>

⁴<https://www.inaoep.mx/~frosales/pings/html/software/>

⁵<https://www.sdss.org/dr15/manga/marvin/>

⁶<https://abittner.gitlab.io/thegistpipeline>

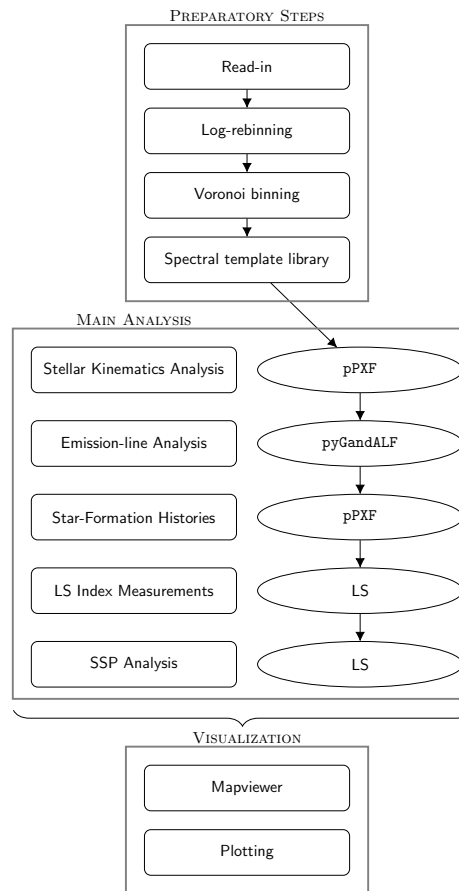


Figure 2.1: Flowchart illustrating the architecture of the pipeline. The code is structured in three parts: preparatory operations, main analysis procedures, and visualisation routines. Each of these parts consists of various individual modules.

Although we provide this pipeline as a convenient, all-in-one framework for the analysis of IFS data, it is of fundamental importance that the user understands exactly how the involved analysis methods work. We warn that the improper use of any of these analysis methods, whether executed within the framework of the GIST pipeline or not, will likely result in spurious or erroneous results, and their proper use is solely the responsibility of the user. Likewise, the user should be fully aware of the properties of the input data before intending to derive high-level data products. Therefore, this pipeline should not be simply adopted as a ‘black box’. To this end, we urge all users to become familiar with the input data and the analysis methods, and with their implementation in this pipeline.

2.2.2 Code Architecture and Workflow

To achieve the design goals presented in the previous section, the pipeline structure has three major elements: preparatory operations, main analysis procedures, and visualisation routines. Each of these parts consists of various individual modules. Figure 2.1 illustrates the code architecture. In Sect. 2.2.3 we present an in-depth discussion of the implementation of each of these modules.

The four major preparatory steps are the read-in of the fully reduced, science-ready data cube; the logarithmic rebinning of the spectra in the wavelength dimension (to obtain spectra that are linearly binned in velocity space); the Voronoi binning of the spectra in the spatial dimensions (using the routine of Cappellari & Copin 2003 to obtain integrated spectra of approximately constant signal-to-noise ratio); and the necessary preparation steps in regards to the spectral template library. These preparatory steps need be executed regardless of any further analysis, and are not repeated afterwards.

The main analysis section consists of four modules: two of these modules exploit the `pPXF` routine in order to extract stellar kinematics (hereafter `PPXF` module) and non-parametric star formation histories (hereafter `SFH` module). Emission-line kinematics and fluxes are extracted by calling a new Python implementation of the original `GandALF` procedure (hereafter `GANDALF` module). Finally, line strength indices and their corresponding SSP-equivalent population properties are measured with the routines already used by Kuntschner et al. (2006) and Martín-Navarro et al. (2018) (hereafter `LS` module). These analysis modules are simply interfaces around the implementations of the mentioned analysis techniques, mainly acting as an interface to the pipeline and handling the input and output. These four modules are fully independent, but may use each other's results as input. In other words, the modules can be turned on and off, or even be replaced by different, user-defined modules without affecting the overall integrity of the pipeline. As these modules are independent, the parallelisation is implemented in each module individually (see Sect. 2.2.3 for a full discussion on the configuration options).

Finally, visualisation routines complement the analysis framework. Publication-quality plots of all results are automatically generated during the analysis. In addition, all plotting routines can also be executed independently from the analysis pipeline in order to allow the user any specific plotting preferences. A fully interactive visualisation method is provided by the routine `Mapviewer`, as discussed in Sect. 2.2.1. A screenshot of this routine can be found in Fig. 2.2.

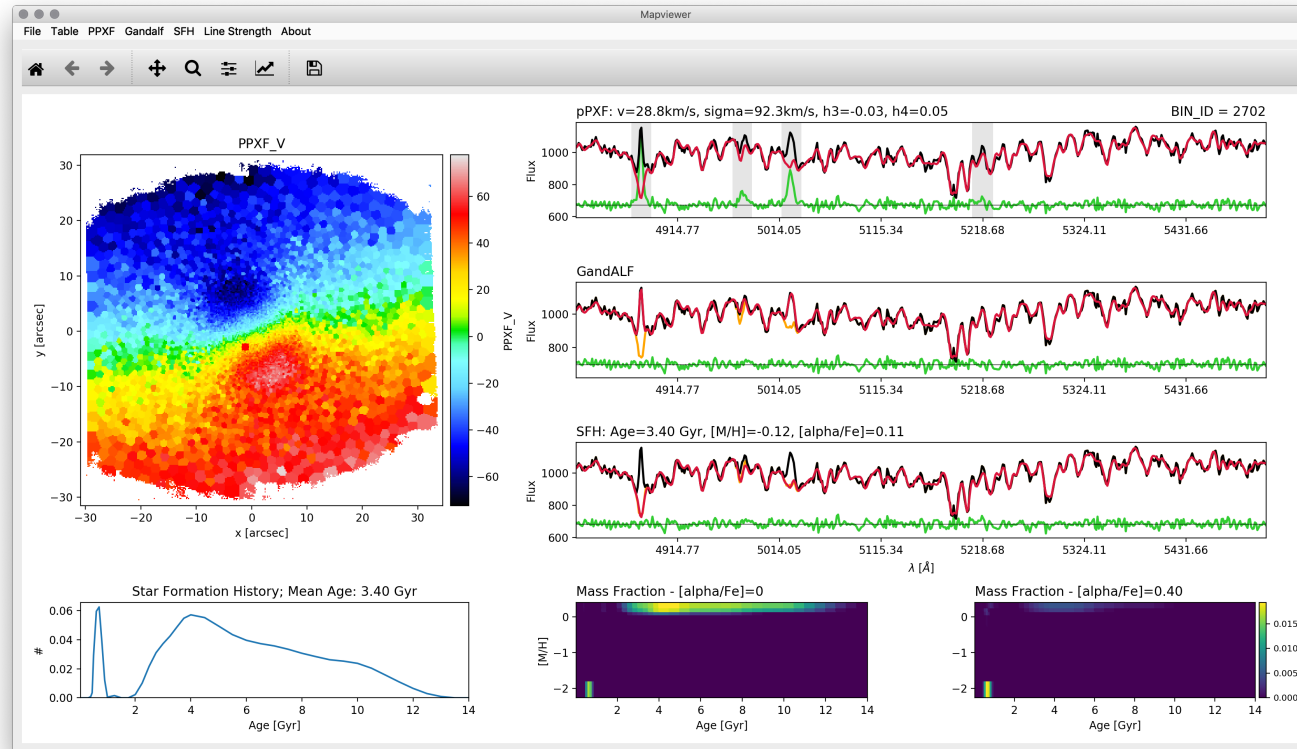


Figure 2.2: Screenshot of the visualisation software `Mapviewer` in its default layout, illustrating the results of the galaxy NGC 1433. High-level data products of previous analysis runs of the `GIST` pipeline can be selected and displayed through the items in the menu bar. A map of the selected quantity is displayed in the upper left panel of the window. Individual bins in this map can be selected by simply performing a mouse-click on the map or providing the bin ID. The selected bin is subsequently shown by a red circle, while the other panels display more detailed information. In particular, the upper three panels on the right side of the window display observed spectra, and the fits generated by the `PPXF` module (first panel), `GANDALF` module (second panel), and `SFH` module (third panel). Observed spectra are displayed in black, fits in red, emission-subtracted continuum spectra in orange, and residuals in green. Masked spectral regions are highlighted in grey. The three bottom panels display further information on the stellar population properties: non-parametric star formation histories are displayed in the left panel, while the centre and right panels illustrate the weights of the templates in the age-metallicity-alpha grid. The corresponding quantitative results of the measurements are provided next to each panel. Different layouts of the `Mapviewer` routine are available to highlight the results of the line strength module.

In addition, the pipeline workflow is optimised in two further ways: firstly, if the user has set unreasonable configuration options, the pipeline will print a warning message and skip the affected module or, if unavoidable, the analysis of the galaxy in consideration. Secondly, the code checks if some of the results are already available in the output directory, thanks to a previous partial run of the GIST pipeline, for instance. If these outputs are detected, the corresponding analysis modules are not executed again.

The automatic determination of whether or not a module has already been executed results in several advantageous features: firstly, it allows the workflow to stop after each analysis module and to continue later. For instance, it is possible to first extract stellar kinematics for a given sample of galaxies, then the gaseous kinematics in a second step, and finally any of the population properties without unnecessarily repeating any operation. Furthermore, this allows the validation of the outcome of any of the previous steps of the workflow before its continuation. In other words, this makes it possible to use the pipeline in a highly interactive manner, which might be helpful for small samples with a large number of spectra per galaxy.

Secondly, this ensures the stability of the workflow against any unforeseen problems (i.e. numerical issues). This is of particular importance if a user intends to use the code as a survey-level pipeline on a large sample of galaxies. The survey-level usage of the pipeline is further supported by the fact that the configuration file can, in principle, be machine generated and contain an arbitrarily large number of objects.

Thirdly, it supports the reutilisation of intermediate results. If the user plans to conduct several test runs on the same galaxy, for example to quantify the impact of the adopted line-spread function on the stellar kinematics, the results of the preparatory operations can be re-used. Similarly, these intermediate results can be modified to perform the analysis in a different manner. For instance, the user can modify the Voronoi map to conduct the analysis in manually defined apertures instead of Voronoi bins.

2.2.3 Implementation of the Framework

Configuration

To provide the maximum convenience to the user, most of the configurations of the GIST pipeline are defined in one file. This file contains the main switches that state which analysis modules need to be executed, and contains the general settings and parameters, such as the instrument used, the wavelength range in consideration, the target signal-to-noise ratio for the Voronoi binning, and the selection of the spectral template library. In addition, more specific settings for any of the four analysis modules are provided. An overview of all configuration switches and a brief description of their functions is presented in Table 2.1. An in-depth description of the effect of these switches follows in this section.

The line-spread function (LSF) of the data is stated by the user in a configuration file that simply contains two columns, defining the spectral resolution of the data at a given wavelength. The information is read-in and a linear interpolation function is generated. Thus, it is possible to reconstruct the spectral resolution at any wavelength. The spectral resolution of the template spectra is handled in a similar way. Spectral regions, which are masked in the analysis of the PPXF and SFH modules, are defined by the user in distinct files stating the wavelength and width of the spectral masks, respectively.

In addition to these files, there are only two more configuration files necessary, one specifying the emission lines to be masked or fitted during the analysis of the GANDALF module and another that states the wavelength bands of the absorption line strength measurements. These configurations are explained in detail in the context of their analysis modules below.

Preparatory Steps

The read-in routine of the GIST pipeline performs five simple operations: it reads the already reduced, science-ready spectral data; it then shifts all spectra to their rest-frame wavelength while adapting their spectral resolution correspondingly (according to the configuration parameter REDSHIFT) and it shortens them to the wavelength range defined by the parameters LMIN and LMAX; it rejects spaxels that contain non-numbers (NaNs) or have a negative median flux. We note that these spaxels are not passed to the pipeline, so that the input and output cubes might not have an identical size. Finally, it computes the signal-to-noise ratio based on the variance spectra obtained during the data reduction or, if these are not available, exploits the `der_snr`-algorithm⁷ which estimates the signal-to-noise ratio S/N using the equations

$$S = \langle F_i \rangle \quad (2.1)$$

$$N = \frac{1.482602}{\sqrt{6}} \langle |2F_i - F_{i-2} - F_{i+2}| \rangle \quad (2.2)$$

with the signal S , the noise N , and the flux F at a spectral pixel i , where brackets represent the median. The pipeline is capable of handling data from any IFS instrument, and from long-slit or fibre-spectrographs if a read-in routine that conducts these five operations is provided. In the default version of the pipeline, read-in routines for the wide- and narrow-field modes of the MUSE spectrograph and for the V500 and V1200 modes of the PMAS/PPAK instrument are included. These read-in routines can be selected with the configuration switch IFU.

To run `pPXF` and `GandALF`, we first logarithmically rebin the spectra to have constant bins in velocity (instead of wavelength). This is implemented in the GIST pipeline by exploiting the log-rebinning function of `pPXF` (Cappellari & Emsellem 2004; Cappellari 2017).

The signal-to-noise ratio of the data is an essential factor in any fitting attempt. In the specific case of using `pPXF` to derive the line-of-sight velocity distribution (LOSVD) parametrised by the line-of-sight velocity v , velocity dispersion σ , and the higher-order Gauss-Hermite moments h_3 and h_4 (Gerhard 1993; van der Marel & Franx 1993), higher-order moments critically depend on the signal-to-noise ratio (see van der Marel & Franx 1993; Gadotti & de Souza 2005). Thus, the pipeline uses the Voronoi binning method of Cappellari & Copin (2003) to spatially bin the data. The resulting binned spectra have an approximately constant signal-to-noise ratio given by the parameter `TARGET_SNR`. We note that spaxels which surpass this target signal-to-noise ratio remain unbinned. In addition, a minimum signal-to-noise ratio threshold can be applied prior to the spatial binning. This threshold removes spaxels below the isophote level which has an average signal-to-noise ratio given by the parameter `MIN_SNR` and can thus avoid possible systematic effects in low surface brightness regions of the data.

⁷http://www.stecf.org/software/ASTROsoft/DER_SNR; see also https://www.spacetelescope.org/static/archives/stecfnewsletters/pdf/hst_stecf_0042.pdf

Config-Switch	Brief Description
<i>Main Switches</i>	
DEBUG	Runs pipeline on one central line of pixels
VORONOI	Performs Voronoi-binning on the data prior to the analysis
GANDALF	Runs the GANDALF module (<code>pyGandALF</code>) on bins or spaxels
SFH	Runs the SFH module (regularised <code>pPXF</code>)
LINE_STRENGTH	Runs the LS module
PARALLEL	Activates multiprocessing
NCPU	Number of cores to use for multiprocessing
<i>General Settings</i>	
RUN_NAME	Name of the analysis run
IFU	Identifier of the read-in routine
LMIN	Minimum rest-frame wavelength [\AA]
LMAX	Maximum rest-frame wavelength [\AA]
ORIGIN	Origin of the coordinate system [arcsec]
REDSHIFT	Redshift of the system [z]
SIGMA	Initial guess of velocity dispersion [km/s]
TARGET_SNR	Target signal-to-noise ratio for the binning
MIN_SNR	Minimum signal-to-noise ratio per spaxel to be accepted for the Voronoi binning
COVAR_VOR	Corrects for spatial correlations of the noise in the Voronoi binning process
SSP_LIB	Defines the spectral template library
NORM_TEMP	Normalises the spectral template library to obtain light- or mass-weighted results
<i>PPXF Settings</i>	
MOM	Number of kinematic moments
ADEG	Degree of the add. Legendre polynomial
MDEG	Degree of the mult. Legendre polynomial
MC_PPXF	Number of Monte Carlo simulations used to extract errors on the stellar kinematics
<i>GANDALF Settings</i>	
FOR_ERRORS	Derives errors on the emission-lines
REDDENING	Includes the effect of reddening by dust
EBmV	De-reddens the spectra for the Galactic extinction in the direction of the target
<i>SFH Settings</i>	
REGUL_ERR	Regularisation error (reciprocal of the <code>pPXF</code> keyword 'REGUL')
FIXED	Fixes stellar kinematics to the results obtained with the <code>PPXF</code> module (See correspondent <code>pPXF</code> keyword)
NOISE	Passes a constant noise vector to <code>pPXF</code>
<i>Line Strength Settings</i>	
CONV_COR	Resolution of the index measurement [\AA]
MC_LS	Number of Monte Carlo simulations used to extract errors on the LS indices
<i>SSP Settings</i>	
NWALKER	Number of walkers for the MCMC algorithm (used for the conversion of indices to population properties)
NCHAIN	Number of iterations in the MCMC algorithm (used for the conversion of indices to population properties)

Table 2.1: Overview of all switches and parameters in the main configuration file of the GIST pipeline. This file contains one line per galaxy in consideration.

Config-Switch	Brief Description
<code>i_line</code>	Unique line index
<code>name</code>	Name of the emission line
<code>lambda</code>	Rest-frame wavelength of the emission line
<code>action</code>	Mask, fit, or ignore the emission line
<code>l-kind</code>	Singlet or doublet line
<code>A_i</code>	Relative amplitude of doublet lines
<code>V_g/i</code>	Initial guess on the velocity (in rest frame)
<code>sig_g/i</code>	Initial guess on the velocity dispersion or width of the spectral mask
<code>fit-kind</code>	Fit lines individually or simultaneously
<code>AoN</code>	Amplitude-over-noise threshold for emission-line subtraction

Table 2.2: Overview of all switches and parameters in the emission-line configuration file of the GIST pipeline. This file contains one line per emission line in consideration.

Config-Switch	Brief Description
<code>b1</code>	Minimum wavelength of blue side bandpass
<code>b2</code>	Maximum wavelength of blue side bandpass
<code>b3</code>	Minimum wavelength of feature bandpass
<code>b4</code>	Maximum wavelength of feature bandpass
<code>b5</code>	Minimum wavelength of red side bandpass
<code>b6</code>	Maximum wavelength of red side bandpass
<code>b7</code>	Atomic or molecular index
<code>names</code>	Name of the index
<code>spp</code>	Consider this index in the SSP modelling
<code>origin</code>	Comments

Table 2.3: Overview of all switches and parameters in the line strength configuration file of the GIST pipeline. This file contains one line per line strength index in consideration.

Some IFS data suffer from spatial correlations of the noise between adjacent spaxels. These correlations can be introduced, for instance, by the combination of individual observations, spatial interpolation procedures in the reduction process, or a point-spread function which significantly surpasses the spatial pixel size of the instrument (see e.g. García-Benito et al. 2015; Sarzi et al. 2018). If multiple spectra with correlated noise are coadded, the noise of the resulting stacked spectrum will be underestimated. Depending on the quality of the data, it is of substantial importance to account for this effect in the Voronoi binning process. García-Benito et al. (2015) estimate the strength of these spatial correlations β by calculating the ratio of the real noise to the analytically expected noise as a function of the number of spaxels per bin N . They find this empirical relation (their Eq. 1),

$$\beta(N) = 1 + \alpha \log N, \quad (2.3)$$

where the slope α is a basic proxy for the strength of any correlations, if present, that need to be provided to the pipeline with the configuration parameter `COVAR_VOR`. For instance, in data release 2 of the CALIFA survey α is found to be 1.06 or 1.07 depending on the set-up of the instrument. To account for spatial correlations in the GIST pipeline, the analytically expected noise is corrected with the above formula during the Voronoi binning procedure. We note that the resulting Voronoi binning scheme is used throughout the analysis with the exception of the GANDALF module that can be run on either the Voronoi bins only or on all spaxels (see Sect. 2.2.3).

In line with the modular structure of the pipeline, spectral template libraries can be selected conveniently with the configuration parameter `SSP_LIB`. While the MILES library (Vazdekis et al. 2010) is included in this software package, other libraries can be provided by the user in distinct directories. We highlight that the GIST pipeline allows the user to pick not just a full set of the pre-loaded spectral template libraries, but also an object-specific subset of such template spectra. The spectra of the template library are read-in, shortened to conform with the spectral range of the observed spectra, and oversampled by a factor of two (Cappellari 2017). Moreover, the templates can be normalised to provide mass- or light-weighted results (parameter `NORM_TEMP`) and broadened from their intrinsic, spectral resolution to the one specified by the line-spread function of the particular instrument.

For the measurement of stellar population properties via full spectral fitting with `pPXF`, the compilation of the spectral library has further requirements. More specifically, `pPXF` necessitates that the templates are sorted in a three-dimensional cube of age, metallicity, and α -element enhancement, according to the population properties encoded in the filename of the templates. This is readily implemented in the pipeline for all libraries that follow the MILES naming convention. Thanks to the modularity of the pipeline, it is straightforward to expand this to distinct naming conventions by simply replacing the read-specific function in the SFH module.

Stellar Kinematics Analysis

The PPXF module utilises the penalised pixel-fitting (`pPXF`) method developed by Cappellari & Emsellem (2004) and advanced in Cappellari (2017) (configuration switch `PPXF`). Its Python implementation derives the underlying galaxy stellar line-of-sight velocity distribution (LOSVD) parametrised in terms of the line-of-sight velocity v , velocity dispersion σ , and higher-order Gauss-Hermite moments (switch `MOM`; Gerhard 1993; van der Marel & Franx 1993). Briefly, the method convolves a non-negative linear combination of the given set of template library spectra with the LOSVD in pixel space by means of a least-squares minimisation seeking to find the set of best-fitting LOSVD parameters and the corresponding weights ascribed to the linear combination of templates library.

The regularisation of `pPXF` is turned off and the default value of the penalisation used. Additive (parameter `ADEG`) and multiplicative (parameter `MDEG`) Legendre polynomials can also be included in the fit to account for any potential deviations in the continuum shape between observed and template spectra or inaccuracies in the flux calibration.

In addition to the default functionality of `pPXF`, extensive Monte Carlo (MC) simulations can be performed to compute errors on the extracted quantities (parameter `MC_PPXF`). To this end, multiple realisations of the input spectra are created by adding random noise on the scale of the residual noise to the best-fitting result from the initial `pPXF` run. Subsequently, the `pPXF` fit is performed again in the same configuration, but without the penalisation term. The standard deviation of the resulting distribution of the measured quantities is saved as error. The formal errors on the initial fit, as returned by `pPXF`, are saved as well.

Moreover, the PPXF module computes maps of the λ parameter (Emsellem et al. 2007), which acts as a quantification of the projected specific angular momentum. Following their Eqs. 5 and 6, the parameter is defined as

$$\lambda \equiv \frac{\langle R|v| \rangle}{\langle R\sqrt{v^2 + \sigma^2} \rangle} \quad (2.4)$$

and measured in every spatial bin individually as

$$\lambda = \frac{\sum_{i=1}^{N_p} F_i R_i |v_i|}{\sum_{i=1}^{N_p} F_i R_i \sqrt{v_i^2 + \sigma_i^2}} \quad (2.5)$$

with the galactocentric radius R and the flux F . We note that the summation is performed over each spaxel in the corresponding bin, using spaxel-level values for flux and radius and bin-level values for velocity and velocity dispersion. As this parameter depends on the galactocentric radius, the pipeline only outputs correct values of λ if the coordinates of the centre of the galaxy are passed with the configuration parameter `ORIGIN`. We note that the `GIST` pipeline computes the λ parameter in every spatial bin individually, in contrast to the aperture integrated quantities presented in Emsellem et al. (2007).

Emission-line Analysis

For the measurement of gaseous kinematics, emission-line fluxes, and the computation of emission-free continuum spectra the `GANDALF` module facilitates a new Python implementation of the original `GandALF` procedure by Sarzi et al. (2006) and Falc3n-Barroso et al. (2006), which is released together with this software package (hereafter `pyGandALF`; configuration switch `GANDALF`). There, the individual emission lines are treated as additional Gaussian templates and their velocities and velocity dispersions are searched for iteratively. These emission-line templates are linearly combined with the set of library spectral templates to solve for the best-fitting emission-line gaseous kinematics (i.e. velocity and velocity dispersion), their strengths (i.e. line amplitudes), and weights on the linear combination of the spectral template library. Such a procedure adequately accounts for both the gaseous emission lines and the underlying stellar continuum present in the spectra of some galaxies (Sarzi et al. 2006).

Following the original implementation of `GandALF`, both the `GANDALF` module and `pyGandALF` only fit emission lines that are specified by the user in the emission-line configuration file (see Table 2.2). In particular, this file states the wavelength of the line and whether the line is a singlet or doublet, and whether different sets of lines share the same kinematics or not. If specified in the emission-line configuration file, multiple emission-line components can be fitted to a single emission feature in order to reproduce non-Gaussian line profiles. For instance, in the presence of an outflow, a narrow emission line might be located on top of a very broad emission feature. In this case, the broad and the narrow component can be fitted independently, thus obtaining an improved fit and results on the two physically distinct components.

Initial guesses on the velocity (relative to the redshift given with the parameter `REDSHIFT`) and velocity dispersion are to be provided by the user in the emission-line configuration file. `pyGandALF` can compensate differences in the continuum from the galaxy and the templates by exploiting a two-component reddening correction (parameter `REDDENING`). As detailed in Oh et al. (2011) and also shown in Sarzi et al. (2018), this allows to construct maps for classical ‘screen-like’ extinction affecting the entire galaxy spectrum in addition to maps for the reddening impacting only on the emission-line regions. Alternatively, if the `REDDENING` option is not used, the same order of multiplicative Legendre polynomials as for the `PPXF` module is applied in `pyGandALF`. Additive Legendre polynomials are not used, regardless of what is set in the configuration parameter `ADEG`. In addition, the `GANDALF` module is capable of correcting the spectra for Galactic extinction in the

direction of the target. To this end, Galactic extinction values (e.g. from Schlegel et al. 1998) are passed with the configuration parameter `EBmV` and the spectra are de-reddened prior to the emission-line analysis by applying the model of Calzetti et al. (2000).

In addition to its measurement of gaseous kinematics, the GANDALF module also computes continuum spectra with subtracted emission lines (hereafter emission-subtracted spectra). A notable complication of this step is the determination of a threshold above which a line detection is considered significant. To this end, Sarzi et al. (2006) introduce the amplitude-to-residual noise ratio (A/rN) which quantifies how much the amplitude of an emission line surpasses the residual noise level of the spectrum, which can be used to justify this choice. In the default set-up of the GIST pipeline, the best-fitting emission-line templates are subtracted from the observed spectra, if this A/rN ratio (using the A/rN value of the main line for doublets of multiplets) exceeds the A/rN threshold defined in the emission-line configuration file (see Table 2.2). The impact of pegging lines together on the minimum A/rN values to robustly detect lines was initially discussed in Sarzi et al. (2006) in the case of SAURON observations, but a more detailed study is needed to robustly address this issue for more complicated line sets as observed within the MUSE wavelength range and for different kind of emission-line systems. Thanks to the modularity of the code, it is straightforward to implement different methods of the emission-line subtraction by simply changing one function in the GANDALF module. We note that we are currently in the process of developing more sophisticated criteria for the selection of such a detection threshold, and a more advanced treatment of the emission-line subtraction problem could be included in a future pipeline release.

Non-parametric Star Formation Histories

The SFH module of the GIST pipeline exploits pPXF to estimate some of the underlying stellar-population properties and their associated non-parametric star formation histories via full-spectral fitting (configuration switch `SFH`). Essentially, the code finds a linear combination of spectral templates that resembles the observed spectrum. Under such an assumption the stellar-population properties and the corresponding star formation histories are derived on the basis of the linear weights ascribed to the chosen set of template spectra. However, recovering this information from the observational data is an inverse, ill-conditioned problem. Small variations in the initial data can translate to large variations in the solution. Thus, regularisation is used to obtain a more physically motivated combination of the template spectra. In particular, of all the solutions that are equally consistent with the observational data, the regularisation algorithm returns the smoothest solution. We refer the interested reader to Sect. 3.5 of Cappellari (2017) for a detailed review of the stellar population analysis with pPXF.

The regularisation parameter, corresponding to the pPXF keyword `REGUL`, acts as a proxy for the strength of the regularisation and is passed to the pipeline with the configuration parameter `REGUL_ERR`, a value that is the reciprocal of the pPXF keyword `REGUL`. The given value is subsequently used for all spectra in the cube. We note that the choice of this regularisation parameter could have a substantial effect on some of the recovered population properties.

The SFH module uses emission-subtracted spectra, as produced by the GANDALF module, for the derivation of population properties. During this process, the parameters representing the stellar kinematics can be extracted simultaneously with the population properties or kept fixed to those obtained with the PPXF module (configuration switch `FIXED`, see also

corresponding pPXF keyword). Deviations in the continuum shape between observed and template spectra can be compensated by including a multiplicative Legendre polynomial in the fit (parameter `MDEG`, same as in the PPXF module). As the use of an additive Legendre polynomial could significantly alter the resulting population properties, these cannot be used in the SFH module regardless of what is set in the configuration parameter `ADEG`.

It should be noted that the estimation of errors on the population properties, as derived from regularised full-spectral fitting, is somewhat ambiguous and thus we do not attempt to provide such a procedure in this software package. An ensemble of different approaches has been previously undertaken (see e.g. Gadotti et al. 2019; Pinna et al. 2019) and we therefore advise the user to find the most suitable procedure depending on the scientific context.

Absorption-line Strength Analysis

Complementary to the derivation of stellar population properties via full-spectral fitting, a wide range of studies has made use of absorption-line strength indices to infer information about the stellar content of galaxies (e.g. Trager et al. 1998; Peletier et al. 2007; Kuntschner et al. 2010; McDermid et al. 2015). The fundamental steps of the line strength measurement are the following: a main absorption feature bandpass is encompassed by two side bandpasses to the red and blue. The side bandpasses act as a proxy for the stellar continuum. To this end, the mean flux in both side bandpasses is computed and their central points connected by a straight line. The flux difference between the observed spectrum and this straight line calculated within the wavelength range of the feature bandpass represents the absorption-line strength index (Faber et al. 1985; Kuntschner et al. 2006).

The LS module of the GIST pipeline makes it possible to measure absorption line strengths in the *Line Index System* (LIS; Vazdekis et al. 2010) by adopting a Python translation of the routine used by Kuntschner et al. (2006) (configuration switch `LINE_STRENGTH`). The wavelengths of the feature and continuum bandpasses are defined by the user in a dedicated configuration file (see Table 2.3). This configuration file further states whether the index will be computed as equivalent width in angstroms or in magnitudes (as commonly used for atomic and molecular absorption features, respectively).

In preparation of this measurement, the LS module uses emission-subtracted spectra, translates those from velocity space back to constant bins in wavelength, and convolves them to the spectral resolution of the measurement (parameter `CONV_COR` in the main configuration file). We note that this convolution accounts for both the instrumental and stellar velocity dispersion. The measured stellar radial velocity is considered to assure the correct placement of the line strength bandpasses. Errors are estimated by means of Monte Carlo simulations, considering errors on the stellar radial velocity and the variance spectra (parameter `MC_LS` in the main configuration file).

As a second independent step, the measured line strengths can be matched to SSP-equivalent properties. The main ingredient is a model file provided together with the selected spectral library (parameter `SSP_LIB` in the main configuration file) at the corresponding measurement resolution (parameter `CONV_COR`) that connects line strength indices to population properties. Taking into account the errors in the indices, radial velocities and variance spectra, a Markov chain Monte Carlo (MCMC) algorithm (Foreman-Mackey et al. 2013) searches for the best SSP to match the derived set of indices (parameters `NWALKER` and `NCHAIN`; see Martín-Navarro et al. 2018, for further details).

2.3 Application to MUSE Data

In this section we illustrate the capabilities of the pipeline by applying it to real data. We present the full set of high-level data products, in particular the resulting stellar kinematics and emission-line analysis, as well as absorption line strength indices and stellar population properties for one galaxy. We highlight that all figures presented in this section, with the exception of Fig. 2.3, are automatically generated by the pipeline. Moreover, the pipeline outputs immediately allow the user to produce additional plots, for instance BPT diagrams and maps of electron densities.

We exploit observations of the galaxy NGC 1433 obtained with the MUSE integral-field spectrograph as part of the TIMER survey. All galaxies in the TIMER sample are barred and exhibit a variety of nuclear structures, such as nuclear rings, nuclear discs, and primary/secondary bars, as well as nuclear spiral arms (see e.g. Méndez-Abreu et al. 2019; de Lorenzo-Cáceres et al. 2019b). The main scientific goal of the project is to study the star formation histories of these nuclear structures. More specifically, this allows us to determine the cosmic time at which the bar initially formed and thus constrain the epoch at which the galaxy’s disc became dynamically mature (see Gadotti et al. 2015, 2019).

We chose the galaxy NGC 1433 as it is a typical example of a spiral galaxy with various structural components, which we expect to be clearly distinguishable in their kinematic and stellar population properties. In addition, this galaxy exhibits a variety of ionised-gas emission, without showing significant emission from an AGN or suffering from severe dust contamination. Therefore, NGC 1433 is a good example to demonstrate the capabilities of the GIST pipeline.

2.3.1 Observations and Data Reduction

The observations of NGC 1433 were performed in ESO Period 97 in August and October 2016 with an average seeing of 0.8 arcsec to 0.9 arcsec. The MUSE field of view (FoV) covers approximately $1 \text{ arcmin} \times 1 \text{ arcmin}$ with a spatial sampling of $0.2 \text{ arcsec} \times 0.2 \text{ arcsec}$. It covers a spectral range from 4750 \AA to 9350 \AA with a spectral pixel size of 1.25 \AA and mean spectral resolution of 2.65 \AA . The data reduction is based on the version 1.6 of the dedicated ESO MUSE data-reduction pipeline (Weilbacher et al. 2012). In summary, bias, flat-fielding, and illumination corrections are applied and the exposures calibrated in flux and wavelength. Telluric features and signatures from the sky background are removed and exposures are registered astrometrically. For details on observations and data reduction we refer the reader to Gadotti et al. (2019).

NGC 1433 is a barred, early-type spiral with an nuclear ring, plume, nuclear ring-lens, and nuclear bar, and with an outer pseudo-ring (classified as $(R'_1)SB(r,p,nr1,nb)a$ by Buta et al. 2015). Its inclination is 34 deg based on the $25.5 \text{ AB mag arcsec}^{-2}$ isophote at $3.6 \mu\text{m}$, and it has a stellar mass of $2.0 \times 10^{10} M_\odot$. The mean redshift-independent distance from the NASA Extragalactic Database⁸ is 10.0 Mpc (see also Gadotti et al. 2019, and references therein).

In Fig. 2.3 we further illustrate the most prominent structures in the MUSE FoV by presenting a colour composite (left panel) and colour map (right panel). The colour composite highlights a star-forming nuclear disc; however, in contrast to previous studies (e.g. Erwin 2004; Buta et al. 2015) we do not find evidence for a nuclear bar in the MUSE

⁸<http://ned.ipac.caltech.edu/>

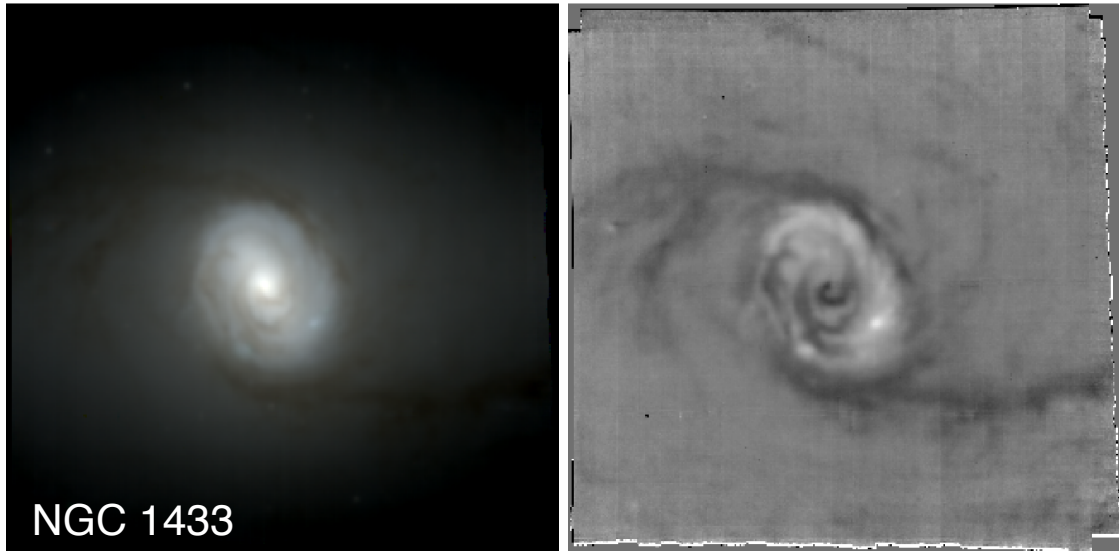


Figure 2.3: Colour composite (left panel) and colour map (right panel) of NGC 1433. Colour composites are built by collapsing the data cube in a blue (4750 Å to 6000 Å), green (6000 Å to 7000 Å), and red (7000 Å to 9000 Å) wavelength band and combining the resulting images. Colour maps are obtained by subtracting the red image from the blue.

reconstructed intensities. The colour map features two strong dust lanes along the leading edges of the main bar. Dust lanes along the leading edges of the bar are expected from theoretical work (Athanasoula 1992b), and in the case of NCG 1433 end at the nuclear disc (see also Sormani et al. 2018).

2.3.2 Data Analysis Set-up

We perform the data analysis with the pipeline configuration set-up discussed in Sect. 2.2. Throughout this analysis, we spatially bin the data to an approximately constant signal-to-noise ratio of 40 per bin. This signal-to-noise level has been widely used in literature as it provides a good compromise between accuracy of the extracted quantities and spatial resolution (see e.g. van der Marel & Franx 1993), thus it is a suitable choice for this demonstration of the GIST pipeline. Spaxels that surpass this ratio remain unbinned in the analysis, while all spaxels below the isophote level which has an average signal-to-noise ratio of 3 are excluded in order to avoid systematic effects at low surface brightness. We note that the emission-line analysis is performed on a spaxel-by-spaxel basis instead, also including spaxels below this signal-to-noise threshold.

The line-spread function of the MUSE observations varies with wavelength. To correct for this effect, we adopt the udf-10 prescription obtained by Bacon et al. (2017). In particular, we broaden all template spectra to the one obtained in their work prior to performing any fits.

For the measurement of stellar kinematics and emission-line properties, we use the E-MILES model library (Vazdekis et al. 2015). The library consists of SSP spectra, covering a wide range of values for age and metallicity at a spectral resolution of ~ 2.51 Å in the relevant wavelength range (Falcón-Barroso et al. 2011). In this analysis, we exploit the rest-frame wavelength range from 4800 Å to 8950 Å in order to maximise the available information. Any emission lines in the considered wavelength range are masked. When extracting stellar kinematics with pPXF, we include a low-order, multiplicative Legendre

polynomial in the fit to correct for any small differences between observed and template spectra. In contrast, the emission-line analysis exploits a two-component reddening correction instead of Legendre polynomials.

In order to infer the stellar population properties, we restrict the wavelength range to 4800 Å to 5500 Å. This allows the use of the MILES SSP model library (Vazdekis et al. 2010), which covers a shorter wavelength range, but provides information on the α -enhancement of the stellar populations. The model library covers ages from 0.03 Gyr to 14.00 Gyr, metallicities of $-2.27 < [M/H] < +0.40$, and α -enhancement values $[\alpha/Fe]$ of either 0.00 dex and 0.40 dex. The models are based on the BaSTI isochrones (Pietrinferni et al. 2004, 2006, 2009, 2013) and a revised Kroupa initial mass function (Kroupa 2001). The measurement of the stellar population content is based on the Voronoi-binned, emission-subtracted spectra, as returned by the GANDALF module.

The inference of the non-parametric star formation histories is performed by a regularised run of pPXF. Stellar kinematics are kept fixed to those obtained from the unregularised run of pPXF. The strength of the regularisation is determined following the criterion introduced by Press et al. (1992) and applied, for instance, in McDermid et al. (2015). In particular, the maximum value of the regularisation corresponds to the fit for which the χ^2 of the best-fitting solution increases from the χ^2 of the unregularised solution by $\Delta\chi^2 = \sqrt{2N_{\text{pix}}}$ with N_{pix} being the number of fitted spectral pixels. This regularisation parameter is determined on the bin with the highest signal-to-noise ratio and subsequently applied to the entire cube.

We measure absorption-line strength indices in the LIS-8.4 system (Vazdekis et al. 2010). To this end, all spectra are convolved to a spectral resolution of 8.4 Å, taking into account both instrumental and local stellar velocity dispersion. Errors on these indices are estimated through 30 Monte Carlo simulations. Subsequently, the MILES SSP model which best predicts the observed combination of the $H\beta_o$ (Cervantes & Vazdekis 2009), Fe5015 (Worthey et al. 1994), Mgb (Burstein et al. 1984), Fe5270 (Burstein et al. 1984), and Fe5335 (Worthey et al. 1994) indices, as used by previous studies to determine SSP properties, is determined by means of the previously mentioned MCMC fitting technique (Martín-Navarro et al. 2018).

2.3.3 Stellar Kinematics

We present the derived maps of stellar kinematics in the upper group of panels in Fig. 2.4 and projected specific stellar angular momentum λ in Fig. 2.5. The typical formal errors on the fit are 4.1 km s^{-1} in velocity, 5.7 km s^{-1} in velocity dispersion, 0.03 in h_3 , and 0.04 in h_4 . Various distinct kinematic features are immediately evident, thanks to the outstanding spatial resolution of the MUSE observations. A rapidly rotating nuclear disc with a radial extent of approximately 10 arcsec is detected in the line-of-sight velocity map. This nuclear disc appears even more pronounced in the map of the λ parameter. The map of the stellar velocity dispersion shows a prominent ring of low-velocity dispersion which coincides with the rapidly rotating nuclear disc found in the line-of-sight velocity map. This ring is surrounded by a region of elevated velocity dispersion. Within the ring, at radii smaller than 3 arcsec to 4 arcsec, the velocity dispersion increases again towards the centre.

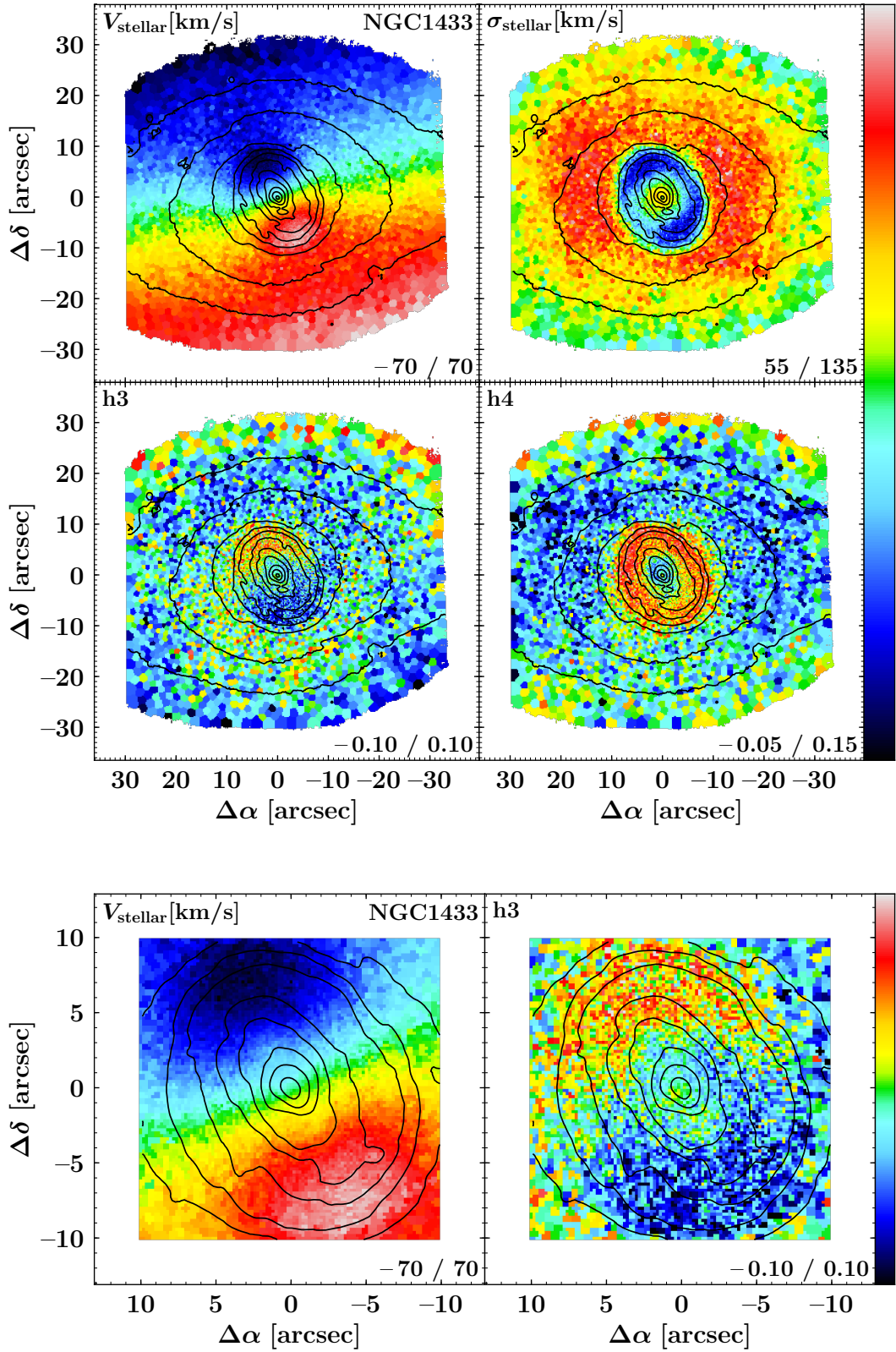


Figure 2.4: Upper group of panels: Line-of-sight velocity (V_{stellar}), velocity dispersion (σ_{stellar}), and higher-order moments h_3 and h_4 of the stellar component of NGC 1433. Lower panels: Spatial distribution of line-of-sight velocities (left) and h_3 moment (right) in the innermost part of the galaxy. The limits of the colour bar is given in the lower right corner of each panel. Isophotes are based on reconstructed intensities from the MUSE cube and are displayed in steps of 0.5 mag. North is up; east is to the left.

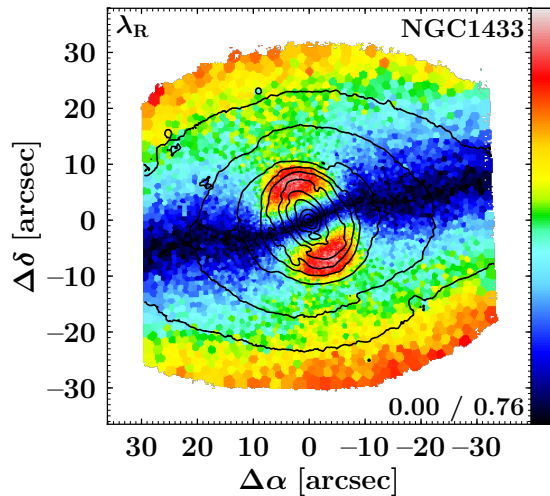


Figure 2.5: Map of the projected specific angular momentum λ of NGC 1433. The limits of the colour bar are stated in the lower right corner. Isophotes are based on reconstructed intensities from the MUSE cube and displayed in steps of 0.5 mag. North is up; east is to the left.

Correlations between the higher-order Gauss-Hermite moment h_3 and the line-of-sight velocity allow us to infer information on the eccentricity of the underlying stellar orbits. For instance, an anti-correlation between line-of-sight velocity and h_3 indicates near-circular orbits as they are typically found in regularly rotating stellar systems, such as stellar discs (Bender et al. 1994; Bureau & Athanassoula 2005). Such an anti-correlation is evident in the region of the nuclear disc, in particular at radii between 4 arcsec and 10 arcsec. In addition, such an anti-correlation is found at radii above 25 arcsec, which corresponds to the main disc of the galaxy. In contrast, a correlation between line-of-sight velocity and h_3 is a signature of orbits with high eccentricity. We find such a correlation at intermediate radii between the nuclear and main stellar disc of NGC 1433. In fact, this region might be dominated by the eccentric x_1 orbits of the bar. Interestingly, a similar correlation between line-of-sight velocity and h_3 is found within the nuclear ring of the galaxy, at radii smaller than 3 arcsec to 4 arcsec (see lower group of panels in Fig. 2.4). This finding is particularly interesting in the context of the potential existence of an inner bar in NGC 1433. However, we note that previous studies (see e.g. Erwin 2004; Buta et al. 2015; de Lorenzo-Cáceres et al. 2019b) remain inconclusive on the existence of an inner bar in this galaxy.

Finally, high values of the higher-order moment h_4 indicate a superposition of structures with different LOSVDs (see e.g. Bender et al. 1994, and references therein). For NGC 1433 this is only the case in the nuclear ring, while in other parts of the galaxy, in particular in the centre, no elevated h_4 values are found.

2.3.4 Emission-line Kinematics and Fluxes

The upper right-hand panel of Fig. 2.6 shows the spatial distribution of measured $H\alpha$ fluxes. A large amount of $H\alpha$ emission is obvious, especially in the nuclear disc. While the emission in the nuclear disc appears patchy, the highest $H\alpha$ fluxes are found in the centre of the galaxy. In the upper left and lower left panels of Fig. 2.6 we present line-of-sight velocity and velocity dispersion maps of the emission-line fit of $H\alpha$. The line-of-sight velocity map clearly shows $H\alpha$ rotation along the major axis of the galaxy. However, significant departures from regular rotation, in particular in the region of the nuclear disc,

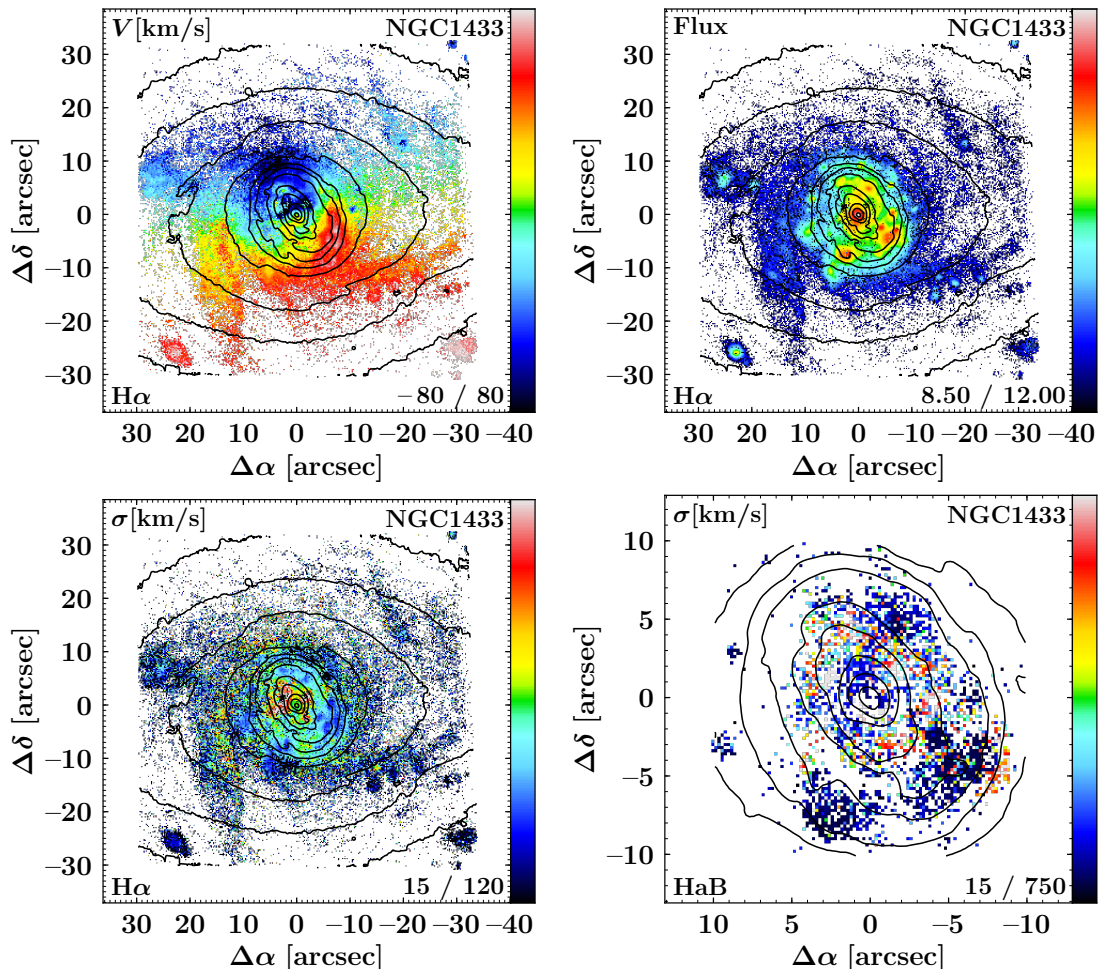


Figure 2.6: Maps of the H α line-of-sight velocity (upper left panel), velocity dispersion (lower left panel) and flux (upper right panel, in arbitrary units with logarithmic scale) of the primary component in the emission-line fit of NGC 1433. The velocity dispersion of the secondary H α component is displayed in the lower right panel. We note that this panel shows a different spatial scale in order to highlight the innermost region of the galaxy. Only spaxels in which the H α line exceeds an A/rN ratio of 4 are displayed in this figure. The limits of the colour bar are given in the lower right corner of each panel. Isophotes are based on reconstructed intensities from the MUSE cube and displayed in steps of 0.5 mag. North is up; east is to the left.

are obvious. The spatial distribution of the H α velocity dispersion reveals several areas of low sigma, in particular in the nuclear ring. These spatially coincide with areas of high H α fluxes, where star formation is proceeding. Close to the centre of the galaxy, three regions of elevated velocity dispersion are evident.

The `pyGandALF` emission-line fit included a secondary component for the H α emission wherever necessary. In particular, a visual inspection of the one-component fits revealed that a secondary component was necessary in a few regions, even though it is fainter than the primary component. Where such a component is not necessary, `pyGandALF` does not recover this component. We note that only few spaxels, mostly located in the nuclear disc, include such a secondary emission-line component. The map of the velocity dispersion of this secondary component is presented in the lower right panel of Fig. 2.6. In three individual regions in the nuclear disc, the secondary component is included as additional, low-dispersion component. These regions have already been identified as low-dispersion regions in the primary component of the fit. Interestingly, in the inner regions of the nuclear disc, the secondary component shows high-velocity dispersion of several hundred

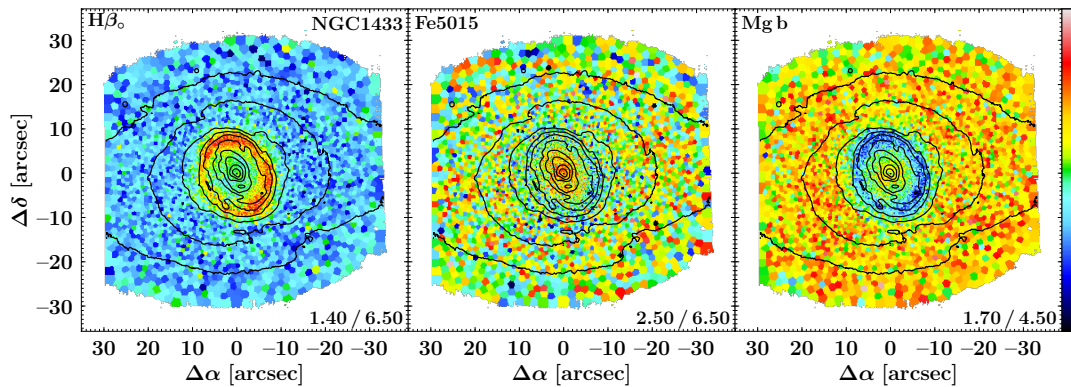


Figure 2.7: Maps of the absorption-line strength indices $H\beta$ (left panel), Fe5015 (central panel), and Mgb (right panel) of the galaxy NGC 1433. The limits of the colour bar are shown in the lower right corner of each panel. Isophotes are based on reconstructed intensities from the MUSE cube and displayed in steps of 0.5 mag. North is up; east is to the left.

km s^{-1} . We note that while the secondary component improved the $H\alpha$ emission-line fit in the shown regions, a detailed investigation on its origin, in particular whether its origin is physical or not, is beyond the scope of this study.

2.3.5 Absorption-line Strength Analysis

In Fig. 2.7 we present maps of the absorption-line strength indices $H\beta$, Fe5015, and Mgb of NGC 1433. Elevated values of the $H\beta$ index are only found in the nuclear ring, while its values are constantly low at larger radii. Within the nuclear disc, the $H\beta$ index is slightly elevated compared to regions outside the nuclear disc. Similarly, the Fe5015 line-strength index is constant over a large part of the FoV. However, the nuclear ring becomes evident through slightly lower index values. In the region inside the nuclear ring, the Fe5015 map shows elevated values which further increase towards the centre. The Mgb line-strength index behaves similarly, with constantly high values at large radii, low values in the nuclear ring, and elevated values that peak in the centre of the galaxy. We note that typical, median errors on the derived indices of $H\beta$, Fe5015, and Mgb are approximately 0.32, 0.54, and 0.26, respectively.

2.3.6 Stellar Population Properties

Single Stellar Population Properties

In Fig. 2.8 we display the SSP-equivalent population properties recovered by performing an absorption-line strength measurement of the $H\beta$, Fe5015, Mgb, Fe5270, and Fe5335 indices. We report constant ages of ~ 8 Gyr for a large part of the galaxy with the exception of the nuclear disc. Notably, there we infer younger stellar populations, down to ages below 1 Gyr. Interestingly, a region of slightly elevated ages is found in the innermost part of the galaxy at radii smaller than ~ 6 arcsec, resulting in a prominent ring-like structure of young stellar populations at radii from ~ 6 arcsec to 10 arcsec. The spatial distribution of $[M/H]$ shows a similar behaviour, but with elevated values in the nuclear ring and the very centre of the galaxy. The values of $[\alpha/Fe]$ are constant at 0.2 dex at large radii from the centre. The nuclear ring is evident as region of higher alpha-enhancement that is encompassed by a region of slightly less α -enhanced stellar populations. The region inside

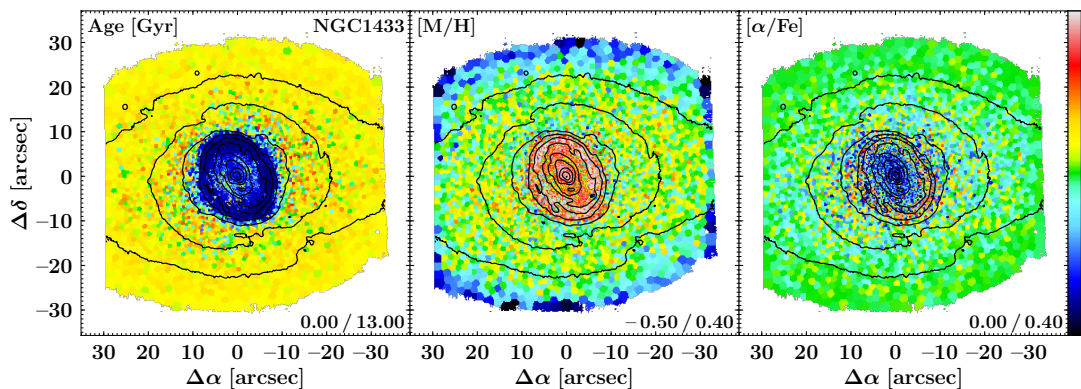


Figure 2.8: Maps of SSP-equivalent population properties of the galaxy NGC 1433, as derived from absorption-line strength measurements. Displayed are age (left panel), $[M/H]$ (centre panel), and $[\alpha/Fe]$ (right panel). The limits of the colour bar are given in the lower right corner of each panel. Isophotes are based on reconstructed intensities from the MUSE cube and displayed in steps of 0.5 mag. North is up; east is to the left.

the nuclear ring shows significantly less α -element enhanced stellar populations with the lowest values of ~ 0.0 dex found at the very centre. We note that typical errors on the ages, metallicities, and α -enhancements of these recovered SSP properties are 2 Gyr, 0.15 dex, and 0.08 dex, respectively.

We note that the stellar population properties derived for the nuclear disc are clearly reminiscent of young (below 1 Gyr) stellar populations. For those young stellar populations the degeneracies between age, metallicity, and alpha sensitive absorption-line features become severe and the conversion of line strength indices to stellar population properties is therefore highly unreliable. Due to the recent inflow of gas towards the nuclear ring and ongoing star formation activity, the assumption that the stellar populations in the nuclear ring can be represented by single age, single metallicity, and single alpha-enhancement values is most likely not valid. Nevertheless, these measurements provide evidence that the stellar populations in the nuclear disc are younger and more metal rich than in the remaining parts of the galaxy, while proving elevated values of alpha abundances in the nuclear ring is beyond the scope of this study.

Mean Stellar Population Properties from Full-spectral Fitting

Spatial distributions of the light-weighted stellar population content, as inferred from full-spectral fitting with pPXF, are presented in Fig. 2.9. These results are in good agreement with the stellar population properties derived from line strength indices above. However, we note the difference in the α -element enhancement values outside of the nuclear region where the inferred SSP $[\alpha/Fe]$ is ~ 0.2 dex, instead of those acquired through the pPXF full-spectral fitting α -element enhancement of ~ 0.1 dex. This difference is only slightly larger than the typical errors on the alpha-enhancement of the SSP properties (0.08 dex). More prominently, the ring of elevated $[\alpha/Fe]$ values in the SSP maps is not found in the maps derived with pPXF. More importantly, both approaches independently converge to their lowest values of the alpha-enhancement in the innermost regions.

Outside the nuclear disc, age and $[M/H]$ agree well, with less prominent scatter in the maps of the SSP properties. We note that maps of the SSP properties show slightly younger and more metal rich populations in the nuclear disc in comparison to the population

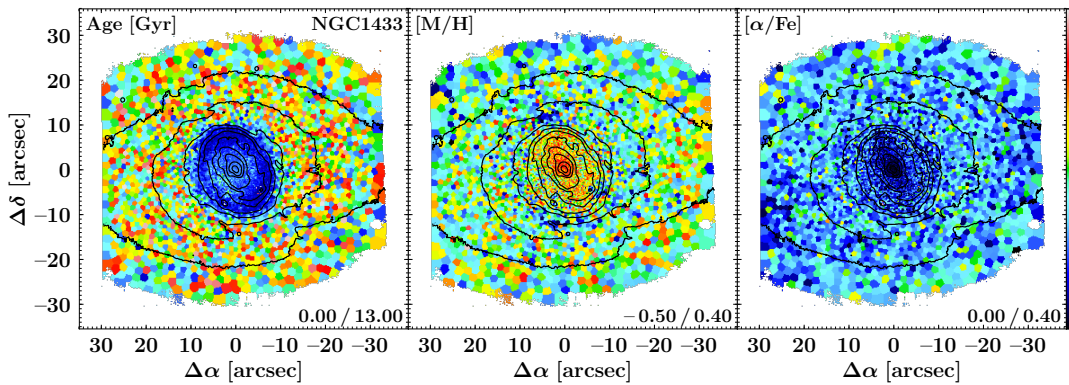


Figure 2.9: Maps of the light-weighted stellar population content of the galaxy NGC 1433, as derived from full-spectral fitting. Displayed are age (left panel), $[M/H]$ (centre panel), and $[\alpha/Fe]$ (right panel). The limits of the colour bar are stated in the lower right of each panel. Isophotes are based on reconstructed intensities from the MUSE cube and displayed in steps of 0.5 mag. North is up; east is to the left.

content derived via full-spectral fitting. Previous studies have found that SSP population properties tend to show younger ages and higher metallicity as compared to those derived from light-weighted full-spectral fitting (see e.g. Serra & Trager 2007; Trager & Somerville 2009). In addition, SSP properties with ages below 1 Gyr cannot be measured reliably and the assumption of observing a single stellar population, in particular in the nuclear disc, is unrealistic. Therefore, stellar population properties in the nuclear disc measured with full-spectral fitting seem more reliable and the ring of elevated $[\alpha/Fe]$ values found in the SSP properties might be an unphysical result. A comparison with mass-weighted results is beyond the scope of this study.

2.4 Summary and Conclusions

In this study, we introduce a convenient, all-in-one framework for the scientific analysis of fully reduced, (integral-field) spectroscopic data. The pipeline presented in this work incorporates all the necessary steps (i.e. read-in and preparation of the science data, modular data analysis, inspection of the data products, etc.) to produce publication-quality figures. In its default set-up, the software extracts in each observed spatial position the underlying stellar LOSVD, complemented with stellar population properties, extracted through either full-spectral or line-strength index fitting. In conjunction, the pipeline also accounts for any ionised-gas emission lines and their corresponding properties. To this end, we introduce a novel Python implementation of **GandALF**.

The **GIST** pipeline is not specific to any IFS instrument, nor is it a particular analysis technique; it provides an easy framework with the means of modification and development, owing to its modular code architecture. An elaborate parallelisation has been implemented and tested on machines, from laptops to cluster scale. We note its unique capabilities to batch-analyse data in a fully automated manner drawing on any previously produced outputs with the possibility to interchange to a more interactive hands-on workflow facilitated by a dedicated visualisation routine with an advanced graphical user interface. This visualisation routine allows easy access to all measurements, spectra, fits, and residuals, and to star formation histories and the weight distribution of the models in fully interactive plots.

The presented analysis framework has been successfully applied to both low- and high-redshift data from MUSE, PPAK (CALIFA), and SINFONI, and to simulated data for HARMONI and WEAVE and is already being used by the TIMER, Fornax3D, and PHANGS surveys. This further highlights the comprehensive features of the GIST pipeline and the need of the scientific community for such a software package.

This code is publicly available through a dedicated webpage⁶ and is subject to ongoing development. Additional analysis modules, for instance the inclusion of STECKMAP and pyPARADISE, will be included in a future release. The webpage provides a thorough documentation of the code; instructions on how to download, install, and use it; as well as a short tutorial. Because the pipeline is applicable to a wide variety of scientific objectives, we encourage the community to exploit the highly modular code architecture by adapting the pipeline to their specific scientific needs or adding further modules. We would also like to remind the user to properly reference any software and spectral template libraries that have been utilised as the base of this software package.

We illustrate the capabilities of the pipeline by applying it to observations of NGC 1433, obtained with the MUSE TIMER survey. We perform measurements of the stellar and gaseous kinematics, and infer the properties of the underlying stellar population content. We find evidence of a rapidly rotating nuclear disc, with a radial extent of approximately 10 arcsec, characterised by low-velocity dispersion and an anti-correlation between radial velocity and the h_3 moment. Interestingly, a correlation between radial velocity and h_3 moment is also found in the innermost region of the galaxy, at radii smaller than 4 arcsec. A large amount of H α emission is detected, indicating gas rotation along the major axis of the galaxy with significant departures from regular rotation. Spatial distributions of the stellar population properties provide evidence of a young and metal-rich nuclear disc with low values of α -enhancement. These findings are all clearly consistent with an nuclear disc built by bar-driven, secular evolution processes. Forthcoming papers on stellar kinematics and population properties of the MUSE TIMER galaxies will investigate the related processes in detail, and will also connect them with the physics of gas and star formation in the nuclear disc.

Kinematic Signatures of Nuclear Discs

Kinematic Signatures of Nuclear Discs and Bar-driven Secular Evolution in Nearby Galaxies

The central regions of disc galaxies hold clues to the processes that dominate their formation and evolution. To exploit this, the TIMER project has obtained high signal-to-noise and spatial resolution integral-field spectroscopy data of the inner few kpc of 21 nearby massive barred galaxies, which allows studies of the stellar kinematics in their central regions with unprecedented spatial resolution. We confirm theoretical predictions of the effects of bars on stellar kinematics and identify box/peanuts through kinematic signatures in mildly and moderately inclined galaxies, finding a lower limit to the fraction of massive barred galaxies with box/peanuts at $\sim 62\%$. Further, we provide kinematic evidence of the connection between barlenses, box/peanuts, and bars. We establish the presence of nuclear discs in 19 galaxies and show that their kinematics are characterised by near-circular orbits with low pressure support and that they are fully consistent with the bar-driven secular evolution picture for their formation. In fact, we show that these nuclear discs have, in the region where they dominate, larger rotational support than the underlying main galaxy disc. In addition, we define a kinematic radius for the nuclear discs and show that it relates to bar radius, ellipticity and strength, and bar-to-total ratio. Comparing our results with photometric studies of galaxy bulges, we find that careful, state-of-the-art galaxy image decompositions are generally able to discern nuclear discs from classical bulges if the images employed have high enough physical spatial resolution. In fact, we show that nuclear discs are typically identified in such image decompositions as photometric bulges with (near) exponential profiles. However, we find that the presence of composite bulges (galaxies hosting both a classical bulge and a nuclear disc) can often be unnoticed in studies based on photometry alone and suggest a more stringent threshold to the Sérsic index to identify galaxies with pure classical bulges.

3.1 Introduction

A large number of observational and theoretical studies have been providing mounting evidence of the important physical processes driven by bars in massive disc galaxies. For example, in the area of the disc within the bar radius, stars are continuously trapped by the bar and gas is funnelled to the central region, where new stellar structures such as nuclear discs, inner bars, nuclear rings and nuclear spiral arms are thus built (see Sanders & Tubbs 1980; Simkin et al. 1980; Kormendy 1982; Prendergast 1983; Louis & Gerhard 1988; Shlosman et al. 1989; Athanassoula 1992b; Knapen et al. 1995; Piner et al. 1995; Sakamoto et al. 1999; Gadotti & dos Anjos 2001; Knapen et al. 2002; Sheth et al. 2005; Allard et al. 2006; Wozniak 2007; Coelho & Gadotti 2011; Ellison et al. 2011; de Lorenzo-Cáceres et al. 2012, 2013; Athanassoula et al. 2013; Cole et al. 2014; Fragkoudi et al. 2016; Kim et al. 2016; Kruk et al. 2018; Seo et al. 2019; Donohoe-Keyes et al. 2019). There is increasing evidence that these processes start to play a major role at redshifts $z \sim 1 - 2$

in the most massive disc galaxies, and at $z \sim 0$ these processes take part in the evolution of about two-thirds of disc galaxies (see e.g. Eskridge et al. 2000; Menéndez-Delmestre et al. 2007; Sheth et al. 2008, 2012; Kraljic et al. 2012; Simmons et al. 2014; Melvin et al. 2014; Gadotti et al. 2015; Pérez et al. 2017).

A major process in the evolution of barred galaxies is the buckling (or bulging) of the inner part of the bar, which grows vertically from the disc plane, creating the so-called box/peanut/X-shaped bulges, such as the one hosted by our own Milky Way (e.g. Combes & Sanders 1981; de Souza & Dos Anjos 1987; Shaw 1987; Combes et al. 1990; Binney et al. 1991; Kuijken & Merrifield 1995; Merrifield & Kuijken 1999; Bureau & Freeman 1999; Lütticke et al. 2000; Chung & Bureau 2004; Bureau & Athanassoula 2005; Bureau et al. 2006; Martínez-Valpuesta et al. 2006; Erwin & Debattista 2017; Fragkoudi et al. 2017b, 2018; Kruk et al. 2019). Naturally, these box/peanuts are easier to identify in galaxies close to or at an edge-on projection, but a number of studies made an effort to produce diagnostics able to uncover box/peanuts in inclined galaxies (e.g. Erwin & Debattista 2013, from photometry), or even in face-on galaxies (e.g. Debattista et al. 2005; Méndez-Abreu et al. 2008b; Łokas 2019; Fragkoudi et al. 2020, from stellar kinematics).

More recently, it has been shown that the inner parts of bars not only expand vertically from the plane of the disc, but also radially, parallel to the disc plane, away from the bar major axis (see Laurikainen et al. 2005, 2007, 2011; Athanassoula et al. 2015; Laurikainen & Salo 2016). When bars are seen face-on, this additional structure appears as a less eccentric central component, wider and shorter than the main body of the bar (see Fig. 8 in Gonzalez & Gadotti 2016). This component was named ‘barlens’, but it is important to note that the terms barlens and ‘box/peanut’ refer to different projections of the same stellar structure, namely the inner part of the bar, which expands due to dynamical processes as the bar evolves. It is also very important to highlight that although box/peanuts have a substantial vertical component (and despite their bulge-like morphology), the formation of this bar structure is a process internal to the bar, unlike and unrelated to the violent formation of kinematically hot spheroids: Box/peanuts and barlenses are simply the same inner part of the bar seen at different projections.

Photometrically, all these bar-built structures produce an excess of light in the central region of the galaxy on top of the inward extrapolation of the exponential profile of the main disc. They would thus satisfy one of the criteria to identify bulges, even though they are unrelated to the classical picture of a bulge as a merger-built, kinematically hot spheroid with stars in radial orbits. To distinguish bar-built structures from classical bulges the term ‘pseudo-bulge’ is commonly used (e.g. Kormendy & Kennicutt 2004; Gadotti 2009; Méndez-Abreu et al. 2014; Fisher & Drory 2016; Neumann et al. 2017, amongst many others). However, as described above, bar-built structures also come in two different flavours according to their physical nature. Nuclear discs, inner bars, nuclear rings and nuclear spiral arms are all thought to be built mostly from gas brought to the central region where star formation takes place, whereas box/peanuts (and barlenses) are composed by stars that gradually move from one bar orbital family to another. Therefore, using the term pseudo-bulge collectively to describe all these structures, these two different flavours of bar-built structures, can be misleading. To minimise confusion, Athanassoula (2005) introduced the term ‘disc-like bulge’ (which later produced variations such as ‘discy pseudo-bulge’ and ‘discy bulge’) to distinguish nuclear discs and related structures from box/peanuts.

Photometric disc-like bulges typically have exponential surface density profiles, and therefore seem to be simply nuclear discs that in contrast to the main galaxy disc are built by bar-driven processes that develop in the main galaxy disc (e.g. Falc3n-Barroso et al. 2004, 2006). These nuclear discs often host inner bars, nuclear spiral arms and nuclear rings. The formation of inner bars and nuclear spiral arms appear to be simply scaled-down versions of the formation of a bar and spiral arms in the main galaxy disc (M39ndez-Abreu et al. 2019; de Lorenzo-C3aceres et al. 2019b), confirming the theoretical work by Wozniak (2015) and Du et al. (2015), who also found that nuclear discs and inner bars can be long-lived. Crucially, however, excluding the nuclear disc, the central regions of disc galaxies are dynamically hotter than the regions where the main disc dominates, and thus these processes still need to be better understood.

On the other hand, the formation of nuclear rings is more strongly connected to the properties of the main bar. In fact, a number of studies using hydrodynamical simulations suggest that nuclear rings form close to the inner Lindblad resonance (ILR) of the main bar, or in the region where the x_2 orbital family of the main bar dominates (e.g. Kim et al. 2012b; Li et al. 2015; Sormani et al. 2018, and references therein). These theoretical studies show that the radius of the nuclear ring depends on the size and other properties of the main bar. Observationally, Knapen (2005) and Comer3n et al. (2010) find indeed corroborating evidence. The interplay and evolutionary connection between nuclear discs and nuclear rings are still unclear, but Cole et al. (2014) argue that the nuclear ring is part of the nuclear disc, namely, its outer rim.

It is important to point out that the build-up of nuclear discs in processes unrelated to bars, as via the accretion of external gas onto unbarred galaxies and mergers, has also been explored in numerical simulations (see Mayer et al. 2008; Chapon et al. 2013). This may explain the presence of nuclear discs in unbarred galaxies, but we note that the nuclear discs produced in these unbarred merger simulations are an order of magnitude less extended than those built by bars. In a different study, Eliche-Moral et al. (2011) argued that their idealised, collisionless simulations of minor mergers do create nuclear discs, sometimes without forming a noticeable bar, provided that the satellite galaxy is not too dense and that the primary galaxy has a massive classical bulge before the merger. We discuss these simulations further below and conclude that they do not reproduce the observed properties of nuclear discs. Another possibility is that nuclear discs would form via gas inflow due to oval distortions in the main disc. This is akin to the bar-driven formation process, only with a weaker non-axisymmetric component. To date, it is still unclear how rare are nuclear discs in unbarred galaxies (but see Comer3n et al. 2010).

In this paper, we take advantage of the integral-field spectroscopy data from the **T**ime **I**nference with **M**USE in **E**xtragalactic **R**ings (TIMER) project to study the kinematic properties of barred galaxies and nuclear stellar structures with unprecedented spatial resolution. We also take advantage of the vast ancillary data for the TIMER sample to **(i)**, provide evidence that bar-driven processes appear to be the main mechanism responsible for the formation of nuclear discs and related structures; **(ii)**, demonstrate more rigorously the connection between nuclear discs, detected via their kinematic properties, and central exponential components, found via photometric decompositions, and **(iii)**, provide further evidence that nuclear rings are the outer rims of nuclear discs (see also our accompanying paper, Bittner et al. 2020).

This paper is organised as follows. In the next section we introduce the TIMER project and summarise the main aspects concerning sample selection, observations and data reduction. In Sect. 3.3, we discuss the derivation of the parameters characterising the stellar kinematics, and describe the detection of kinematic signatures of nuclear discs, bars and box/peanuts, as well as the observed kinematic properties of galaxies showing barlenses. We connect the kinematic and photometric properties of nuclear discs in Sect. 3.4, and discuss the origin of nuclear discs in Sect. 3.5. In Sect. 3.6 we present a more general discussion and summarise our main conclusions.

3.2 The TIMER Survey

The TIMER project is a survey with the Very Large Telescope (VLT) MUSE integral-field spectrograph (Bacon et al. 2010) of 24 nearby barred galaxies¹ with prominent central structures, such as nuclear rings, nuclear spiral arms, inner bars and nuclear discs (see Gadotti et al. 2019, hereafter Paper I). One of the projects' main goals is to study the star formation histories of such structures to infer the cosmic epoch of the formation of the bar and the dynamical settling of the main disc of the host galaxy. The methodology was demonstrated with a pilot study of NGC 4371 (Gadotti et al. 2015).

The TIMER sample was drawn from the Spitzer Survey of Stellar Structure in Galaxies (S⁴G, Sheth et al. 2010), which includes only galaxies at distances below 40 Mpc, brighter than 15.5 B-mag, and larger than 1 arcmin. The TIMER galaxies are all barred, with stellar masses above $1 \times 10^{10} M_{\odot}$, inclinations below approximately 60 deg, and nuclear stellar structures. The presence of the bar and nuclear structures was assessed from the morphological classifications of Buta et al. (2015), who used the S⁴G images for their work. The TIMER sample is thus biased towards conspicuous bars and nuclear structures, and it is important to keep this in mind when considering the results discussed in this paper.

Most of the observations were performed during ESO Period 97 (April to September 2016) with a typical seeing of 0.8 arcsec to 0.9 arcsec, mean spectral resolution of 2.65 Å (full width half maximum; FWHM), and spectral coverage from 4750 Å to 9350 Å. MUSE covers an almost square 1 arcmin² field of view with a contiguous sampling of 0.2 arcsec \times 0.2 arcsec, which corresponds to a massive dataset of about 90 000 spectra per pointing. The spectral sampling is 1.25 Å per pixel. The total integration time on source for each galaxy was typically 3840 s.

The MUSE pipeline (version 1.6) was used to reduce the dataset (Weilbacher et al. 2012), correcting for bias and applying flat-fielding and illumination corrections, as well as wavelength calibration. The exposures were flux-calibrated through the observation of a spectrophotometric standard star, which was also used to remove telluric features. Dedicated empty-sky exposures and a PCA methodology were employed to remove signatures from the sky background. Finally, the exposures were also finely registered astrometrically, so that the point spread function (PSF) of the combined cube is similar to that in individual exposures. Typically, the averaged signal-to-noise ratio (S/N) per spectral and spatial pixel at the central spaxels of our fully reduced data cubes is approximately 100. We refer the reader to Paper I for further details on the sample selection, observations and data reduction.

¹Observations are still lacking for three galaxies.

Within the TIMER collaboration, Méndez-Abreu et al. (2019) presented the discovery of the first box/peanut found in an inner bar, and de Lorenzo-Cáceres et al. (2019b) found evidence indicating that inner bars are long-lived. Neumann et al. (2020) discovered variations in the stellar population properties across galaxy bars that were predicted in idealised simulations and can be reproduced by state-of-the-art cosmological simulations. Furthermore, Leaman et al. (2019), adding data from ALMA, showed a spectacular example of the effects of bars on the interstellar medium, central star formation and stellar feedback.

3.3 Stellar Kinematics of Nuclear Discs

3.3.1 Data Analysis

The technical details behind our derivation of the stellar kinematics in TIMER were extensively presented in Paper I and Gadotti et al. (2015). Here we simply summarise the essential aspects. The stellar line of sight velocity distributions (LOSVDs) were parameterised as Gauss-Hermite functions with four parameters (following van der Marel & Franx 1993): velocity (v), velocity dispersion (σ), and the h_3 and h_4 higher-order moments. The h_3 and h_4 parameters can be used to examine in further detail the orbital structure of the stellar systems in question. For instance, near-circular orbits, with a distribution of v/σ , produce h_3 values that are anti-correlated with v , whereas elongated orbits result in a correlation between v and h_3 . High values of h_4 suggest the superposition of structures with different LOSVDs (see e.g. Bender et al. 1994, and references therein). For the derivation of 2D maps of v , σ , h_3 and h_4 , the spectra from the data cube of each galaxy were spatially binned to ensure a minimum S/N of approximately 40 per spectral pixel. This was done using the Voronoi binning technique as described in Cappellari & Copin (2003). To derive systemic velocities and central velocity dispersions, we combined all spectra within a circular aperture. The spectra from each Voronoi bin or aperture were fitted with the pPXF code of Cappellari (2017, see also Cappellari & Emsellem 2004 and Cappellari et al. 2011a). The entire ensemble of procedures was performed using the GIST² pipeline (which employs pPXF; Bittner et al. 2019).

The only fundamental difference between the kinematic maps presented in Paper I (where we presented the maps corresponding to NGC 1097 and NGC 4643 only) and the ones derived here is the rest-frame wavelength range employed. In Paper I we opted to use the range between 4750 Å and 5500 Å after checking that similar results are obtained when the full MUSE wavelength range is employed. That approach has the advantage of necessitating less computation time. In addition, it avoids complications arising from bright emission lines, particularly if they are not masked, but modelled. Some emission lines are nevertheless present in the restricted wavelength range, and those were masked before the fitting procedure. However, in this paper, we used an extended wavelength range (4800 Å to 8950 Å) that is close to the full wavelength range provided by MUSE. A comparison between the maps derived employing these two different approaches shows that the results are qualitatively identical and quantitatively very similar. However, the maps derived using the extended wavelength range reveal some results in a more enhanced fashion. For example, regions with elevated absolute values of h_3 and h_4 appear more conspicuously and sharply defined. This seems to be related to the fact that the instrumental spectral resolution increases with wavelength, and thus lower values of velocity dispersion, as well as deviations from a pure Gaussian function for the LOSVDs (i.e. values of h_3 and h_4 different from zero), can be more robustly measured. Further, the signal is boosted by

²Available at asc1.net/1907.025.

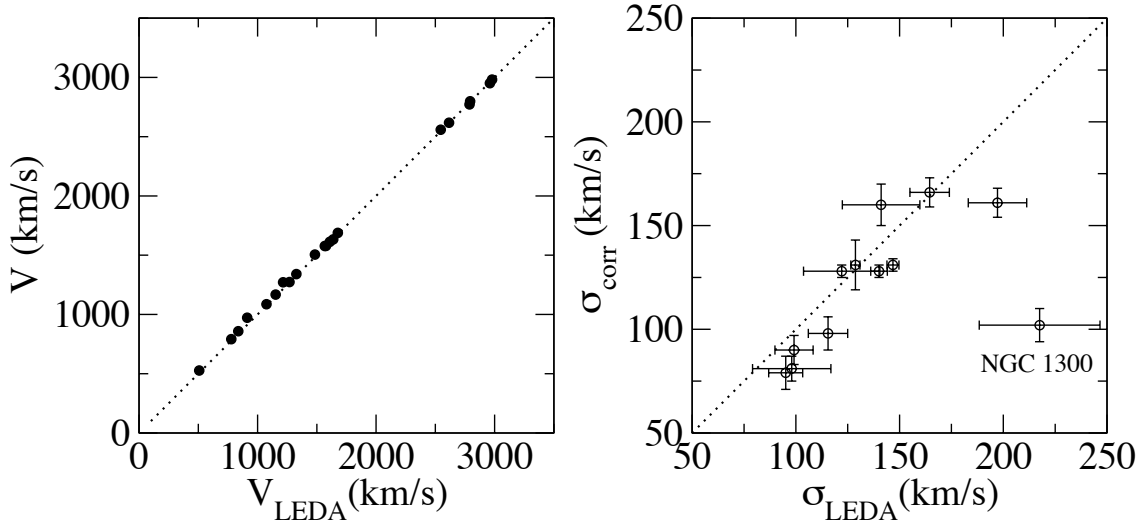


Figure 3.1: *Left:* TIMER measurements of systemic velocity against the values available at LEDA. *Right:* TIMER measurements of central velocity dispersion against the LEDA values. The TIMER velocity dispersions were adapted to follow the same aperture corrections of LEDA, and the error bars in both panels correspond to 1σ errors. NGC 1300 is the only significant outlier but this is due to a mistake in LEDA (see text for further details; the LEDA team has been informed).

the addition of several absorption features, including the calcium triplet. When using the extended wavelength range, for two galaxies (NGC 7140 and NGC 7755) small differences in the continuum shape between the galaxy spectra and the input library of synthetic models required more than a multiplicative low-order Legendre polynomial included in the fit (as done in Paper I). We thus included in the fit an 8th-order multiplicative polynomial plus a 4th-order additive Legendre polynomial to account for such small differences. In addition, in this paper, we also employed a non-constant line spread function (LSF) to account for the wavelength dependence of the instrumental spectral resolution. We adopted the LSF derived in Bacon et al. (2017, their equation 8).

3.3.2 Systemic Velocities and Central Velocity Dispersions

For each galaxy, the heliocentric systemic radial velocity and central velocity dispersion were measured by combining all central spectra within a circular aperture corresponding to one eighth of the galaxy effective radius, $r_e/8$. For r_e we use the measurements derived by Muñoz-Mateos et al. (2015) using S⁴G 3.6 μm growth curves. These measurements are presented in Table 3.1, along with error estimates and the corresponding values available at the Lyon Extragalactic Data Archive (LEDA). Our error estimates were derived from 30 Monte Carlo realisations. We note that to properly compare the measurements of central velocity dispersion we adapted our measurements to follow the same aperture corrections of LEDA, which correspond to an aperture of $0.595 h^{-1} \text{ kpc}$.

Galaxy	r_e arcsec	v_{LEDA} km s^{-1}	$\text{err}(v_{LEDA})$ km s^{-1}	v km s^{-1}	$\text{err}(v)$ km s^{-1}	$\sigma_{r_e/8}$ km s^{-1}	$\text{err}(\sigma)$ km s^{-1}	σ_{corr} km s^{-1}	σ_{LEDA} km s^{-1}	$\text{err}(\sigma_{LEDA})$ km s^{-1}
(1)	(2)	(3)	(4)	(5)	(6)	(7)	(8)	(9)	(10)	(11)
IC 1438	11.5	2616	5	2618	2	101	2	99		
NGC 613	51.6	1484	3	1506	2	125	3	128	122	18
NGC 1097	58.8	1269	7	1274	2	196	3	198		
NGC 1291	60.7	837	8	858	6	168	7	166	165	10
NGC 1300	71.9	1578	2	1579	5	100	8	102	218	29
NGC 1365	67.2	1638	4	1633	7	157	10	160	141	19
NGC 1433	67.5	1076	2	1086	4	95	13	94		
NGC 3351	64.5	778	1	791	4	98	8	98	116	10
NGC 4303	56.0	1567	2	1577	3	79	8	79	95	8
NGC 4371	33.5	913	4	972	8	132	12	131	129	2
NGC 4643	24.2	1328	2	1341	2	133	3	131	147	3
NGC 4981	29.9	1678	2	1688	2	95	3	95		
NGC 4984	18.1	1215	10	1271	2	113	3	109		
NGC 5236	145.9	508	2	527	2	75	6	75		
NGC 5248	45.7	1152	2	1168	4	91	7	90	99	9
NGC 5728	28.8	2788	4	2773	5	160	7	161	197	14
NGC 5850	49.4	2546	3	2558	2	123	3	128	140	4
NGC 6902	24.0	2793	4	2799	2	119	2	120		
NGC 7140	38.1	2978	4	2982	2	98	3	100		
NGC 7552	12.2	1609	5	1612	3	84	6	81	98	19
NGC 7755	32.2	2960	3	2952	2	114	3	116		

Table 3.1: Systemic velocities and central velocity dispersions. Column (1) gives the galaxy designation and column (2) shows their effective radii r_e as derived in Muñoz-Mateos et al. (2015). Columns (3) and (4) show, respectively, the tabulated values of systemic radial velocity and the corresponding errors as presented in the Lyon Extragalactic Data Archive (LEDA), whereas our own measurements are presented in columns (5) and (6). In column (7) we show our measurements of the central velocity dispersions as measured within an aperture of $r_e/8$, with the corresponding errors shown in column (8). Column (9) shows again our measurements of the central velocity dispersions but now adapted to follow the same aperture corrections as in LEDA. Finally, columns (10) and (11) show the LEDA values of central velocity dispersions and their errors, respectively. See text for further details.

In Fig. 3.1 we compare our measurements with the LEDA values. The agreement in the measurements of systemic velocity is excellent. Concerning the central velocity dispersion, although there are no available measurements in LEDA for nine galaxies, the agreement is very good, with only one significant outlier, NGC 1300. The LEDA values for the central velocity dispersion in NGC 1300 are a factor of two larger than ours. Curiously, most of the LEDA measurements are quoted as from Davies et al. (1987) but an inspection of the article shows that NGC 1300 is not part of the sample of galaxies in that study. In fact, the measurements by Davies et al. correspond to NGC 2300. Another measurement quoted in LEDA is from an unpublished study that reports $(145 \pm 22) \text{ km s}^{-1}$, a value closer to our measurement $((102 \pm 8) \text{ km s}^{-1})$. Part of the differences between our measurements and the values quoted in LEDA can be due to differences in seeing and pixel size amongst the different observations.

3.3.3 Maps of the Stellar Kinematics

In this section, we present and discuss signatures found in the kinematic maps derived with GIST that reveal the presence of different structural components. Here we focus on the general trends and leave to Appendix A.1 a discussion on the more complex cases. The high-level data products derived to produce all kinematic maps discussed in this study are publicly available³.

Kinematic Signatures of Nuclear Discs

The 2D kinematic maps provide a test to understand if the observed nuclear stellar structures indeed arise from bar-driven secular evolution processes. If they were built via such dissipative processes within the main disc, they are foreseen to have dynamical properties similar to main discs (which are also formed through dissipative processes, albeit not induced by bars), namely, elevated rotational support, low velocity dispersion and near-circular orbits⁴ with an angular momentum vector aligned to that of the main disc. Further, since they should be dynamically distinct from the underlying main galaxy disc, the LOSVDs measured from spectra from such structures are likely to show elevated values of h_4 (and elevated absolute values of h_3), a signature of the overlapping of stellar structures with different velocity distributions: the nuclear structure that dominates the light in such regions and the underlying main galaxy disc (see Cole et al. 2014). In principle, external gas accretion unrelated to the bar could also build stellar structures with these properties, but such structures are likely to show at some stage an angular momentum vector that is not aligned to that of the main disc. Moreover, in simulations, bars are the most common mechanism to remove angular momentum from the gas in a uniform fashion down to the central few hundred parsecs (see e.g. Athanassoula 1992b). On the other hand, if violent processes such as dry mergers build such nuclear structures, then they are expected in most merger configurations to have elongated orbits (showing no $v - h_3$ anti-correlation) with relatively low rotational support and high velocity dispersion. We discuss such scenarios further in Sect. 3.5.

A careful analysis of Figs. 3.2 and A.1 reveals that indeed the TIMER galaxies fit remarkably well the picture in which nuclear structures originate from bar-driven processes. For example, IC 1438 clearly hosts a rapidly rotating nuclear component within a radius of about 5 arcsec, with a kinematic axis well aligned with that of the main disc, as seen

³<https://www.muse-timer.org/data>

⁴In the presence of an inner bar one expects to see signatures of elongated orbits where the inner bar dominates.

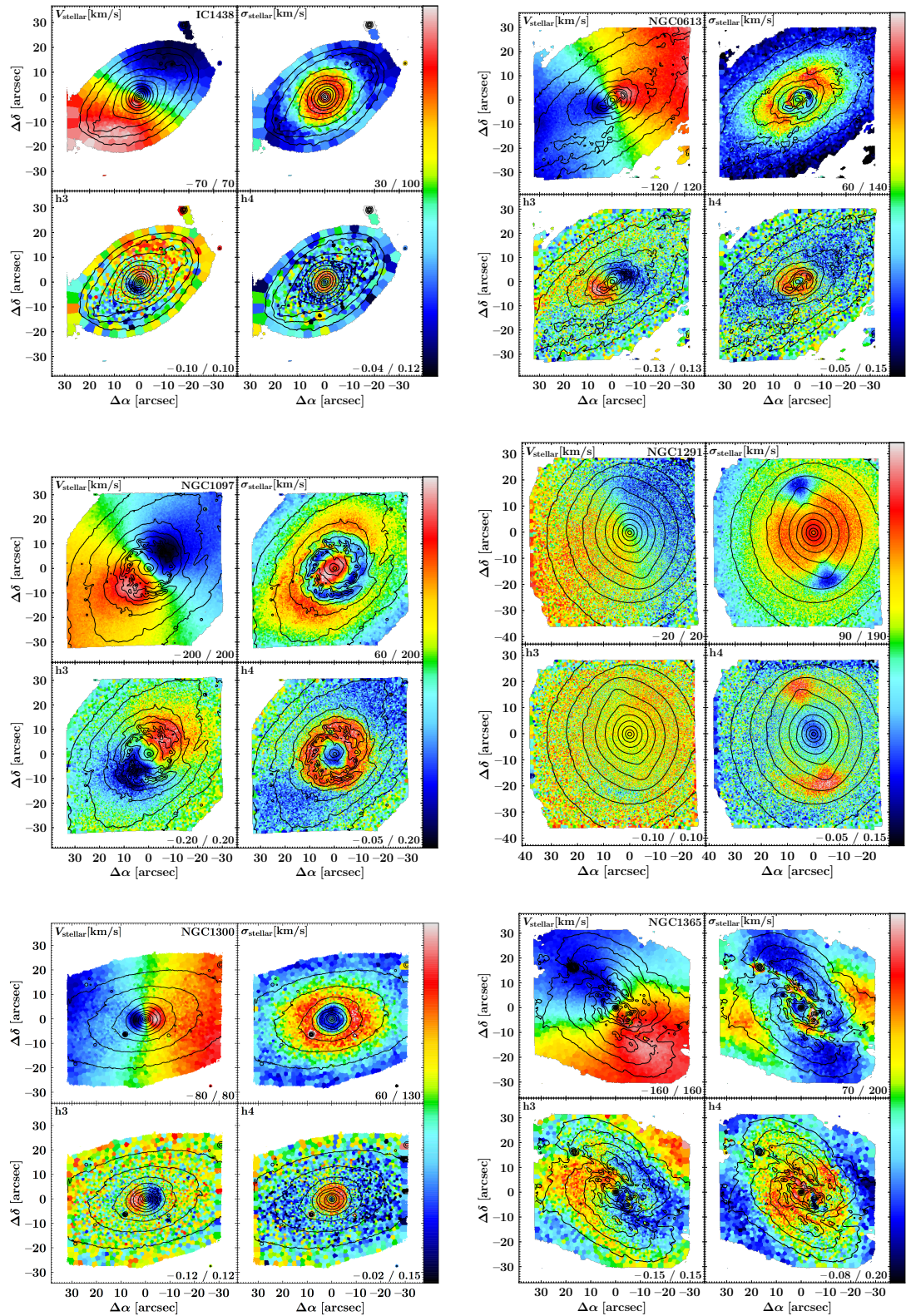


Figure 3.2: Radial velocity, velocity dispersion, h_3 and h_4 maps for the stellar components in the TIMER galaxies, as indicated. The plotted range of the parameter measured is indicated at the bottom right corner of each panel. For radial velocity and velocity dispersion these are given in km s^{-1} . The isophotes shown are derived from the MUSE data cube reconstructed intensities and are equally spaced in steps of about 0.5 mag. On average, 1 arcsec corresponds to approximately 100 pc. North is up, east to the left. See Appendix A.1 for the maps corresponding to the rest of the galaxies in TIMER.

in the corresponding velocity map. The velocity dispersion map shows that the rapidly rotating component is characterised by low velocity dispersion, producing a well defined and well localised dip in the central region of the velocity dispersion map, which would, in the absence of this component, simply show an increasing trend in σ . The h_3 map shows also very clearly that this moment of the LOSVD is anti-correlated with v , a robust signature of near-circular orbits with a range of values for v/σ . This is also the case for the outer, main disc of the galaxy, for example at radii around 15 arcsec. Finally, the h_4 map shows a sharp increase at the region dominated by the rapidly rotating nuclear component, due to the superposition of the low- σ nuclear component on top of the relatively high- σ underlying component.

IC 1438 thus satisfies all the kinematic criteria discussed above that need to be satisfied by nuclear stellar discs built from dissipative processes on a pre-existent underlying disc. In addition, it is important to stress that the kinematic maps show that the properties of the nuclear stellar disc are not part of a continuous distribution covering the whole MUSE field. For example, one sees clearly in IC 1438 that v does not vary monotonically from the outer radii inwards. The stellar velocity peaks at the outer parts of the field and steadily decreases until it increases sharply again at the region of the nuclear disc. This is a clear indication that the nuclear disc is a separate component from the main galaxy disc. In fact, at the same galactocentric radius, stars in the nuclear disc are rotating around the galaxy centre faster than the stars in the main disc (see Fig. 3.2). This implies that – in the region where the nuclear disc resides – the nuclear disc is dynamically colder than the main disc and its stars have orbits closer to near-circular orbits⁵. As discussed above, this is also the reason behind the high values of h_4 in the nuclear disc.

To corroborate these findings we also produced maps of local v/σ (see Fig. 3.3). The figure shows again and even more clearly that the nuclear structures morphologically identified by means of visual inspection by Buta et al. (2015) are stellar structures with very elevated dynamical rotational support and separate from the main galaxy disc. We note that Buta et al. have not necessarily identified these nuclear structures as nuclear discs but rather as nuclear disc features, such as rings, lenses, spiral arms and bars. However, Figs. 3.2 and 3.3 show that these nuclear structures are extended, and in our accompanying paper (Bittner et al. 2020) we present evidence from the stellar population properties that these nuclear structures appear to extend all the way to the galaxy centre. We thus have very strong evidence that the TIMER galaxies host nuclear discs with kinematic properties consistent with a bar-driven origin. In Sect. 3.5 we elaborate on alternative scenarios for the building of these nuclear discs, and also discuss further the connection between nuclear discs and nuclear rings.

Figure 3.4 shows deprojected radial profiles of the v/σ measurements at each Voronoi bin, after correcting v for inclination. We use the values determined with S⁴G data by Muñoz-Mateos et al. (2015) for the inclination and position angle of each galaxy. NGC 1365 and NGC 6902 are not included in this figure, since the signatures of a nuclear disc in these galaxies are not as clear as in the remaining of the sample (these cases are discussed in Appendix A.1). NGC 1291 is also excluded, as determining v/σ is difficult due to the low inclination of the galaxy (11 deg). These profiles allow us to obtain the maximum value of v/σ in the nuclear discs, assuming that the nuclear disc is in the same plane as the main disc. The region within which the maximum is searched for is delimited by a circumference centred at the galaxy centre and crossing the position of the first minimum in v/σ along

⁵Here we assume that both discs are in the same plane, which is justified by the alignment of their kinematic axes seen in Figs. 3.2, 3.3 and A.1.

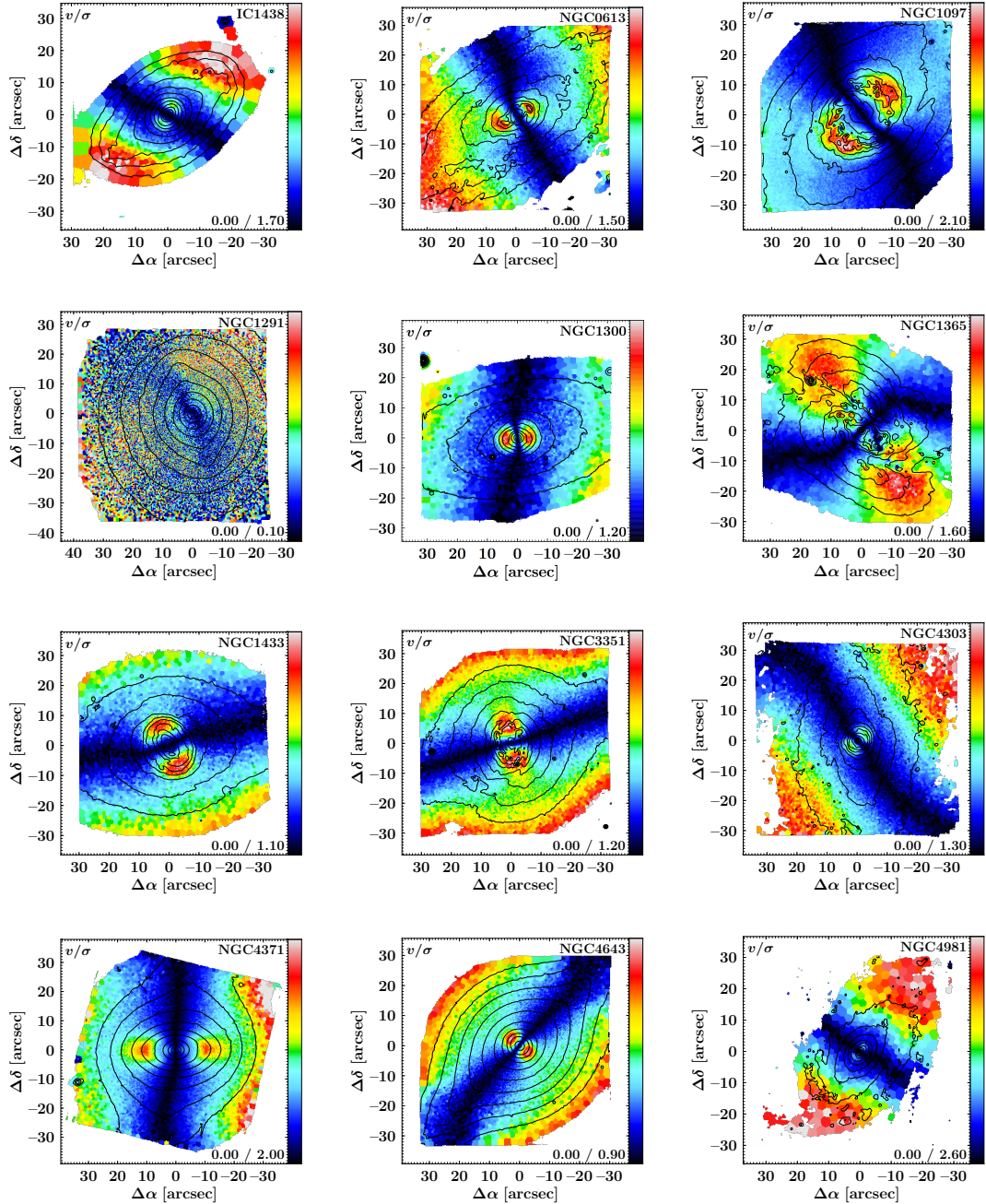


Figure 3.3: Maps of v/σ for the stellar components in the TIMER galaxies, as indicated. The plotted range is indicated on the bottom right corner. The isophotes shown are derived from the MUSE data cube reconstructed intensities and are equally spaced in steps of about 0.5 mag. On average, 1 arcsec corresponds to approximately 100 pc. North is up, east to the left.

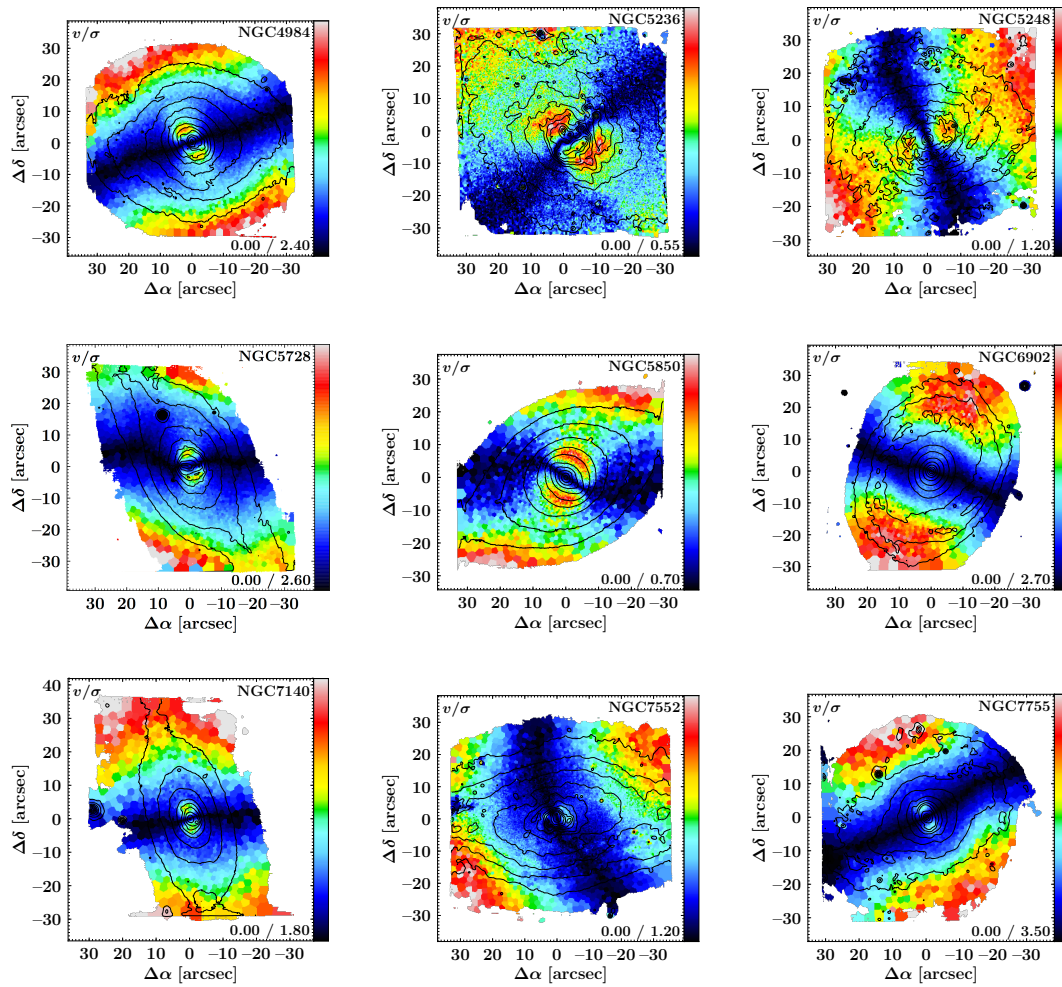


Figure 3.3: Continued.

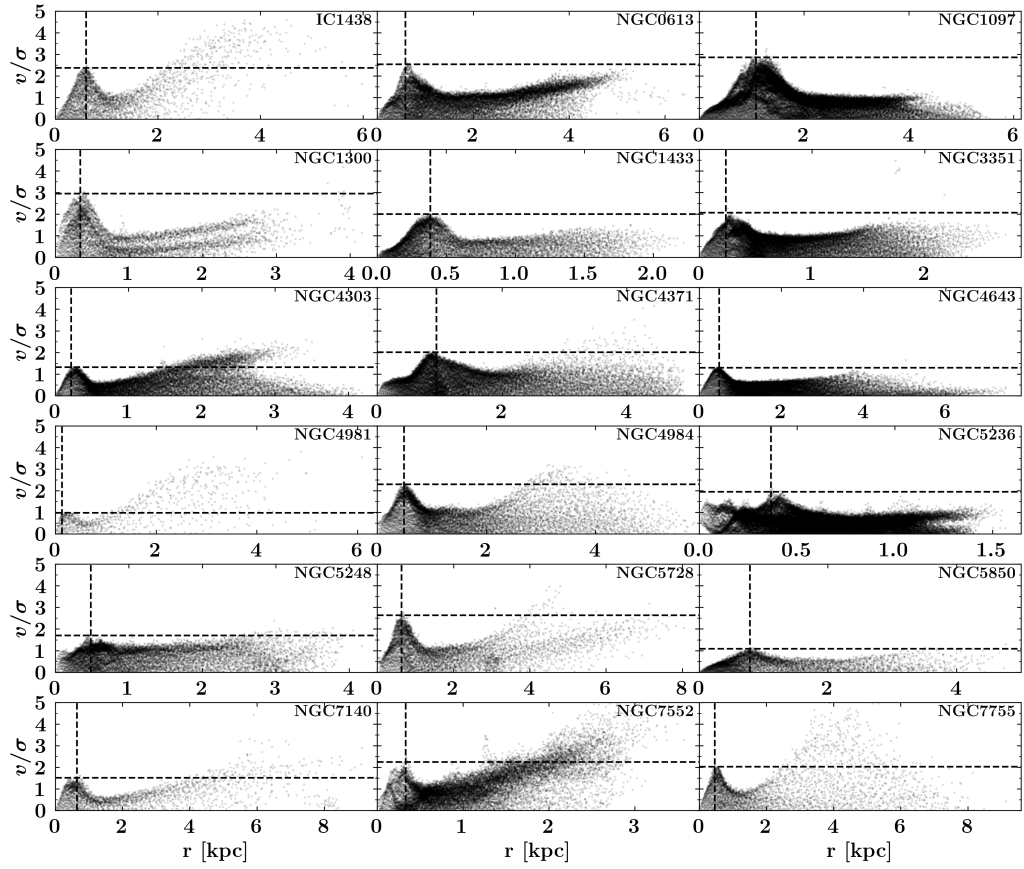


Figure 3.4: Deprojected radial profiles of v/σ at each Voronoi bin, with v corrected for inclination. NGC 1291, 1365 and NGC 6902 are not included. The values of maximum v/σ and r_k are shown with the horizontal and vertical dashed lines, respectively.

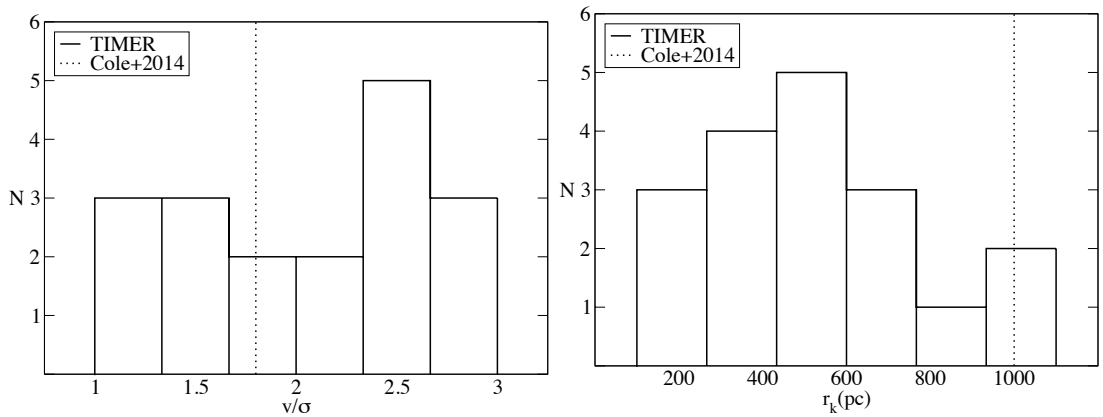


Figure 3.5: Distribution of the maximum value of v/σ (top) and of the kinematic radius (bottom) of the observed nuclear discs. NGC 1291, 1365 and NGC 6902 are not included. The vertical dotted lines mark the values corresponding to the bar-built nuclear disc in the model of Cole et al. (2014).

the disc major axis, beyond the centre. The measurements of v/σ considered in this region are those for each Voronoi bin. We also define the kinematic radius (r_k) of the nuclear disc as the deprojected distance from the galaxy centre of the Voronoi bin showing the maximum value of v/σ in the region dominated by the rapidly rotating nuclear disc. The values of maximum v/σ and r_k are shown in Fig. 3.4 with the horizontal and vertical dashed lines, respectively.

In Fig. 3.5 we present the distributions of the values of maximum v/σ and r_k . Interestingly, although the v/σ distribution is skewed towards higher values, it also shows a broad range of v/σ values, as low as unity. We note that the bar-built nuclear disc in the hydrodynamical simulations of Cole et al. (2014) has a peak v/σ of ≈ 1.8 (the vertical dotted line in Fig. 3.5), fitting well within the distribution of observed values. The same is true for the size of the simulated nuclear disc, although it lies on one of the extremes of the observed r_k distribution. The simulated nuclear disc is as large as the largest observed nuclear discs. We note that the values of v/σ and r_k taken from Cole et al. (2014) correspond to the end of their simulation, at 10 Gyr, when the nuclear disc has reached its maximum size.

Finally, further insights can be gained by employing the λ_R parameter introduced by Emsellem et al. (2007), which quantifies the projected stellar angular momentum per unit mass. We thus calculated λ_{r_k} , which is λ_R integrated within the radius r_k , as in Emsellem et al. (2007), again using the position angle and ellipticity derived for the main disc by Muñoz-Mateos et al. (2015) with S⁴G data. In Fig. 3.6 we plot λ_{r_k} against the observed (projected) ellipticity at the radius of the nuclear disc, r_k , derived with the S⁴G radial profiles of ellipticity. The positions of our measurements in this diagram show clearly that the region within r_k in the TIMER galaxies has the same angular momentum support as the fast rotators of Emsellem et al. (2011). In addition, most systems are consistent with the elevated edge-on ellipticities (or intrinsic flatness) of disc systems. However, as discussed in Cappellari et al. (2007), this diagram is only rigorously valid for stellar systems with a density stratified on homologous oblate ellipsoids (as in the model of Binney 2005), which is evidently not the case of our sample galaxies. The central region of the TIMER galaxies hosts not only the nuclear disc but at least also the main disc and bar, which means that the intrinsic flatness of the TIMER nuclear discs as seen in this diagram is at best a lower limit.

Kinematic Signatures of Bars

The kinematic maps in Figs. 3.2 and A.1 also show kinematic signatures of the presence of bars. Take IC 1438 again as an example. Between the main disc and the rapidly rotating nuclear disc, both showing an anti-correlation between v and h_3 , one sees a region along the bar in which v and h_3 are actually correlated. From the bottom-left corner of the h_3 map, towards the top-right, one first sees blue/green bins, then red/yellow bins, then blue bins again and the inverse patterns after crossing the centre. The correlation between v and h_3 was shown by Bureau & Athanassoula (2005) and Iannuzzi & Athanassoula (2015) to result from the superposition of a bar and a disc, and is seen where both components contribute more or less equally (see also Li et al. 2018).

A similar signature is also seen in NGC 1300, 1433, 3351, 4643, 5850, 7140 and NGC 7755. Possibly due to projection effects, dust extinction and/or lower physical spatial resolution, this signature is somewhat less clear in NGC 613, 4303, 4981, 4984, 5248, 5728 and

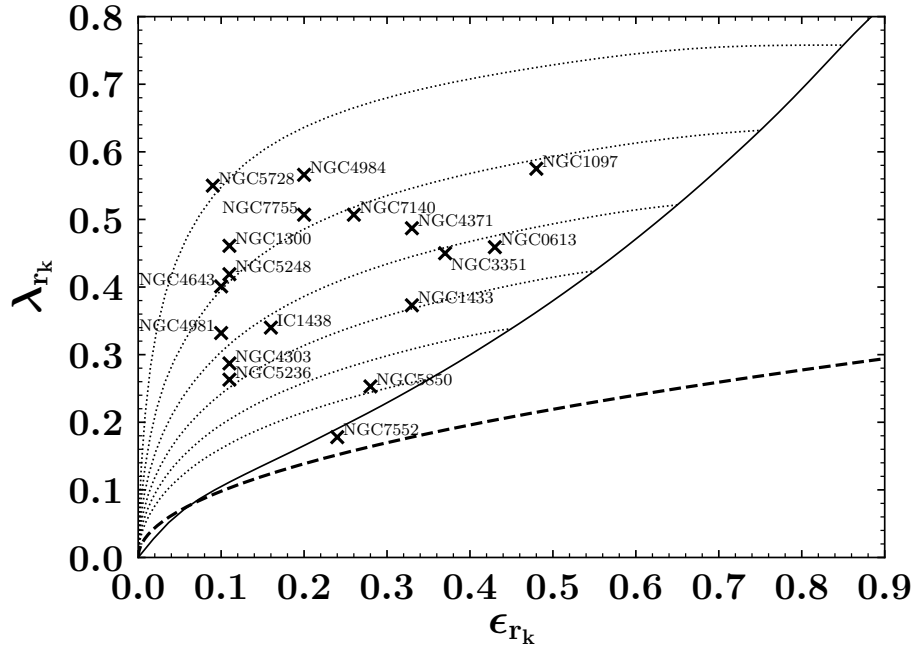


Figure 3.6: λ_{r_k} plotted against the observed (projected) ellipticity at the radius of the nuclear disc. The dashed line is the upper envelope of slow rotators in Emsellem et al. (2011). The solid line shows the relation for a model of oblate stellar systems viewed edge-on (see Binney 2005; Cappellari et al. 2007; Emsellem et al. 2007). The dotted lines correspond to the location of the same model for varying edge-on ellipticity (intrinsic flatness), from top (0.85) to bottom (0.35) in steps of 0.1, with edge-on systems on the relation and face-on systems towards the origin, as in Emsellem et al. (2011). NGC 1291, 1365 and NGC 6902 are not included.

NGC 7552. Since all these galaxies are known to have bars from studies of their morphology, this result is not terribly surprising, but it lends support to our theoretical understanding of the stellar dynamics in barred galaxies.

Interestingly, NGC 1433 shows a correlation between v and h_3 also within ~ 4 arcsec from the centre, which suggests the presence of an inner bar (see also Bittner et al. 2019, for a zoom-in view of the kinematics in this region). However, archival HST images inspected by de Lorenzo-Cáceres et al. (2019b) show no clear morphological signature of an inner bar (but see Erwin 2004; Buta et al. 2015).

We also point out the conspicuous drops in velocity dispersion at the ends of the inner bars in NGC 1291 and NGC 5850. These σ -hollows were found by de Lorenzo-Cáceres et al. (2008) to be a characteristic signature of inner bars, and these two galaxies were studied in detail already in Méndez-Abreu et al. (2019) and de Lorenzo-Cáceres et al. (2019b).

Kinematic Signatures of Box/Peanuts

Our maps also reveal kinematic signatures of the presence of box/peanuts. Debattista et al. (2005) employed numerical simulations to show that box/peanuts can be detected in face-on galaxies by examining the spatial distribution of h_4 : Box/peanuts imprint two significant minima along the bar major axis at the positions of the box/peanut vertices (see also Iannuzzi & Athanassoula 2015; Li et al. 2018). Méndez-Abreu et al. (2008b) showed that this diagnostic works observationally, detecting box/peanuts in primary bars, and, more recently, Méndez-Abreu et al. (2019) were able to find for the first time a box/peanut in an inner bar, that of NGC 1291.

IC 1438 provides again a good example. The very central region, that is, within a radius of about 2 arcsec, shows values of h_4 close to zero. This region is surrounded by elevated values of h_4 where the rapidly rotating nuclear disc dominates, as discussed above. Just outside this region – at radii between about 5 and 10 arcsec – h_4 takes negative values, becoming close to zero again at larger radii. This is the signature just mentioned of the presence of a box/peanut.

We find the same signature clearly in NGC 613, the inner bar of NGC 1291 (as shown already in Méndez-Abreu et al. 2019), NGC 1300, 4303, 4643, 4981, 4984, 5728, 5850, 7140, 7552, and NGC 7755. Simulations show that this signature is weaker for galaxies with inclination angles larger than 30 deg (see e.g. Fig. 30 in Iannuzzi & Athanassoula 2015). Most of the aforementioned galaxies are below or close to this threshold, with the exception of NGC 4981, 4984, 7140 and NGC 7755, where this interpretation should be taken carefully.

NGC 5728 is an interesting case. The h_4 map shows clear minima along the bar major axis, and the isophotal contours show regions that are slightly offset from the bar major axis on opposite sides of the bar at each side from the centre. This S-shape configuration is produced by what Erwin & Debattista (2013) called spurs. Such spurs are photometric signatures of box/peanuts seen at an angle (Athanassoula & Beaton 2006, see also Beaton et al. 2007), and thus this galaxy is a beautiful illustration where both photometric and kinematic signatures of box/peanuts coincide.

Considering the TIMER sample altogether, we find a clear signature of the presence of a box/peanut in 13 of the 21 galaxies. As discussed in Appendix A.1, at least in some cases, the signature absence may be due to the restricted fields studied here. Therefore, our results indicate a lower limit for the fraction of box/peanuts in our sample of massive barred galaxies of at least 62 %. This is consistent with the estimate presented by Erwin & Debattista (2017) also for massive barred galaxies, namely, 79 %, even though our analysis relies entirely on kinematics and theirs on photometry. On the other hand, in a study employing the kinematic diagnostic on a sample of 10 galaxies, Méndez-Abreu et al. (2014) found a box/peanut fraction of 50 %.

Kinematic Signatures of Barlenses

As mentioned in the Introduction, barlenses are thought to be the face-on projection of box/peanuts, and thus also part of the bar, even though they extend further from the bar major axis than the remaining of the bar. (Laurikainen et al. 2005, 2007, 2011; Athanassoula et al. 2015; Laurikainen & Salo 2016). If that is the case, one expects to see, in the region dominated by the barlens, both the h_4 minima that characterise box/peanuts and the $v - h_3$ correlation that characterise bars (see Iannuzzi & Athanassoula 2015, although one should be careful to disregard regions dominated by a nuclear disc). In the S⁴G images, we see a clear barlens morphology in five of the galaxies studied here: NGC 1300, 3351, 4643, 4984 and NGC 7755. Except for the latter, all are classified by Buta et al. (2015) as indeed showing a barlens. In these five galaxies, but more strongly in NGC 4984 and NGC 7755, the expected signatures are seen. In NGC 4984, the h_4 minima form a thick ring with inner and outer radii of about 10 arcsec and 20 arcsec, respectively. In the same region one sees the $v - h_3$ correlation. Likewise, NGC 7755 shows the same signatures in radii between 5 arcsec and 10 arcsec. These features are very similar to what is seen in the simulations of Iannuzzi & Athanassoula (2015, their fig. 29).

While this is consistent with our current understanding of barlenses and box/peanuts, we point out that seven other galaxies in this sample are classified by Buta et al. (2015) as having barlenses, but the expected signatures are not clear. Evidently, part of the reason could be attributed to the relatively small spatial coverage in some of these galaxies. On the other hand, the visual classification of barlenses is prone to ambiguities and should be considered carefully, as nuclear discs, and even classical bulges, can be confused as barlenses. As discussed in Gadotti et al. (2015), the case of NGC 4371 is very illustrative. Morphologically, the signature of a barlens appears very clear. However, once kinematic information is included in the analysis, one concludes that the concerned structure is actually a rapidly rotating – and rather large – nuclear disc. This demonstrates the importance of assessing the nature of morphological components through a detailed analysis of the corresponding stellar kinematics.

Apart from NGC 4371, Buta et al. also include NGC 613, 1097, 1291, 5728, 5850 and NGC 7552 as having barlenses. In the case of NGC 1097 and NGC 1291 the TIMER fields are too restricted to properly study the corresponding regions. Recently, de Lorenzo-Cáceres et al. (2019b) found that the component visually classified by Buta et al. in NGC 5850 as a barlens is actually the nuclear disc, and that this is possibly the case for NGC 1291 also but it is difficult to ascertain that in the case of this galaxy given its low inclination. For the remaining three galaxies, the signatures are weak: The h_4 minima, clearly seen along the bar major axis are not prominent in the perpendicular direction. As discussed in Sect. 3.3.3, the presence of a $v - h_3$ correlation is not very significant in NGC 613, 5728 and NGC 7552, possibly due to projection effects, dust extinction and/or lower physical spatial resolution.

3.3.4 Previous Observations with Integral-field Spectrographs

Some galaxies in the TIMER sample have been observed before with different integral-field spectrographs. It is particularly instructive to qualitatively compare our observations with those performed with SAURON (Bacon et al. 2001; de Zeeuw et al. 2002) and WiFeS (Dopita et al. 2007, 2010), which as MUSE operate in the optical wavelength range. Four TIMER galaxies were studied previously with SAURON: NGC 4371 (Cappellari et al. 2011a), NGC 4643 (Cappellari et al. 2011a; Seidel et al. 2015b), NGC 5248 (Dumas et al. 2007) and NGC 5850 (de Lorenzo-Cáceres et al. 2008, 2013). NGC 7552 was studied with WiFeS by Seidel et al. (2015a). The spectral resolution obtained with SAURON is about a factor of two lower than in MUSE observations, which in turn is a factor of $\gtrsim 2$ lower than that provided by WiFeS. However, MUSE excels in sensitivity and spatial sampling. Part of the gains in sensitivity comes from the hosting telescopes. The collecting area of the VLT is roughly about four times larger than that of the William Herschel Telescope, which hosts SAURON, and roughly 16 times larger than the 2.3 m telescope at Siding Spring Observatory, which hosts WiFeS. The spatial sampling of MUSE corresponds to 0.2 arcsec per spatial element, whereas in both SAURON and WiFeS this is about 1 arcsec.

The remarkable spatial sampling and sensitivity of MUSE weigh significantly in studies of central structures in disc galaxies, such as this study. This can be appreciated when comparing the TIMER observations with those mentioned above. The MUSE kinematic maps reveal a multitude of details that remain hidden in the SAURON and WiFeS datasets (see e.g. the analysis concerning NGC 5850 in de Lorenzo-Cáceres et al. 2019b). Surely, indications of a kinematically colder nuclear component are seen in the SAURON and WiFeS data, but the lower spatial sampling makes it more difficult to ascertain that the component is a nuclear disc, separate from the main galaxy disc. Furthermore, a

more detailed analysis of the kinematic maps, for example by searching for the kinematic signatures of bars, box/peanuts and barlenses, as performed above, is certainly precluded by the relatively low spatial resolution of the SAURON and WiFeS data.

We can also compare our measurements of velocity and velocity dispersion with those presented by Venturi et al. (2018, for NGC 1365), Shimizu et al. (2019, for NGC 5728), and Bosma et al. (2010, for NGC 1291). The first two studies employed the exact same datasets as employed here, but performed independent analyses, and, reassuringly, the maps presented agree both qualitatively and quantitatively with those we present in Figs. 3.2 and A.1. The study presented in Bosma et al. (2010) is based on spectra taken with the deployable integral-field units of the FLAMES/GIRAFFE spectrograph at the VLT. The spectral resolution is about five times better than that of MUSE but the spectra are restricted to the calcium triplet wavelength range. The authors reported a central velocity dispersion of approximately 195 km s^{-1} , which is slightly above the value we derive, namely 168 km s^{-1} , but given the typical uncertainty of $\sim 10 \text{ km s}^{-1}$, the two measurements are statistically equivalent. Bosma et al. also reported measurements off the main bar in NGC 1291 at about 20 arcsec from the centre: One can see a drop in velocity dispersion to $\approx 110 \text{ km s}^{-1}$ and a radial velocity of only a few km s^{-1} (the galaxy is very close to face-on), and both features match our own measurements very well (see Fig. 3.2).

3.4 Comparison with Results from Photometric Decompositions

As shown above, detailed maps of v , σ , h_3 and h_4 are a powerful tool to understand the nature of the different stellar structures in a galaxy. These maps show that in all galaxies studied here (with no more than two possible exceptions) there clearly is a fast rotating nuclear disc, separate from the main galaxy disc.

In photometric decompositions, the central component in disc galaxies is often fitted using the Sérsic (1968) function, where the Sérsic index n regulates how centrally concentrated stars are, with large values of n produced by high concentrations of stars. Typically, one would expect that nuclear discs have an exponential surface brightness radial profile (i.e. with $n \approx 1$), just as main discs. In practice, it is common to associate disc-like bulges to values of $n \leq 2$, whereas classical bulges are associated to higher values.

However, establishing the physical nature of bulges via photometric structural analysis is not straightforward, since a stellar component with $n \approx 1$ is, in principle, not necessarily dynamically supported by rotation. The latter can only be directly probed with measurements of the stellar kinematics. Conversely, a stellar structure with $n > 2$ may not necessarily be dispersion-dominated. Given the large body of ancillary data for the TIMER galaxies, we are in an excellent position to directly compare our stellar kinematic measurements with results from studies on the photometric properties of these galaxies. This allows us to test whether the nuclear discs we find in the TIMER sample are correctly identified via photometric structural analysis, and this is the main goal of this section.

It is important to stress that an accurate image decomposition depends on the physical spatial resolution, depth and nature of the data (dust effects at short wavelengths are known to bias the results, see e.g. de Jong 1996; Gadotti et al. 2010; Pastrav et al. 2013). It also depends on the procedures employed to account for the exceedingly complex stellar structure in disc galaxies. In fact, many authors have argued that the distinction between disc-like and classical bulges using the Sérsic index alone is prone to uncertainties, and

that this analysis is only more robust when several criteria are used together, including criteria based on stellar kinematics and intrinsic shape (see e.g. Fisher & Drory 2016; Neumann et al. 2017; Costantin et al. 2018a,b).

Despite these caveats, to keep the comparison straightforward, we will simply verify what values of the Sérsic index n are obtained for the photometric bulges in decompositions of the TIMER galaxies, and use the criterion $n \leq 2$ for a successful identification of a nuclear disc, as opposed to a classical bulge. We will base this comparison on two recent studies separately in the following subsections. These studies were chosen here given the large overlap with the TIMER sample and the effort made to produce accurate results, with sophisticated models and careful procedures (which typically include individual inspection of the fits and numerous fits per galaxy to understand the uncertainties and avoid local χ^2 minima).

3.4.1 Kim et al. 2014

This work made use of S⁴G 3.6 μm images of 144 barred galaxies to derive structural parameters of bulges, bars and discs using BUDDA (de Souza et al. 2004; Gadotti 2008), taking advantage of the exquisite depth of the S⁴G data and the minimised impact of dust at these wavelengths. Nuclear point sources and outer disc breaks were accounted for to avoid biasing the bulge parameters. The PSF was determined for each image separately and modelled as a circular Moffat (1969) function. The surface brightness radial profiles of bars were modelled using a Sérsic function, and a bar was included in the models of all 13 TIMER galaxies that also belong to their sample.

For eight of the 13 galaxies, the photometric bulge Sérsic index is less than two, so in the majority of the cases the photometric bulge is identified as a disc-like bulge, in agreement with our kinematic analysis. For the remaining five galaxies, the bulges are found to have $n > 2$, which would in principle indicate that in these cases the Sérsic index fails to correctly identify the nature of the central component. However, one important caveat is that some galaxies may host composite bulges, that is, a small classical bulge at the very centre surrounded by a nuclear disc (see e.g. Erwin et al. 2015, who reported effective radii for small classical bulges ranging from 25 pc to 430 pc). For example, NGC 1291 clearly has a nuclear disc and an inner bar, and other studies have shown that it has also a small classical bulge with an effective radius of 416 pc within the nuclear disc (see Méndez-Abreu et al. 2019; de Lorenzo-Cáceres et al. 2019b). Thus, the bulge component in the fits of Kim et al. (2014) accounts for both the nuclear disc and the small classical bulge, which pushes the Sérsic index of the central component to $n = 2.7$. The other bulges with $n > 2$ are those in IC 1438, NGC 1433, NGC 4303 and NGC 7140. In IC 1438 there is a clear and substantial peak in the stellar velocity dispersion in the inner 1 arcsec to 2 arcsec, combined with a drop in h_4 , that suggests that this galaxy too has a small dispersion-dominated component within the nuclear disc. Nevertheless, for the remaining three galaxies we see no evidence of a small classical bulge in the kinematic maps.

In this context, it is important to note that the S⁴G images, with a typical PSF FWHM of about 2 arcsec, are inadequate to separate central components on those spatial scales. Therefore, the issue of composite bulges highlights the importance of high physical spatial resolution in imaging data, and the accounting of the different structural components in the models used to fit galaxy images.

We also point out that no bulge was found to have $n \approx 4$, which is expected for central regions dominated by classical bulges and for massive elliptical galaxies (e.g. Gadotti 2009, and references therein). In fact, the largest value of n found is below 3, which indicates that there is no galaxy in the TIMER sample with a dominant classical bulge, a conclusion that is corroborated in our accompanying paper (Bittner et al. 2020) through an analysis of stellar populations properties. This may result from the selection of the TIMER sample, which favours galaxies hosting nuclear components with a disc-like morphology. However, it is not clear if this criterion rejects galaxies hosting large classical bulges.

3.4.2 Salo et al. 2015

All galaxies in the TIMER sample were studied in Salo et al. (2015), which also employed S⁴G 3.6 μm images but did not account for disc breaks. A single oversampled PSF image that accurately reproduces the particular PSF 2D shape in the S⁴G images was used in all decompositions, and bars were modelled using a modified Ferrers profile. The decompositions were performed using GALFIT (Peng et al. 2002, 2010). Interestingly, bars were not included in the models for NGC 4303, 4981, 5248 and NGC 6902.

Only two of the photometric bulges were modelled with $n > 2$. One is again in NGC 1291, and the other is in NGC 7552. As discussed above, NGC 1291 hosts a small classical bulge, but we find no evidence for a similar component in NGC 7552. As in the study by Kim et al. no bulge was found with $n > 3$.

A comparison between the values obtained by the two studies for the Sérsic index of the photometric bulges shows some noticeable discrepancies, which again highlight how large is the uncertainty in the measurement of the Sérsic index. While for many galaxies the agreement between the two studies is remarkable, with an absolute difference in n of only 0.1 – 0.2, in some cases the difference reaches values above unity, and the measurements of Kim et al. are systematically above those of Salo et al. The median and mean values of the absolute difference in the Sérsic index measurements are 0.9 and 0.7, respectively. These discrepancies also show that even using the same dataset, a different outcome may result if models and/or techniques employed are different.

3.4.3 Exponential Photometric Bulges are Nuclear Discs

In the previous two subsections we have seen that photometric decompositions can retrieve reasonably well the nature of photometric bulges, and do so in the majority of the cases studied here. It is important to stress, however (and in addition to the caveats on photometric decompositions mentioned above), that the TIMER sample consists of nearby galaxies, and thus the physical spatial resolution of the images employed in these studies is relatively high. Decompositions employing images of more distant galaxies, with lower physical spatial resolution, will presumably not perform as well, but to quantify this is beyond the scope of this paper.

A powerful comparison to further test whether the photometric bulges modelled by Kim et al. and Salo et al. are indeed the rapidly rotating nuclear discs we identify with the MUSE TIMER data cubes – or are at least dominated by them, in the case of composite bulges – concerns comparing their sizes, as measured by the different techniques. The photometric decompositions readily provide the effective radii (r_e) of the fitted component, but a different approach is needed to derive the dimensions of the nuclear discs from the

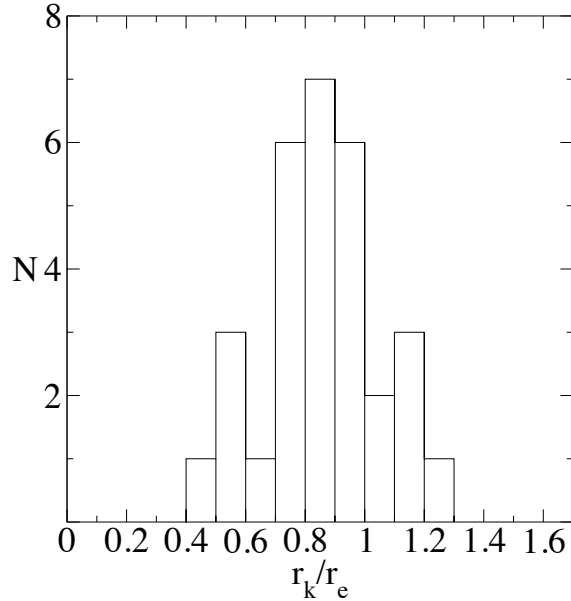


Figure 3.7: Distribution of the ratio between nuclear disc size, defined kinematically as the radius with maximum v/σ , and the effective radius of the photometric bulge component fitted through careful 2D multicomponent photometric decompositions. The values are clustered around a single value, following a normal distribution ($r_k/r_e = 0.86 \pm 0.19$), which shows that the photometric component defined as the bulge is (or is dominated by) the rapidly rotating nuclear disc.

kinematic measurements. To this end, we use the kinematic radius (r_k) defined above as the distance from the galaxy centre of the spatial bin showing the maximum value of v/σ in the region dominated by the rapidly rotating nuclear disc. If the photometric and kinematic components are in fact the same physical entity then the ratio r_k/r_e must be clustered around a single value, following a normal distribution. Figure 3.7 shows that this is indeed the case: r_k/r_e is clustered around 0.86. Fitting a normal distribution to our measured values of r_k/r_e yields a mean value of 0.86 and $\sigma = 0.19$. In addition, we applied to our data the statistical tests presented in D’Agostino et al. (1990) and Anscombe & Glynn (1983) to verify that the distribution in Fig. 3.7 has indeed both skewness and kurtosis that are statistically compatible with a normal distribution. Furthermore, the value of σ derived above is compatible with the typical uncertainty in the measurement of r_e , which is $\approx 20\%$.

One important aspect to consider is that correlations between r_k and r_e with other parameters could produce the results presented in Fig. 3.7, even if there is no physical connection between the nuclear discs and photometric bulges in our sample. For example, one could argue that a galaxy with a large disc would naturally have a large photometric bulge and a large nuclear disc, and thus the correlation between r_k and r_e would be trivial. We test this possibility using as a proxy for disc size ($R_{25.5}$) the 25.5 mag arcsec $^{-2}$ isophotal radius at 3.6 μm , as derived by Muñoz-Mateos et al. (2015) with S 4 G images (see Table 3.2). We find that the Pearson correlation coefficient R for the three relations, r_k versus r_e , r_k versus $R_{25.5}$, and r_e versus $R_{25.5}$, is, respectively: 0.87, 0.63 and 0.75. Thus, the correlation between r_k and r_e is stronger, and therefore not trivial. Considering these results altogether, we can safely state that exponential ‘bulges’ in photometric decompositions are nuclear discs. It is also important to bear in mind that r_k and r_e are measured through completely different techniques, which lends support to this conclusion.

3.5 The Origin of Nuclear Discs

While the results above are consistent with the scenario in which bars drive gas to the central region and ultimately build the observed nuclear discs, they do not rule out that, at least in some cases, accretion of gas could have been promoted by an interaction for example, before the formation of the bar, and therefore be unrelated to it. Thus, to shed more light in this discussion (and given that bars are expected to grow longer and stronger with time; e.g. Athanassoula 2003), in this section, we explore the properties of nuclear discs as derived from the TIMER kinematic maps in conjunction with other relevant bar properties. Table 3.2 presents the physical parameters we explore. In particular, we use the values determined by Kim et al. (2014) from their photometric decompositions for the bar radius (R_{bar}), ellipticity (ϵ) and bar-to-total luminosity ratio (Bar/T). Further, Díaz-García et al. (2016), presented a number of measurements of bar strength, from which we use Q_{B} and A_2 . Q_{B} indicates how strong the non-axisymmetric potential of the bar is as compared to the axisymmetric component of the total stellar mass distribution. It thus provides an indication of the impact of the bar on the dynamics of gas and stars in the host galaxy, by taking into consideration the effects of any central spheroid and the main disc itself. On the other hand, A_2 is a measure of the $m = 2$ Fourier component that is directly connected to the bar non-axisymmetry. More specifically, A_2 is calculated radially, normalised by the value of A_0 (the axisymmetric Fourier component) at each radius, and the value we employ here is the peak value of A_2/A_0 in the bar. Therefore, Q_{B} and A_2 provide complementary information on the bar and associated secular evolution processes.

Figure 3.8 shows that the radii of nuclear discs correlate significantly with bar radii, which is expected in the theoretical framework of the orbital structure in bars and how it evolves. In fact, the gas brought to the central region by bars is expected to accumulate in the region where the x_2 orbits of the bar dominate over the bar x_1 orbits⁶, where a nuclear stellar structure is thus formed (Athanassoula 1992b; Kim et al. 2012b; Li et al. 2015; Sormani et al. 2018; Seo et al. 2019, see also Romeo & Fathi 2015, 2016 who suggested that the disc instability radial profile can be used to predict the sizes of nuclear structures). As the bar evolves and grows, the region where the x_2 orbits dominate grows as well, hence the expected correlation⁷. This correlation between r_{k} and R_{bar} is therefore consistent with the picture in which the nuclear stellar discs studied here were formed from gas brought to the central region by the bar, and not built before the formation of the bar. In addition, in this picture, gas falling onto the outer boundary of the region dominated by x_2 orbits is prone to form stars and produce star-forming nuclear rings. Indeed, Seo et al. (2019) found in their simulations that nuclear rings are larger when bars evolve for a longer period of time. As expected, Comerón et al. (2010) found that the relation between the sizes of bars and nuclear rings is such that the upper limit of the distribution of nuclear ring sizes correlates with bar size. It is unclear if the larger scatter seen in their work is due to uncertainties in the measurements, or whether it is real and brought out by the larger sample. Nevertheless, the connection between nuclear ring size and bar radius in that work is also clear.

⁶The x_1 orbits are eccentric and parallel to the bar major axis, and are present throughout the bar. They are thus considered the ‘backbone’ of bars. The x_2 orbits are less eccentric and perpendicular to the bar major axis, and are only found in the bar inner region.

⁷We point out that, with all things being equal, more eccentric bars will have smaller nuclear discs, since the extent of the x_2 orbits is then shorter (see Athanassoula 1992b). A nuclear disc will not grow in a bar that gets longer but keeps its semi-minor axis constant. In fact, Fig. 3.8 shows that more eccentric bars tend to have smaller nuclear discs.

Galaxy (1)	v/σ (2)	r_k (3)	$r_{e,K}$ (4)	$r_{e,S}$ (5)	R_{bar} (6)	ϵ_{bar} (7)	Bar/T (8)	Q_B (9)	A_2 (10)	$R_{25.5}$ (11)
IC 1438	2.57	0.60	0.77	0.56	4.43	0.53	0.11	0.178	0.838	12.76
NGC 613	2.35	0.59	0.71	0.68	9.72	0.62	0.26	0.489	0.903	23.60
NGC 1097	2.82	1.07	0.95	1.24	10.40	0.45	0.26	0.254	0.709	36.24
NGC 1300	2.98	0.33	0.44	0.38	6.70	0.75	0.08	0.58	0.603	17.88
NGC 1433	2.00	0.38	0.42	0.42	3.63	0.68	0.08	0.366	0.560	12.82
NGC 3351	2.57	0.24	0.41	0.33	4.02	0.70	0.09	0.227	0.513	12.41
NGC 4303	1.36	0.21	0.39	0.29	3.52	0.56	0.06	0.535	0.550	18.14
NGC 4371	2.02	0.95		0.82				0.234	0.618	16.38
NGC 4643	1.31	0.50		0.86				0.272	0.813	24.45
NGC 4981	0.99	0.14		0.29				0.093	0.172	13.56
NGC 4984	2.49	0.49	0.53	0.55	6.18	0.48	0.14	0.176	0.836	18.98
NGC 5236	1.89	0.37		0.32				0.472	0.467	19.35
NGC 5248	1.66	0.49		0.58				0.138	0.324	17.28
NGC 5728	2.84	0.63	0.83	0.86	9.70	0.51	0.28	0.387	1.149	20.58
NGC 5850	1.13	0.80	0.62	0.74	7.84	0.64	0.16	0.327	0.742	20.80
NGC 7140	1.45	0.63	0.99	0.66	11.16	0.36	0.23	0.399	0.805	24.86
NGC 7552	2.61	0.33	0.34	0.36	4.90	0.64	0.32	0.358	1.060	9.79
NGC 7755	2.20	0.47		0.53				0.401	0.841	20.29

Table 3.2: Properties of nuclear discs, bars and galaxies in the TIMER sample. Column (1) gives the galaxy designation, while columns (2) and (3) show, respectively, the peak value of v/σ in the nuclear disc, and the radius at which this peak is located, r_k . In columns (4) and (5) we show the effective radius of the photometric bulge derived by Kim et al. (2014) and Salo et al. (2015), respectively. Columns (6), (7) and (8) present the bar radius, ellipticity and bar-to-total luminosity ratio as derived by Kim et al. (2014). In columns (9) and (10) we present the values of Q_B and A_2 calculated by Díaz-García et al. (2016). Finally, column (11) shows the values of $R_{25.5}$ obtained by Muñoz-Mateos et al. (2015). All radii are in kpc, using the distances tabulated in Paper I, and the bar radii and ellipticities derived by Kim et al. are deprojected following the 2D approach described in Gadotti et al. (2007).

Interestingly, in the pioneering work of Shlosman et al. (1989), a model is put forward in which the bar sweeps gas from the region of the main disc within R_{bar} , building a nuclear disc that is limited by the ILR radius. In their model, this radius is of the order of $0.1R_{bar}$, and the relation between r_k and R_{bar} we show in Figure 3.8 is close to that. This is an indication of the correctness of their model.

Figure 3.8 also shows that r_k tends to be larger for lower values of bar ellipticity and higher values of Bar/T. Again this can be naturally understood considering the connection between nuclear discs and the extent of the bar x_2 orbits. As x_2 orbits cannot extend past the bar edges, more elongated bars will tend to have less extended x_2 orbits, and therefore smaller nuclear discs, as we observe. As bars evolve, they capture stars from the disc, grow longer and become more massive, which increases Bar/T. In addition, with the buckling of the inner parts of the bar, and the formation of the box/peanut and barlens structure, the inner region of the bar becomes less elongated, decreasing the overall bar ellipticity. The less elongated inner region promotes the expansion of the x_2 orbits, creating the trends between r_k with bar ellipticity and Bar/T. Nevertheless, it is important to point out that in this study some of the observed trends are not strong correlations, and therefore more work is needed to confirm these conjectures (see Appendix A.2 for an analysis of the statistical properties of these relations).

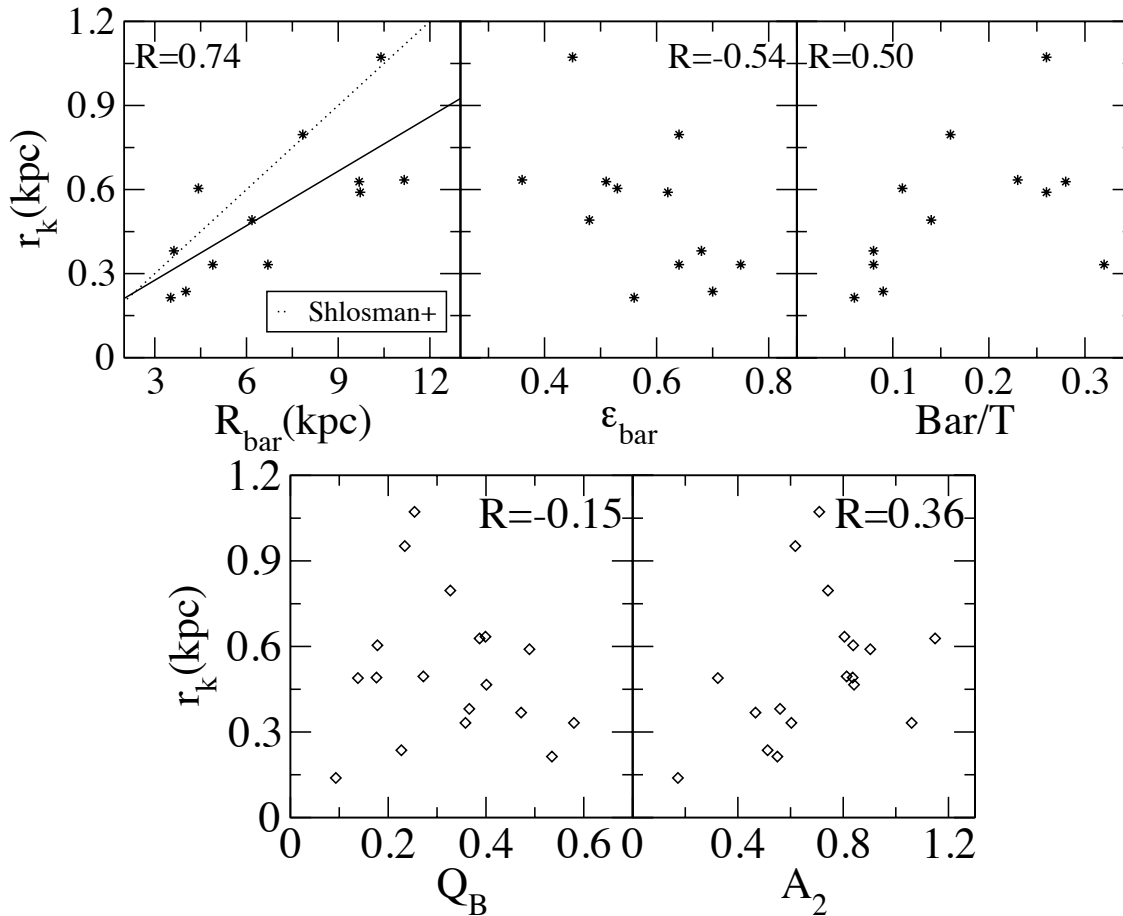


Figure 3.8: Relations between the kinematic sizes of nuclear discs and selected bar properties. The top left panel shows that r_k is correlated with bar size (semi-major axis). The solid line is a simple linear regression fit to the data, whereas the dotted line corresponds to $r_k = 0.1R_{\text{bar}}$, the relation suggested in Shlosman et al. (1989). In the top middle and right panels we present how the kinematic size of nuclear discs relates to bar ellipticity and bar-to-total luminosity ratio, respectively. The bottom panels show the relations between r_k and different measures of bar strength (from Díaz-García et al. 2016, see text for details). Bar radii and ellipticities are from Kim et al. (2014) and are deprojected. The Pearson correlation coefficient R is indicated in each panel. In Appendix A.2 we present an analysis of the statistical properties of these relations.

It is interesting to note that the range of bar radii in Fig. 3.8 spans a factor of ≈ 4 , although in simulations bars grow by factors no larger than ≈ 2 (see e.g. Martínez-Valpuesta et al. 2006). This implies that the trends discussed here are not only the result of the way bar properties evolve, but also of the initial bar properties. On the other hand, the bar radius has been shown to be an increasing function of the bulge-to-total luminosity ratio (B/T) when normalised by $R_{25.5}$ (Kim et al. 2014). Moreover, the function appears to be the same whether the photometric bulge component is a classical bulge or a nuclear disc. Kim et al. (2014) suggested that this relation is expected since more prominent classical bulges can absorb substantial angular momentum from the bar, which leads to more significant bar growth (see Athanassoula & Misiriotis 2002; Athanassoula 2003). On the other hand, Kim et al. argue that a similar relation is expected also in the case of nuclear discs, as longer bars will push more gas inwards to the central region, leading to more prominent nuclear discs (Athanassoula 1992b). However, understanding why the relation is the same for classical bulges and nuclear discs remains a puzzle.

One also sees in Fig. 3.8 that the relation between r_k and Q_B is such that for low values of Q_B nuclear discs show a wide range of sizes, but only small nuclear discs are seen when Q_B is large. This can in part be explained by the reduced extent of x_2 orbits in more eccentric bars. Again, a similar result was found by Comerón et al. (2010) for the sizes of nuclear rings. Interestingly, we find a trend (albeit with some scatter) between r_k and A_2 that to the best of our knowledge has not been reported elsewhere. While A_2 is a purely photometric parameter, r_k is a purely kinematic one, and therefore this trend too is consistent with a picture in which the formation of the nuclear disc is connected to the bar.

Interestingly, the relation between r_k and A_2 does not show the same properties as the relation between r_k and Q_B . While the connection between r_k and Q_B is similar to the connection between r_k and bar ellipticity, the correlation between r_k and A_2 resembles that between r_k and Bar/T . This can be understood in the way A_2 and Q_B are defined. Although both A_2 and Q_B are measurements of bar strength, Q_B takes into account the overall axisymmetric galactic potential, whereas A_2 accounts for it only at the radius where A_2 is measured, typically close to the end of the bar. As described above, this is done with the normalisation of A_2 by the value of A_0 at that radius. Higher values of A_2 are produced if the density of stars in the bar increases while it decreases in the region of the disc outside the bar but within the bar radius. Kim et al. (2016) showed that, as bars evolve, they capture stars in the disc region within the bar radius, reducing the density of stars in the region. Further, they showed that evolved bars thus tend to have elevated values of A_2 , a result that was confirmed in Buta (2017). This is corroborated by the finding from Díaz-García et al. (2016) that longer bars are stronger and that this correlation is particularly tight if bar strength is measured as A_2 , since bars are expected to grow longer as they evolve. Therefore, the trend between r_k and A_2 suggests that galaxies with more evolved bars tend to have larger nuclear discs. We already discussed above that more evolved bars should naturally host larger nuclear discs due to the increase in the extension of the bar x_2 orbits as bars evolve. Furthermore, we speculate that this is also a result of the bar being able to induce gas inflows for longer, thus producing more massive nuclear discs. In fact, Cole et al. (2014) found that their simulations produce smaller nuclear discs if the inflow of gas is halted. Nevertheless, we stress that there is substantial scatter in the relation between r_k and A_2 seen in Fig. 3.8, and thus further studies are needed to confirm this relation (see Appendix A.2). In addition, more work is necessary to understand if the scatter is caused not only by difficulties in the measurements, but if other physical properties or processes play a role in the evolution of r_k and A_2 .

Further work with larger samples would also be helpful to rule out that some of these correlations could result from underlying correlations, such as between bar size and disc size (see Erwin 2005; Gadotti 2011). However, we highlight that the anti-correlation we observe between r_k and bar ellipticity cannot be explained by the underlying correlation between bar size and ellipticity, simply because these correlations have opposite signs. Since the anti-correlation between r_k and bar ellipticity is predicted by the bar-driven model for the formation of nuclear discs, it suggests that the nuclear discs in the TIMER sample are indeed built by the bar.

We point out that while all galaxies plotted in Fig. 3.8 have nuclear discs, not all of them have nuclear rings, according to the evaluation by Comerón et al. (2010). These galaxies are NGC 4643, 4981, 4984, 5850, 7140 and NGC 7755. Nuclear rings are found at the edge of nuclear discs when both structures are present, close to or at the radius where v/σ peaks, that is, at r_k . We verified that these galaxies are not systematically off in any of the relations shown in this section. Therefore, both nuclear rings and nuclear

discs follow the same relations, suggesting that the formation of both structures stems from the same fundamental process. The results discussed above suggest that the main processes providing the gaseous content for the formation of both nuclear rings and nuclear discs are bar-driven, and the connection between nuclear rings and nuclear discs suggests that a single set of joint mechanisms is in charge of transforming the gas component into these stellar structures. In our accompanying paper (Bittner et al. 2020) we study this connection in more detail through the analysis of the stellar population properties of nuclear discs and nuclear rings.

Processes unrelated to bars have also been studied as possible drivers of the building of nuclear discs. Recent simulations have shown that nuclear discs can be produced at the late stage of gas-rich mergers (see Querejeta et al. 2015; Wang et al. 2015; Sauvaget et al. 2018). However, we note that most of these nuclear discs are substantially larger than the largest nuclear disc we find. Also, it is important to point out that even in this case bar-driven secular evolution processes can still play a major role in the building of the nuclear disc. The merger may simply serve as a mechanism to bring gas to the disc region within the bar radius, and from this point the bar is responsible to stream the gas further inwards. The merger can also trigger the bar instability if it was not spontaneously triggered before the interaction. Bars can be short-lived in major mergers, so it is unclear whether bars have played no role in the aforementioned simulations. While we present above suggestive evidence that in the TIMER sample of barred galaxies the nuclear discs are built by bars, such mergers can result in unbarred galaxies hosting nuclear discs, even if a bar played a major role but is later dissolved due to the merger.

On the other hand, gas-poor mergers are not expected to produce such regular and rapidly rotating structures. However, as we described in the Introduction, Eliche-Moral et al. (2011) argue that nuclear discs are built in their collisionless simulations when specific conditions are met. Nevertheless, an inspection of the corresponding kinematical maps (see their figures 12 to 15) reveals that these simulations do not reproduce the signatures of nuclear discs we discussed in Sect. 3.3.3. Specifically, our nuclear discs are characterised by conspicuous drops in σ and an anti-correlation between v and h_3 (indicating near-circular orbits). In contrast, in the aforementioned simulations, the central region shows an inward increase in σ , and, in most cases, a correlation between v and h_3 . Therefore, we conclude that, to date, there is no evidence that the nuclear discs in TIMER could have been built in gas-poor mergers.

This is not to say that the building of nuclear discs through bar-driven processes is perfectly well understood in simulations. In fact, the bar-built nuclear disc in the model of Cole et al. (2014) is too large compared to its bar and does not fit in the observed relation we present in Fig. 3.8. While the observed ratio between nuclear disc size and bar size is of the order of 10%, the nuclear disc size in the model of Cole et al. is about 30% of the bar size. More theory work is necessary, and it would be particularly helpful to understand how simulations can reproduce the observed trends in Fig. 3.8.

3.6 Discussion and Conclusions

The results presented in Sects. 3.3.3 and 3.5 show a good agreement with the bar-driven secular evolution scenario for the building of nuclear stellar components in disc galaxies, at least for massive galaxies with conspicuous bars and nuclear structures. The nuclear discs found with the TIMER data have all the kinematic properties expected in a stellar

structure built via the collapse of molecular clouds brought to the central region along the leading edges of the bar and put into near-circular orbits in the region where the bar x_2 orbits dominate: Large rotational support, low velocity dispersion and an anti-correlation between v and h_3 consistent with near-circular orbits (see Figs. 3.2 and A.1). Further, these nuclear discs are clearly an additional component on top of the original main galaxy disc. This can be seen from the elevated values of h_4 , resulting from the fact that the stars in the nuclear discs have orbits closer to circular than those in the main discs at the radii where the nuclear disc dominates (Figs. 3.2, A.1 and 3.3). These properties are also consistent with a formation scenario with gas accretion that is unrelated to bars. However, Fig. 3.8 shows how the size of the nuclear disc depends on the bar radius, ellipticity, bar-to-total ratio and bar strength, which is qualitatively understood in the theoretical framework of bar evolution and the impact of bars on the gas component. These connections between the nuclear disc size and bar properties are only expected in a scenario where the accretion of gas that builds the nuclear disc is due to the bar. Figure 3.8 also suggests that more evolved bars tend to build larger nuclear discs, which may help putting constraints on the ages of bars, although more theoretical work on the formation and evolution of nuclear discs is necessary. Finally, in our accompanying paper (Bittner et al. 2020), we present stellar population properties of the TIMER nuclear discs, and discuss how these properties too are consistent with the picture in which such nuclear discs are built via bar-driven processes.

As mentioned above, it is still unclear how rare are nuclear discs in unbarred galaxies (but see Comerón et al. 2010). Weak bars and oval distortions in the disc can be difficult to identify morphologically but may as well produce nuclear discs in the same way as prominent bars. Nevertheless, a similar study as we present here but with a sample of unbarred galaxies showing nuclear discs would be very beneficial. A comparison between the physical properties of nuclear discs in barred and unbarred galaxies (such as size and angular momentum) would shed light on their formation process.

As we have seen in Sect. 3.4, in photometric decompositions of galaxy images, one often finds an exponential or near-exponential central component, that is, a photometric bulge with low Sérsic index ($n \lesssim 2$), which is thought to originate from bar-driven secular processes. In agreement with this expectation, the results presented in Sect. 3.4 show that the nuclear discs we find spectroscopically in TIMER, through an assessment of the stellar kinematics, are indeed often recognised as (near) exponential bulges in the photometric studies we considered. This is encouraging, despite the caveats discussed above on using the Sérsic index alone to separate nuclear discs from classical bulges. However, we stress again that the TIMER sample was built to include galaxies for which a visual assessment alone is already capable of identifying nuclear components that appear to have disc-like properties. This is a result of the relatively high physical spatial resolution of the images employed. Arguably, the recovery of nuclear discs via photometry is more prone to errors when the spatial resolution is not suitable, for example for more distant galaxies.

Even in these optimal circumstances, Sect. 3.4 shows that some difficulties are encountered, for example when performing photometric decompositions of galaxies with composite bulges. A small classical bulge within a nuclear disc can dominate the light emission in such a way that the presence of a bar-built nuclear component goes unnoticed in the photometry. This problem is of course exacerbated if the spatial resolution is not high enough to separate the two components, and/or a single model is used to fit the central region, erroneously encompassing all structures therein. It is as yet not clear how often disc galaxies host small classical bulges embedded in nuclear discs so the severity of this

problem is still unknown. However, our results show that composite bulges may produce values for the Sérsic index between 2 and 3, suggesting that pure classical bulges can be identified only by putting a more stringent threshold at $n > 3$ (especially considering the corresponding uncertainties). Nevertheless, this is to be considered with caution and, particularly, in a statistical sense (see Méndez-Abreu et al. 2018).

The TIMER maps shown in Figs. 3.2, 3.3 and A.1 show several kinematic signatures corroborating theoretical work on the dynamical properties of bars and inner bars. This is also the case for box/peanuts (Sect. 3.3.3). This allows us to put a lower limit in the fraction of massive barred galaxies with box/peanuts at 62%, in broad agreement with previous results (with the caveat that our sample selection favours conspicuous bars and nuclear components). The case of NGC 5728 is remarkable, in that it shows an agreement between kinematic and photometric considerations on the properties of box/peanuts in inclined disc galaxies. Concerning barlenses (Sect. 3.3.3), we find evidence corroborating previous studies that find that barlenses are simply the face-on projection of box/peanuts, that is, of the inner parts of bars, since we see in the barlens region kinematic signatures of both a bar and a box/peanut, as expected from numerical simulations. This is the first time kinematic evidence is presented to support this picture. Barlenses are often difficult to identify photometrically and have morphologies similar to classical bulges, and therefore identifying them through their kinematic properties can help putting more accurate constraints on the impact of mergers in the evolution of disc galaxies. Altogether, these results show the power of spatially resolved kinematics in producing a straightforward understanding of the physical properties and nature of stellar structures in the inner regions of galaxies, and suggest that high-quality integral-field spectroscopy data is necessary to accurately decompose these complex inner regions.

Stellar Populations of Nuclear Discs

Inside-out Formation of Nuclear Discs and the Absence of Old Central Spheroids in Barred Galaxies

The centres of disc galaxies host a variety of structures built via both internal and external processes. In this study, we constrain the formation and evolution of these central structures, in particular, nuclear rings and nuclear discs, by deriving maps of mean stellar ages, metallicities, and $[\alpha/\text{Fe}]$ abundances. We use observations obtained with the MUSE integral-field spectrograph for the TIMER sample of 21 massive barred galaxies. Our results indicate that nuclear discs and nuclear rings are part of the same physical component, with nuclear rings constituting the outer edge of nuclear discs. All nuclear discs in the sample are clearly distinguished based on their stellar population properties. As expected in the picture of bar-driven secular evolution, nuclear discs are younger, more metal-rich, and exhibit lower $[\alpha/\text{Fe}]$ enhancements, as compared to their immediate surroundings. Moreover, nuclear discs exhibit well-defined radial gradients, with ages and metallicities decreasing, and $[\alpha/\text{Fe}]$ abundances increasing with radius out to the nuclear ring. Often, these gradients show no breaks from the edge of the nuclear disc up through the centre, suggesting that these structures extend to the very centres of galaxies. We argue that continuous (stellar) nuclear discs may form from a series of bar-built (initially gas-rich) nuclear rings that expand in their radius as the bar evolves. In this picture, nuclear rings are simply the (often) star-forming outer edge of nuclear discs. Finally, by combining our results with those taken from an accompanying kinematic study, we do not find evidence for the presence of large, dispersion-dominated components in the centres of these galaxies. This could be a result of quiet merger histories, despite the large galaxy masses, or, perhaps, due to high angular momentum and strong feedback processes preventing the formation of these kinematically hot components.

4.1 Introduction

Bars are prominent stellar structures that are frequently found in disc galaxies. Approximately 2/3 of all local disc galaxies exhibit a bar and this proportion decreases monotonically with increasing redshift, down to bar fractions of 10% to 15% at $z > 1$ (see e.g. Eskridge et al. 2000; Menéndez-Delmestre et al. 2007; Sheth et al. 2008; Aguerri et al. 2009; Méndez-Abreu et al. 2010; Kraljic et al. 2012; Sheth et al. 2012; Melvin et al. 2014). Nonetheless, in massive galaxies, strong bars have been identified up to higher redshifts ($z \sim 2$; Simmons et al. 2014) and their existence at these redshifts has been inferred from studies of their stellar age distribution (see e.g. Gadotti et al. 2015; Pérez et al. 2017). In addition, it appears unlikely that bars can be destroyed, at least, once they have grown sufficiently strong (Athanasoula et al. 2005). Altogether, these studies suggest that bars influence the evolution of their host galaxies over timescales as long as about 10 Gyr.

Bars evolve and influence galaxies in a variety of ways, which becomes clear when we compare barred and unbarred galaxies. For instance, the inner regions of barred galaxies show systematically higher metallicities and star-formation rates (Ellison et al. 2011) as well as increased nuclear activity and accretion onto central black holes (Alonso et al. 2018). Moreover, bars typically exhibit flat age and metallicity gradients along their major axis, a clear indication of their influence on the inner discs of galaxies (see e.g. Sánchez-Blázquez et al. 2011; Fraser-McKelvie et al. 2019; Neumann et al. 2020). This influence is also evident in the fact that barred galaxies often show a light deficit in the disc surrounding the bar, an effect that is absent in unbarred galaxies and thought to be caused by the capture of disc stars (see e.g. James et al. 2009; James & Percival 2016; Kim et al. 2016; Donohoe-Keyes et al. 2019).

One particularly interesting effect of bars is the creation of substructures in the nuclear region of disc galaxies such as nuclear rings and nuclear discs by redistributing angular momentum (Combes & Gerin 1985). More specifically, the non-axisymmetric potential of the bar exerts strong tangential forces in the main disc, which cause interstellar gas to shock and lose angular momentum. As a result, the gas streams inward along the leading edges of the bar. These large-scale streaming motions are typically highlighted by prominent dust lanes and are clearly evident in both numerical and observational studies (see e.g. Athanassoula 1992b; Knapen 2007; Cole et al. 2014; Fragkoudi et al. 2016). This inward gas flow is halted in the nuclear region of the galaxy, where the gas, due to its collisional nature, often settles in a nuclear ring where star formation proceeds. It has also been suggested that nuclear discs could be formed via the same mechanism, but extend to smaller radii (Piner et al. 1995; Sakamoto et al. 1999; Sheth et al. 2005; Sormani et al. 2015).

While there is convincing evidence that these nuclear rings and nuclear discs are built from gas that was funnelled to the centre by the bar, it remains unclear what physical mechanism determines the size of these structures. It has been suggested that the radius of nuclear rings is related to the Inner Lindblad Resonance (ILR) of the bar. Observationally, nuclear rings are often found close to the ILR and therefore it is argued that nuclear rings are a result of bar resonances¹ (see e.g. Combes & Gerin 1985; Knapen 2005; Comerón et al. 2010). More precisely, Athanassoula (1992a,b) argues that the size of the nuclear ring is limited by the radial extent of the x_2 orbit family. However, Kim et al. (2012a) suggests that the size of the nuclear ring is not determined by bar resonances, but, instead, it is given by the residual angular momentum of the inflowing gas. Another scenario was given by Sormani et al. (2018), who present a mechanism explaining the origin of nuclear rings and find that the size of the ring is set by the effect of viscous shear forces. Using numerical simulations, Seo et al. (2019) show that nuclear rings grow in size as the bar grows longer and funnels in gas from larger radii in the galactic disc. In line with this result, Knapen (2005), Comerón et al. (2010), and Gadotti et al. (subm., hereafter G20) find that the radii of nuclear rings and nuclear discs are correlated with the bar length.

Due to the collisional nature of the gas, the subsequent star formation generates stars in (near) circular orbits. More precisely, stellar nuclear discs are expected to be characterised by high rotational velocities and low velocity dispersions (see e.g. Cole et al. 2014). In an accompanying study, G20 uses the same integral-field spectroscopic observations of the TIMER survey (Time Inference with MUSE in Extragalactic Rings) employed in this study to confirm these expectations. In addition, they show that nuclear discs have exponential surface brightness profiles and dominate the stellar light in the centre of the

¹However, the ILR used in these studies only holds in the mildly non-axisymmetric regime and, therefore, it is ill-defined for strong bars.

galaxy. Similarly, numerical simulations expect nuclear discs to be younger and more metal-rich than the bar. In particular, in the framework of secular evolution, nuclear discs form only after the formation of the bar and, thus, they are expected to have stellar populations younger than those found in the bar. As star formation in these central regions continues, it is also expected that their metal content will increase (Cole et al. 2014).

Numerical simulations show that the formation of nuclear discs can also be initiated by galaxy mergers (see e.g. Mayer et al. 2008; Chapon et al. 2013). However, the nuclear discs in these simulations are at least one order of magnitude smaller than those commonly produced in the bar-driven formation scenario. Interestingly, Comerón et al. (2010) finds that 19% of all nuclear rings occur in unbarred galaxies. However, they show that in most of these cases there is evidence of some non-axisymmetry in the potential of the galaxy which might cause the formation of nuclear rings through mechanisms similar to those in the bar-driven scenario, albeit weaker.

Secular evolution continues to take effect within these stellar nuclear discs themselves. In fact, some nuclear discs develop bars themselves, resulting in the remarkable situation of having a small disc with a small bar embedded within a large disc with a large bar. These inner bars do not only resemble the shape of regular bars, but they also seem to form and evolve in the same way main bars do (de Lorenzo-Cáceres et al. 2019b, 2020). In fact, inner bars buckle vertically just like main bars (Méndez-Abreu et al. 2019) and even exhibit the same $v - h_3$ correlation typically associated with bars (Bittner et al. 2019).

A variety of nomenclatures for these central substructures of galaxies have been established. Particularly common is the term ‘bulge’ and its variations such as, for instance, ‘pseudo-bulge’ and ‘disc-like bulge’. In this paper, we avoid the term ‘bulge’ and, instead, we use more physical descriptions of the stellar structures. In particular, we refer to a ‘kinematically hot spheroid’ instead of using the term ‘classical bulge’. Bar-built central discs with typical sizes of hundreds of pc that are rotationally supported but kinematically distinct from the main galactic disc, are denoted as ‘nuclear discs’ (see G20). This choice is made to avoid confusion with inner and outer discs in the context of breaks in the light profile of main discs of galaxies. Rings associated with the outermost edge of nuclear discs are named ‘nuclear rings’ in order to clearly distinguish them from inner and outer rings typically found close to and outside of the bar radius, respectively. Similarly, large-scale bars found in main stellar discs of galaxies are simply referred to as ‘bars’ while smaller bars that form and evolve within nuclear discs themselves are referred to as ‘inner bars’².

While the formation of nuclear rings and nuclear discs is thought to be bar-driven, the connection between nuclear rings and nuclear discs is still elusive. In particular, little is known about how the settling of gas near the ILR can originate a stellar disc that seems to extend from the nuclear ring inwards. In the present study, we build upon an accompanying study which investigates the stellar kinematics of nuclear discs (G20). Here, we characterize nuclear discs based on their spatially resolved, mean stellar population properties. For the first time, we observe nuclear discs at a sufficiently high spatial resolution (~ 100 pc or less) to investigate detailed spatial changes in their population properties, even including $[\alpha/\text{Fe}]$ abundances. In addition, we aim to establish if nuclear discs extend all the way to the galactic centre and how their properties compare to those of nuclear rings. Thanks to the superb quality of the data, we further explore the presence of composite structures consisting of nuclear discs and kinematically hot spheroids in the centres of these galaxies (see e.g. Méndez-Abreu et al. 2014; Erwin et al. 2015).

²In the literature inner bars are often also referred to as *nuclear bars*.

This paper is organised as follows. In Sect. 4.2, we introduce the TIMER survey and summarise its observation and data reduction strategy. The measurement of mean stellar population properties is described in Sect. 4.3 and its reliability and uncertainties discussed in Sect. 4.4. Our main observational results are presented in Sect. 4.5 and we discuss their physical implications in Sect. 4.6. We close with a summary of our findings in Sect. 4.7.

4.2 The TIMER Survey

The TIMER project is a survey aiming to reconstruct the star formation histories of nuclear structures in order to constrain the formation time of bars and establish when the main discs of galaxies became dynamically mature. Building upon the results of a pilot study of NGC 4371 (Gadotti et al. 2015), the current TIMER sample consists of 24 barred galaxies with a large variety of bar-built central structures, such as nuclear rings, nuclear discs, and inner bars (Gadotti et al. 2019). To date, 21 galaxies have been observed with the Multi-Unit Spectroscopic Explorer (MUSE; Bacon et al. 2010) on the Very Large Telescope.

The TIMER sample has been selected from the Spitzer Survey of Stellar Structure in Galaxies (S⁴G; Sheth et al. 2010), thus, naturally constraining the sample to nearby ($d < 40$ Mpc), bright ($m_B < 15.5$ mag), and large ($D_{25} > 1$ arcmin) objects. In addition, we required all galaxies to have inclinations below 60 deg and central substructures as classified by Buta et al. (2015). The resulting sample covers a range in stellar mass from $2.0 \times 10^{10} M_{\odot}$ to $17.4 \times 10^{10} M_{\odot}$.

All observations were taken in ESO's period 97 between April and September 2016. Using the wide-field-mode of the MUSE spectrograph, we obtained observations covering a wavelength range from 4750 Å to 9350 Å with a spectral sampling of 1.25 Å and a field of view of 1 arcmin² at a spatial sampling of 0.2 arcsec. The typical seeing of the observations was 0.8 arcsec to 0.9 arcsec. Each galaxy was observed with approximately one hour of integration on source and dedicated sky exposures.

The data reduction is based on version 1.6 of the MUSE data reduction pipeline (Weilbacher et al. 2012). In summary, bias, flat-fielding, and illumination corrections were applied, the data was calibrated in flux and wavelength, and telluric features were removed. Thanks to the dedicated sky exposures, the sky background was removed, exploiting a principal component analysis. Finally, the observations are accurately registered astrometrically. A detailed accounting of the physical properties of the TIMER sample, observations, and data reduction is presented in Gadotti et al. (2019).

4.3 Data Analysis

The analysis of the data, as reviewed in detail below, was conducted within the modular analysis framework of the GIST pipeline³ (Galaxy IFU Spectroscopy Tool; Bittner et al. 2019). More specifically, this software provides an all-in-one framework for the analysis of spectroscopic data, including all tasks from the preparation of the input data, over its scientific analysis, to the generation of publication quality plots.

³<http://ascl.net/1907.025>

We spatially binned the data to a signal-to-noise ratio (S/N) of approximately 100 per bin, exploiting the adaptive Voronoi tessellation routine of Cappellari & Copin (2003). The S/N per spaxel is measured within the wavelength range of 4800 Å to 5800 Å, identical to the fitted wavelength range. The notably high S/N is chosen to assure the robustness of the analysis, in particular, as the derivation of stellar population properties is a S/N sensitive measurement. In a series of tests, we found that increasing the S/N from 40 to 80 results in more homogeneous stellar populations across contiguous spatial bins, as illustrated in Fig. 4.1. In other words, using a higher S/N reduces the level of stochasticity in the stellar population properties in adjacent bins. This is at least partly due to an improved accuracy in the subsequent emission-line subtraction (see below). Further increasing the S/N from 80 to 100 only has meagre effect on the obtained population properties. Nonetheless, we prefer to follow the more conservative approach of using a S/N level of 100. Owing to the high quality of our data, this does not significantly reduce the obtained spatial resolution in the nuclear discs. We further note that spaxels which surpass this S/N threshold, as commonly found in the centre of our fields, remain unbinned. Spaxels below the isophote level, which has an average S/N level of 3 are excluded from the analysis, in order to avoid systematic effects in the low surface brightness regime.

Prior to any analysis, we de-redshifted the spectra to the rest-frame based on an initial guess of the systemic redshift. We further adopted as the line-spread function the udf-10 parametrisation by Bacon et al. (2017) and broaden all template spectra to this resolution before conducting any fits. Through a series of tests, we explore the effect of different wavelength ranges on the derivation of stellar population properties. The results indicate that the red part of the spectra (beyond 5800 Å) is, in contrast to the derivation of stellar kinematics, not suited for the measurement of the stellar population content. In particular, the lower sensitivity to stellar population properties in this part of the spectrum, small residuals from the sky subtraction, and absorption features from the interstellar medium add complexities to the analysis. Therefore, we restrict the analysis to the wavelength range from 4800 Å to 5800 Å.

The actual analysis is conducted in three separate steps. Firstly, we derive the stellar kinematics by performing an unregularised run of the pPXF routine (Cappellari & Emsellem 2004; Cappellari 2017). In order to account for small differences in the shape of the continuum between spectra and templates, we include a low order multiplicative Legendre polynomial in the fit. At this stage, all emission lines are masked. In the next step, we model emission lines by fitting single Gaussian templates with pyGandALF (Bittner et al. 2019), a new Python implementation of the original GandALF routine (Sarzi et al. 2006; Falcón-Barroso et al. 2006). The fitting routine linearly combines Gaussian emission-line templates with a set of spectral templates to obtain the emission-line properties. In this process, the stellar continuum and emission-lines are fit simultaneously, while keeping the stellar kinematics of the continuum fixed to those obtained previously. Instead of a Legendre polynomial, pyGandALF exploits a two-component reddening correction. This correction accounts for ‘screen-like’ dust extinction of the entire spectrum as well as for reddening that affects only the emission line regions. We note that the kinematics of the H β and [OIII] lines are kept as free parameters in the fit, while the kinematics of [NI] are tied to that of [OIII]. If the amplitude-to-residual noise ratio of a measured emission line is at least four, we consider the line detection significant and subtract the emission line from the observed spectrum. In this way, we obtain emission-subtracted spectra. In addition to this quantitative check, the quality of the emission-line modelling is inspected visually. While the quality of the fits is good for the majority of the spectra, deviations are found in some regions that show starbursts or a significant contribution from active

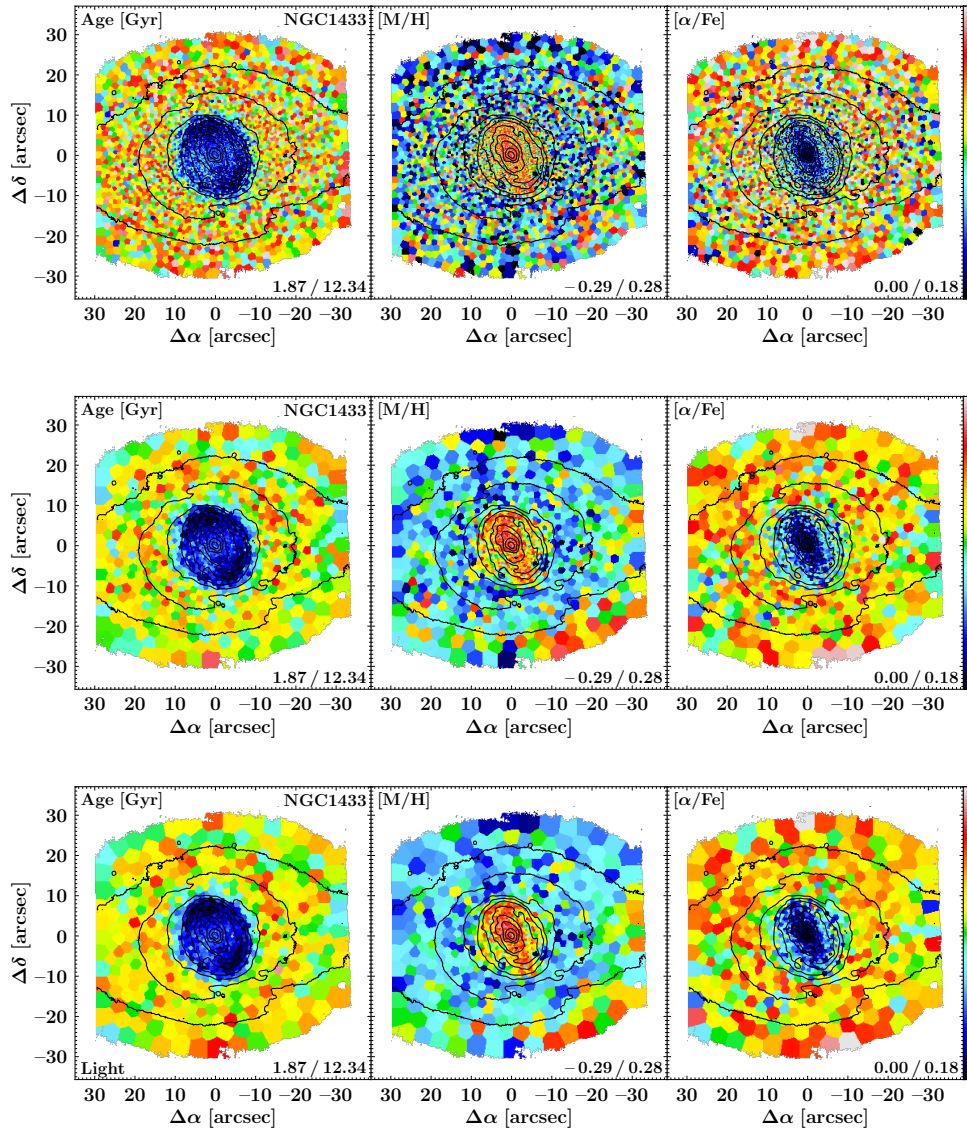


Figure 4.1: Comparison of light-weighted, mean stellar population properties of NGC 1433, derived at a S/N of 40 (upper panels), 80 (centre panels), and 100 (lower panels). Each set of panels displays age, metallicity, and $[\alpha/\text{Fe}]$ enhancements. The limits of the colour bar are stated in the lower-right corner of each panel. Based on the reconstructed intensities from the MUSE cube, we display isophotes in steps of 0.5 mag. North is up; east is to the left.

galactic nuclei (AGN). This is a result of the different dynamics and the superposition of distinct components (star-forming regions, AGN, etc.) in these regions, which, therefore, cannot be modelled by a single Gaussian template. However, performing a detailed multi-component emission-line analysis for the entire sample is beyond the scope of this study, particularly as these small deviations in starbursting and AGN-affected regions do not affect our general conclusions on nuclear discs.

Finally, based on these emission-subtracted spectra, we performed a regularised run of the pPXF routine to estimate the mean stellar population properties. In order to avoid possible degeneracies between velocity dispersion and metallicity (see e.g. Sánchez-Blázquez et al. 2011), we fixed the stellar kinematic to those obtained before. In addition, we apply a 8th order multiplicative Legendre polynomial in the fit that also accounts for extinction and other continuum effects. Here, pPXF estimates non-parametric star-formation histo-

ries by assigning weights to the spectral templates such that the observed spectrum is best reproduced. However, this measurement represents an inverse, ill-conditioned problem. Therefore, in order to obtain a physically meaningful solution, **pPXF** applies a regularisation during the fit (Press et al. 1992; Cappellari 2017). Thus, of all equally consistent solutions, the regularised run of **pPXF** returns the smoothest solution that is still statistically consistent with the data in consideration. While the strength of the regularisation can have a substantial impact on the shape of individual star formation histories, the derived mean population properties we consider in this study show only a meagre dependence on the chosen regularisation. Nonetheless, we follow the procedure of determining the maximum allowed regularisation parameter, as described, for instance, in McDerimid et al. (2015). Firstly, the noise is rescaled in such a way that the resulting χ^2 of the unregularised run is unity. Subsequently, the regularisation strength is increased iteratively until the χ^2 of the regularised run exceeds that of the unregularised run by approximately $\sqrt{2N_{\text{pix}}}$, with N_{pix} being the number of spectral pixels included in the fit. This procedure is applied to the bin with the highest S/N in each cube. In case of contamination of this spectrum by strong extinction, features from active galactic nuclei, or intense star formation, a spatial bin with similarly high S/N in its close vicinity is used instead. The obtained regularisation strength is then applied to the entire galaxy. We note that for NGC 1365 and NGC 5728, the above procedure allowed conspicuously high regularisation strengths, possibly due to large-scale outflows from the active galactic nuclei. For these cases, we therefore chose a lower regularisation strength of 10, similar to that obtained for the rest of the sample.

In Sect. 4.4, we investigate if the derived population properties depend on whether the $[\alpha/\text{Fe}]$ enhancement is modelled in the **pPXF** fit or not. Therefore we repeat the analysis with two variants of the MILES single stellar population (SSP) models. Firstly, we use the MILES ‘base models’, which follow the abundance pattern of stars in the solar neighbourhood (Vazdekis et al. 2010). At low metallicities, these models show elevated values of $[\alpha/\text{Fe}]$ enhancements, although the used isochrones are scaled-solar, while at high metallicities, the $[\alpha/\text{Fe}]$ values resemble the solar abundance. Secondly, we employ a combination of scaled-solar and $[\alpha/\text{Fe}]$ enhanced MILES models (Vazdekis et al. 2015). These provide two values of $[\alpha/\text{Fe}]$, namely 0.00 (solar abundance) and 0.40 (supersolar abundance). While the use of a SSP model library that covers only two values of $[\alpha/\text{Fe}]$ is not optimal, **pPXF** is capable of interpolating between these two values and returns intermediate $[\alpha/\text{Fe}]$ enhancements (see also Pinna et al. 2019). We note that full-spectral fitting codes are typically measuring an average $[\alpha/\text{Fe}]$ ratio. In other words, in the models, all α elements are increased or decreased while in realistic galaxies, different α elements are decoupled from each other. In addition, different wavelength ranges are more sensitive to different α elements. Therefore, the $[\alpha/\text{Fe}]$ abundances returned by **pPXF** are a convoluted average of the underlying abundances of individual α elements. For the sake of clarity, we chose to refer to $[\alpha/\text{Fe}]$ abundances throughout this study.

Both sets of SSP models assume a Kroupa Revised IMF with a slope of 1.30 (Kroupa 2001), use BaSTI isochrones (Pietrinferni et al. 2004, 2006, 2009, 2013), and have a spectral resolution of 2.51 Å (Falcón-Barroso et al. 2011). The parameter space is sampled in 53 values of age between 0.03 Gyr and 14.0 Gyr and 12 values of stellar metallicity ($[M/H]$) between -2.27 dex and 0.40 dex.

Over the past years, several fitting routines for the measurement of stellar population properties have been implemented. To assess the systematic effects related to different software implementations, we repeat the analysis with STECMAP (Ocvirk et al. 2006b,a).

To this end, we employ the same emission-subtracted spectra and fix the stellar kinematics to those initially obtained with pPXF. Since STECMAP is not designed to model $[\alpha/\text{Fe}]$ abundances, we only use the base models here.

The above analysis is performed in such a way that light-weighted results are obtained. This is achieved by normalising each spectral template by its own mean flux within the used wavelength range. In order to convert those light-weighted stellar population properties to mass-weighted ones, we employ the mass-to-light ratio predictions of the SSP models. In particular, this mass-to-light ratio includes not only the remaining mass in the stellar component but also the mass of all resulting stellar remnants.

Light- and mass-weighted population properties are averaged with the following relations

$$\langle t \rangle = \frac{\sum_i w_i t_{\text{SSP},i}}{\sum_i w_i} \quad (4.1)$$

$$\langle [\text{M}/\text{H}] \rangle = \frac{\sum_i w_i [\text{M}/\text{H}]_{\text{SSP},i}}{\sum_i w_i} \quad (4.2)$$

$$\langle [\alpha/\text{Fe}] \rangle = \frac{\sum_i w_i [\alpha/\text{Fe}]_{\text{SSP},i}}{\sum_i w_i}, \quad (4.3)$$

with the weight w_i assigned to the i th template with age $t_{\text{SSP},i}$, metallicity $[\text{M}/\text{H}]_{\text{SSP},i}$, and an $[\alpha/\text{Fe}]$ enhancement of $[\alpha/\text{Fe}]_{\text{SSP},i}$. Hence, stellar ages are averaged in linear scale while metallicities and $[\alpha/\text{Fe}]$ abundances are averaged logarithmically.

4.4 Stability and Errors of the Measurements

In this section, we further explore the reliability of the derived mean stellar population properties. First, we discuss the effect that modelling the $[\alpha/\text{Fe}]$ abundances has on ages and metallicities, before comparing results obtained with the pPXF and STECMAP routines. We do not intend to provide a thorough software comparison here, but simply mean to check our results with a second, independent analysis. This also allows us to better understand error estimates on the derived stellar populations properties.

4.4.1 Population Properties with and without $[\alpha/\text{Fe}]$ Modelling

To date, most stellar population spectral libraries do not provide spectra with varying $[\alpha/\text{Fe}]$ abundances. Similarly, not all full spectral fitting codes are designed to model $[\alpha/\text{Fe}]$ enhancements in the fitting process. Here we test whether stellar ages and metallicities obtained with or without the modelling of $[\alpha/\text{Fe}]$ abundances are consistent. In Fig. 4.2, we plot population properties derived with pPXF without the modelling of $[\alpha/\text{Fe}]$ and using base models as a function of those derived with $[\alpha/\text{Fe}]$ modelling and the enhanced templates.

In the case of the light-weighted results, we find a very good agreement between the two runs, with the median standard deviation of all 17 bins being 0.34 Gyr and 0.05 dex in age and $[\text{M}/\text{H}]$, respectively. For the mass-weighted results, the correspondence is good as well, with slightly older ages and lower metallicities being obtained without the $[\alpha/\text{Fe}]$ modelling. The corresponding median standard deviation of all bins is 0.57 Gyr in age and 0.04 dex in metallicity. We thus conclude that ages and metallicities obtained with pPXF depend only little on whether $[\alpha/\text{Fe}]$ abundances are included in fitting processes or not.

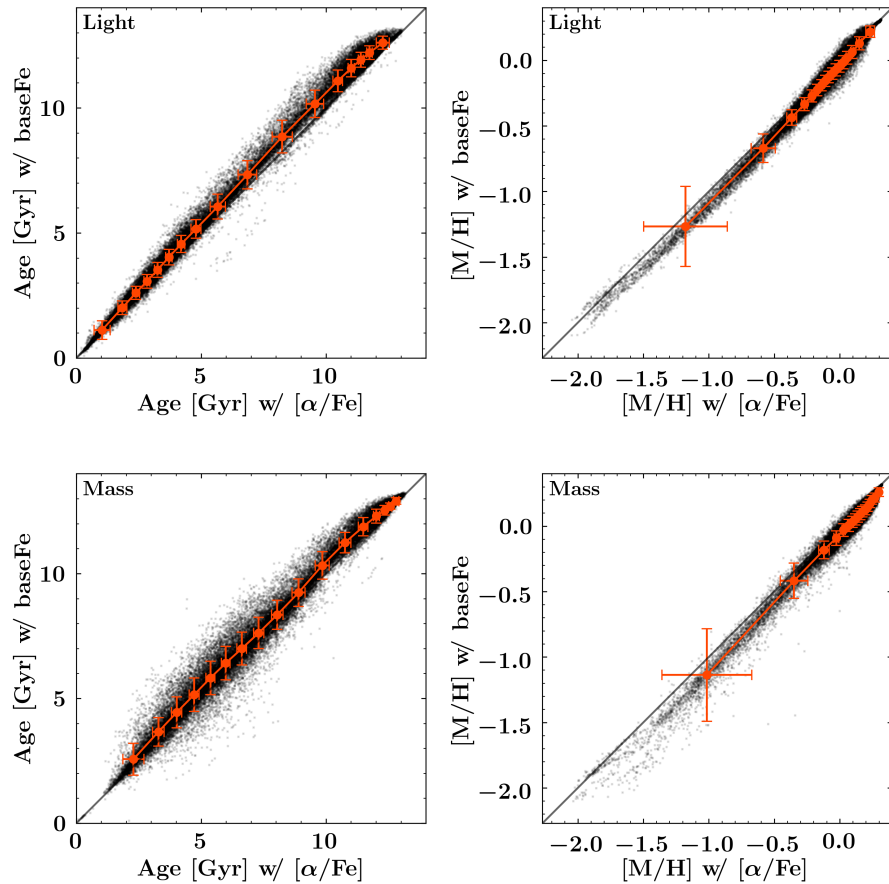


Figure 4.2: Light-weighted (upper panels) and mass-weighted (lower panels) population properties derived with pPXF without $[\alpha/\text{Fe}]$ modelling as a function of those derived with $[\alpha/\text{Fe}]$ modelling. This figure includes all spatial bins from all galaxies in the present TIMER sample. Highlighted in orange are the means and standard deviations in 17 bins, each combining the results from approximately 2600 observed spectra. We note that the large standard deviation in the bin with the lowest metallicity is a result of the large range of metallicities included in this bin and does not necessarily result from an increased scatter.

Nonetheless, we find a small systematic offset in the measured metallicities. At the lowest metallicities, the fit that uses the MILES base models returns systematically lower metallicities. This effect seems to be related to the chemical composition of the base models that might differ from the abundance pattern of the observed spectra. This is confirmed by repeating the analysis of NGC 1097, now using models with $[\alpha/\text{Fe}]$ enhancements of 0.00 dex and 0.40 dex separately. While the analysis using models with $[\alpha/\text{Fe}] = 0.00$ returns slightly lower metallicities compared to the run with varying $[\alpha/\text{Fe}]$ abundances, the fits with $[\alpha/\text{Fe}] = 0.40$ return systematically higher metallicities. In fact, this behaviour is expected, as the typical $[\alpha/\text{Fe}]$ abundances measured in the low metallicity bins of NGC 1097 is approximately 0.2 dex. Nonetheless, the measured systematic differences of approximately 0.1 dex are slightly smaller than the typical errors estimated for this measurement (0.14 dex, see Sect. 4.4.3) and only a relatively small number of bins in the TIMER sample have such low metallicities.

4.4.2 Population Properties from pPXF and STECMAP

Over time, a large set of well-known fitting routines for the derivation of non-parametric star formation histories was developed, for instance, MOPED (Heavens et al. 2000), pPXF (Cappellari & Emsellem 2004; Cappellari 2017), STARLIGHT (Cid Fernandes et al. 2005), STECMAP (Ocvirk et al. 2006b,a), VESPA (Tojeiro et al. 2007), ULySS (Koleva et al. 2009), FADO (Gomes & Papaderos 2017), or FIREFLY (Wilkinson et al. 2017). As different routines are based on distinct fitting methodologies with diverse code implementations, the results obtained with different software might vary. Therefore, it is important to repeat the data analysis with various routines in order to better understand the involved systematics. In the following, we compare the stellar population properties obtained with the pPXF and STECMAP routines.

In Fig. 4.3 we plot population properties derived with STECMAP as a function of those measured with pPXF. We emphasise that we perform both runs using exactly the same emission-subtracted spectra, MILES base models, and stellar kinematics, in order to isolate the differences due to the fitting algorithms. The light-weighted age results obtained with pPXF and STECMAP are in reasonable agreement, as indicated by the median standard deviation of all 17 bins being 1.06 Gyr. However, STECMAP returns systematically lower stellar ages. More precisely, the deviation between pPXF and STECMAP is increasing with age: little deviation is found at low ages ($\Delta t \approx 0$ Gyr at 1 Gyr) while the discrepancy for old populations is the largest ($\Delta t \approx 4$ Gyr at 13 Gyr). The measured metallicities conform well, with STECMAP providing slightly lower [M/H] values, except for the lowest metallicities. The median standard deviation of all bins is 0.14 dex.

We find only a few outliers at low ages, in particular at STECMAP ages below 1 Gyr and pPXF ages of 1 Gyr to 5 Gyr, which is caused by two strongly starbursting regions in NGC 5236. A visual inspection of the corresponding spectra and fits has shown complex $H\beta$ profiles for which the emission line modelling with pyGandALF is imperfect. In fact, this discrepancy is absent when repeating the analysis of this galaxy while masking all wavelength regions affected by emission lines. We emphasise that the derived stellar population quantities in all other parts of this galaxy are identical, whether or not emission-lines are masked or subtracted. A more detailed modelling of such complex emission-line profiles for the entire sample is beyond the scope of this study. However, as there are no other clear discrepancies found, the emission-line modelling appears to be sufficiently good for all other galaxies.

For mass-weighted stellar population properties, the scatter is substantially higher, as compared to the light-weighted results. However, mean ages and metallicities within each bin are still in reasonable agreement. Similarly to the comparison of light-weighted ages, a systematic deviation of the measured ages is found. At young ages, STECMAP detects older stellar populations while for old ages, it derives younger stellar ages, as compared to pPXF. The median standard deviation of all bins amounts to 2.15 Gyr. Metallicities again conform well, with a similar median standard deviation of 0.13 dex. We speculate that this increased deviation between pPXF and STECMAP might be a result of the conversion from light- to mass-weighted population properties. This conversion is calculated using mass-to-light ratio predictions of the employed SSP models. These predictions have intrinsic uncertainties which result from the used stellar evolution models, but are also a function of both the derived stellar age and metallicity. Thus, the mass-weighted ages and metallicities depend on the uncertainty in both light-weighted ages and metallicities, as well as the mass-to-light ratio predictions themselves. Therefore, it is not surprising that the obtained uncertainties are significantly higher for mass-weighted results.

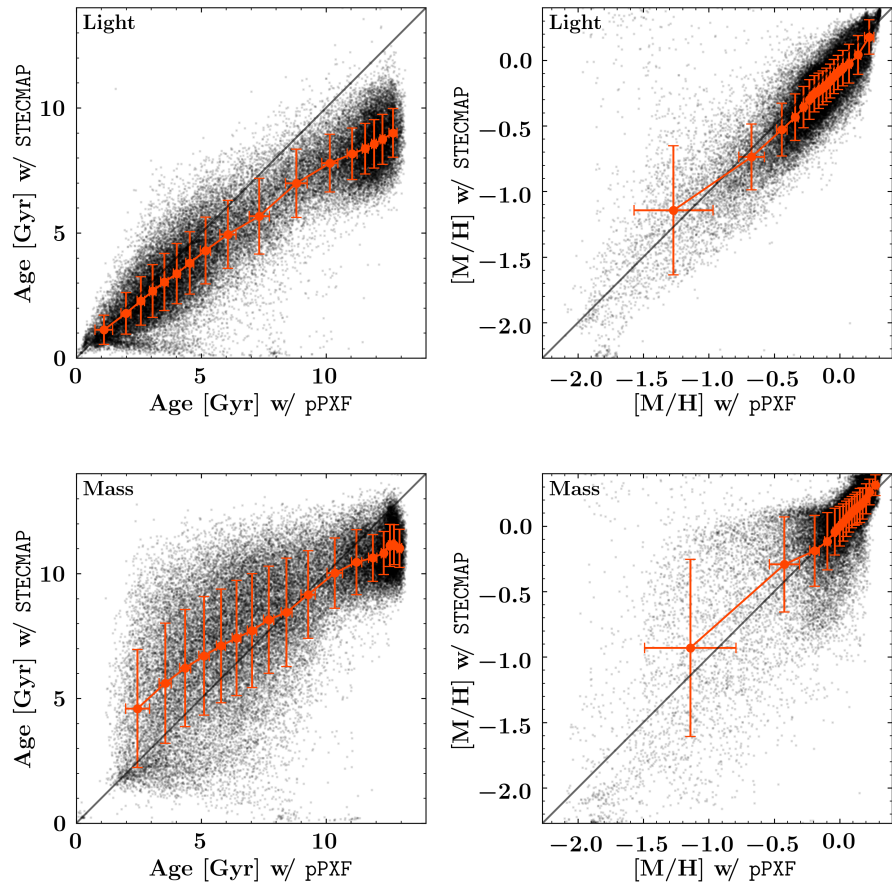


Figure 4.3: Same as Fig. 4.2, but showing mean stellar population properties derived with STECMAP as a function of those derived with pPXF.

4.4.3 Error Estimates on Stellar Population Properties

Estimating measurement uncertainties on mean stellar population properties or non-parametric star formation histories derived with full spectral fitting is not trivial. Firstly, it is not possible to assign formal errors, as the population properties are simply averaged from the used subset of spectral templates and not measured in the actual fitting process. Secondly, errors derived by repeating the measurement on multiple Monte Carlo realisations of the data, as commonly used for the estimation of errors on the stellar kinematics, might be significantly underestimated due to the effect of regularisation.

Here we propose to use the median standard deviations from the comparisons between pPXF and STECMAP, as stated in Sect. 4.4.2, as error estimates. While such an uncertainty does not represent a real measurement error, the scatter between two different fitting routines does provide a realistic estimate. Of course, this approach cannot account for errors introduced by other systematics, such as intrinsic problems with the spectral models, template mismatch, or IMF variations. Nonetheless, these error estimates compare well to those discussed by other authors.

For instance, Gadotti et al. (2019) repeated the analysis on 100 Monte-Carlo realisations in order to estimate errors. Using STECMAP at a signal-to-noise level of 40, they find typical errors in ages of 0.5 Gyr to 1 Gyr and 0.005 to 0.010 in metallicities (Z) which translate to errors of approximately 0.11 dex to 0.23 dex in $[M/H]$ when evaluated at solar metallicity.

In addition, their error estimates depend on both age and metallicity, and whether light- or mass-weighted results are considered. They further conclude that for STECMAP the chosen initial conditions and smoothness parameter have no effects. In contrast, Pinna et al. (2019) used 50 Monte Carlo realisations and also investigate how much the applied corrective polynomial and regularisation parameter of pPXF affect the resulting error estimates. Fitting stellar kinematics and population properties simultaneously at a S/N level of 40, they find typical errors of 3 Gyr, 0.1 dex, and 0.06 dex for mass-weighted age, $[M/H]$, and $[\alpha/Fe]$. Ruiz-Lara et al. (2015) performed an extensive comparison of star formation histories derived from colour-magnitude diagrams of resolved stars and the analysis of integrated light spectroscopy with STECMAP, ULySS, and STARLIGHT and reached similar conclusions.

4.5 Results

In this section, we present our general findings concerning the mean stellar population properties in the central regions of all TIMER galaxies. In addition, we complement these results by presenting maps of $H\alpha$ emission-line fluxes, which help inform our analysis. We do not focus on the properties of individual objects here but, instead, we intend to provide an overview of the common characteristics of nuclear discs. We refer the reader to Appendix B.1 for more detailed descriptions of each observed galaxy.

Observationally it seems that the gaseous nuclear ring simply highlights the outer edge of the stellar nuclear disc. In this section, we provide further evidence supporting this picture. We remind the reader that the term nuclear disc refers to the kinematically cold and regularly rotating stellar discs in the central regions of the galaxies. According to the kinematic analysis of the TIMER sample in an accompanying paper (see G20), these nuclear discs extend to the centres of the galaxies and have a well-defined outer edge. In contrast, we use the term nuclear ring only to describe the outermost part of these nuclear discs, as these regions are often highlighted by gaseous nuclear rings. Therefore, the denomination nuclear disc includes both the stellar nuclear disc and the gaseous nuclear ring, while the term nuclear ring refers only to the outer edge of the nuclear disc.

4.5.1 Maps of Dust-corrected $H\alpha$ Emission-line Fluxes

We use $H\alpha$ emission-line fluxes as a tracer of HII regions in order to reliably distinguish star-forming from non-star-forming nuclear rings/discs in the TIMER sample. This distinction allows to investigate their stellar population properties separately and detect areas in which the derived stellar population content might have been affected by strong star formation.

For the purpose of deriving emission-line fluxes, it is not necessary to spatially bin the data to high S/N, as the S/N of individual emission lines are typically higher compared to that of the stellar continuum. Therefore, we prefer to consider $H\alpha$ maps on a spaxel-by-spaxel basis. To this end, we use results derived in previous TIMER papers (Gadotti et al. 2019; Neumann et al. 2020), exploiting the software `PyParadise`, an extended Python implementation of `Paradise` (Walcher et al. 2015). The obtained emission-line fluxes are corrected for dust extinction by measuring the Balmer decrement and applying the models of Calzetti et al. (2000) to account for the wavelength dependency.

Galaxy	i	PA	M_{stellar}	Spatial scale	R_{kin}	H α	Central	Age
(1)	deg	deg	$10^{10} M_{\odot}$	pc/arcsec	pc	morphology	emission	gradient
(1)	(2)	(3)	(4)	(5)	(6)	(7)	(8)	(9)
Non-star-forming nuclear rings								
IC 1438	24	-25.4	3.1	164	604	NR	LINER	SYM
NGC 1291	11	-8.9	5.8	42	—	IRR	LINER	—
NGC 1300	26	-45.9	3.8	87	332	NR	LINER	FLAT
NGC 1433	34	18.2	2.0	49	381	IRR	LINER	FLAT
NGC 4371	59	88.1	3.2	82	952	NO	NO	—
NGC 4643	44	55.5	10.7	125	495	C	LINER	SYM
NGC 5248	41	-75.6	4.7	82	489	U	SF/LINER	SYM
NGC 5850	39	-26.5	6.0	112	796	C	NO	SYM
NGC 7140	51	4.1	5.1	180	634	NR	SF	FLAT
NGC 7755	52	23.9	4.0	153	466	NR	LINER	SYM
Star-forming nuclear rings								
NGC 613	39	-50.1	12.2	120	590	NR	LINER	—
NGC 1097	51	-52.1	17.4	100	1072	NR	LINER	—
NGC 3351	42	11.2	3.1	49	236	NR	SF	—
NGC 4303	34	-36.7	7.2	80	214	NR	LINER	—
NGC 4981	54	-28.2	2.8	120	139	NR	LINER	—
NGC 4984	53	29.6	4.9	103	491	NR/C	AGN	—
NGC 5236	21	47.0	10.9	34	368	IRR	SF	—
NGC 7552	14	54.9	3.3	83	332	NR	SF	—
Peculiar nuclear regions								
NGC 1365	52	42.0	9.5	87	—	NR/IRR	AGN	—
NGC 5728	44	1.1	7.1	149	628	NR/C	AGN	—
NGC 6902	37	-49.6	6.4	187	—	PECULIAR	NO	—

Table 4.1: Overview of the different subsamples and some general properties of nuclear rings, nuclear discs, and their host galaxies. Column (1) states the galaxy name, while columns (2) and (3) provide the inclination and position angle of the galaxy disc (Muñoz-Mateos et al. 2015). Columns (4) to (6) state the total stellar mass of the galaxy derived within S⁴G, the spatial scale of the observations, and the kinematic radius of the nuclear discs (see G20), respectively. Column (7) states whether the morphology of the H α emission is dominated by a nuclear ring (NR), central emission (C), a uniform nuclear disc (U), an irregular emission pattern (IRR), or no ionised gas emission throughout the field of view (NO). In column (8) we provide the ionisation source in the innermost region of the galaxy (at $r \ll R_{\text{kin}}$), as determined with BPT-diagrams (we note, nonetheless, that the main ionisation source in the nuclear rings the majority of the radial extent of the nuclear disc is star formation). Column (9) describes the shape of the age profile inside/outside of the nuclear disc as symmetric (‘SYM’) or flatter within the nuclear disc (‘FLAT’). This classification is given only for the non-star-forming galaxies, as the age profiles are often hard to distinguish in the other subsamples. In NGC 1291 and NGC 4371 the age profiles are dominated by the inner bar and projection effects, respectively, and, thus, we omit these galaxies in this classification.

In Fig. B.1, we present the maps of the dust-corrected H α fluxes for all TIMER galaxies. The maps reveal a large variety of ionised gas structures in the galaxy centres. While some galaxies exhibit little to no H α emission, other objects show large amounts of H α emission. In most galaxies, in particular in the cases with significant H α emission, the star formation is concentrated in a well-defined nuclear ring. In order to compare the stellar population properties of galaxies with and without such star-forming nuclear rings, we split the sample in two groups of galaxies. All nuclear rings with H α emission-line fluxes above $5 \times 10^{-10} \text{ erg s}^{-1} \text{ cm}^{-2} \text{ arcsec}^{-2}$ are classified as star-forming, while galaxies with lower H α emission-line fluxes are classified to host non-star-forming nuclear rings. We note that this threshold is an empirical finding chosen to reproduce the morphological

differences evident in the galaxies. The classification in star-forming and non-star-forming nuclear rings does not depend on the precise value of this threshold. An overview about the different subsamples and the basic properties of the respective galaxies, in particular, their $H\alpha$ morphology, is provided in Table 4.1.

A total of eight galaxies were found to have star-forming nuclear rings (NGC 613, NGC 1097, NGC 3351, NGC 4303, NGC 4981, NGC 4984, NGC 5236, NGC 7552). The high $H\alpha$ emission-line fluxes in the nuclear rings of these galaxies suggest strong ongoing star formation or even a starburst episode. It is only in the case of NGC 5236 that the ionised gas emission is not concentrated to the nuclear ring, but irregularly distributed in the centre of the galaxy. We note that the derived stellar population properties might be affected by the strong star formation in these regions, for instance, by residuals in the emission-line subtraction of the $H\beta$ line. Moreover, the measurement of stellar population properties might be affected by the nebular continuum and contributions from active galactic nuclei (AGN). However, the nebular continuum is only important in very young, star-forming regions, while possible AGN contributions are restricted to the centremost spaxels. In addition, unphysical results might be obtained if the stellar light is dominated by a population that is not represented in the employed set of SSP models. In our set-up, this could be the case for stellar populations with ages below 30 Myr, as this is the youngest population included in the MILES models. In any case, distinguishing the ages of stellar populations younger than 1 Gyr is not relevant for our conclusions presented in Sect. 4.6.

The subsample of non-star-forming nuclear rings consists of 10 galaxies (IC 1438, NGC 1291, NGC 1300, NGC 1433, NGC 4371, NGC 4643, NGC 5248, NGC 5850, NGC 7140, NGC 7755). The $H\alpha$ morphology in the centres of these galaxies exhibits a larger variety. While NGC 4371 does not show any ionised gas emission, other galaxies show irregular emission patterns (NGC 1291, NGC 1433), centrally concentrated emission (NGC 4643, NGC 5850), or a more uniform gas disc (NGC 5248). Nonetheless, IC 1438, NGC 1300, NGC 7140, and NGC 7755 still show some concentration of gas in a nuclear ring. We note that in these galaxies the derived stellar populations are presumably not affected by low star-formation activity.

Three galaxies are excluded from above subsamples. NGC 1365 and NGC 5728 are significantly affected by outflows from their AGN (see e.g. Venturi et al. 2018; Durré & Mould 2018) on large spatial scales. However, we note that other galaxies in the sample, for instance, NGC 613 (Falcón-Barroso et al. 2014), host AGN outflows as well, but these appear weaker and do not significantly affect the derived stellar population properties (see also Appendix B.1). The third excluded galaxy is NGC 6902 which is only weakly barred and does not show unequivocal signatures of a nuclear disc. Unless specifically noted, these galaxies are excluded from the discussions below.

While star formation is an efficient ionisation source, the observed $H\alpha$ emission could also be triggered by AGN. In order to distinguish between ionisation from star formation and AGN, we apply the standard BPT methodology (Baldwin et al. 1981). We find that the $H\alpha$ emission in the very centres of many galaxies, at spatial scales much smaller than that of the nuclear disc, is often generated by AGN or LINER (see Table 4.1 for an overview). However, we also confirm that the $H\alpha$ emission observed in the nuclear rings and the large majority of the nuclear discs indeed originates from star formation. We refer the reader to Gadotti et al. (2019) for a detailed analysis and classification of the emission-line ratios and ionisation sources of all TIMER galaxies.

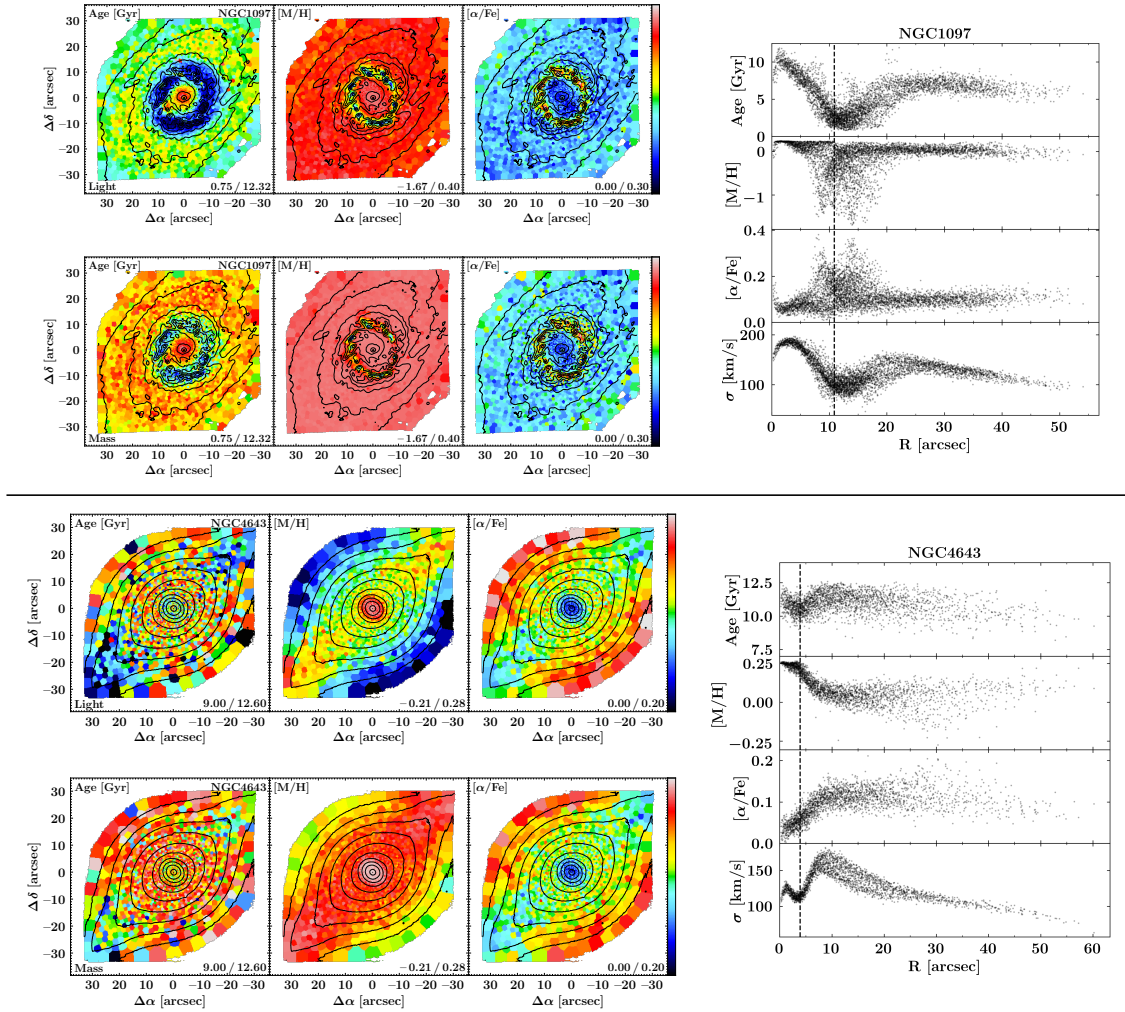


Figure 4.4: *Left:* Maps of the mean stellar population properties of NGC 1097 from the star-forming subsample (upper half) and NGC 4643 from the non-star-forming subsample (lower half). We present for each galaxy the light-weighted (upper panels) and mass-weighted (lower panels) population content. The maps have been generated with pPXF and include the modelling of $[\alpha/\text{Fe}]$ abundances. The figures display age, $[\text{M}/\text{H}]$, and $[\alpha/\text{Fe}]$ enhancements in the left-hand, centre, and right-hand panels, respectively. The limits of the colour bar are stated in the lower-right corner of each panel. Based on reconstructed intensities from the MUSE cube, we display isophotes in steps of 0.5 mag. North is up; east is to the left. *Right:* Radial profiles of light-weighted stellar ages (first panels), metallicities (second panels), $[\alpha/\text{Fe}]$ enhancements (third panels), and velocity dispersions (fourth panels) as a function of the galactocentric radius of all spatial bins in the field of view. The profiles have been deprojected using inclinations and position angles derived in S⁴G (Muñoz-Mateos et al. 2015), as presented in Table 4.1. The vertical dashed lines represent the kinematic radii of the nuclear discs, which was defined in G20 as the radius at which V/σ reaches its maximum in the region dominated by the nuclear disc.

4.5.2 Maps of Mean Stellar Population Properties

The kinematic analysis of the sample in an accompanying study (see G20) has already shown that nuclear discs are clearly present in all TIMER galaxies except perhaps NGC 6902, which is a rather peculiar object. These nuclear discs are also found in the maps of the mean stellar population properties (see left columns of Figs. 4.4 and Appendix B.3). While these structures are unambiguously present, the general appearance of nuclear discs and nuclear rings varies significantly between the star-forming and non-star-forming subsample.

Nuclear discs in the non-star-forming subsample appear as well-defined discs with mean stellar populations that are younger, more metal-rich, and less $[\alpha/\text{Fe}]$ enhanced as compared to their immediate surroundings. Since these galaxies do not host a starbursting nuclear ring, the maps of the mean stellar population properties do also not show signs of such nuclear rings, that is, significantly different populations at the outer edges of the nuclear discs.

A particularly notable nuclear disc in the non-star-forming subsample is hosted by NGC 1291. Previous studies of the TIMER team have already claimed that this galaxy hosts a nuclear disc with an effective radius of 15.6 arcsec, as determined through photometric decompositions (de Lorenzo-Cáceres et al. 2019b; Méndez-Abreu et al. 2019) and the stellar populations in its centre are dominated by an inner bar. This is most clear in the maps of metallicities and $[\alpha/\text{Fe}]$ enhancements where the inner bar is clearly visible. In addition, the ends of this inner bar exhibit younger stellar populations, as compared to the rest of the field of view. de Lorenzo-Cáceres et al. (2019b) already discussed the different stellar populations in the inner bar, nuclear disc, and all other components in this complex galaxy and we will complement this analysis in a dedicated, forthcoming study. It is only in NGC 4371 that the nuclear disc is not immediately apparent, but this is a result of projection effects. The high inclination of 59 deg, together with the fact that the bar is seen almost end-on, makes the detection of the nuclear disc challenging. Nonetheless, a inspection of the stellar population map reveals the same trends found for the other non-star-forming galaxies. The nuclear disc appears almost edge-on, with young, metal-rich, and $[\alpha/\text{Fe}]$ depleted stellar populations observed approximately 10 arcsec east and west of the galaxy centre. For a detailed analysis of this galaxy, we refer the reader to Gadotti et al. (2015).

Nuclear discs in the star-forming subsample follow, in general, the same trends. Over the majority of the radial extent of the nuclear discs these appear as well younger, more metal-rich, and $[\alpha/\text{Fe}]$ depleted. However, the star-forming nuclear rings, that is, the outer edges of the nuclear discs, show significantly different stellar population properties. These nuclear rings are often characterised by very low ages (often below 1 Gyr), exceptionally low metallicities (even below $[\text{M}/\text{H}] = -1.5$), and significantly enhanced $[\alpha/\text{Fe}]$ abundances (up to $[\alpha/\text{Fe}] = 0.30$). In fact, these distinctive nuclear rings spatially coincide with the regions of elevated $\text{H}\alpha$ emission-line fluxes and, based on the standard BPT methodology, are attributed to effects from ongoing star formation or a starburst episode (see Sect. 4.5.1). As discussed above, in these cases, the derived population properties might be unreliable, as the light in the star-forming regions could be dominated by very young stellar populations (below 30 Myr) which are not included in the employed set of SSP models, or affected by uncertainties in the $\text{H}\beta$ emission-line subtraction.

In the surroundings of the nuclear discs, other structural components of the galaxies are evident. In some cases (almost) the entire bar is covered by the MUSE field of view. In these galaxies (see e.g. IC 1438, NGC 4643, NGC 7755), the bar is visible through its elevated metallicities and low $[\alpha/\text{Fe}]$ enhancements (see also Neumann et al. 2020). Nonetheless, the metallicities and $[\alpha/\text{Fe}]$ abundances of the bars are not as elevated/depleted as those detected in the nuclear discs. In almost all galaxies, the nuclear discs are also surrounded by a region of older stellar populations. A comparison with the kinematic analysis of G20 shows that these areas spatially coincide with regions showing a correlation between radial velocity and the higher order moment, h_3 , of the line-of-sight velocity distribution or drops in the higher order moment, h_4 , along the bar major axis. These are kinematic signatures

of the strongly elongated stellar orbits in bars and their vertically thickened, box/peanut structure. Therefore, the regions of old stellar populations surrounding the young nuclear discs are probably related to the main bars in these galaxies.

A comparison of the light- and mass-weighted stellar population maps shows qualitatively the same results. Mass-weighted maps indicate, as expected, systematically higher ages and metallicities, but similar (or in some cases lower) $[\alpha/\text{Fe}]$ abundances. Nuclear discs often appear less pronounced in mass-weighted age maps; however, this is expected, as mass-weighted results highlight the old stellar component while nuclear discs are generally found to be comparatively young.

Interestingly, the orientation of the nuclear ring in NGC 1097 seems to vary between the map of stellar age and those of metallicity and $[\alpha/\text{Fe}]$ enhancement. While in the age map, the nuclear ring is elongated in the north-west direction (along the bar major axis), the metallicity and $[\alpha/\text{Fe}]$ maps indicate an elongation towards the north-east (perpendicular to the bar major axis). However, this apparent discrepancy is an effect of the chosen colourbar limits in the maps and the fact that ages are displayed linearly while metallicities are plotted on a logarithmic scale. In fact, the regions with the youngest stellar populations correspond precisely to the regions with the lowest metallicities and $[\alpha/\text{Fe}]$ abundances. Hence, there is no physical difference in the orientation of the nuclear between the age and metallicity map.

4.5.3 Radial Profiles of Mean Stellar Population Properties

Spatially resolved maps are an indispensable tool to investigate how stellar population properties vary between different structural components of a galaxy. Nevertheless, it can be instructive to reduce those maps to one dimension, in order to emphasise, for instance, the dependency of the population properties on the galactocentric radius. In the right-hand side of Fig. 4.4 and Appendix B.3 we plot light-weighted stellar ages, metallicities, $[\alpha/\text{Fe}]$ enhancements, and velocity dispersions as a function of the deprojected galactocentric radius of the respective spatial bin.

All galaxies in the non-star-forming subsample exhibit well-defined radial profiles in the regions of the nuclear discs. More specifically, we find that ages and metallicities are radially decreasing while $[\alpha/\text{Fe}]$ abundances are increasing with radius. Interestingly, the lowest $[\alpha/\text{Fe}]$ enhancements are always found in the very centre of the galaxies and almost always reach values of 0. Outside the nuclear disc the stellar ages increase again, and the kinematic radii coincide with this turn-around point in age. Similarly, metallicities and $[\alpha/\text{Fe}]$ abundances frequently show changes in their radial profiles close to the kinematic radius, often exhibiting flat profiles outside the nuclear discs. The fact that the slopes of these profiles appear to be constant throughout the nuclear discs and, in most cases, to the very centre, supports the idea that nuclear discs are radially continuous components often extending all the way to the centres of the galaxies. Only NGC 1291 and NGC 4371 show more complicated radial profiles, but this is due to the prominent inner bar in NGC 1291 and the high inclination and projection effects in NGC 4371 (see above).

In contrast, galaxies in the star-forming subsample show a more complicated behaviour. The galaxies show distinctive extrema of low ages, low metallicities, and high $[\alpha/\text{Fe}]$ enhancements, in particular at the outer edge of the nuclear discs. These are again the nuclear rings with distinct stellar populations and high $\text{H}\alpha$ emission-line fluxes discussed above. These features appear to be a result of ongoing star formation or a present starburst.

Thus, the well-defined radial trends found in the non-star-forming subsample might actually be present in all galaxies but could be temporarily outshone by current star formation. In fact, in various galaxies, for instance, NGC 1097, the radial profiles inside of the starbursting nuclear ring appear similar to the well-defined gradients observed in galaxies unaffected by star formation. Only NGC 5236 exhibits strongly irregular radial profiles in which extrema of young ages, low metallicities, and increased $[\alpha/\text{Fe}]$ abundances are not confined to the nuclear ring. Instead, these are widely distributed within the nuclear disc, in line with our findings from the maps of the stellar population content and $\text{H}\alpha$ emission-line fluxes.

A few galaxies (e.g. NGC 1097, NGC 4303, NGC 4984) show abrupt changes of their population content in the very centres of these galaxies. More precisely, these changes appear on radial scales much smaller than that of the nuclear disc, meaning that they are confined to the innermost spaxels. We speculate that these changes are connected to AGN activity and we will explore this aspect in a dedicated TIMER study in the future.

4.5.4 Stellar Population Content in Nuclear Discs and Nuclear Rings

The maps and radial profiles presented above indicate that the stellar population content of nuclear discs and nuclear rings are significantly different from the populations detected in their direct surroundings (e.g. the inner part of the main bar). To better quantify these differences, we calculate light-weighted mean ages, metallicities, and $[\alpha/\text{Fe}]$ abundances in the radial region of the nuclear disc ($0.1 R_{\text{kin}}$ to $0.7 R_{\text{kin}}$), nuclear ring ($0.8 R_{\text{kin}}$ to $1.2 R_{\text{kin}}$), and outside of these structures ($2.0 R_{\text{kin}}$ to $3.0 R_{\text{kin}}$). Figure 4.5 illustrates the results.

The figure highlights the large range of mean ages covered by nuclear discs, especially when considering the non-star-forming subsample. While some galaxies (e.g. NGC 5248) have young nuclear discs with ages around 2 Gyr, other galaxies (e.g. NGC 4371, NGC 4643) have nuclear discs which are dominated by old stellar populations with ages above 10 Gyr.

Regardless of the observed absolute mean ages, all nuclear discs in the non-star-forming subsample are younger, more metal-rich, and less $[\alpha/\text{Fe}]$ enhanced as compared to their immediate surroundings. Nuclear rings, as the outer edges of the nuclear discs, often show slightly younger ages compared to the nuclear discs, as expected from the radial profiles, and intermediate values of metallicities and $[\alpha/\text{Fe}]$ abundances. Only in three cases (NGC 5248, NGC 7140, and NGC 7755), nuclear rings exhibit lower metallicities and elevated $[\alpha/\text{Fe}]$ abundances, probably a result of weak star-formation activity. The only galaxy with a deviating behaviour is NGC 4371, but this is a result of projection effects, as discussed above. The same trends are found for the star-forming subsample. In general, nuclear discs are found to be younger, more metal-rich, and less $[\alpha/\text{Fe}]$ enhanced. Nuclear rings often exhibit low metallicities and elevated $[\alpha/\text{Fe}]$ abundances. This dichotomy is a result of the ongoing star formation that is concentrated in the nuclear rings but relatively low throughout the nuclear discs (see also Sect. 4.5.1). In contrast to the non-star-forming subsample, more exceptions are evident, for instance, the metal-poor and $[\alpha/\text{Fe}]$ enriched nuclear discs of NGC 5236 and NGC 7552, and the old nuclear discs in NGC 1097 and NGC 4981. In fact, the mean values substantially depend on where and how violent star formation proceeds in the nuclear rings of these galaxies. Therefore, we urge the reader to carefully inspect both maps and profiles of these galaxies in addition to the mean values presented in Fig. 4.5.

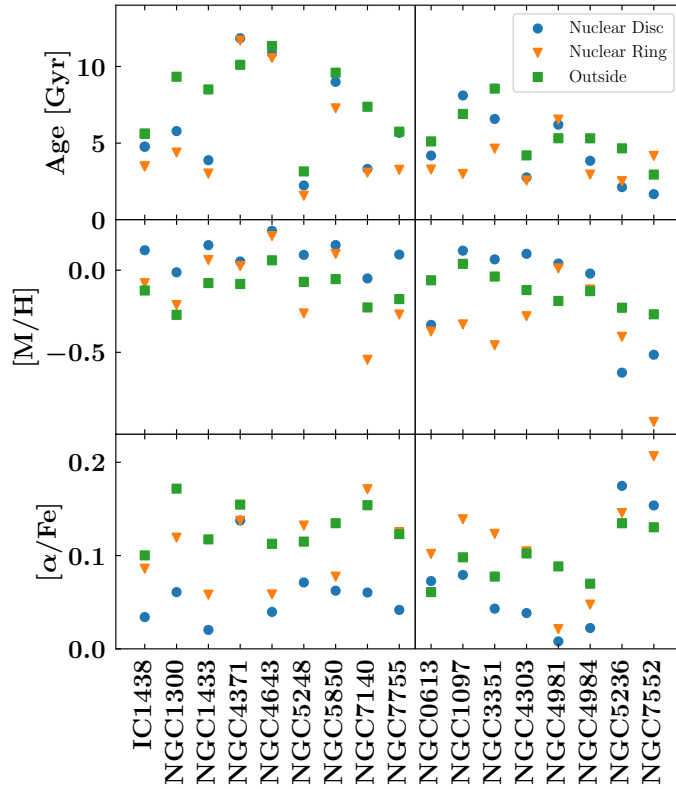


Figure 4.5: Overview of light-weighted mean ages (upper panel), metallicities (central panel), and $[\alpha/\text{Fe}]$ abundances (lower panel) in the nuclear discs (blue circles), nuclear rings (orange triangles), and outside of the central regions (green square). The light-weighted averages are calculated in the radial range from $0.1 R_{\text{kin}}$ to $0.7 R_{\text{kin}}$ for the nuclear discs, $0.8 R_{\text{kin}}$ to $1.2 R_{\text{kin}}$ for the nuclear rings, and $2.0 R_{\text{kin}}$ to $3.0 R_{\text{kin}}$ for the surrounding regions. The non-star-forming subsample is displayed in the left, separated by a vertical line from the galaxies in the star-forming subsample. As no kinematic radius could be determined for NGC 1291, this galaxy is not included in this plot.

4.6 Discussion

In this section, we put our observational results in the context of secular evolution. In addition, we discuss the connection between nuclear rings and nuclear discs, the coevolution of bars and nuclear discs, as well as the possible rejuvenation of an old nuclear disc in NGC 1097. We further investigate the absence of central spheroids in the TIMER sample in the context of galaxy formation.

4.6.1 The Connection between Nuclear Rings and Nuclear Discs

Nuclear discs and nuclear rings are intimately connected through their bar-driven formation histories. Nonetheless, these structures are more or less prominent in different galaxies. Based on our high-resolution observations of stellar population properties, and in the context of $\text{H}\alpha$ emission-line fluxes, as well as previously derived kinematic maps, we explore similarities and differences between these two components in greater detail. In Fig. 4.6, we illustrate these similarities and differences by presenting maps of V/σ , $[\alpha/\text{Fe}]$ abundances, and $\text{H}\alpha$ emission-line fluxes focussed on the spatial region of the nuclear disc. We show the maps of the galaxy NGC 4643 from the non-star-forming subsample and NGC 1097, which is a poster-child example of a galaxy with a prominent, starbursting nuclear ring.

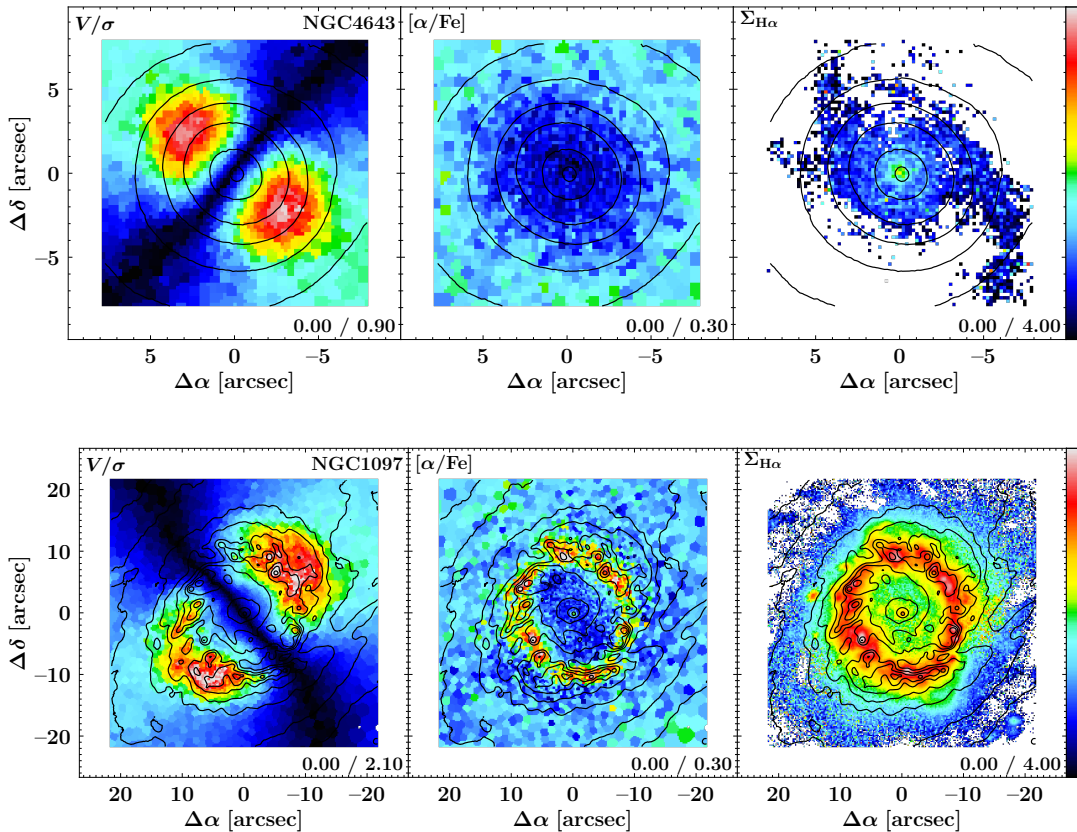


Figure 4.6: Maps of V/σ (left-hand panels), $[\alpha/\text{Fe}]$ abundances (centre panels), and H α emission-line fluxes (right-hand panels) of the galaxies NGC 4643 from the non-star-forming subsample (upper panels) and NGC 1097 from the star-forming subsample (lower panels). The maps do not display the full MUSE field of view, but focus on the region of the nuclear discs. The limits of the colour bar are stated in the lower-right corner of each panel. Based on reconstructed intensities from the MUSE cube, we display isophotes in steps of 0.5 mag. North is up; east is to the left.

In G20, we showed that the kinematic signatures of nuclear discs in the TIMER sample are strikingly clear. Nuclear discs are well aligned with the main disc, show stellar kinematics with a strong rotational support and low velocity dispersion, and, thus, appear as kinematically distinct components in V/σ maps. Based on such V/σ maps, no specific signatures of nuclear rings as a separate stellar component are evident, and thus the two structures appear indistinguishable regardless of whether the galaxy is part of the star-forming or a non-star-forming subsample. This is further highlighted in the left-hand panels of Fig. 4.6, where we show maps of V/σ for two TIMER galaxies, one with and the other without a star-forming nuclear ring.

As shown above, nuclear discs are also spatially well-defined features in maps of mean stellar population properties, show clear radial gradients in their stellar populations, and extend to the very centre of their host galaxy. However, the stellar population properties at the outer edge of the nuclear discs depend significantly on whether a star-forming nuclear ring is present or not (see central and right-hand panels of Fig. 4.6). In the cases of non-star-forming nuclear regions, it is not possible to distinguish nuclear rings and nuclear discs. The outer edges of these nuclear discs are their youngest, most metal-poor, and highest $[\alpha/\text{Fe}]$ region, which only sometimes show faint H α emission. Nevertheless, these features are smoothly connected to the radial gradients of the nuclear disc. In contrast, in the star-forming subsample nuclear rings are much more significantly young, metal-poor, and

show very high $[\alpha/\text{Fe}]$ abundances, features that are also clearly visible as discontinuities in the radial profiles. While some of these findings might be spurious due to the fact that young stellar populations (<30 Myr) are not included in the employed set of SSP models, it illustrates, nonetheless, how starbursting nuclear rings are distinguished in their measured mean population properties.

These observations suggest that nuclear rings and nuclear discs should not be referred to as two separate physical components, nor should their denomination be used interchangeably. Instead, nuclear rings are simply the outermost part of nuclear discs. In galaxies with non-star-forming nuclear regions, the nuclear ring represents the youngest and outermost part of the nuclear disc. In the galaxies of the star-forming subsample, however, the nuclear ring merely highlights the region in which the majority of the gas is located and efficiently forms stars. As above, this region is the outermost part of the nuclear disc.

4.6.2 Nuclear Discs in the Global Context of Secular Evolution

A number of studies have established a theoretical framework for the formation of nuclear structures. If nuclear rings and discs are indeed built by secular, bar-driven processes, this provides theoretical expectations for the stellar kinematics and population properties of these structures. While in G20, we recently showed that the kinematics of nuclear discs, in particular their high rotational velocities and low velocity dispersions, are consistent with the picture of bar-driven secular evolution, here we further consider their stellar population properties.

To some extent, secular evolution in disc galaxies first requires a sequential process: a bar can only arise after the main stellar disc becomes dynamically unstable to bar formation, while the formation of a nuclear disc fundamentally depends on the presence of such a bar. More precisely, stars in the nuclear disc or nuclear ring form in-situ from gas that has been funnelled to the centre by the bar (see e.g. Athanassoula 1992a,b; Piner et al. 1995; but also Kormendy & Kennicutt 2004 for a review). Following this sequential process, we naturally expect that nuclear discs are, on average, younger compared to the other galaxy components. The finding that this holds for the mean stellar population properties, as observed in Sect. 4.5.2, is consistent with this picture. More precisely, the bar is efficient in transporting gas from the main galaxy disc to its centre. However, at least at low redshifts, there is typically no star formation observed along the bar, as strong shear forces suppress the collapse of gas clouds (see e.g. Reynaud & Downes 1998; Emsellem et al. 2015; Neumann et al. 2019). Instead, the gas aggregates in a small volume in the centres of the galaxies, which typically constitutes a nuclear ring (i.e. the outer edge of the nuclear disc). Star formation progresses in this nuclear ring and, depending on the amount of available gas, can be very intense. While star formation might also proceed in other parts of the galaxy, in particular, the main disc, at least in some cases, the star-formation density is higher in the nuclear rings. This would result in a nuclear ring whose mean ages appear younger compared to the main disc. Even if star-formation proceeds at similar rates in the nuclear ring and the main disc, we expect to have, at least, similar ages in these structures. In fact, similar ages in the nuclear ring and main disc are, for instance, observed in IC 1438. Both at the radius of the nuclear ring (3.7 arcsec) and at the largest radii in the field of view (e.g. 20 arcsec to 25 arcsec) stellar ages of approximately 3 Gyr are evident. However, we note that the present TIMER observations sample the main discs of the galaxies only partially. In fact, the outer parts of the main disc might still appear younger than the nuclear discs.

The mean ages of the nuclear discs and rings vary significantly across different galaxies. In fact, the nuclear rings of some nuclear discs are as young as ~ 2 Gyr, while other nuclear discs are older than 10 Gyr in their entire radial extent. This is not surprising as the initial formation time of the nuclear disc depends on various factors, such as the availability of gas, and is further limited by that of the bar itself and, thus, the cosmic epoch at which the main galaxy disc first settled. In fact, according to this scenario, the oldest nuclear discs indicate the early formation of the bar.

The increased metallicities detected throughout all non-star-forming nuclear discs are also in agreement with our present understanding of bar-driven secular evolution. As the nuclear disc is built from gas brought there from other parts of the galaxy, in particular, the main disc, this gas should typically be as metal-enriched as the gas in these other galaxy components. With the formation of the nuclear disc and subsequent generations of stars, the metallicity in this central component should continuously increase. This is further supported by the fact that nuclear discs are located in the centres of their host galaxies where the deep potential well confines the metals that have been produced. This result also corroborates previous numerical studies. For instance, Cole et al. (2014) find increased values of $[\text{Fe}/\text{H}]$ in nuclear discs compared to the surrounding bar, as a result of continuing star formation in the nuclear discs.

We have also, for the first time, derived $[\alpha/\text{Fe}]$ element abundances in spatially resolved nuclear discs. We find that all nuclear discs in the non-star-forming subsample have low $[\alpha/\text{Fe}]$ enhancements, indicating that their build-up takes a long time and is indeed a slow and continuous process, just as expected in the context of bar-driven secular evolution. In fact, if nuclear discs were built by more violent processes such as mergers (Davies et al. 2007; Chapon et al. 2013), one would expect a singular, rapid period of star formation that results in more elevated values of $[\alpha/\text{Fe}]$, similar to those found in elliptical galaxies. In addition, the entire nuclear disc would be formed at the same time, either through star formation or the violent re-distribution of existing stars. In both cases, one would expect to find flat age profiles, in contrast to the observations presented here (see Breda et al. 2020, for a detailed account of radial age profiles in galaxy bulges).

The extremely low metallicities and increased $[\alpha/\text{Fe}]$ abundances detected in the nuclear rings of the star-forming subsample could result from uncertainties in the measurement (see Sect. 4.3). However, such low-metallicity populations in the nuclear rings could also be consistent with the bar-driven formation scenario, if external, low-metallicity gas is accreted onto the galaxy. Such low-metallicity gas could originate from the circum-galactic-medium of the galaxy, or encounters with dwarf galaxies. If the subsequent bar-driven gas inflow to the nuclear ring proceeds rapidly enough to avoid the enrichment of the gas in the main galaxy disc, a nuclear ring showing very low metallicities can be formed. The elevated $[\alpha/\text{Fe}]$ enhancements in the nuclear rings are probably just a transient signatures of the strong, ongoing star formation from low-metallicity gas and not a persistent property of the underlying stellar nuclear disc, particularly since all nuclear discs in the non-star-forming subsample show low $[\alpha/\text{Fe}]$ abundances.

4.6.3 The Simultaneous Growth of Nuclear Discs and Bars

The bar-driven transport of gas to the centre of a galaxy is a rather well-understood process. In the galaxy centre the gas is usually deposited in a nuclear ring with a well-defined inner and outer edge, although it remains unclear what physical process determines the width of these nuclear rings. In fact, the presence of gaseous nuclear discs without more

prominent gaseous nuclear rings is uncommon. However, the results above suggest that often stellar nuclear discs extend from the radial region of the nuclear ring all the way to the very centre of the galaxy. These extended nuclear discs are not only detected in the maps of stellar population properties presented here, but also found based on stellar kinematics and photometric studies (see G20, and references therein). To date, it remains unclear if and how initially gaseous nuclear rings with well-defined inner and outer edges are transformed into the observed stellar nuclear discs that extend to the very centres of the galaxies.

It is also not clear what physical process determines the radius of the gaseous nuclear rings. Studies suggest that the sizes of nuclear rings are related to bar resonances (see e.g. Piner et al. 1995), determined by viscous shear forces (Sormani et al. 2018; Sormani & Li 2020), or simply set by the residual angular momentum of the inflowing gas (Kim et al. 2012a; Seo et al. 2019). In Sect. 4.5.3, we have shown that the kinematic radii are a good tracer of the radius of nuclear discs and, thus, their nuclear rings. In an accompanying study, G20 show that these kinematic radii correlate well with the bar length and other properties, corroborating the scenario in which nuclear discs are built by bars.

Interestingly, many studies argue that bars grow longer and stronger as they evolve (see e.g. Athanassoula 2003; Martinez-Valpuesta et al. 2006; Gadotti 2011, but also de Lorenzo-Cáceres et al. 2020 for inner bars). If indeed bars grow longer with time and the radii of nuclear rings depend in some way on the bar length, we would expect that bars and nuclear rings evolve simultaneously. Following the mechanism suggested by Seo et al. (2019), as the bar grows longer it triggers the inflow of gas from larger radii in the main galaxy disc. This gas has a larger residual angular momentum and, thus, settles at larger radii in the galaxy centre resulting in a larger nuclear ring. However, the residual angular momentum of the inflowing gas might not only depend on the length of bar, but also on various other bar properties, for instance, the axial ratio of the bar. Therefore, a direct causal connection between the bar length and the radius of the gaseous nuclear ring is questionable. Other studies argue that the size of the nuclear ring is not linked to the residual angular momentum of the gas, but instead limited by the radial extent of the bar x_2 orbits, a parameter that fundamentally depends on the axisymmetric central mass concentration and the bar pattern speed (see e.g. Athanassoula 1992a,b; Fragkoudi et al. 2017a). In fact, the bar pattern speed typically decreases, as bars are transferring angular momentum to the disc and halo, while simultaneously increasing the central mass concentration through gas inflow, thus allowing more extended x_2 orbits and the nuclear ring to grow with time. In this framework, a correlation between bar length and nuclear ring radius might naturally arise as well, without requiring a direct causal connection between nuclear ring radius and bar length. While it remains unclear which physical mechanism determines the size of the nuclear rings, both mechanisms hint towards a scenario in which nuclear rings continuously increase their radius as bars evolve.

In this framework, star formation only needs to proceed in the gaseous nuclear ring in order to produce a continuous stellar nuclear disc. As the radius of the location of the nuclear ring increases, a star-forming nuclear ring is located at a given point in time at a range of radii, thus producing stars on near-circular orbits at all such radii, or, in other words, a disc. In this way a continuous stellar nuclear disc can be formed without the necessity of forming a gaseous nuclear disc.

This possible scenario translates into predictions that are in good agreement with the nuclear discs found in the TIMER sample. While $H\alpha$ emission is predominantly detected in nuclear rings at the outer edge of the nuclear discs, the nuclear discs themselves are continuous and extend to the centres of the galaxies. It is also in agreement with the fact that nuclear discs are rapidly rotating and exhibit low velocity dispersions. Similarly, it predicts that nuclear discs are relatively old in the centre and become increasingly younger towards their outer edge. This behaviour is evident in the radial gradients presented in Sect. 4.5.3. We note that the negative gradients in $[M/H]$ do not necessarily contradict this picture. In fact, old stars are not always less metal-enriched than young stars, particularly since metallicities can increase very rapidly in star-forming systems. In addition, the more the gas is bound in the potential well of the galaxy, the more difficult it is for feedback processes to expel this gas. Therefore, it is expected that in most evolved systems, regardless of their formation history, the metallicity increases towards the centre.

This formation mechanism still predicts the presence of an inner edge of the stellar nuclear disc, particularly at the radius, where the first gaseous nuclear ring had formed. Such an inner edge is not obvious from the observations presented here. While a few galaxies show systematically different population properties in their very centres, these features might well be caused by contamination of the stellar continuum from an AGN. In addition, such an inner edge might be well beyond the resolution limit of our MUSE observations, which is typically around 100 pc or less.

Seo et al. (2019) suggest the same mechanism for the formation of nuclear discs, based on a numerical study. They performed simulations of individual Milky Way-like galaxies ($M_{\text{disc}} = 5 \times 10^{10} M_{\odot}$) with varying gas fractions (between 0% and 10%) and velocity anisotropy parameters. Depending on the simulation set-up, they find that the initial nuclear ring is very small (down to 40 pc) and subsequently grows as the bar grows longer and funnels in gas from larger radii. Gas located in preceding nuclear rings is quickly consumed by star formation. In this way, an increase in radius of the nuclear ring of up to a factor of 10 is found, which matches the typical sizes of the nuclear discs we find in TIMER.

The proposed mechanism of nuclear disc formation is based on the assumption that gas and star formation are predominantly located in the nuclear ring. While this is in agreement with the observational appearance of nuclear discs and nuclear rings, the presence of gas within the nuclear disc itself is not surprising and does not contradict the picture above. Star formation in the nuclear rings is often very strong and, thus, it is expected that stellar feedback significantly affects the gas. More precisely, a fraction of the gas should be expelled from within the nuclear ring to both larger and smaller radii, a process that was studied in detail for NGC 3351 by Leaman et al. (2019). Therefore, the presence of gas and continuing star formation within the nuclear disc is expected, although in small amounts, as compared to the nuclear ring. This further supports the continuing enrichment of the nuclear disc with metals, as evident in the metallicity maps. In addition, this also explains why there is no sharp, step-like transition between the stellar populations of the nuclear discs and the regions outside of them. Instead, a gradual change in stellar populations is observed, for instance, the typical V-shape in age that might result from the contamination of these regions by gas expelled from the star-forming nuclear ring.

Our observational results in combination with the current theoretical framework of bar evolution hint towards an inside-out formation of nuclear discs through a series of star-forming nuclear rings. Nonetheless, various crucial questions related to their bar-driven

formation remain unanswered, in particular which physical processes determine the size and the width of nuclear rings. Further studies are needed to answer these questions, especially numerical models of nuclear disc formation in a cosmological context. These studies will shed light on alternative scenarios (e.g. formation from a gaseous disc) that will have to reproduce the radial gradients of stellar age, metallicities, and $[\alpha/\text{Fe}]$ abundances reported in this study.

4.6.4 The Absence of Kinematically Hot Spheroids

In Sect. 4.5.3, we find well-defined radial gradients in the stellar population properties of nuclear discs. As we argue above, these gradients, particularly the negative gradient in stellar age, might suggest that nuclear discs form out of consecutive generations of gaseous nuclear rings. However, one might speculate if such gradients could also be caused by a superposition of physically different stellar components with the nuclear discs, for instance, a kinematically hot spheroid, the main galactic disc, or the bar and its box/peanut.

In fact, a superposition of the nuclear disc and the main disc as well as bar is likely, in particular since these components are dynamically expected to extend to the spatial region covered by the nuclear disc. Indeed, such a superposition becomes evident in the observed kinematic properties (see G20), indicated by elevated values of the higher-order moment h_4 of the Gauss-Hermite parametrisation of the line-of-sight velocity distribution. This kinematic analysis nevertheless indicates that the nuclear discs clearly dominate the stellar light, as rapidly rotating discs with low velocity dispersions are evident. This shows that there is no major dispersion-dominated component in the central region, excepts perhaps in NGC 6902. A small, kinematically hot spheroid could, nevertheless, be located at the very centre of the galaxies (see Erwin et al. 2015). In fact, due to the typically large photometric concentrations of kinematically hot spheroids, we expect that these components, if present, dominate the stellar light at least in the innermost part of the nuclear discs.

To further assess the presence of small, kinematically hot spheroids, we carefully inspected radial profiles of the stellar velocity dispersion. The majority of all galaxies show relatively low velocity dispersions throughout the nuclear discs. Nonetheless, seven galaxies exhibit velocity dispersions in their centre which surpass the velocity dispersions measured just outside of their nuclear discs. These galaxies are IC 1438, NGC 1097, NGC 1291, NGC 4984, NGC 5728, NGC 5850, and NGC 6902; their velocity dispersion profiles are shown in the left-hand panel of Fig. 4.7. The central and right-hand panels display the remaining galaxies of the non-star-forming and star-forming subsamples, respectively.

Although the large velocity dispersions in the centres of these galaxies can be connected to kinematically hot spheroids, at least some of the signatures found here can be attributed to other galaxy components. More precisely, NGC 5728 is significantly influenced by AGN activity and a large-scale outflow. Thus, the increased central velocity dispersion in this galaxy might not be a property of the underlying stellar component but related to the AGN. While the other galaxies do not show such strong AGN activity, deviations from a single velocity dispersion profiles in the innermost spaxels could indeed be related to AGN activity. In contrast, NGC 6902 is only weakly barred and does not show clear signatures of a rapidly rotating nuclear disc (see G20). The stellar velocity dispersion continuously increases towards its centre, consistent with the presence of a kinematically hot spheroid that dominates the stellar light in the centre of this galaxy. On the other hand de Lorenzo-Cáceres et al. (2019b) claim that NGC 1291 and NGC 5850 host a small, kinematically hot

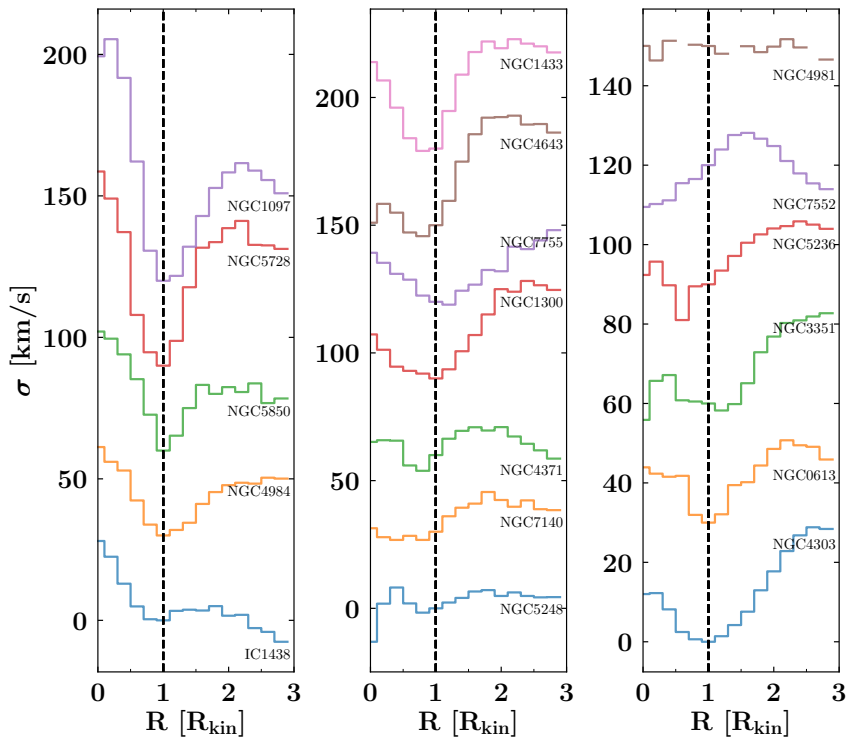


Figure 4.7: Overview of the radial profiles of stellar velocity dispersions in the region of the nuclear disc. The left-hand panel shows all galaxies in which the velocity dispersions within the nuclear disc exceed the values observed in their direct surroundings. The central and right-hand panels display the remaining galaxies from the non-star-forming and star-forming subsample, respectively. The profiles are vertically offset by 30 km s^{-1} , according to the values measured at the kinematic radius. Using the galactocentric radius, the data is binned in radial steps of $0.2 R_{\text{kin}}$ and the median velocity dispersions displayed. The vertical dashed line highlights the kinematic radius of the nuclear discs. We note that NGC 1291, NGC 1365, and NGC 6902 are not included in this figure, as no kinematic radii are available for these galaxies. Unbinned radial profiles without any vertical offset are provided in Appendix B.3.

spheroid within their (more prominent) nuclear discs (see also Méndez-Abreu et al. 2019; de Lorenzo-Cáceres et al. 2019a) and, thus, they constitute galaxies with composite bulges. Only the elevated central velocity dispersions in IC 1438, NGC 1097, and NGC 4984 might indeed be related to previously undetected kinematically hot spheroids.

Signatures of kinematically hot spheroids are not only expected in the kinematics but also in the stellar population properties. Therefore, we present an overview of the radial profiles of ages, metallicities, and $[\alpha/\text{Fe}]$ enhancements for the non-star-forming subsample in Fig. 4.8. These gradients, in particular that of stellar age, do not show breaks within the radial range of the nuclear disc. In other words, in most galaxies with non-star-forming nuclear discs, the slopes of the population gradients are constant from the very centre to the nuclear ring. However, if there was a distinct physical component dominating in a given radial range, we would expect the mean population properties to change in that location, particularly since nuclear discs are relatively young components while kinematically hot spheroids are expected to be old. Such breaks should be further enhanced by the different central concentrations of nuclear discs and hot spheroids. The only two galaxies in the non-star-forming subsample that show breaks in their age profiles are NGC 4371 and NGC 1291. The deviations in NGC 4371 may be a result of the peculiar geometrical projection of this galaxy, in which the nuclear disc is seen almost edge-on (see Gadotti et al. 2015 for a detailed discussion, but see also Erwin et al. 2015). In NGC 1291, the stellar populations

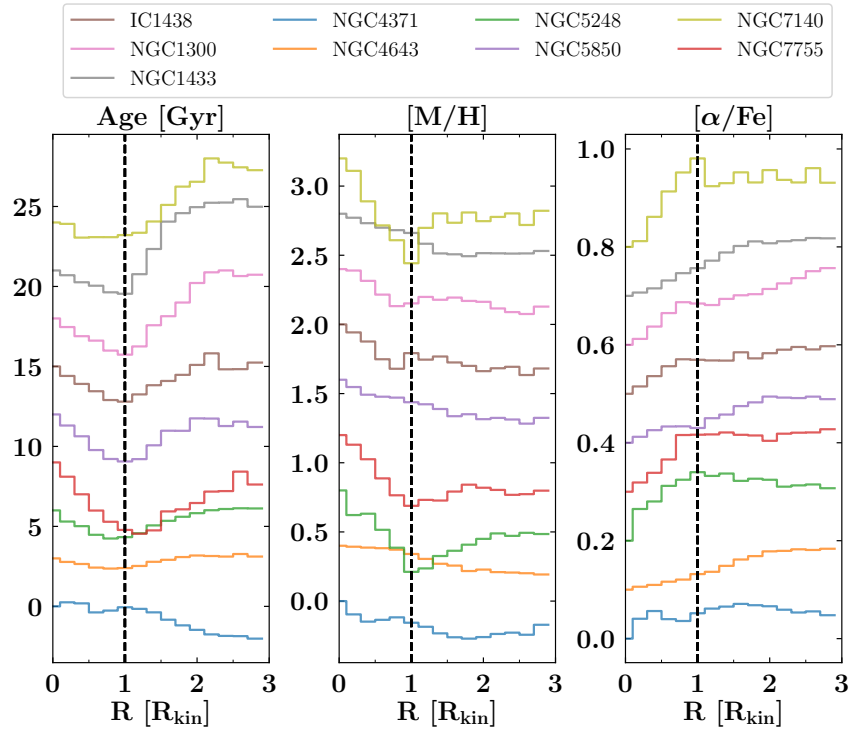


Figure 4.8: Overview of the radial profiles of light-weighted ages (left-hand panel), metallicities (centre panel), and $[\alpha/\text{Fe}]$ enhancements (right-hand panel) of the non-star-forming subsample. Using the galactocentric radius, the data is binned in radial steps of $0.2 R_{\text{kin}}$ and the median stellar population properties displayed. The vertical dashed line highlights the kinematic radius of the nuclear discs. The profiles are vertically offset by 3 Gyr for ages, and 0.4 dex and 0.1 dex for metallicities and $[\alpha/\text{Fe}]$ abundances, according to the values measured in the innermost bin. We note that NGC 1291 is not included in this figure, as no kinematic radius is available for this galaxy. Unbinned radial profiles without any vertical offset are provided in Appendix B.3.

in the nuclear disc are dominated by an inner bar and we explore these stellar population profiles in a dedicated study in the future. Nonetheless, previous studies of the TIMER team suggest that the centre of NGC 1291 is dominated by a kinematically hot spheroid (de Lorenzo-Cáceres et al. 2019b; Méndez-Abreu et al. 2019). This idea is consistent with the stellar population and velocity dispersion profiles presented here: the oldest ages, highest metallicities, and highest velocity dispersion are detected in the centre of the galaxy. In addition, the radial gradients of the hot spheroid clearly deviate from the flat gradients associated with the inner bar and nuclear disc.

Identifying possible breaks in the stellar population profiles of the star-forming subsample is challenging given that any gradients that are present are often outshone or confused with the starbursting regions. Breaks in the stellar population profiles that do not seem to be associated with star-forming regions are only detected in a few galaxies, namely NGC 1097, NGC 4303, NGC 4984, and NGC 5728. However, the breaks in NGC 1097 and NGC 4984 are confined to the innermost spaxels, hinting towards a possible contamination with light from the AGN in these galaxies (Gadotti et al. 2019). The same seems to be the case for NGC 5728 which is affected from a large-scale AGN outflow. These aspects will be explored further in a forthcoming study of the TIMER team. Only NGC 4303 shows a significant break in its age profile at around $0.5 R_{\text{kin}}$, but not so in the profiles

of $[M/H]$, $[\alpha/Fe]$ abundances, and velocity dispersions. In fact, the low central velocity dispersion of approximately 75 km s^{-1} does not hint towards the presence of a kinematically hot spheroid.

Interestingly, the inspection of the stellar population profiles of NGC 6902 is consistent with the presence of a massive, kinematically hot spheroid in this galaxy. In contrast to the non-star-forming nuclear discs, the stellar populations in the centre of this galaxy are comparably old and show high velocity dispersions. In addition, no well-defined, single gradients are observed. Moreover, this galaxy lacks clear kinematical signatures of a rapidly rotating nuclear disc, but it does show a $v-h_3$ anticorrelation at all radii from the main disc of the galaxy to its central region (see G20). In other words, NGC 6902 exhibits properties that are consistent with the presence of a kinematically hot spheroid as well as a regularly rotating disc.

In fact, kinematically hot spheroids are expected to be very old, as these are typically thought to form in the early phases of galaxy formation⁴. But as described above, often we see that the oldest stars in the TIMER galaxies reside in the bar and not in the centre. This fact, connected to the typical absence of breaks in the stellar population gradients from the nuclear ring all the way to the centre and the relatively low velocity dispersions in the galaxy centres, suggests that in almost all TIMER galaxies, there are no kinematically hot spheroids present. More precisely, the stellar light in the centres of these galaxies is dominated by the nuclear disc and not by kinematically hot spheroids. Only NGC 6902 shows some signatures that are consistent with the presence of a dynamically hot spheroid. In NGC 1291 and NGC 5850, such a spheroid dominates only at radii much smaller than that of the nuclear disc. In a few cases, the evidence is unclear, but the unambiguous presence of nuclear discs, as inferred from the kinematic and stellar population analysis, shows that these components dominate the stellar light.

Nonetheless, some minor contribution from kinematically hot spheroids might be present, but remain undetected in the analysis of the mean stellar population properties performed here. A careful analysis of star formation histories could provide further insights and show to what extent underlying, old stellar populations are present in the nuclear discs of the TIMER galaxies. While this analysis is beyond the scope of this paper, we will report on this aspect in a forthcoming study.

At least in the context of a Λ CDM cosmology, kinematically hot spheroids are expected in the central regions of massive disc galaxies. However, the considerations above show that in the large majority of the present TIMER sample no kinematically hot spheroids, not even small ones, contribute substantially to the stellar light in the nuclear regions. How much of a challenge this poses for Λ CDM cosmology is not clear. For example, the large majority of the bulges found in the Auriga cosmological simulations are classified as pseudo or composite bulges, while none are identified to be kinematically hot spheroids (Gargiulo et al. 2019). Moreover, in approximately 20% of the Auriga galaxies, the fraction of stars in the galaxy centres that formed ex situ (and thus would end up in a spheroid) is below 1% (Fragkoudi et al. 2020). In addition, strong feedback processes may preferentially remove low angular momentum gas in mergers, allowing for the formation of a disc but preventing the formation of central, kinematically hot components (Brook et al. 2011, 2012). On the other hand, Kormendy et al. (2010) also highlight on statistical grounds that the large presence of massive bulgeless galaxies is a challenge in the current galaxy

⁴If a substantial merger had occurred within the last few Gyr, its effects on the galaxy would be directly observable, for instance, as tidal tails.

formation paradigm (see also Kormendy 2016, and references therein). Clearly, this issue has to be addressed with further analyses of the results from cosmological simulations and a TIMER-like study that would include a broader variety of galaxies.

4.6.5 Rejuvenation of an old Nuclear Disc in NGC 1097

NGC 1097 is a poster-child example of a galaxy with a bright, starbursting nuclear ring with a clearly defined inner and outer edge. However, in the framework of the downsizing scenario, it is a rather intriguing case. The downsizing scenario (see e.g. Cowie et al. 1996; Thomas et al. 2010; Sheth et al. 2012) predicts that more massive galaxies form earlier, that is, their discs become dynamically mature at an earlier cosmic epoch resulting in an earlier bar formation (see e.g. Sheth et al. 2008). Hence, considering the large stellar mass of NGC 1097 ($17.4 \times 10^{10} M_{\odot}$; see e.g. Gadotti et al. 2019), we would expect a comparably old bar and also, for the same reason, an old nuclear disc. However, while this galaxy is the most massive one in the present sample, it exhibits a prominent and extremely young starbursting ring, in contrast to the less massive but extremely old galaxies in TIMER (see e.g. NGC 4371, as discussed by Gadotti et al. 2015). In the following, we discuss how an interaction of NGC 1097 with a small companion galaxy could explain this peculiarity, which is consistent with the expectations from the downsizing scenario.

As discussed above and illustrated in Fig. 4.6, the starbursting ring of NGC 1097 is characterised by high H α fluxes, young ages, extremely low metallicities, and elevated $[\alpha/\text{Fe}]$ abundances. While the H α measurements are robust, the derived population properties might be erroneous (see Sect. 4.5.1). In particular, the extremely low metallicity and elevated values of $[\alpha/\text{Fe}]$ could simply be a result of ongoing star formation. Nevertheless, the galaxy seems to show signatures of an old nuclear disc within the nuclear ring, in particular at radii below ~ 7 arcsec. This feature exhibits well-defined gradients in its population properties, much like what was found for many other nuclear discs in the sample.

A possible interpretation for this peculiar composition of stellar population and galaxy properties could be the rejuvenation of an old nuclear disc, particularly since NGC 1097 is interacting with its companion NGC 1097A (see e.g. Ondrechen et al. 1989; Prieto et al. 2019). In this picture, the bar forms very early, as expected in the downsizing scenario, and naturally triggers the formation of a nuclear disc. The subsequent evolution of the galaxy presumably continued with star formation in the nuclear ring, as discussed in Sect. 4.6.3, or proceeded in a more quiescent state, one that is similar to that of NGC 4643 presently, for instance. At a later point in time, NGC 1097 started to interact with its small companion. In fact, the tidal forces exerted by this companion might efficiently promote the inflow of gas. This inflowing gas could originate either from the outskirts of the main disc of NGC 1097, the companions itself, or the surrounding circumgalactic medium. Our observations are not suited to determine the precise origin of the gas, but if it indeed originated from outside of the main disc of NGC 1097, it is expected to be metal-poor. Although the measured low metallicities in the nuclear ring are somewhat unreliable, this measurement is well consistent with this picture. If this is true, it would further indicate that the inflow of gas proceeds very rapidly, hence, preventing any significant metal enrichment of the gas in the main galaxy disc prior to its accumulation in the nuclear ring.

In summary, the set-up of population properties in the centre of NGC 1097 might simply originate from the rejuvenation of an old nuclear disc by an interaction-driven gas inflow. However, the discussed picture assumes that the inner region of NGC 1097 does indeed contain an old nuclear disc. While the gradients of the population properties in this region

appear to be very similar to those of other TIMER galaxies with nuclear discs that are unaffected by significant star formation, the kinematic analysis indicates elevated velocity dispersions in the centre. This is rather untypical for nuclear discs in general, but there may be mechanisms that could efficiently heat them. It remains unclear if the passage of the companion could be responsible for the heating of the nuclear disc. In fact, the high velocity dispersion might as well be explained by the presence of a small, kinematically hot spheroid (see Sect. 4.6.4).

4.7 Summary and Conclusions

In this study, we used MUSE observations of the central regions of 21 massive, barred galaxies obtained within the TIMER survey. The galaxies exhibit a large variety of bar-built central structures, such as nuclear rings, nuclear discs, and inner bars. We derived high-resolution, spatially resolved maps of their mean stellar population properties in order to determine the current properties of nuclear rings and nuclear discs, and further investigate processes related to their formation and evolution. To this end, we performed the analysis with both the pPXF and STECMAP routines and found that the obtained results are consistent within standard deviations of 1.06 Gyr in age and 0.14 dex in metallicity, however, with STECMAP returning systematically lower stellar ages. In addition, we show that derived ages and metallicities do not depend on whether $[\alpha/\text{Fe}]$ enhancements are modelled in the fitting process or not. Our main results are as follows:

- (i) Nuclear discs are clearly distinguished from other galaxy components by their mean population properties. All non-star-forming nuclear discs appear younger, more metal-rich, and less $[\alpha/\text{Fe}]$ enhanced compared to their immediate surroundings, as expected in the framework of bar-driven secular evolution. In particular, these findings corroborate that the formation of nuclear discs is a slow and continuous process, clearly contradicting the idea of merger-built nuclear discs.
- (ii) The mean ages of nuclear discs vary significantly across different galaxies. While some nuclear discs and nuclear rings are very young and star-forming, other objects exhibit extremely old nuclear discs that appear to have evolved quiescently over the past ~ 10 Gyr. Based on the example of NGC 1097, we discuss how such old nuclear discs can be rejuvenated by recently accreted gas.
- (iii) In all non-star-forming nuclear discs, we detect exceptionally well-defined radial gradients of the mean population properties. More specifically, stellar ages and metallicities are decreasing with radius with a single slope within the nuclear disc while $[\alpha/\text{Fe}]$ enhancements are increasing with a single slope. Interestingly, the lowest $[\alpha/\text{Fe}]$ abundances are always found in the very centre. The absence of breaks in these gradients within the nuclear discs suggest that nuclear discs are extending all the way from the nuclear ring to the very centre of the galaxies. Breaks in these population profiles, associated with the outer edge of nuclear discs, are consistent with their kinematic radii determined by G20.
- (iv) To date, it remains unclear how radially extended nuclear discs can be formed by star formation that typically proceeds in radially well-defined and relatively narrow nuclear rings. Based on the detected radial stellar population gradients and recent observational and numerical results, we argue that nuclear rings and bars evolve

simultaneously, resulting in nuclear rings that grow in radius. In this way a continuous nuclear disc could simply be built by a series of nuclear rings that have increasing radii with time.

- (v) Combining the results from this study with those reported in G20, we find no clear evidence for large, kinematically hot spheroids in most of the sample. This is indicated by the smooth stellar population gradients within the nuclear discs and the fact that the very centre is often dominated by a stellar population that is younger, or has the same age, as that of the bar, along with low stellar velocity dispersion. Most of the galaxies in this study do not show any signatures of even a small spheroid.

Stellar Populations of Inner Bars

Galaxies within Galaxies: Stellar Populations of Inner Bars are Scaled Replicas of Main Bars

Inner bars are frequent structures in the local Universe and thought to substantially influence the nuclear regions of disc galaxies. In this study we explore the structure and dynamics of inner bars by deriving maps and radial profiles of their mean stellar population content and comparing them to previous findings in the context of main bars. To this end, we exploit observations obtained with the integral-field spectrograph MUSE of three double-barred galaxies in the TIMER sample. The results indicate that inner bars can be clearly distinguished based on their stellar population properties alone. More precisely, inner bars show significantly elevated metallicities and depleted $[\alpha/\text{Fe}]$ abundances. Although they exhibit slightly younger stellar ages compared to the nuclear disc, the typical age differences are small, except at their outer ends. These ends of the inner bars are clearly younger compared to their inner parts, an effect known from main bars as orbital age separation. In particular, the youngest stars (i.e. those with the lowest radial velocity dispersion) seem to occupy the most elongated orbits along the (inner) bar major axis. We speculate that these distinct ends of bars could be connected to the morphological feature of ansae. Radial profiles of metallicity and $[\alpha/\text{Fe}]$ enhancements are flat along the inner bar major axis, but show significantly steeper slopes along the minor axis. This radial mixing in the inner bar is also known from main bars and indicates that inner bars significantly affect the radial distribution of stars. In summary, based on maps and radial profiles of the mean stellar population content and in line with previous TIMER results, inner bars appear to be scaled down versions of the main bars seen in galaxies. This suggests the picture of a ‘galaxy within a galaxy’, with inner bars in nuclear discs being dynamically equivalent to main bars in main galaxy discs.

5.1 Introduction

Bars are a frequent structure in disc galaxies and important for their secular evolution (see e.g. Kormendy & Kennicutt 2004; Athanassoula et al. 2005; Barazza et al. 2008; Sheth et al. 2008; Aguerri et al. 2009; Masters et al. 2011; Kraljic et al. 2012; Fragkoudi et al. 2020). But some galaxies indeed host more than only one bar: such double-barred systems have a large-scale bar located in their main discs, while another, smaller bar (which we refer to as inner bar¹ throughout this paper) can be found in their centres. The first double-barred galaxies were already discovered in the 1970s (NGC 1291; de Vaucouleurs 1974, 1975) and early on these objects were thought to be part of a small group of dynamically peculiar galaxies. However, some studies suggest that 30% of all barred galaxies are actually double-barred systems (see e.g. Erwin & Sparke 2002; Laine et al. 2002; Erwin 2004; Buta et al. 2015), while more recently Hildebrandt et al. (2020) estimate a lower limit for the volume-corrected fraction of double bars of 12% in the CALIFA survey (Sánchez et al. 2012).

This chapter is based on Bittner, de Lorenzo-Cáceres et al., A&A 2021, Volume 646, A42

Despite the amount of known double-barred galaxies and the important secular processes inner bars might induce (Shlosman et al. 1989, 1990), to date, few studies have explored their stellar population content in detail. The first attempt was made by de Lorenzo-Cáceres et al. (2012) using long-slit observations of the galaxy NGC 357. Their results indicate that the bulge and inner bar have similar stellar population properties, while the main bar is less metal-rich and more $[\alpha/\text{Fe}]$ enhanced. Subsequent integral-field spectroscopic observations (de Lorenzo-Cáceres et al. 2013) of four additional galaxies are compatible with these results, but further show that inner bars appear slightly younger than their surroundings. Radial profiles reveal positive age and negative metallicity gradients along both the inner and main bars, while $[\alpha/\text{Fe}]$ abundances are flat.

The TIMER project (Time Inference with MUSE in Extragalactic Rings; Gadotti et al. 2019) is a survey focussing on central structures, for instance nuclear discs, nuclear rings, and inner bars, observed in massive, barred disc galaxies in the local Universe. To date, 21 galaxies of the sample have been observed with the Multi-Unit Spectroscopic Explorer (MUSE; Bacon et al. 2010) at the Very Large Telescope. While the main goal of the project is to infer the epoch of bar formation from the star formation histories in the central components, previous TIMER studies also explored the nature of inner bars in greater detail. Méndez-Abreu et al. (2019) investigated the face-on galaxy NGC 1291 and, for the first time, detected kinematic signatures of a box/peanut structure associated with the inner bar in this galaxy. More precisely, bi-symmetric minima of the higher-order moment h_4 of the line-of-sight velocity distribution are observed along the inner bar major axis, which is as expected from numerical simulations and identified in the context of main bars (see e.g. Debattista et al. 2005; Méndez-Abreu et al. 2008b, 2014). Similarly, Bittner et al. (2019) observed a correlation between radial velocity and the higher-order moment h_3 in the spatial region of the inner bar of NGC 1433. This correlation is a well-known kinematic signature of main bars, arising from the strongly elongated x_1 orbits within them (Bureau & Athanassoula 2005; Iannuzzi & Athanassoula 2015; Li et al. 2018; Gadotti et al. 2020). Detecting this correlation for an inner bar again suggests that both types of bars are dynamically similar structures. Finally, de Lorenzo-Cáceres et al. (2019b) combined multi-component photometric decompositions of NGC 1291 and NGC 5850 with measurements of kinematics and the stellar population content. The results show that nuclear discs and inner bars have similar radii, suggesting that inner bars form via dynamical instabilities in nuclear discs in the same way main bars arise in the main discs of galaxies. In addition, the star formation histories indicate that the inner bars in NGC 5850 and NGC 1291 are at least 4.5 Gyr and 6.5 Gyr old, implying that inner bars are dynamically stable, long-lived structures.

The stellar population properties of main bars have been studied in greater detail. Pérez et al. (2007) and Pérez et al. (2009) detected large variations of ages and metallicities in bars, with positive, null, and negative metallicity gradients along their major axis. Sánchez-Blázquez et al. (2011) compared the stellar content of bars with that in the main discs of these galaxies, indicating that bars host, on average, older stellar populations with higher metallicities than the galaxy discs. The gradients in both parameters appear flatter along the bar major axis compared to the gradients found in the main disc. Using 128 galaxies from the MaNGA survey (Bundy et al. 2015), Fraser-McKelvie et al. (2019) found that the gradients of age and metallicity along the bar are typically flatter compared to the region outside of the bar but within the bar radius (see also Seidel et al. 2016). Neumann et al. (2020) exploited the high spatial resolution observations of the TIMER survey to explore

¹In the literature inner bars are often also referred to as nuclear bars. We warn the reader that sometimes the term nuclear bar is also used to refer to particularly small bars in single-barred systems.

stellar population gradients not only along the bar major axis, but also perpendicular to it. The results show that the youngest stellar populations in bars are located closest to the bar major axis, suggesting that the youngest stars populate the most elongated orbits.

The large number of morphological features in disc galaxies, especially in their centres, has led astronomers to introduce a variety of nomenclatures for these structures. In this study, we use the term nuclear disc to refer to rotationally supported central discs with typical sizes of a few hundred parsecs that are kinematically distinct from the main galaxy disc. We choose this nomenclature to distinguish nuclear discs from inner and outer discs, as often referred to in the context of disc breaks. The outermost edge of nuclear discs are often distinguished by gaseous and/or star-forming rings. These structures are named nuclear rings, in order to discriminate them from inner rings typically found at the radius of the main bar and outer rings located well outside of the main bar. For the double-barred systems presented here, we use the term inner bar when referring to small-scale bars associated with nuclear discs while large-scale bars found in the main discs of galaxies are simply denoted bar or main bar, as appropriate.

In this paper, we investigate the similarities between the stellar populations of main bars and inner bars by exploiting two-dimensional stellar population maps and radial profiles, based on the high-resolution, integral-field spectroscopic observations of the TIMER survey. We further complement the study of de Lorenzo-Cáceres et al. (2019b) by exploring how the stellar population properties vary along and perpendicular to inner bars. In particular, we present for the first time radial profiles of stellar population properties along the inner bar major and minor axis. We then compare these results to those obtained by Neumann et al. (2020) in the context of main bars. Based on these investigations, we explore the dynamical structure of inner bars, argue that main and inner bars appear to be scaled versions of each other, and speculate about the nature of ansae.

This paper is structured as follows: in the next section we summarise observations, data reduction, sample selection, and analysis which are already detailed in previous papers. In Sect. 5.3 we show our results on the stellar population content of inner bars before discussing them in the context of main bars in Sect. 5.4. Finally, we summarise our conclusions in Sect. 5.5.

5.2 Sample, Observations, and Data Analysis

In this section we briefly summarise our sample of inner bars, the TIMER observations and data reduction, as well as the performed data analysis.

5.2.1 Double-barred Galaxies in TIMER

The TIMER sample is selected from the *Spitzer* Survey of Stellar Structures in Galaxies (S⁴G, Sheth et al. 2010). Therefore, all galaxies are nearby ($d < 40$ Mpc), bright ($m_B < 15.5$ mag), and large ($D_{25} > 1$ arcmin) objects. In addition, only barred galaxies with central structures, as determined by Buta et al. (2015), stellar masses above $10^{10} M_{\odot}$, and inclinations below 60 deg are included.

Among the 21 TIMER galaxies observed so far, only NGC 1291 and NGC 5850 exhibit prominent inner bars. These inner bars have already been detected in previous studies on the subject (see e.g. Erwin 2004; Buta et al. 2015; de Lorenzo-Cáceres et al. 2008, 2013)

and recently investigated within the TIMER survey (de Lorenzo-Cáceres et al. 2019b; Méndez-Abreu et al. 2019). In contrast, the presence of an inner bar in the centre of NGC 1433 remains debated: previous photometric studies (Buta 1986b; Jungwiert et al. 1997; Erwin 2004; Buta et al. 2015) show some evidence of an inner bar and Bittner et al. (2019) finds consistent kinematic signatures. However, de Lorenzo-Cáceres et al. (2019b) inspected recent *Hubble* Space Telescope images of the galaxy and concluded that NGC 1433 does not host an inner bar. They argue that the presence of a variety of central structures, such as a nuclear ring, nuclear disc, and nuclear spiral arms has led to a misclassification in this galaxy. Moreover, they state that the absence of clear σ -hollows, a kinematic feature typically associated with inner bars, further suggests that this galaxy does not host an inner bar.

In Fig. 5.1 we present H-band observations of the central regions of the three galaxies, recently obtained with the HAWK-I imager (Kissler-Patig et al. 2008) at ESO’s Paranal Observatory. These observations were performed employing the Adaptive Optics correction produced by the GRAAL AOF module (Paufigue et al. 2010) on UT4, leading to a typical point-spread function of about 0.4 arcsec to 0.5 arcsec. The high-resolution photometric observations not only highlight the structure of the inner bars in NGC 1291 and NGC 5850, but also show the inner bar in NGC 1433 more clearly. Although the inner bar in this galaxy does not appear as prominent as in the two other cases, the isophotes reveal the elongated structure of this inner bar within an almost axisymmetric nuclear disc. In fact, the detection of inner bars with varying strength is not surprising, as main bars also exhibit a large range of structural properties.

In addition, we carefully inspected the inner regions of all other TIMER galaxies using S⁴G images, our recent HAWK-I photometry, reconstructed intensities from MUSE, and maps of kinematics and stellar population properties (Bittner et al. 2020; Gadotti et al. 2020). Although some studies report inner bar fractions of 30% (e.g. Erwin & Sparke 2002), no other inner bars are detected in the TIMER sample. In fact, the detected number of inner bars in the sample is consistent with more recent estimates of a 12% frequency of double-barred systems (Hildebrandt et al. 2020).

In Table 5.1 we present an overview about some of the fundamental properties of the three galaxies considered in this study, including inclination, position angle, stellar mass, and distance. All galaxies exhibit clear evidence of a nuclear disc and we show their kinematic radii, defined as the radius at which v/σ within the nuclear disc reaches its maximum (Gadotti et al. 2020). Finally, we present the basic properties of the inner bars, that is their position angles, radii, and axis ratios, based on the visual inspections of Herrera-Endoqui et al. (2015) and careful multi-component decompositions of de Lorenzo-Cáceres et al. (2019b). In fact, these decompositions include 6 different galaxy components and thus highlight how complicated the inner regions of these galaxies are. We discuss the differences in the estimated parameters in Sect. 5.3.1.

5.2.2 Observations and Data Reduction

Exploiting the wide-field mode of the MUSE spectrograph, most TIMER observations were obtained in ESO’s period 97 from April to September 2016. The observations use a wavelength range from 4750 Å to 9350 Å at a spectral sampling of 1.25 Å. The field of view covers 1 arcmin² with a spatial sampling of 0.2 arcsec at a typical seeing of 0.8 arcsec to 0.9 arcsec. Each observation included approximately 1 hour of integration on source. Since all galaxies are larger than the field of view, dedicated sky exposures were obtained.

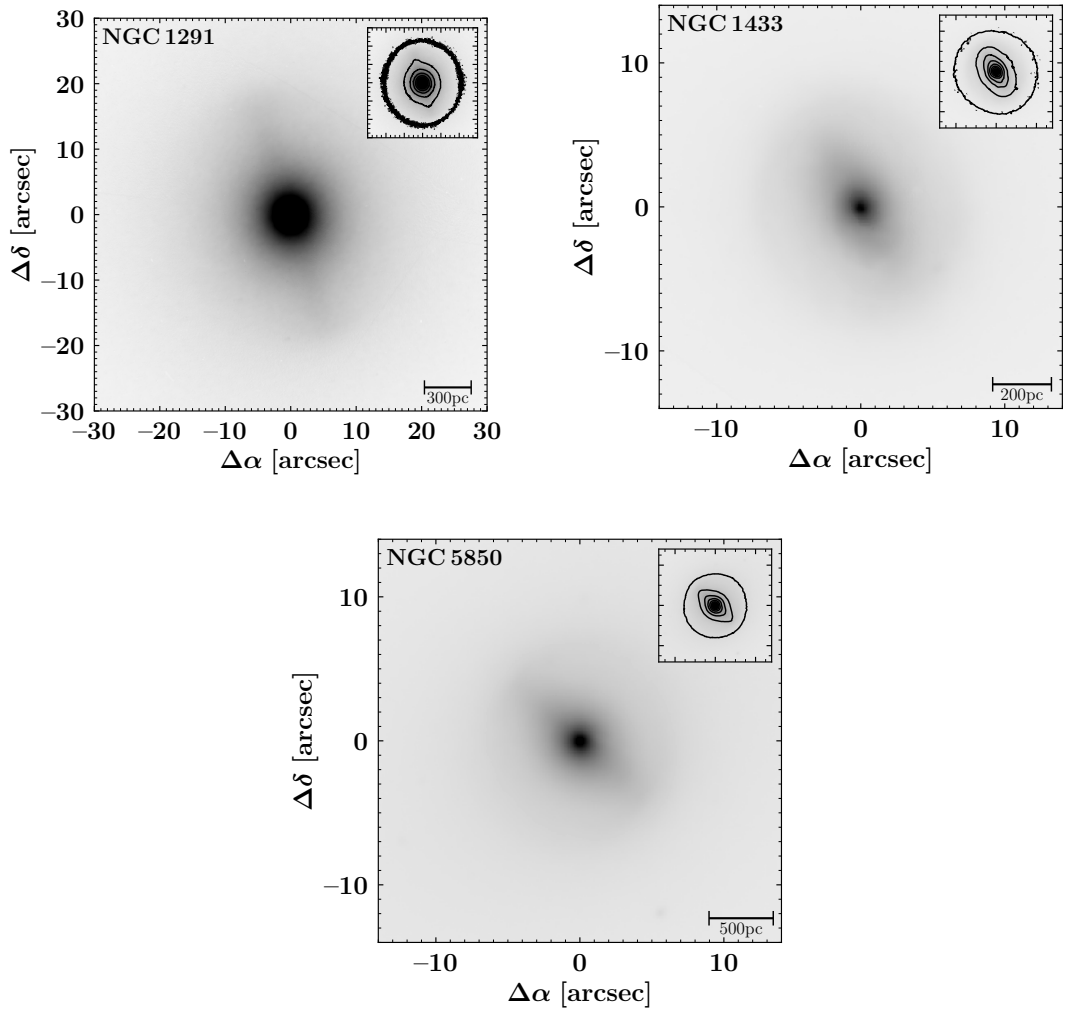


Figure 5.1: Photometric H-band observations of the inner bars and nuclear discs in NGC 1291, NGC 1433, and NGC 5850, obtained with HAWK-I. The insets show exactly the same field of view as the main images and illustrate the isophotes in the galaxy centres which highlight not only the axisymmetric structure of the nuclear discs but also the significantly elongated inner bars. For the three galaxies the inner bar is clearly distinguishable, in particular also the relatively weak inner bar of NGC 1433 whose existence has been debated. North is up; east is to the left.

Following the standard TIMER data reduction procedure, the observations were reduced with version 1.6 of the MUSE data reduction pipeline (Weilbacher et al. 2012, 2020). More specifically, the data are calibrated in flux and wavelength, and bias, flat-fielding, and illumination corrections are applied. Telluric features as well as the sky background are removed, the latter using principal component analysis. Finally, the data is registered astrometrically. A detailed overview of observations and data reduction of the TIMER survey is presented in Gadotti et al. (2019).

5.2.3 Data Analysis

The analysis of the MUSE data is performed within the fully modular software framework of the GIST pipeline² (Galaxy IFU Spectroscopy Tool, Bittner et al. 2019). This tool provides extensive capabilities for the analysis of spectroscopic data, facilitating all necessary steps

²<http://ascl.net/1907.025>

Name	i deg	M_* $10^{10} M_\odot$	PA_{gal} deg	d Mpc	Spatial scale pc/arcsec	r_{kin} kpc	Source	PA_{ib} deg	a_{full} arcsec	a_{vis} arcsec	b/a
(1)	(2)	(3)	(4)	(5)	(6)	(7)	(8)	(9)	(10)	(11)	(12)
NGC 1291	11	5.8	-8.9	8.6	42	—	HE	18	—	19.3	0.78
							LC	17	29.0	—	0.35
NGC 1433	34	2.0	18.2	10.0	49	0.381	HE	30	—	7.1	0.67
							LC	—	—	—	—
NGC 5850	39	6.0	-26.5	23.1	112	0.796	HE	45	—	7.1	0.72
							LC	48	11.3	—	0.21

Table 5.1: Overview of some fundamental properties of the sample. Shown are the inclination i of the galaxy disc relative to the plane of the sky in column (2), the total stellar mass M_* in column (3), the position angle of the galaxy disc PA_{gal} in column (4) (all from S⁴G; Sheth et al. 2010; Muñoz-Mateos et al. 2013, 2015), the mean redshift-independent distance d from the NASA Extragalactic Database (NED, <http://ned.ipac.caltech.edu/>) in column (5), the spatial scale of the observations in column (6), and the kinematic radius of the nuclear disc in column (7) (Gadotti et al. 2020). Column (8) states the source of the structural components described in the following columns: HE refers to the results from Herrera-Endoqui et al. (2015) while LC designates the multi-component decompositions of de Lorenzo-Cáceres et al. (2019b). We refer the reader to Sect. 5.3.1 for a comparison of the results of both methods. Columns (9) to (12) provide the position angle of the inner bar PA_{ib} , its full semi-major axis a_{full} from photometric decompositions, the inner bar semi-major axis from visual inspections a_{vis} , and the inner bar axial ratio b/a . We note that no kinematic radius could be determined for NGC 1291, due to the face-on orientation of the galaxy. NGC 1433 is not included in the photometric decompositions of de Lorenzo-Cáceres et al. (2019b).

from the read-in and preparation of input data, over its scientific analysis, to the production of publication quality plots. In the following, we only summarise the conducted data analysis while a more detailed description is provided in Bittner et al. (2020).

We use the GIST framework to exploit the adaptive Voronoi tessellation routine of Cappellari & Copin (2003), in order to spatially bin the data to an approximately constant signal-to-noise ratio of 100. This high signal-to-noise ratio is employed to ensure the reliability of the measurement (see Bittner et al. 2020, for an assessment of the influence of the signal-to-noise ratio on the derived population properties).

We adopt the udf-10 parametrisation of Bacon et al. (2017) to model the line-spread function of the MUSE spectra. All template spectra are broadened to this resolution before any fits are performed. We further employ the wavelength range from 4800 Å to 5800 Å in this analysis. This relatively short portion of the MUSE wavelength range is chosen because the red part of the spectra is not optimal for the measurement of stellar population properties. In particular, the lower sensitivity to young stellar populations, residuals from the sky subtraction, as well as absorption lines originating in the interstellar medium would complicate the analysis (see e.g. Gonçalves et al. 2020).

The measurement of the stellar population properties is performed in three separate steps, using the full-spectral fitting approach. Firstly, we employ the pPXF routine (Cappellari & Emsellem 2004; Cappellari 2017) to derive the stellar kinematics, while keeping emission lines masked. A low order multiplicative Legendre polynomial is employed, in order to account for differences in the continuum shape between spectra and templates. Secondly, we apply pyGandALF (Bittner et al. 2019), a new Python implementation of the original GandALF routine (Sarzi et al. 2006; Falcón-Barroso et al. 2006), in order to fit any present emission lines while taking into account the results from the previous stellar kinematics fit. pyGandALF uses a two-component reddening correction instead of corrective Legendre polynomials that accounts for extinction within the emission-line regions as well as for

‘screen-like’ extinction that affects the entire spectrum. The detection of emission lines is considered significant if the amplitude-to-residual-noise ratio exceeds four. In these cases, the emission line is subtracted from the spectrum, thus obtaining emission-subtracted spectra.

Thirdly, a regularised run of **pPXF** is performed in order to measure the mean stellar population properties, using the emission-subtracted spectra. In this process, we apply an 8th order multiplicative Legendre polynomial. We further fix the stellar kinematics to those derived with the unregularised run of **pPXF** in order to avoid degeneracies between metallicity and velocity dispersion (see e.g. Sánchez-Blázquez et al. 2011). In fact, **pPXF** does not directly derive mean stellar population properties but instead non-parametric star formation histories. This is achieved by assigning weights to the spectral models so that the observed spectra are best reproduced. However, it is not straightforward to obtain a physically meaningful solution, as this is an ill-conditioned inverse problem. Therefore, **pPXF** applies a regularisation, such that the smoothest solution that is consistent with the data is returned (Press et al. 1992; Cappellari 2017). We determine the regularisation strength following the prescription applied, for instance, by McDermid et al. (2015) and detailed in Bittner et al. (2020).

Throughout the analysis, we use the MILES single stellar population (SSP) models (Vazdekis et al. 2015) as spectral templates. These models use a Kroupa Revised IMF with a slope of 1.30 (Kroupa 2001) and BaSTI isochrones (Pietrinferni et al. 2004, 2006, 2009, 2013). The models cover ages from 0.03 Gyr to 14 Gyr, metallicities from -2.27 dex to 0.40 dex, and $[\alpha/\text{Fe}]$ enhancements of 0.00 dex and 0.40 dex at a spectral resolution of 2.51 \AA (Falcón-Barroso et al. 2011).

In this study, we derive light-weighted stellar population properties, in order to emphasise differences in the stellar ages. Such light-weighted population properties are obtained by normalising each MILES model by its own mean flux. Average population properties are then calculated from the weight w_i assigned to the model i via

$$\langle t \rangle = \frac{\sum_i w_i t_{\text{SSP},i}}{\sum_i w_i} \quad (5.1)$$

$$\langle [\text{M}/\text{H}] \rangle = \frac{\sum_i w_i [\text{M}/\text{H}]_{\text{SSP},i}}{\sum_i w_i} \quad (5.2)$$

$$\langle [\alpha/\text{Fe}] \rangle = \frac{\sum_i w_i [\alpha/\text{Fe}]_{\text{SSP},i}}{\sum_i w_i} \quad (5.3)$$

with the i th model having an age of $t_{\text{SSP},i}$, metallicity $[\text{M}/\text{H}]_{\text{SSP},i}$, and an $[\alpha/\text{Fe}]$ enhancement of $[\alpha/\text{Fe}]_{\text{SSP},i}$.

These $[\alpha/\text{Fe}]$ enhancements are an indicator of the longevity of star formation in galaxies. As α -elements are predominantly formed in the fusion processes leading to type II supernovae while iron is mostly produced in type Ia supernovae (see e.g. Worthey et al. 1992; Weiss et al. 1995), the $[\alpha/\text{Fe}]$ abundance gives an estimate of their relative importance. Since the progenitor stars of type II supernovae are massive and short-lived while those of type Ia supernova have long lifetimes, the timescale of star formation in a galaxy is constrained by these $[\alpha/\text{Fe}]$ enhancements: High abundances hint towards short and intense star-formation episodes, while low $[\alpha/\text{Fe}]$ abundances are a signature of slow but continuous star formation.

5.3 Results

In the following we present our results on the stellar population content of inner bars. In particular, we present maps of the mean population properties and their radial profiles along and perpendicular to the inner bar major axis. The measurements of the stellar population properties employed in this study are made publicly available³.

5.3.1 Mean Stellar Population Properties in Inner Bars

In Fig. 5.2 we present light-weighted maps of the mean stellar population properties of NGC 1291, NGC 1433, and NGC 5850, similar to the ones presented in Bittner et al. (2020) but focussed on the spatial region of the inner bar. In all three galaxies, the inner bars are easily distinguishable, based on their mean stellar populations alone, as previously claimed by de Lorenzo-Cáceres et al. (2013). Most strikingly, the inner bars show significantly elevated metallicities and reduced $[\alpha/\text{Fe}]$ enhancements. This effect is most pronounced in NGC 1291 and NGC 5850 in which the deviating metallicities and $[\alpha/\text{Fe}]$ abundances are clearly confined to the long and thin inner bar. To some degree, the same holds for NGC 1433: while the inner bar in this galaxy appears slightly rounder, this structure is still distinct in the $[\text{M}/\text{H}]$ and $[\alpha/\text{Fe}]$ abundance maps.

In contrast to metallicities and $[\alpha/\text{Fe}]$ enhancements, inner bars do not show significantly different mean stellar ages in the largest part of their spatial extent. However, in all cases the ends of the inner bars are associated with relatively younger stellar populations, although these populations can still be very old, especially in the case of NGC 1291. These younger ends of the inner bars are broader perpendicular to the inner bar major axis. Thanks to the superior physical resolution of the observation of NGC 1291 (simply because this galaxy is closer), this effect is again most prominent in this galaxy and in line with the morphological properties of its inner bar (Méndez-Abreu et al. 2019; de Lorenzo-Cáceres et al. 2019b).

The ends of the inner bars are located close to the outer edge of the nuclear disc, a region that is often highlighted by gaseous nuclear rings (see Bittner et al. 2020, for a discussion of the differences between nuclear discs and nuclear rings). Therefore, the relatively young ends of the inner bar might be affected by recent star formation in the nuclear ring. At least for the galaxies in the present sample this is likely not the case. Maps of the $\text{H}\alpha$ emission-line fluxes which trace HII regions and hence star formation, do not show concentrated emission at the ends of the inner bars (Neumann et al. 2020; Bittner et al. 2020). Moreover, the galaxies in the present sample do not host gaseous (star-forming) nuclear rings that might cause the observed effect of inner bars having young stellar populations at their ends. In addition, star formation that did not proceed very recently and, thus, might not be traceable with the $\text{H}\alpha$ emission-line fluxes anymore should not result in such spatially well-defined young ends of the inner bars. Due to the short dynamical timescale in these radial regions, the young stellar populations would mix and their signature at the bar ends vanish rapidly.

Further, we overplot the maps of the mean stellar population properties in Fig. 5.2 with ellipses highlighting the spatial extent of the inner bars, as previously determined based on photometric data from S^4G . The black dash-dotted ellipses are based on the visual estimates of the inner bar structural properties from Herrera-Endoqui et al. (2015). While the length of the inner bar major axis coincides well with the appearance of the stellar

³<https://www.muse-timer.org>

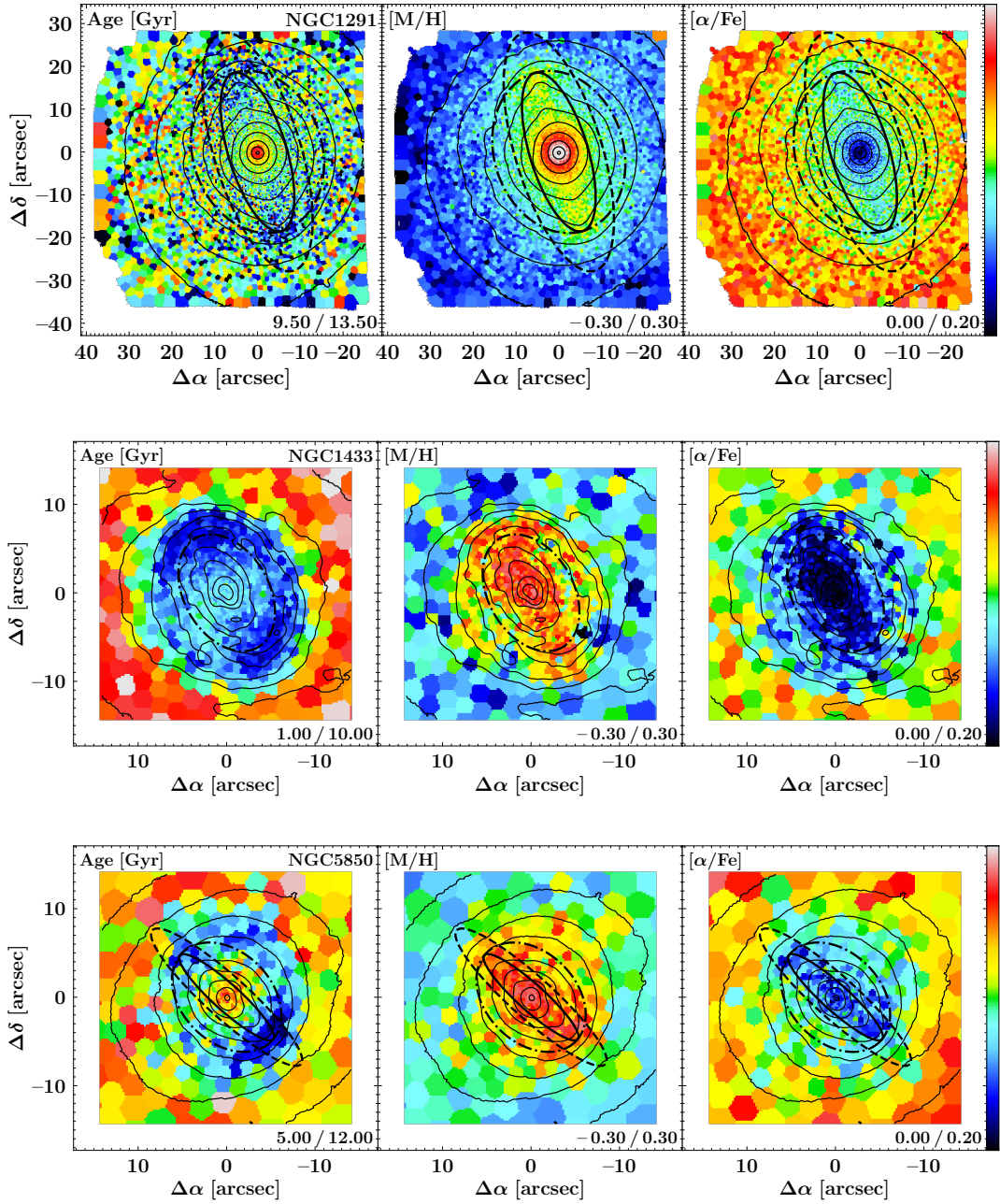


Figure 5.2: Maps of light-weighted, mean stellar population properties of NGC 1291 (upper panels), NGC 1433 (central panels), and NGC 5850 (lower panels), focussed on the spatial region of the inner bar (see Bittner et al. 2020, for maps showing the entire MUSE field of view). Each set of panels displays age, [M/H], and [α/Fe] enhancements and the limits of the respective colour bar are stated in the lower-right corner of each panel. The dash-dotted ellipses display the approximate extent of the inner bars according to the visual measurements of Herrera-Endoqui et al. (2015), while dashed ellipses show the results from the multi-component decompositions of de Lorenzo-Cáceres et al. (2019b). Solid ellipses combine the inner bar lengths from Herrera-Endoqui et al. (2015) with the ellipticities of de Lorenzo-Cáceres et al. (2019b) and trace the appearance of the inner bars excellently. NGC 1433 is not included in the photometric decompositions of (de Lorenzo-Cáceres et al. 2019b), hence only a dash-dotted ellipse is displayed. Based on the reconstructed intensities from the MUSE cube, we display isophotes in steps of 0.5 mag. North is up; east is to the left.

population maps (in particular considering metallicities and $[\alpha/\text{Fe}]$ abundances), the ellipses are in all cases too round. However, this behaviour is expected, as the measurement is performed on integrated light from multiple overlapping galaxy components (see also de Lorenzo-Cáceres et al. 2020). In particular the axisymmetric structure of nuclear discs is expected to bias the inner bar ellipticity towards rounder shapes. In contrast, the black dashed ellipses in Fig. 5.2 are derived using detailed, multi-component decompositions (de Lorenzo-Cáceres et al. 2019b). Such photometric decompositions actually separate the light from the different galaxy components and are, thus, able to better reproduce the elongated shapes of the inner bars observed in the mean population maps. However, the inner bar full radii are larger than the inner bars appear in the maps. This is a result of the fact that the bar ends are faint and contaminations from other components, for instance stars in the main bar and main disc, become significant. In fact, these systematic differences of bar lengths and ellipticities derived via different methods have already been noted in the case of main bars (Gadotti 2008, 2011). Taking into account these differences, in the remainder of this paper we use inner bar lengths from the visual estimates of Herrera-Endoqui et al. (2015) and ellipticities from the multi-component decompositions of de Lorenzo-Cáceres et al. (2019b) in order to highlight the spatial extent of inner bars (solid ellipses in Fig. 5.2). This combination of photometric estimates traces the appearance of inner bars in the stellar population maps excellently. Nonetheless, the differences between the measurement methods again show how complicated the central regions of these galaxies are due to multiple, overlapping galaxy components.

The stellar population properties of the inner bar of NGC 5850 were first studied by de Lorenzo-Cáceres et al. (2013), based on observations with the SAURON spectrograph (Bacon et al. 2001). To this end, they derived single stellar population equivalent population properties from the measurement of line strength indices at a signal-to-noise level of 60. In agreement with the results presented here, they find that the inner bar of NGC 5850 has systematically higher metallicities compared to its immediate surroundings. However, in their study the inner bar shows only a weak indication of systematically lower $[\alpha/\text{Fe}]$ abundances. We speculate that this is a result of the different measurement methods, that is the use of line strength indices to infer an $[\text{Mg}/\text{Fe}]$ overabundance, as compared to the use of full spectral fitting to derive $[\alpha/\text{Fe}]$ enhancements here.

In a previous TIMER publication, de Lorenzo-Cáceres et al. (2019b) investigated various possible formation scenarios for inner bars based on an independent analysis. In their study, they choose to spatially bin the MUSE data to a signal-to-noise ratio of 40 (as compared to a signal-to-noise of 100 used here), model and remove emission lines with *GandALF*, and fit ages and metallicities with *STECMAP* (Ocvirk et al. 2006a,b). $[\alpha/\text{Fe}]$ enhancements are estimated based on a set of line-strength indices. While their analysis uses different techniques and routines, the stellar population properties agree qualitatively well with the results presented here, in particular when considering that *pPXF* returns systematically higher stellar ages than *STECMAP* (see Bittner et al. 2020). In fact, the stellar population properties of the inner bar of NGC 5850 agree well with the ones presented here. de Lorenzo-Cáceres et al. (2019b) conclude that the middle part of the inner bar in NGC1291 is slightly older compared to its surroundings, while in the present study no age difference is detected in this part of the inner bar. In fact, as *STECMAP* returns systematically younger stellar ages, subtle differences in age are emphasised that remain unnoticed with *pPXF*, especially at the observed ages of >10 Gyr at which it is challenging to reliably distinguish stellar ages. Nonetheless, a careful visual comparison reveals that the young ends of the inner bar appear to be already detected by de Lorenzo-Cáceres et al. (2019b). Hence, the stellar population properties estimated in the two studies are consistent.

		age-slope	[M/H]-slope	[α /Fe]-slope	<Age>	<[M/H]>	<[α /Fe]>
NGC 1291	MA	$(-5.15 \pm 0.69) \times 10^{-2}$	$(-2.8 \pm 0.4) \times 10^{-3}$	$(1 \pm 1) \times 10^{-4}$	10.97	0.04	0.08
	MI	$(-8.1 \pm 8.4) \times 10^{-3}$	$(-1.08 \pm 0.05) \times 10^{-2}$	$(3.3 \pm 0.3) \times 10^{-3}$	11.22	-0.04	0.11
NGC 1433	MA	$(-3.11 \pm 0.16) \times 10^{-1}$	$(-1.1 \pm 0.2) \times 10^{-2}$	$(5.2 \pm 0.5) \times 10^{-3}$	3.43	0.16	0.02
	MI	$(-1.10 \pm 0.24) \times 10^{-1}$	$(-2.97 \pm 0.32) \times 10^{-2}$	$(11.5 \pm 0.7) \times 10^{-3}$	4.03	0.12	0.03
NGC 5850	MA	$(-5.338 \pm 0.297) \times 10^{-1}$	$(-6.0 \pm 2.2) \times 10^{-3}$	$(1.5 \pm 0.8) \times 10^{-3}$	8.28	0.16	0.06
	MI	$(-3.236 \pm 0.339) \times 10^{-1}$	$(-2.33 \pm 0.25) \times 10^{-2}$	$(7.5 \pm 0.9) \times 10^{-3}$	8.73	0.12	0.07

Table 5.2: Slopes of the linear fits to the stellar population properties along the inner bar major (MA) and minor axis (MI) in the radial range of the inner bar (in units of Gyr arcsec^{-1} and dex arcsec^{-1}). We further provide the mean stellar population properties in this radial range (in units of Gyr and dex).

5.3.2 Profiles along the Inner Bar Major and Minor Axis

In Fig. 5.3 we plot light-weighted stellar ages, metallicities, and [α /Fe] abundances as a function of the deprojected galactocentric radius. These profiles are calculated based on pseudo-slits crossing the galaxy centre and being oriented along and perpendicular to the major axis of the inner bar, according to the position angles presented in Table 5.1. We include all spatial bins within a pseudo-slit with a width of 2 arcsec but check that using different widths, for instance 1 arcsec or 4 arcsec, do not alter the profiles qualitatively.

Naturally, the radial population profiles clearly corroborate the findings from the stellar population maps. In Table 5.2 we provide an overview of the mean stellar population properties measured along and perpendicular to the inner bar major axis. Average differences vary between galaxies, but indicate that inner bars are systematically more metal-rich and less [α /Fe] enriched (see Table 5.2). We note that the differences between the major and minor axis depend on the radius and, hence, the typical differences at the inner bar radius are significantly larger than the average differences in the radial region of the inner bar. Considering stellar ages, inner bars seem to be slightly younger, although typical age differences are relatively small. In line with our findings from the population maps, the largest age differences are found close to or just outside of the inner bar radius, reaching maximum age differences of 2 Gyr for NGC 5850, and between 1 Gyr to 2 Gyr in the case of NGC 1433. These absolute age differences at the ends of the inner bar remain below 1 Gyr only for NGC 1291. In fact, the observed age differences somewhat depend on the absolute values of stellar age. Distinguishing the ages of stellar populations at old ages, for instance in the case of the >10 Gyr populations in NGC 1291, is very difficult, possibly indicating that in this case the age differences are not significant.

Another interesting aspect are the slopes of the stellar population profiles inside the inner bars, especially when considering metallicity and [α /Fe] abundances. The [M/H] and [α /Fe] profiles along the inner bar major axis of NGC 1291 are steeply decreasing/increasing from the centre, an effect that is most likely due to the small kinematically hot spheroid in this galaxy with an effective radius of 9.9 arcsec (de Lorenzo-Cáceres et al. 2019b). However, the profiles are remarkably flat in the radial range occupied by the inner bar (shaded area in Fig. 5.3). A prominent break in the profiles is evident at the inner bar radius where [M/H] and [α /Fe] steeply decrease/increase and converge to the lower/higher values typically observed outside of the nuclear disc. In contrast, the slopes along the inner bar minor axis differ significantly from those along the inner bar major axis. In fact, the minor axis profiles smoothly connect the steep slopes in the innermost region to the values at large radii, showing a larger/lower slope. The inner bar of NGC 5850 follows exactly the same trends, however, the effect is less prominent for NGC 1433. The latter is not surprising, as the inner bar in this galaxy is somewhat weaker and less elongated. Interestingly, such flat radial profiles are not evident when considering the stellar ages of any galaxy in the

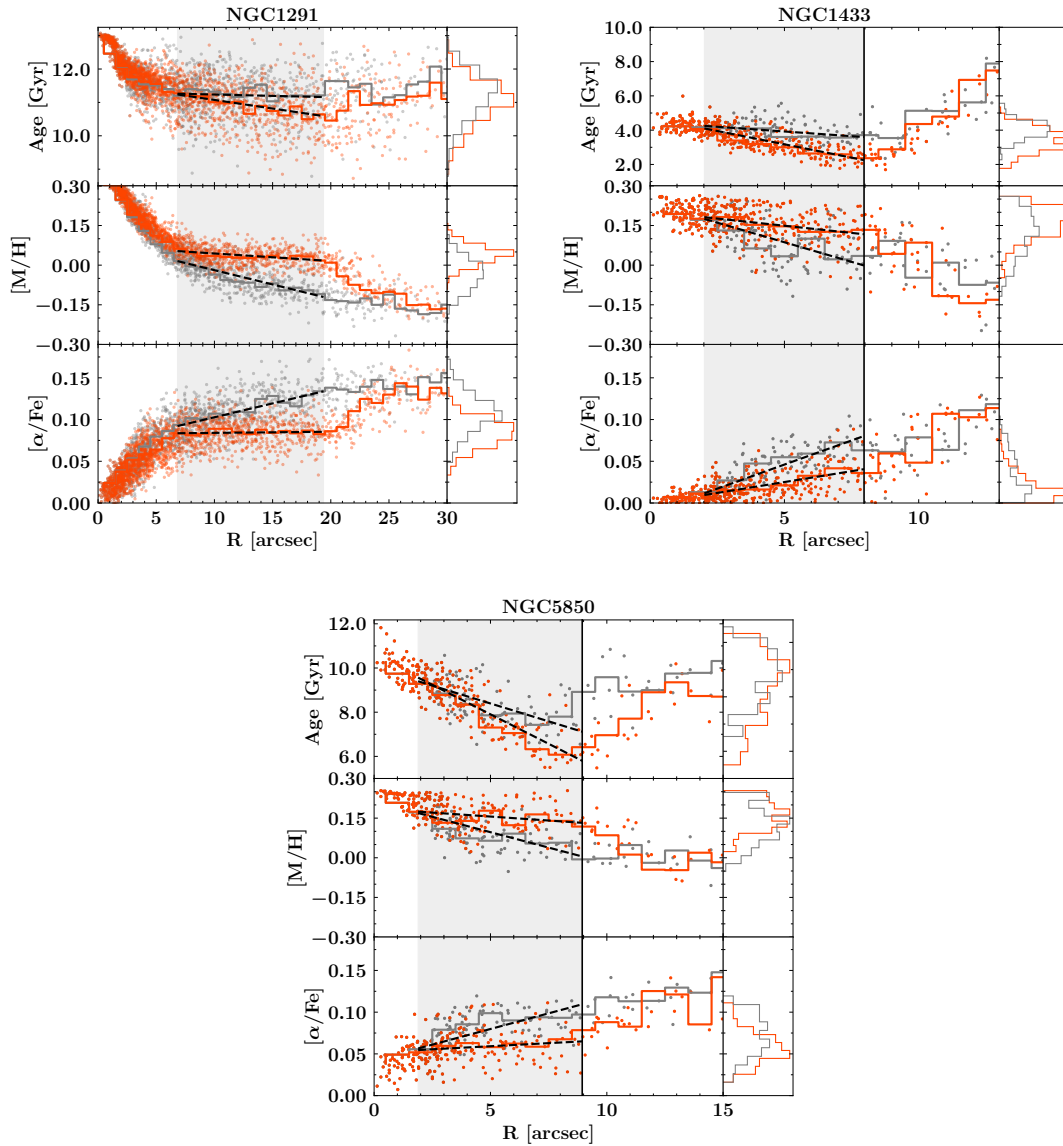


Figure 5.3: Radial profiles of ages (upper panels), metallicities (central panels), and $[\alpha/\text{Fe}]$ abundances (lower panels) as a function of the galactocentric radius. The profiles have been deprojected using inclinations and position angles derived in S^4G , as presented in Table 5.1. Profiles along the major axis of the inner bar are displayed in orange and grey, respectively. To better highlight the radial trends, we also plot the median population properties in bins of 1 arcsec (solid lines). Shaded regions highlight the radial range of the inner bars, i.e. for NGC 1291 and NGC 5850 the range between the inner bar minor and major axis radius, calculated using the inner bar radius from Herrera-Endoqui et al. (2015) and ellipticity from de Lorenzo-Cáceres et al. (2019b). Since the inner bar properties of NGC 1433 are not constrained by photometric studies, we highlight the radial range between 2 arcsec (in order to approximately exclude the range in which both the minor and major axis profiles probe the inner bar) and the kinematic radius of the nuclear disc from Gadotti et al. (2020). Dashed lines show linear fits to the population profiles within the radial range of the inner bar. The histograms on the right display the distribution of stellar population properties in the inner bar major and minor axis, again within the radial range of the inner bar. The vertical solid lines represent the kinematic radii of the nuclear discs (Gadotti et al. 2020). We note that for NGC 1291 no kinematic radius could be determined, due to the face-on orientation of the galaxy.

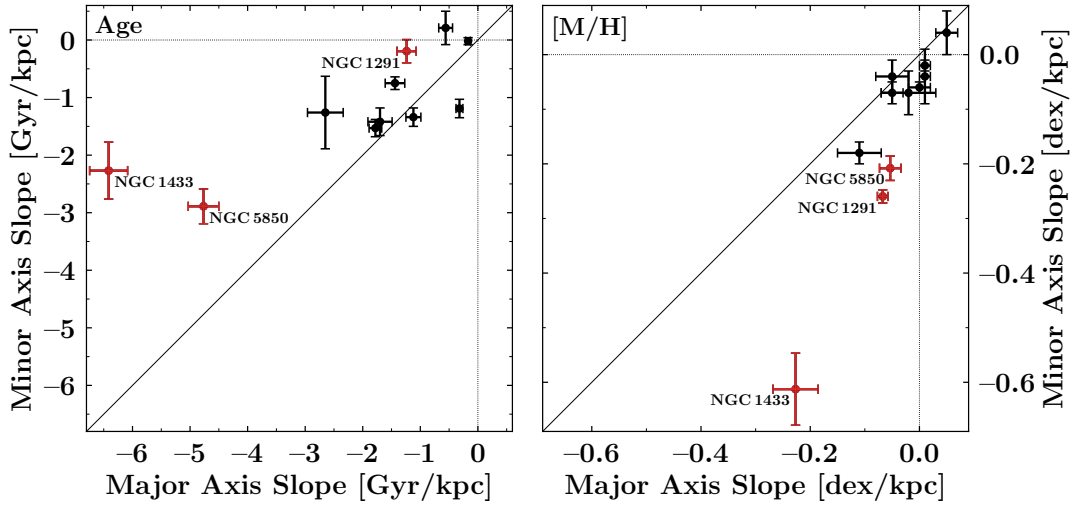


Figure 5.4: Comparison of the age (left-hand panel) and metallicity (right-hand panel) slopes measured along the major and minor axis of the inner bars in this study (red data) and the main bars from Neumann et al. (2020, black data).

sample. Instead, the observed stellar ages are continuously decreasing both along and perpendicular to the inner bar. In all three galaxies of the present sample, the stellar ages are decreasing more strongly along the inner bar major axis than perpendicular to it.

In order to better quantify these findings, we fitted ages, metallicities, and $[\alpha/\text{Fe}]$ abundances of the three galaxies in the radial range of the inner bar (shaded area in Fig. 5.3). For NGC 1291 and NGC 5850, this is the radial range between the inner bar minor and major axis radius, as determined from the measurements of de Lorenzo-Cáceres et al. (2019b) and Herrera-Endoqui et al. (2015). Equivalently, for NGC 1433 we chose the radial range between 2 arcsec (in order to exclude the radial region where both major and minor axis still probe the inner bar) and the kinematic radius of the nuclear disc from (Gadotti et al. 2020). The resulting fits are shown in Fig. 5.3 and the results summarised in Table 5.2. These measurements support the considerations above and confirm that the radial profiles of metallicity and $[\alpha/\text{Fe}]$ are significantly flatter along the inner bar major axis, as compared to the minor axis profiles.

In Fig. 5.4, we compare the absolute values of the age and metallicity slopes along the inner bar major and minor axis with those obtained by Neumann et al. (2020) for main bars in different TIMER galaxies. The relative steepening/flattening of the age/metallicity profiles along the inner bar major axis – as compared to the minor axis – is well compatible with the results for main bars, as indicated by the systematic offset from the one-to-one correspondence line. The absolute values of the slopes of the inner bars may vary substantially from those of main bars but this is expected from the different assembly history of nuclear discs and main galaxy discs. In contrast to main discs, nuclear discs are formed through bar-driven processes (Bittner et al. 2020), hence the absolute age slope is set by the timescale of these processes. Similarly, a comparison of minor axis fits between inner and main bars is elusive, as those probe distinct structural components of the galaxies, that is nuclear discs and main discs.

Finally, we point out that the relative differences in the stellar population properties discussed above are of the same order of magnitude as the typical measurement errors presented in the literature (see e.g. Gadotti et al. 2019; Pinna et al. 2019; Bittner et al. 2020). However, while comparing absolute values of stellar population properties between different galaxies involves large uncertainties, this is not the case when considering trends within the same galaxy. In other words, it is unlikely that the observed systematic differences in the population content within one galaxy arise from random uncertainties in the measurement procedure, in particular since the trends presented in Fig. 5.3 are averaged over many spatial bins. In the right-hand panels of Fig. 5.3 we compare the distributions of stellar population properties along and perpendicular to the inner bar major axis within its radial range. For ages, metallicities, and $[\alpha/\text{Fe}]$ abundances of both galaxies, an Anderson-Darling test confirms at a 99.9% significance level that both observed distributions are not drawn from an identical parent distribution.

5.4 Discussion

In this section we discuss our findings on the stellar population properties of inner bars in comparison with analogous measurements in main bars. We further highlight these results in the context of the dynamical mechanisms of orbital age separation and orbital mixing. We remind the reader that the galaxies in the present sample exhibit high total stellar masses (see Table 5.1) and low-mass barred galaxies might follow trends different from those discussed in the following (see e.g. Elmegreen & Elmegreen 1985; Kruk et al. 2018; Zurita et al. 2020).

5.4.1 Stellar Populations in Bars, Inner Bars, and their Star Formation Deserts

Main bars are not only detectable based on their morphology or kinematic features, but can also be identified by their stellar population content. In particular, bars typically exhibit higher metallicities and show lower $[\alpha/\text{Fe}]$ abundances, as compared to their immediate surroundings or the main disc (see e.g. Pérez et al. 2007, 2009; Sánchez-Blázquez et al. 2011, 2014; Fragkoudi et al. 2020; Neumann et al. 2020). While this finding does not necessarily hold true when comparing bars to the outer parts of the main galaxy disc (see e.g. Seidel et al. 2016), it does when bars are compared to the part of the disc within the bar radius but outside of the bar itself, a region often denoted as ‘star formation desert’ (SFD; see e.g. James et al. 2009; James & Percival 2016; Donohoe-Keyes et al. 2019). Basically, these studies suggest that star formation in the SFD is suppressed very rapidly after bar formation. In contrast, star formation in the bar itself continues at least for a limited amount of time, although at relatively low rates, resulting in slightly younger stellar populations in the bar. Due to this continuing self-enrichment, the bar eventually reaches higher metallicities and depleted $[\alpha/\text{Fe}]$ enhancements, as compared to the SFD. Hence, the star formation desert can be identified as a region within the bar radius but outside of the bar itself that is characterised by relatively low metallicities and elevated $[\alpha/\text{Fe}]$ abundances.

Interestingly, in Sect. 5.3.1 we find similar results for the stellar population content of inner bars. In particular, inner bars exhibit elevated values of $[M/H]$ and depleted $[\alpha/\text{Fe}]$ abundances, as compared to the region outside of the inner bar but within the inner bar radius (i.e. the star formation desert of the inner bar). Moreover, Fig. 5.3 indicates that inner bars are slightly younger along than perpendicular to their major axis. Nonetheless,

previous findings (e.g. de Lorenzo-Cáceres et al. 2019b) indicating that the inner bar of NGC 1291 is slightly older compared to its SFD suggest that, at least in some cases, star formation is suppressed more rapidly in the bar itself (see also Verley et al. 2007; Neumann et al. 2019; Fraser-McKelvie et al. 2020; Díaz-García et al. 2020; Neumann et al. 2020).

In general, based on maps of the mean stellar population properties alone, bars and inner bars appear similar in terms of their relative population content. To date, inner bars were only marginally resolved in integral-field spectroscopic observations, due to the different spatial scales of main and inner bars. However, this limitation is now overcome by the high spatial sampling of the MUSE spectrograph. Visually comparing the inner bars in this study to the main bars observed in the TIMER survey (see Neumann et al. 2020), highlights the similarities of the stellar population content between bars and inner bars. In addition, a comparison of the properties of inner bars to the area within the inner bar radius but outside of the inner bar itself suggests the presence of a star formation desert related to inner bars, again as in main bars.

5.4.2 Flat Population Gradients along Inner Bars: Orbital Mixing

Another relevant aspect when considering mean stellar population properties of bars are their gradients along the bar major axis, an aspect that holds information on their dynamical structure. More specifically, bars are elongated components which are built-up by a large number of elongated stellar orbits. These orbits might be composed of different stellar populations, show distinct levels of elongation, and reach different maximum radii in the bar. However, this does not only result in more elongated orbits dominating the spatial regions at the ends of the bars (see Sect. 5.4.3), but also causes different orbits to come very close to each other within the majority of the radial extent of the bar. In other words, stars on different orbits cross the same spatial region in the galaxy (see e.g. Binney & Tremaine 1987; Contopoulos & Grosbol 1989; Athanassoula 1992a). Therefore, at each location in the bar the light contributions of different stellar populations on different orbits appear mixed and the gradients of the stellar population content in the main parts of the bars, in particular $[M/H]$ and $[\alpha/Fe]$, are expected to be comparably flat.

In fact, recent observations suggest a flattening of the stellar populations gradients along the major axis of the bar, well consistent with the theoretical considerations above (see e.g. Sánchez-Blázquez et al. 2011; Williams et al. 2012; Seidel et al. 2016; Fraser-McKelvie et al. 2019; Neumann et al. 2020). To date, radial population gradients could only be derived for main bars, as the spatial resolution remained a limiting factor.

In this study, we present for the first time radial gradients of the mean stellar population properties along both the inner bar major and minor axis. Similar to main bars, we find that the radial gradients of metallicities and $[\alpha/Fe]$ abundances along the inner bars major axis are significantly flatter compared to the profiles along the minor axis. This flattening resembles the stellar population profiles previously observed in main bars. This suggests that inner bars have a significant impact on the radial distribution of stellar populations in nuclear discs and hence that the orbital mixing which is evident in bars occurs in inner bars as well. Again, this result reinforces the idea that inner bars are dynamically distinct components that form and evolve in the same way main bars do.

Interestingly, while a flattening of the radial gradients along the inner bar major axis is prominent for metallicities and $[\alpha/Fe]$ abundances, no such gradient is evident in the stellar age profiles. Instead, the measured stellar ages typically decrease from the centre

of the galaxy to the outer edge of the nuclear disc. In fact, such negative gradients in age are frequently observed in nuclear discs, regardless of the presence of an inner bar, and appear to be a result of their inside-out formation scenario (Bittner et al. 2020). In addition, orbital age separation, that is the dynamical effect that the ends of bars are younger than their central parts, should also hinder the development of flat age profiles. We detail this aspect in the following subsection.

5.4.3 Young Ends of Inner Bars: Orbital Age Separation

Main bars do not only appear distinguished from their surroundings by their elevated metallicities and depleted $[\alpha/\text{Fe}]$ abundances, but also show spatially well-defined variations in age. The ends of main bars generally appear significantly younger compared to the rest of the bar. While this effect could be a result of enhanced star formation in these regions, the inspection of $\text{H}\alpha$ emission-line maps has shown that no signatures of ongoing star formation are detected. Instead, this observation is a result of orbital age separation (also referred to as kinematic fractionation) and known from both observational and numerical studies on the stellar population content of bars (see e.g. Pérez et al. 2007; Wozniak 2007; Fragkoudi et al. 2017b, 2018; Athanassoula et al. 2017; Debattista et al. 2017; Neumann et al. 2020).

These studies find that distinct kinematic components of the galaxy disc participate in bars in different ways. Kinematically cold stars (i.e. those with a low radial velocity dispersion) preferably end up in highly elongated x_1 orbits (oriented along the bar major axis) while kinematically hot stars (i.e. those with high radial velocity dispersion) form rounder and less elongated bar x_1 orbits. Since more elongated orbits extend to larger radii, the ends of the bars are dominated by stars on the most elongated orbits. In the main disc of a typical galaxy, these kinematically cold and hot components could be the thin and thick disc (Fragkoudi et al. 2017b; Debattista et al. 2017; Athanassoula et al. 2017). While the thick disc is typically thought to be old, metal-poor, and shows high velocity dispersions, the thin disc is younger, more metal-rich, and exhibits low velocity dispersions (see e.g. Prochaska et al. 2000; Cheng et al. 2012; Pinna et al. 2019). As a consequence of this, the young stars of the thin disc end up on more elongated bar orbits and thus dominate the spatial region at the ends of the bar, hence creating the effect that the ends of bars show younger stellar populations. Interestingly, this effect is most prominent for stellar ages, but absent when considering metallicities and $[\alpha/\text{Fe}]$ abundances, in contrast to the simulations of Fragkoudi et al. (2018). A possible explanation could be that age is a better tracer of the stellar kinematics, or, more precisely, of the velocity dispersion (see e.g. Peletier et al. 2007; Falcón-Barroso 2016). The longer a stellar population was present in the disc of a galaxy, the longer it was exposed to dynamical heating processes, resulting in an increased velocity dispersion. Hence, the velocity dispersion should be a function of stellar age and, therefore, the ends of bars can be observed to exhibit younger stellar populations. In contrast, stars of a given age can have a range of metallicities and $[\alpha/\text{Fe}]$ enhancements, so that these quantities are not necessarily a function of stellar velocity dispersion, and therefore the ends of bars and inner bars do not necessarily show distinct $[\text{M}/\text{H}]$ and $[\alpha/\text{Fe}]$ values.

In all galaxies in this study, we do detect such younger stellar populations in a spatially confined region at the ends of the inner bars. As a result, these relatively young ends spatially coincide with σ -hollows in these galaxies (de Lorenzo-Cáceres et al. 2019b; Méndez-Abreu et al. 2019; Bittner et al. 2019). These regions of significantly lower stellar velocity dispersion are typically detected towards the ends of inner bars, that is in areas

in which the inner bar dominates the stellar light (de Lorenzo-Cáceres et al. 2008, 2013). Observing younger stellar populations in the same regions hints towards the existence of the dynamical effect of orbital age separation in inner bars. This again suggests that inner bars work dynamically identical to bars, differing only in the spatial scale on which they form from disc instabilities.

This result also indicates that stars from kinematically different components participate in the inner bar. Analogous to the main bar existing in both the thick and thin main disc, one might speculate if nuclear discs consist of hotter and colder nuclear disc components as well or that the hot main disc component might participate in the inner bar. However, dedicated studies, in particular numerical simulations of nuclear disc formation in a self-consistent cosmological context, are necessary to shed further light on these aspects.

Finally, a frequent photometric feature of strong bars in early-type spirals are surface brightness enhancements at their ends, a structure typically referred to as ansae (Martinez-Valpuesta et al. 2007; Buta et al. 2015). To date, these structures have not been studied intensively and their physical origin as well as presence in inner bars remains elusive. Here we speculate that the systematically younger stellar populations at the ends of inner and main bars could be connected to photometric ansae. In fact, these younger stellar populations, in particular in the case of NGC 1291, resemble the morphological appearance of ansae in photometric studies. Such younger stellar populations are expected to be relatively brighter and (at a given surface mass density) should result in elevated surface brightnesses. Other mechanisms, such as enhanced star formation at the ends of bars, or the dynamical trapping of stars around the ansae (Martinez-Valpuesta et al. 2007), might as well contribute to this phenomenon.

5.5 Summary and Conclusions

We have exploited MUSE observations of the central regions of the three galaxies NGC 1291, NGC 1433, and NGC 5850, observed as part of the TIMER survey. All galaxies clearly exhibit nuclear discs, and two of them host prominent inner bars. The inner bar in NGC 1433 appears weaker and less elongated particularly in earlier imaging data, but is clearly detected in our new, AO-assisted, H-band photometric observations. In the present study, we have used the full spectral fitting code `pPXF` in order to derive spatially resolved maps and radial profiles of the mean stellar population properties in the inner bars. We compare these results to those obtained for main bars, and further use them to constrain their dynamical structure. Our main results are as follows:

- (i) Inner bars can be clearly distinguished, based on their mean stellar population properties alone. In particular, they are characterised by elevated metallicities and depleted $[\alpha/\text{Fe}]$ abundances, as compared to the region outside of the inner bar but within the inner bar radius. Although inner bars show systematically younger ages, these differences are generally small. Based on spatially resolved, high-resolution maps of the mean population properties and their relative values, inner and main bars appear identical.
- (ii) Radial profiles of metallicities and $[\alpha/\text{Fe}]$ abundances along the inner bar major axis are flat, while minor axis profiles exhibit steeper slopes. This observational effect of radial mixing is known from main bars, and suggests that inner bars significantly

affect the distribution of stars in the nuclear discs. This effect is consistent with inner bars being built by stars on strongly elongated orbits, analogous to the x_1 orbits in main bars.

- (iii) The ends of the inner bars exhibit younger mean ages, as compared to the rest of the inner bars. This effect is known from main bars as kinematic fractionation or orbital age separation and suggests that the youngest stars, that is those with the lowest radial velocity dispersion, occupy the most elongated x_1 orbits. This effect might as well explain the formation of σ -hollows at the ends of the inner bars.
- (iv) We speculate that the observed young ends of bars and inner bars could be one possible mechanism to create the morphological feature of ansae, in particular as younger stellar populations have a higher surface brightness at a given stellar mass surface density.

The above results, in particular orbital mixing and orbital age separation, together with results from de Lorenzo-Cáceres et al. (2019b) and Méndez-Abreu et al. (2019) reinforce the idea that barred galaxies can be rather like Babushka dolls, in which we have a ‘galaxy within a galaxy’: inner bars appear to be dynamically very similar to the main bars of disc galaxies. The main difference between these galaxy components is the spatial scale on which they form and evolve.

Summary and Conclusions

Bars are not only a prominent and very frequent component of disc galaxies but also one of the major drivers of their secular evolution. The non-axisymmetric gravitational potential induced by bars promotes the exchange of angular momentum throughout galaxy discs which substantially affects the dynamics and distribution of gas and stars across them. The exchange of angular momentum allows bars to grow in radius, become stronger as they evolve, buckle vertically and build box/peanut structures, while triggering the formation of inner and outer rings, as well as star-formation deserts. However, one of the most striking effects of bars is the inflow of gas from the main galaxy disc to its central regions. More precisely, the bar exerts strong tangential forces on the gas in the main disc which eventually shocks, loses angular momentum, and streams along the leading edges of the bar towards the galaxy centre. This gas inflow is halted a few hundred parsecs from the galaxy centre where it settles, cools, and eventually forms new stellar structures, in particular nuclear discs, nuclear rings, and inner bars. In this thesis, we present four projects investigating the structure, formation, and evolutionary histories of these central stellar components in barred galaxies. After developing a sophisticated software framework for the analysis and visualisation of integral-field spectroscopic data, we discuss the stellar kinematics and mean stellar population properties of nuclear discs in detail. Finally, we constrain the physical nature of inner bars by comparing their stellar population content with that of main bars.

We use integral-field spectroscopic observations of the central regions of 21 massive disc galaxies in the local Universe, obtained as part of the TIMER survey. The data was taken with the MUSE spectrograph at ESO's Very Large Telescope atop Cerro Paranal in the Atacama desert in Chile. With its superb spatial sampling of 0.2 arcsec, this data set consisting of a total of 2 177 373 spectra provides unprecedented possibilities for investigating the nature of nuclear discs.

To efficiently explore this massive data set, we develop a dedicated software framework for the analysis and visualisation of spectroscopic data, the GIST pipeline (see Chapter 2). This software not only facilitates the measurement of stellar kinematics, emission-line properties, and non-parametric star formation histories by exploiting the well-known pPXF and pyGandALF routines, but also provides a sophisticated graphical user interface for the inspection of all data products. The modular code architecture of GIST enables the modification of the code, the usage of different fitting routines, and the analysis of data from various instruments.

Using this software framework, we derive stellar kinematics and mean population properties in nuclear discs and nuclear rings. Given the large amount of information in both kinematics and population properties, this work is detailed in two separate studies, as presented in Chapters 3 and 4. We find that nuclear discs are rotationally supported, that is have a higher rotational velocity and a lower velocity dispersion compared to the main disc at

similar radii, while consisting of stellar populations that are younger, more metal-rich, and exhibit lower $[\alpha/\text{Fe}]$ abundances, as compared to their surroundings. These findings are consistent with the picture of a bar-driven formation while contradicting a gas-poor and violent merger-driven formation scenario. A careful comparison of our spectroscopic results with those of detailed photometric decompositions of the same galaxies shows that nuclear discs are indeed the disc-like bulges with exponential light profiles that have been previously detected in photometric studies. These results thus clearly reveal the physical nature of disc-like bulges, which is not possible with photometry alone. Moreover, composite bulges, that are spatially co-existing classical bulges and nuclear discs, can often remain unnoticed in photometric studies and significantly bias photometric classifications of bulges. In contrast, integral-field spectroscopic observations more directly probe the physical nature of galaxy components and hence are better suited to reveal such systems.

Nuclear discs further show well-defined radial gradients of their mean stellar population properties, with $[\alpha/\text{Fe}]$ enhancements continuously increasing and ages and metallicities decreasing from the galaxy centre out to their outer edges. We propose that these continuous, stellar nuclear discs form in an inside-out formation scenario from a series of gaseous nuclear rings, which increase in radius as the bars evolve. Therefore, nuclear rings can be understood as the star-forming outer edge of stellar nuclear discs. While nuclear discs are present in the TIMER galaxies, no signatures of large classical bulges are detected based on our spectroscopic analysis. In principle, a quiet merger history or strong feedback from stars and active galactic nuclei could prevent the formation of classical bulges and hence explain their ubiquitous absence in the TIMER sample. Even though the TIMER sample is biased towards galaxies exhibiting signs of bar-built central substructures, the lack of classical bulges in the sample supports various photometric studies that detect only low fractions of galaxies hosting dispersion-dominated components in their centres, even at high galaxy masses. In fact, the smooth radial gradients in the stellar population properties of nuclear discs suggest that often such structures dominate to the very centres of their host galaxies.

In another, dedicated study (see Chapter 5), we use the same measurements of mean stellar population properties to further constrain the dynamical structure of the three inner bars in the TIMER sample. In spatially resolved maps of the stellar population content, all inner bars do appear clearly distinguished from the nuclear discs in which they reside. More precisely, they exhibit even higher metallicities and depleted $[\alpha/\text{Fe}]$ abundances. Nonetheless, inner bars show similar mean stellar ages as their surroundings but exhibit slightly younger populations at their outer ends. This effect has also been observed in main bars and is known as orbital age separation: the youngest stellar populations, that is those with the lowest radial velocity dispersion, occupy the most elongated orbits along the bar and, hence, dominate the stellar light at the ends of the bar. For the first time, we produce radial profiles of mean stellar population properties along both the inner bar major and minor axis. Similar to main bars, the radial profiles of metallicities and $[\alpha/\text{Fe}]$ enhancements are flat along the inner bar major axis but exhibit steeper slopes along their minor axis. This radial mixing is a clear sign that inner bars substantially affect the radial distribution of stars in nuclear discs and suggests that inner bars are supported by stars on strongly elongated orbits along their major axis, analogous to main bars. Together with the results from other recent TIMER studies, this supports the concept that inner bars in nuclear discs function dynamically similar to the main bars in main galaxy discs. In this picture, the main difference between inner and main bars is only the spatial scale on which they exist.

With the projects presented in this thesis, we did not only simplify some technical challenges in the analysis of integral-field spectroscopic data but also provided an unparalleled view of the centres of disc galaxies. The GIST framework grew into a flexible analysis tool that is widely used in the community, analysing data from many of the largest astronomical observatories on this planet, and being used to address scientific questions ranging from active galactic nuclei, over planetary nebulae, to the secular evolution in galaxies. The revolutionary MUSE spectrograph enabled us to produce unprecedented studies of nuclear discs and nuclear rings, analysing their stellar kinematics and population content at the highest spatial resolutions. With this data, we characterised their properties, constrained their formation scenarios, and provided a more reliable way to observationally distinguish them from classical bulges. At the same time, we added to the growing amount of evidence that inner and main bars are actually scaled versions of each other, simply by better constraining their stellar population content. In summary, as an anonymous referee recently stated, this “[...] adds to the recent body of work by the TIMER survey, which is making significant advances in understanding the central regions of barred galaxies.”

Nonetheless, many open questions regarding the centres of disc galaxies remain:

- How can the proposed inside-out formation scenario of nuclear discs be further tested? Could new observations help to constrain this process? Can it be reproduced in numerical simulations of galaxies, possibly even within a cosmological context?
- Can this inside-out formation scenario help to identify the oldest peak of star formation in the nuclear disc and, hence, allow to constrain the ages of bars?
- Are classical bulges as rare as recent studies suggest? How frequent are classical bulges and nuclear discs in the local Universe, and how is stellar mass distributed between them? Can this help to better understand galaxy evolution in general and constrain the paradigm of hierarchical structure formation?
- Are all inner bars just scaled-down version of main bars? Although we provided new insights into their dynamics and stellar population content, so far only very small samples of inner bars could be examined spectroscopically.
- Inner bars appear to be dynamically similar to main bars, however, they reside in nuclear discs that typically exhibit higher V/σ values than the main discs of galaxies. How does this comparably high stellar velocity dispersion affect the formation of the inner bar? Can this help us to better understand the formation of main bars at high redshifts when galaxy discs were kinematically hotter?

Undoubtedly, upcoming instruments and new observatories, as well as the vast amounts of already existing archival data will help to address these questions. More precisely, archival MUSE data covering the centres of local disc galaxies, together with the observing time we propose for as part of the BANG survey (see Chapter 7.1) will provide a comprehensive and unbiased view of the centres of galaxies. At the same time, the high spectral resolution of integral-field spectrographs like MEGARA at the Gran Telescopio Canarias in La Palma can help to better disentangle the many spatially co-existing stellar components in galaxy centres, while other forthcoming instruments, in particular HARMONI at ESO’s Extremely Large Telescope, will allow repeating these studies at significantly higher redshifts, directly witnessing the first formation of bars and their nuclear discs.

With the investigation of central stellar structures in disc galaxies presented in this thesis, we shed new light on various aspects of their formation processes, characterised their stellar kinematics and population content, and discussed these findings in the context of bar-driven secular evolution. However, in doing so, we did not only attempt to answer some open questions in this field of research but also found evidence that is deepening existing controversies. In the following, we discuss some of these aspects and propose means to further investigate these issues.

7.1 The BANG Survey: Bulge Assembly in Nearby Galaxies

While in this thesis we focus on secularly built nuclear discs, it is known that disc galaxies often also host dispersion-dominated spheroids in their centres, typically referred to as classical bulges. In contrast to nuclear discs, classical bulges are thought to be formed in violent accretion and merger events early in the evolutionary history of galaxies. More precisely, minor mergers are expected to produce disc galaxies with compact classical bulges in their centre, by triggering strong gas flows to the central parts of the galaxy where a burst of star formation transforms this gas into a dispersion-dominated stellar spheroid (see e.g. Bournaud et al. 2005b; Hopkins et al. 2009a; Brooks & Christensen 2016). An alternative scenario for the formation of classical bulges is based on the inward migration of clumps in high-redshift galaxies. The globally unstable discs at high redshifts are expected to fragment into giant clumps of gas and stars which undergo dynamical friction and sink towards the galaxy centre where they contribute to the build-up of a classical bulge (Noguchi 1999; Elmegreen et al. 2008; Bournaud 2016).

In our understanding of hierarchical structure formation (White & Rees 1978), galaxy mergers are expected to be very common. While approximately half of all galaxies underwent a major merger since $z \sim 1$ (Maller et al. 2006), minor mergers – which should be able to trigger the formation of classical bulges without transforming a disc galaxy into an elliptical galaxy – occur even more frequently, especially for high mass galaxies (see e.g. Stewart et al. 2008). At early cosmic epochs the merger rate is thought to be even higher (see e.g. Fakhouri et al. 2010). More precisely, Stewart et al. (2008) conclude that since $z \sim 1.7$ approximately 95% of all Milky Way-like halos underwent at least one minor merger with a mass ratio of 1:20 and approximately 70% had a minor merger with a ratio of 1:10. If minor mergers are so frequent and indeed facilitate the formation of dispersion-dominated spheroids in disc galaxies, classical bulges should be ubiquitously present in the Universe (see also Brooks & Christensen 2016). Since classical bulges could also form via clump migration, the frequency of minor mergers should only provide a lower limit on the frequency of classical bulges.

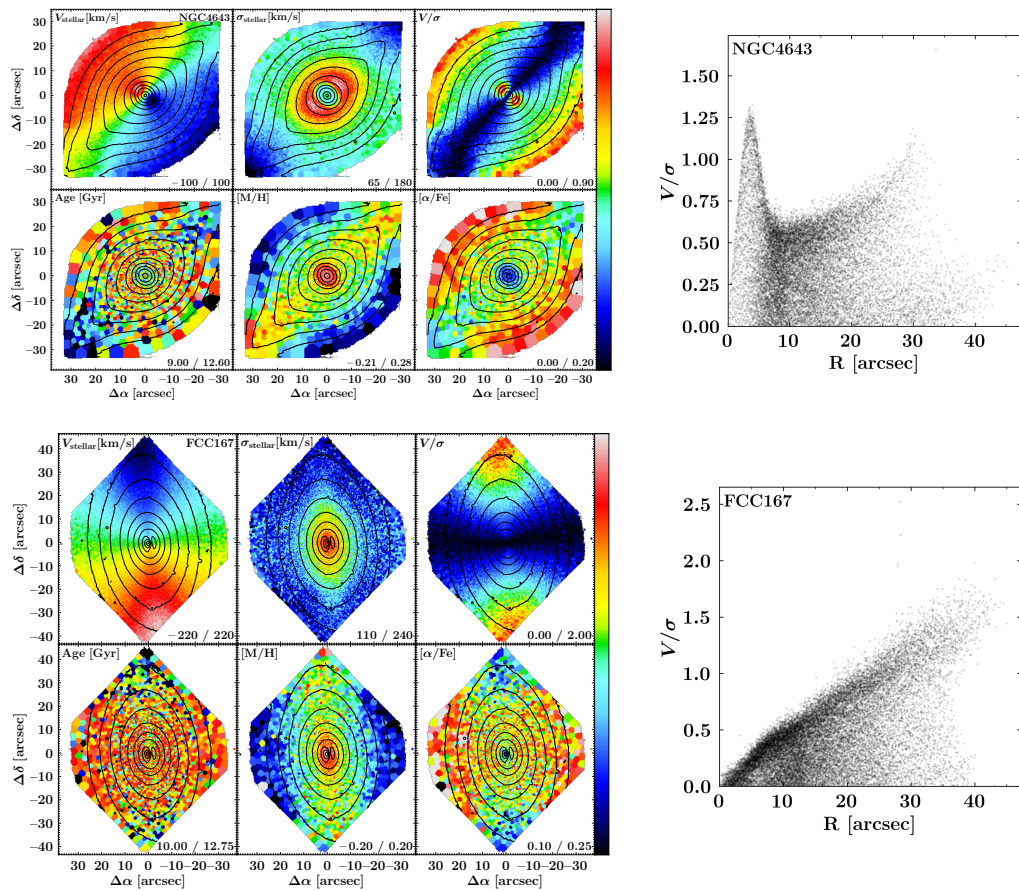


Figure 7.1: Spatially resolved kinematics and mean stellar population properties (left-hand panels) and radial profiles of V/σ (right-hand panels) of the galaxy NGC 4643 (upper panels) which hosts a prominent nuclear disc and the galaxy FCC 167 (lower panels) that has a classical bulge.

In Chapters 3 and 4 we inspected the stellar kinematics and average population content in the centres of all TIMER galaxies. Based on these measurements, it should be possible to unambiguously detect classical bulges as spheroidal components that are dispersion-dominated, that is exhibit low rotational support and high stellar velocity dispersions. In addition, their stellar populations should be systematically older and more $[\alpha/\text{Fe}]$ enhanced, as compared to the inner part of the main galaxy disc. The fundamentally different properties of nuclear discs, that is their high rotational support, young stellar ages, and low $[\alpha/\text{Fe}]$ abundances, should make it straightforward to distinguish them from classical bulges (see Fig. 7.1).

However, in the 21 galaxies of the TIMER survey, we detect hardly any evidence of large classical bulges. Only one galaxy exhibits some signatures consistent with the presence of a dispersion-dominated spheroid, while in two other galaxies such a component dominates only at very small radii significantly below the size of the nuclear discs. Although the TIMER sample is, by selection, biased towards barred galaxies with secularly built central substructures, this result is very surprising, especially when considering that the sample consists of massive galaxies (up to stellar masses of $2 \times 10^{11} M_{\odot}$) for which minor mergers, and hence the presence of classical bulges, are expected to be frequent.

Numerous photometric studies performing structural decompositions of disc galaxies by fitting their surface brightness distributions arrived at similar results. For instance, Fisher & Drory (2011) conclude that more than 80 % of disc galaxies in the local 11 Mpc volume do

not contain a classical bulge. The total stellar mass in elliptical galaxies and classical bulges together constitute only 25 % of the total stellar mass in this volume. Other photometric studies also concluded that classical bulges are not very common in the local Universe (see e.g. Weinzirl et al. 2009; Kormendy et al. 2010; Sachdeva & Saha 2016).

However, although nuclear discs and classical bulges exhibit fundamentally different kinematic and stellar population properties, as well as distinct levels of central light concentrations, distinguishing them based on photometric studies alone is prone to large uncertainties (see e.g. Fisher & Drory 2016; Neumann et al. 2017). While numerous sophisticated routines for the modelling of their surface brightness profiles are available (e.g. de Souza et al. 2004; Peng et al. 2010; Erwin 2015), the results substantially depend on the spatial resolution of the data and the models used in the fitting process. For the latter there are often no objective constraints and, especially for large galaxy samples, detailed decompositions including multiple galaxy components are not feasible. Therefore it is inherently difficult, in particular for statistically significant samples of galaxies, to distinguish nuclear discs from classical bulges based on photometric decompositions alone.

In summary, there is large observational uncertainty about the frequency of classical bulges, more precisely their number density and stellar mass distribution in the local Universe. Studies of bulge properties at higher redshifts are even more unreliable due to the limited physical spatial resolution. However, having solid constraints on the frequency of classical bulges is of fundamental importance as it provides clues on the frequency of minor mergers and the hierarchical build-up of structure in the Universe. If classical bulges are indeed so rare, this could pose a challenge to Λ CDM cosmology itself and there are only a few possible explanations for the putative lack of classical bulges (Brooks & Christensen 2016):

- (i) Minor mergers are much less frequent than expected in the picture of hierarchical structure formation. In line with other small-scale discrepancies (see e.g. Bullock & Boylan-Kolchin 2017, for a review), this could potentially challenge our understanding of the Λ CDM cosmological model itself. In fact, some recent cosmological simulations indicate that at least some massive disc galaxies do not have a violent merger history (see e.g. Fragkoudi et al. 2020).
- (ii) Classical bulges exist indeed in most of the galaxies but are hidden by secularly built nuclear discs of higher surface brightness. Disentangling such composite bulge systems using photometric observations is challenging (see e.g. Chapter 3, Méndez-Abreu et al. 2014), however, high-resolution integral-field spectroscopic observations in combination with photometry, as presented in this thesis, should facilitate their detection.
- (iii) Nuclear discs are frequently formed in mergers. However, this contradicts our current understanding of the formation and evolution of nuclear discs, as detailed in this thesis. It is difficult to explain that the majority of nuclear discs is found in barred galaxies (Comerón et al. 2010) while unbarred galaxies with nuclear discs typically show other non-axisymmetric structures in their discs or signatures of weak, previously undetected bars.
- (iv) Minor mergers do typically not result in the formation of classical bulges. Strong feedback processes from active galactic nuclei or stellar feedback during a starburst episode in the merger process could indeed hinder the formation of classical bulges (see e.g. Brooks & Christensen 2016).

Solid measurements of the number density and stellar mass distribution in classical bulges and nuclear discs are indispensable to better understand if there indeed is a discrepancy between observations and cosmological simulations, or which of the above possibilities might resolve this issue. In any case, reliable measurements of the classical bulge and nuclear disc population in galaxies are needed as a constraint for cosmological simulations. With the advent of high spatial resolution integral-field spectrographs such as MUSE, it is now possible to gain an unprecedented view at the stellar kinematics and population properties, as well as star formation histories in the central regions of disc galaxies and reliably provide such constraints.

Therefore, we are proposing the BANG survey (Bulge Assembly in Nearby Galaxies), a volume-complete survey of the central regions of massive disc galaxies in the local Universe. We will use the MUSE integral-field spectrograph to observe the central parts of all disc galaxies with stellar masses above $3 \times 10^{10} M_{\odot}$ in the local 40 Mpc volume, resulting in a sample of 133 galaxies. For a total of 44 galaxies of this sample archival data is already available, so that the exploration of data can already begin before any new observations are obtained. By combining information on the morphological structure of central stellar components with their kinematic and stellar population properties, we will be able to reliably distinguish secularly built nuclear discs from violently formed classical bulges and, for the first time, produce a complete and accurate census of these structures in the local Universe.

Beyond this main scientific question, the BANG data set will further provide insight into numerous other open questions. In particular, the survey will provide a large sample of nuclear discs covering a range of ages and sizes, and thus help to even better understand their evolution and formation scenario. Moreover, it might shed light on the claimed existence of nuclear discs in unbarred galaxies or better establish their ubiquitous absence. In addition, the BANG survey might help to discover more double-barred galaxies and increase the number of inner bars with integral-field spectroscopic observations by a multiple. At the same time, the data will allow obtaining more complete comparisons of galaxies with and without inner bars, but also of those with and without main bars. Finally, the survey might also facilitate more detailed studies of the central star cluster population in disc galaxies, including nuclear stellar clusters.

7.2 Kinematic Decompositions of Galaxies

The centres of disc galaxies are highly complex systems. A multitude of different galaxy components, in particular the main galaxy disc, bar, nuclear disc, and possibly inner bars and classical bulges, spatially coexist. Therefore, the observed stellar light is a mixture of these overlapping galaxy components, making studies on individual structures challenging. In photometric studies of galaxies, this problem is approached by employing multi-component decompositions of the galaxy light: the integrated radial surface brightness profile (or its two-dimensional distribution) of the galaxy is modelled with the expected surface brightness profiles of various components. This approach has successfully been employed for many years (see e.g. de Souza et al. 2004; Méndez-Abreu et al. 2008a; Peng et al. 2010; Erwin et al. 2015).

However, such photometric decompositions are degenerate, that is there exists no unique solution. In other words, there are often no objective criteria on the number and type of models included in the fit and it is unclear how well these models represent the different components. Spectroscopic observations which directly reveal the kinematic properties of these galaxy components might be key to a more physically motivated decomposition.

Nonetheless, similar challenges present themselves in spectroscopic studies of galaxies, as the observed spectra consist of light from different components. If the contributing components have significantly different physical properties, for instance radial velocities, velocity dispersions, and orbital structure, the resulting absorption lines will show non-Gaussian line profiles. This is simply a result of the non-Gaussian line-of-sight velocity distribution (LOSVD). In state-of-the-art full-spectral fitting codes, such as `pPXF`, the LOSVD is typically parametrized by the radial velocity, velocity dispersion, and higher-order Gauss-Hermite moments h_3 and h_4 (Gerhard 1993; van der Marel & Franx 1993) and this parametrization offers sufficient flexibility to properly model a range of non-Gaussian LOSVDs in the data. Even the presence of spatially overlapping galaxy components can be determined in this way and is typically indicated by elevated values of the higher-order moment h_4 (see e.g. Bender et al. 1994). However, the Gauss-Hermite parametrization is not suited to describe the most complicated LOSVDs, as they could arise in the centres of disc galaxies. In fact, a parametrized measurement of the LOSVD by itself is not necessarily suited to separate the contributing galaxy components. Moreover, it allows unphysical results for the LOSVD, in particular solutions in which the wings of the distribution are assigned negative values.

Recently, Falc3n-Barroso & Martig (2021) developed a Bayesian framework for the extraction of non-parametric LOSVDs (`BAYES-LOSVD`; see also Saha & Williams 1994). Naturally, this method overcomes the above-mentioned issues of the parametric recovery of LOSVDs and, at the same moment, also provides a deeper insight into the distinct kinematics of overlapping galaxy components. This non-parametric recovery of velocity distributions could present a chance to advance methods for the kinematic decomposition of physically different galaxy components.

One possible approach could be the following: firstly, one estimates the non-parametric LOSVD of the spectra using the novel routine from Falc3n-Barroso & Martig (2021). If the LOSVD exhibits a non-Gaussian shape, the velocity distribution is modelled by a set of Gaussian distributions, with each of them representing the LOSVD of one of the kinematic components. With this constraint on the velocity and velocity dispersion of each kinematic component, the (Bayesian) spectral fit can now be repeated with multiple components. A similar approach for kinematic decompositions has previously been attempted by Coccato et al. (2018), using the maximum penalized likelihood method of Gebhardt et al. (2000) for the extraction of a non-parametric LOSVD. However, these previous attempts typically focussed on the decomposition of stellar components with substantially different kinematic properties, for instance counter-rotating discs, polar discs, or the distinction between rotationally and dispersion supported structures (see e.g. Coccato et al. 2011, 2014; Fabricius et al. 2014; Coccato et al. 2018).

It remains to be seen if a kinematic decomposition based on the new Bayesian fitting approach of Falc3n-Barroso & Martig (2021) can advance the previous attempts and eventually allow the distinction of the kinematically more similar components (e.g. the main

galaxy disc and nuclear disc) in the centres of galaxies. It is also unclear if this approach is feasible for realistic, noisy galaxy spectra, would require additional structural constraints from photometric decompositions, or observations with higher spectral resolution.

In summary, a reliable algorithm for kinematic decompositions would not only help to better explore the physical properties of all overlapping galaxy components separately, but also to identify and distinguish them in galaxies, and possibly even provide constraints on their stellar population content separately. This is specifically important in the context of the BANG survey (see Sect. 7.1) where it could facilitate the detection of small classical bulges located within more prominent nuclear discs.

7.3 Extending the Efforts of the TIMER Survey

The TIMER survey (Gadotti et al. 2019) has recently made significant advances in understanding the central regions of disc galaxies in the local Universe. Beyond the studies presented in this thesis, the collaboration investigated the nature and formation processes of inner bars (de Lorenzo-Cáceres et al. 2019b; Méndez-Abreu et al. 2019), the impact of stellar feedback on the molecular gas in gaseous nuclear rings (Leaman et al. 2019), and the stellar population properties of galaxy bars (Neumann et al. 2020). With these studies, the team laid the groundwork to eventually address the main goal of the TIMER survey: estimating the age of bars from non-parametric star formation histories in the central stellar components.

As already summarized in Sect. 1.5, measuring the ages of bars is not straightforward, since the stars the bars consist of are typically older than the bar itself. Nonetheless, the cosmic time when bars first formed marks a fundamental point in the evolutionary history of galaxies: galaxy discs become dynamically mature, that is they are kinematically cold and supported by rotation, and internal secular evolution processes start to substantially influence their evolution.

In this thesis, we have shown that the nuclear discs in the TIMER sample are indeed built via bar-driven gas inflow to the galaxy centre and, hence, the oldest peak of star formation unique to the nuclear disc could indeed provide a lower limit on the age of the bar. This lower limit on the age of bars is probably close to their actual age, as bars are expected to push gas to the galaxy centre quickly after their formation (see e.g. Athanassoula 1992a; Emsellem et al. 2015). We have further proposed that nuclear discs form in an inside-out formation scenario from a series of star-forming nuclear rings, suggesting that the oldest peak of star formation in the nuclear disc is located close to the centre. Therefore, the natural next step in extending the work presented in this thesis is to attempt the measurement of bar ages in the TIMER galaxies.

To this end, we will derive non-parametric star formation histories in concentric rings around the galaxy centre, extending from their innermost regions to radii beyond the extent of the nuclear disc. Firstly, we expect to find a clear distinction between the star formation histories within and outside of the nuclear disc, owing to their distinct formation scenario. Secondly, the age of the oldest peak of star formation in the nuclear disc is expected to decrease with radius, at least if nuclear discs indeed form in an inside-out formation scenario. Thirdly, given the above considerations, the oldest peak of star formation in the nuclear disc is identified and therewith a lower limit on the age of bars determined. In this way, the evolutionary history of individual galaxies can be constrained and its dependency

on galaxy mass and environment studied. Measuring the ages of bars allows to further test the downsizing scenario suggesting that more massive galaxies mature earlier in cosmic history (see e.g. Cowie et al. 1996; Thomas et al. 2010; Sheth et al. 2012).

Direct observations of galaxies well beyond the local Universe could provide a complementary approach to better constrain the cosmic time when galaxies first became dynamically mature. This was already attempted by the KMOS^{3D} survey (Wisnioski et al. 2015) by deriving the H α emission-line kinematics of over 600 galaxies at redshifts between $z \sim 0.7$ and $z \sim 2.7$. The survey detected galaxies with regularly rotating discs up to very high redshifts, however, the robustness of this result is limited by the spatial resolution of the data. Nonetheless, this limitation can be overcome through the superb capabilities of some forthcoming observational facilities.

For instance, the integral-field spectrograph NIRSpec (Bagnasco et al. 2007) in NASA's James Webb Space Telescope (JWST; Gardner et al. 2006) will be able to obtain observations of unprecedented spatial resolution. With its wavelength coverage in the near-infrared, it is suited to measure the H α emission-line kinematics of galaxies up to high redshifts and, hence, allows to directly infer the kinematic structure of disc galaxies as a function of redshift.

Similarly, the integral-field spectrograph HARMONI (Thatte et al. 2010b) at ESO's Extremely Large Telescope (ELT; Gilmozzi & Spyromilio 2007) provides another opportunity to obtain spectroscopic observations of galaxies at high redshifts with high spatial resolution. With a spatial sampling down to 4×10^{-3} arcsec and a wavelength coverage from 4600 Å to 24 600 Å, it is also well-equipped for such studies. It might even allow to facilitate a TIMER-like survey at redshifts of approximately $z \sim 1$ and directly witness the formation of the first bars, nuclear discs, and the onset of secular evolution in the Universe.

Kinematic Signatures of Nuclear Discs

A

A.1 Kinematic Maps and Discussion of Exceptional Cases

In this appendix we present in Fig. A.1 the kinematic maps for the remainder of the sample as in Fig. 3.2. We also elaborate on exceptions to the general trends discussed in Sect. 3.3.3, where we presented kinematic signatures of nuclear discs, bars and box/peanuts.

A.1.1 Nuclear Discs

As discussed in Sect. 3.3.3, we find clear kinematic signatures of the presence of nuclear discs in most galaxies in this study. Apart from NGC 1291 – where the fact that the galaxy is very close to face-on prevents us from performing this assessment meaningfully – there are only two possible exceptions: NGC 1365 and NGC 6902. In NGC 1365, the maps of v and v/σ do not show a discontinuous behaviour and the clear presence of an additional rapidly rotating nuclear component, even though a nuclear star-forming ring is evident in S⁴G images, as well as in our MUSE reconstructed images (see Paper I). The galaxy is quite inclined (52 deg) and our MUSE field is heavily affected by dust, which complicates the interpretation of the kinematic maps. Moreover, it hosts an active galactic nucleus with associated large scale outflow and shock-induced emission lines. Nevertheless, it shows elevated values of h_4 in the central region, covering about half of the MUSE field¹. In addition, it shows a peculiar spiral-shaped region of elevated absolute values of h_3 anti-correlated with v . Furthermore, an extended region of low σ is seen at an angle with the bar, which is consistent with a nuclear, kinematically cold stellar structure seen in projection. It is therefore plausible that the MUSE field is dominated by the nuclear component, which precludes one from seeing the main galaxy disc. The spiral pattern in the h_3 map is likely a result from the overly strong dust lanes seen along the leading edges of the bar.

On the other hand, NGC 6902 is not heavily affected by dust and has a mild inclination angle (37 deg), but it appears to host a rather modest nuclear stellar structure. The v and h_3 maps show no clearly distinguished and rapidly rotating nuclear component, although this is better seen in the v/σ map. Nevertheless, the central region of the MUSE field, where the nuclear component resides, is dominated by high values of σ rather than low values. In addition, the h_4 map shows a ring-shaped region of elevated values around the central region, not so much in the region dominated by the nuclear component. Therefore,

¹These appendices are based on Gadotti, Bittner et al., *A&A* 2020, Volume 643, A14

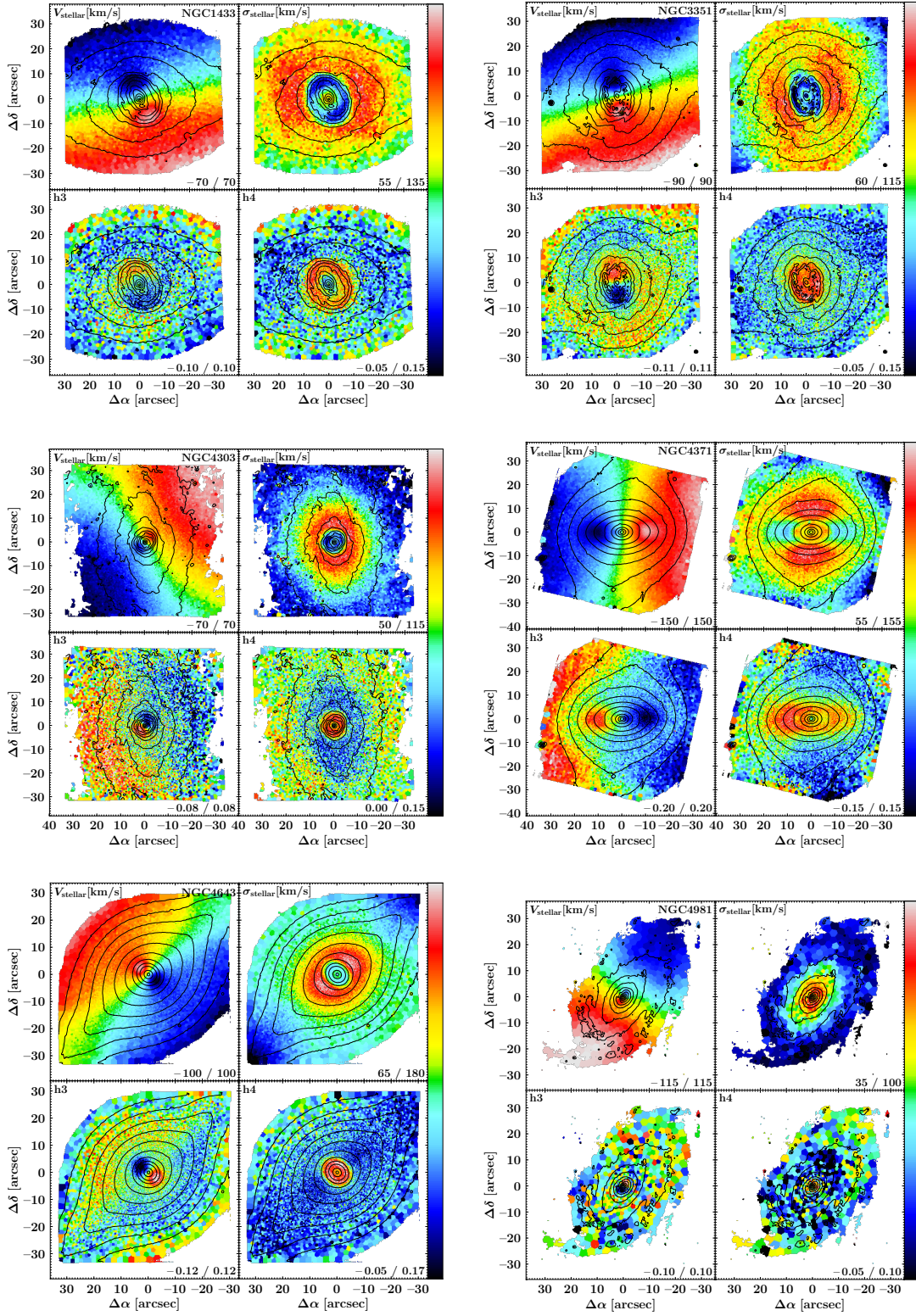


Figure A.1: Same as Fig. 3.2 but for the remainder of our sample.

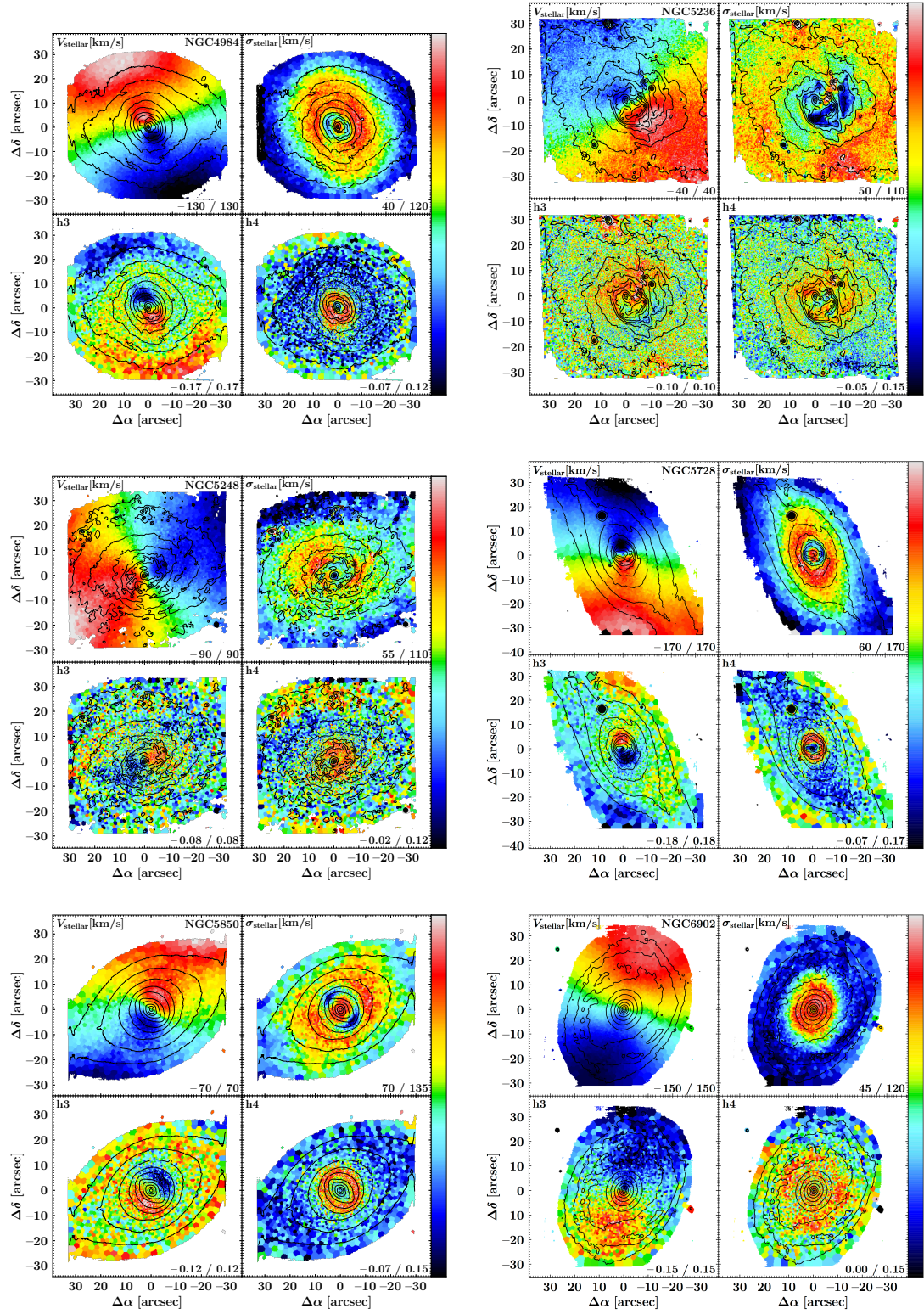


Figure A.1: Continued.

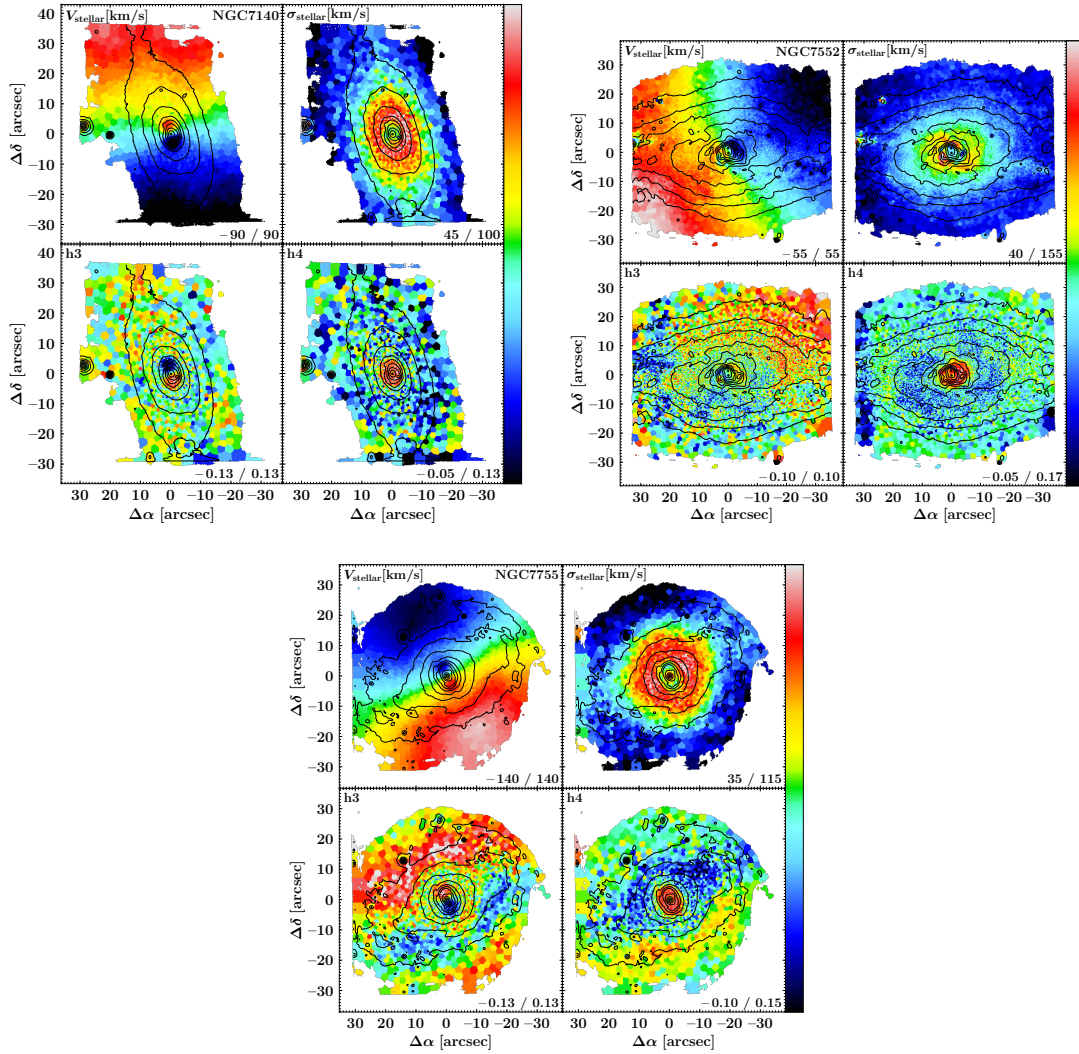


Figure A.1: Continued.

the interpretation of the kinematic maps for NGC 6902 is not as straightforward as for most of the TIMER sample. We note that NGC 6902 has the weakest bar of the TIMER sample, in the morphological classification of Buta et al. (2015).

A.1.2 Bars

We do not find the $v - h_3$ correlation foreseen in bars in six barred galaxies: NGC 1097, 1291, 1365, 4371, 5236, and NGC 6902. Apart from the latter, all these galaxies show prominent bars, but in most of these cases it is likely that the TIMER data do not cover enough of the bar to show this signature. In fact, NGC 5236, 1291, 1097 and NGC 1365 are, in this order, the largest projected bars in the TIMER sample, and our MUSE fields cover less than a third of the bar in these cases. The bar of NGC 4371 is well covered by our MUSE pointing but this is the most inclined galaxy in this study and the bar is close to perpendicular to the line of nodes, and thus projection effects may be preventing us from seeing the $v - h_3$ correlation. As mentioned above, NGC 6902 is the weakest bar in the sample and again appears as an exception.

¹We note, however, that elevated values of h_4 can be produced by radial orbits in non-rotating or slowly rotating systems (see Fig. 2 in van der Marel & Franx 1993).

A.1.3 Box/Peanuts

Since our MUSE fields seem to not go much further than any box/peanut vertices, the h_4 drops expected for box/peanuts are not clearly present in NGC 1097, 1365, 1433, and NGC 3351. We also do not find this box/peanut kinematic signature in NGC 4371, but in this case this is possibly due to projection effects. The bar is seen inclined around an axis close to its minor axis, and the galaxy inclination angle is relatively large (at 59 deg, this galaxy is the most inclined galaxy in this study).

In NGC 5236 the signature is not so clear. One sees regions of low h_4 on average along the bar major axis but the MUSE field seems to not be large enough to show where h_4 would rise again. NGC 5248 shows h_4 minima but it is not clear how they are associated to the rather weak bar, which in addition becomes harder to distinguish due to projection effects.

NGC 6902 is again an interesting case. As discussed above, it is the weakest bar in TIMER and there are no clear kinematic signatures of the presence of a nuclear disc. Its weak bar also does not show in the kinematic maps. Tentatively, there is weak evidence for a box/peanut, since inside the ring of elevated values of h_4 mentioned above one sees dips to values close to zero along the bar major axis.

Finally, NGC 4643 shows a curious behaviour. Along the bar major axis outwards, h_4 drops to a minimum after the central region of elevated values, further out rises again reaching values close to zero, and then drops again to very low values towards the end of the bar. This behaviour would be produced if the galaxy has an inner bar with its own box/peanut (as does NGC 1291) plus the box/peanut of the primary bar. However, this cannot be the case here as the inner bar should be within the nuclear disc radius, but the first pair of h_4 minima is outside that radius. In addition, the two pairs of h_4 minima are very well aligned, suggesting that the properties they indicate concern only the (main) bar. To understand the presence of two pairs of h_4 minima in NGC 4643 is beyond the scope of this paper.

A.2 Statistical Analysis of Trends between the Kinematic Radii of Nuclear Discs and Bar Properties

In order to better understand the statistical significance of the relations presented in Fig. 3.8 and discussed in Sect. 3.5, we present in Table A.1 the values of the slope and correlation coefficient as determined through different methods for each relation. We employed the SIXLIN IDL implementation of the formulae provided by Isobe et al. (1990) to calculate the slopes through ordinary least squares regression (OLS) and orthogonal regression (OR). OLS can be calculated with the Y variable (in this case, r_k) as the dependent variable ($Y|X$) or as the independent variable ($X|Y$). The slope of the bisector of the region between the two OLS lines is also shown.

Isobe et al. (1990) discussed how, by definition, $OLS(Y|X)$ and $OLS(X|Y)$ can often lead to different results, why the former is typically preferred over the latter, and why OR should only be used with scale-free variables. The authors then recommend that the OLS bisector estimate is to be preferred, in particular when the goal is to probe the underlying relation between two variables.

Table A.1 also shows the slopes derived using the reweighted least squares regression (RLS) of Rousseeuw (1984), which is particularly robust against contamination from outliers. We used the code `PROGRESS` (Rousseeuw & Leroy 1987) to calculate the RLS slopes, as well as three correlation coefficients also shown in Table A.1: the Pearson correlation coefficient, the Spearman rank correlation coefficient and the RLS correlation coefficient.

One sees that the correlation between r_k and R_{bar} is strong: The RLS correlation coefficient is particularly strong and the slope derived via the different methods is relatively stable (within the expected differences). The $r_k \times A_2$ relation also sees a significant increase in the Spearman and RLS correlation coefficients, as compared to the Pearson coefficient. However, the three correlation coefficients are similar for the relations between r_k and ϵ_{bar} and Bar/T . The relatively large variation between the slopes derived with $OLS(Y|X)$ and the OLS bisector indicates that the correlations between r_k and A_2 , ϵ_{bar} and Bar/T are only moderately significant. As already mentioned in Sect. 3.5, there is no significant correlation between r_k and Q_B , and this is shown again by the results in Table A.1.

We stress again that further work is necessary to fully probe and understand these relations, in particular with larger samples. While the correlation between r_k and R_{bar} is strong, and the trends between r_k and ϵ_{bar} , Bar/T and A_2 do not seem fortuitous, these are not proofs that nuclear discs are built by bars. However, these relations are consistent with that picture, and there is currently no obvious reason to think that a scenario in which bars are irrelevant to the formation of nuclear discs would produce such relations.

Relation	OLS($Y X$) slope	OLS($X Y$) slope	OR slope	OLS bi slope	RLS slope	Pearson CC	Spearman CC	RLS CC
$r_k \times R_{bar}$	0.065±0.018	0.119±0.020	0.065±0.018	0.092±0.017	0.051±0.009	0.74	0.77	0.91
$r_k \times \epsilon_{bar}$	-1.170±0.472	-4.027±1.423	-3.461±1.318	-1.943±0.495	-1.170±0.578	-0.54	-0.59	-0.54
$r_k \times Bar/T$	1.339±0.792	5.451±2.116	4.908±1.776	2.292±0.760	1.339±0.742	0.50	0.56	0.50
$r_k \times Q_B$	-0.262±0.412	-11.887±18.039	-8.187±12.157	-1.189±0.320	-0.135±0.378	-0.15	-0.11	-0.09
$r_k \times A_2$	0.360±0.169	2.826±1.764	1.023±0.676	1.005±0.148	0.392±0.149	0.36	0.44	0.57

Table A.1: Slope (with standard deviation) and correlation coefficient corresponding to the relations shown in Fig. 3.8, as determined through various statistical methods as indicated (see main text for details).

Stellar Populations of Nuclear Discs

B

B.1 Descriptions of Individual Galaxies

IC 1438: This is a typical example of a barred galaxy with a nuclear disc. The bar is fully included in the field of view and characterised by high $[M/H]$ and low $[\alpha/Fe]$ abundances. The nuclear disc shows even higher metallicities and lower $[\alpha/Fe]$ enhancements, as compared to the bar. A young nuclear disc is clearly visible and surrounded by a region of older stellar populations.

NGC 613: The nuclear ring of this galaxy appears rather asymmetric, in particular in north-eastern part of the ring where a region of old stellar populations is detected. However, this detection of old stellar populations is probably not real: a visual inspection of the spectra show a broad emission-line component that is not included in the emission-line modelling performed here. According to high $H\alpha$ emission-line fluxes, the ring is starbursting and we detect low metallicities and high $[\alpha/Fe]$ abundances in the ring.

NGC 1097: A poster-child example of a galaxy with a starbursting nuclear ring. Interestingly, the nuclear ring shows a significant width, especially in age, an exceptionally low metallicity, and elevated $[\alpha/Fe]$ abundances. Since this galaxy is currently undergoing an interaction (see e.g. Ondrechen et al. 1989; Prieto et al. 2019), we speculate that this interaction could serve as the origin of the low-metallicity gas. Within the starbursting nuclear ring, a nuclear disc with its typical gradients is evident. See Sect. 4.6.5 for a detailed discussion of this galaxy.

NGC 1291: This quiescent galaxy highlights a very prominent inner bar that almost fills the field of view. While the main bar is almost not visible, the inner bar appears clearly distinguished by its increased metallicity and low $[\alpha/Fe]$ enhancement. Interestingly, the ends of the inner bar show slightly younger stellar populations as it is also seen in main bars (Neumann et al. 2020). The inner bar of this galaxy is discussed in greater detail in Méndez-Abreu et al. (2019), de Lorenzo-Cáceres et al. (2019b) and a forthcoming paper.

NGC 1300: This galaxy exhibits a typical nuclear disc with young ages, elevated metallicities, and low $[\alpha/Fe]$ abundances. We highlight the excellent agreement between the kinematic radius of the nuclear disc and the minimum of the age profile.

NGC 1365: The analysis of this galaxy is hampered by various effects: strong dust extinction is found along a spiral-like pattern, several regions of violent ongoing star formation are evident, and a significant, large-scale contribution from an AGN is found, especially towards the south-east (see e.g. Venturi et al. 2018). In contrast to the other galaxies in the sample, the nuclear ring or nuclear disc is hard to distinguish.

NGC 1433: A noteworthy example of a young and metal-rich nuclear disc with low $[\alpha/\text{Fe}]$ abundances. In contrast to previously shown stellar population maps of this galaxy (see Bittner et al. 2019), the maps shown here highlight a strongly elongated feature of increased $[\text{M}/\text{H}]$ and low $[\alpha/\text{Fe}]$, thanks to the higher signal-to-noise ratio employed in this paper. In fact, it has been proposed that this galaxy has an inner bar (Erwin 2004; Buta et al. 2015) and we will discuss this issue further in a forthcoming paper. We highlight the excellent agreement between the kinematic radius and changes in the stellar population profiles in this galaxy.

NGC 3351: Similarly to NGC 1097, this galaxy hosts a starbursting nuclear ring with very low metallicities and increased $[\alpha/\text{Fe}]$ enhancements. Intense stellar feedback originates from this starbursting ring (see Leaman et al. 2019). Interestingly, this galaxy is member of a group (see e.g. Garcia 1993) that might facilitate the accretion of low-metallicity gas. Encompassed within the nuclear ring, a nuclear disc consisting of comparably young and metal rich stellar populations with low $[\alpha/\text{Fe}]$ enhancements is evident.

NGC 4303: In this galaxy, almost the entire bar is included in the field of view and characterised by high metallicities and low $[\alpha/\text{Fe}]$ enhancements. In addition, a typical young nuclear disc with a star-forming nuclear ring, encompassed by a region of old stars, is found. The population gradients generally follow the typical well-defined profiles, except in the very centre of the galaxy where a clear break in these profiles is found which could result from effects of the AGN in the spectral analysis, or indicate the presence of an additional stellar component.

NGC 4371: This galaxy has a nuclear disc with the typical stellar population properties: young ages, low $[\alpha/\text{Fe}]$ enhancement and high metallicity. However, it is peculiar in the sense that interior to that region, older ages and variations in metallicity and $[\alpha/\text{Fe}]$ abundances are found. These may be produced by projection effects, since the inclination is ~ 59 deg and the line of nodes is almost perpendicular to the bar. Alternatively, it may be produced by additional stellar components (see Erwin et al. 2015). For a detailed discussion of this galaxy, we refer to Gadotti et al. (2015).

NGC 4643: Another typical example of a nuclear disc: a young, metal-rich nuclear disc with low $[\alpha/\text{Fe}]$ enhancement is embedded in a region of older stellar populations. The bar of the galaxy is oriented from the south-east to north-west and prominently highlighted by its relatively young ages, high metallicities, and low $[\alpha/\text{Fe}]$ abundances. Interestingly, these trends along the bar seem to become stronger with increasing radius. While $\text{H}\alpha$ emission is barely detected, it is arranged in a small, two-armed spiral structure.

NGC 4981: After applying the spatial binning, this is the galaxy with the lowest spatial resolution of the present TIMER sample. In this galaxy it is difficult to distinguish the nuclear structures but, nonetheless, the highest metallicities and lowest $[\alpha/\text{Fe}]$ enhancements are observed in the centre of the galaxy.

- NGC 4984:** This galaxy hosts a typical nuclear disc, showing radial population gradients that appear similar but less well-defined than in other galaxies, most likely due to an inclination effect. The populations found in the very central bins deviate strongly from these profiles. In particular, old ages, low metallicities, and high $[\alpha/\text{Fe}]$ abundances are detected. We speculate that these deviations might be from effects on the spectral analysis caused by the AGN in this galaxy.
- NGC 5236:** This galaxy shows a highly irregular nuclear structure. Star formation, as traced by the $\text{H}\alpha$ emission, is irregularly distributed in the central region, not forming a nuclear ring or nuclear disc. It is also heavily obscured by dust. As a result, also the stellar population maps and gradients do not show regular features.
- NGC 5248:** This galaxy has a typical nuclear disc. While the radial population gradients are well-defined, a slight deviation is evident in the central bins which, again, can be an AGN effect. In the region of the nuclear ring a few small, star-forming spots are found, showing significantly lower ages and metallicities and increased $[\alpha/\text{Fe}]$ abundances. Interestingly, the $\text{H}\alpha$ emission is not restricted to the nuclear ring but appears rather smoothly distributed over the entire nuclear disc.
- NGC 5728:** While this galaxy seems to host a common nuclear disc, the observed stellar population properties are severely contaminated by an AGN jet. This jet is strikingly visible in the maps as an elongated feature of old ages and low metallicities crossing the nuclear disc from north-west to south-east and extending into an even larger cone outside of the nuclear region (see e.g. Durré & Mould 2018).
- NGC 5850:** A prominent example of a galaxy hosting an inner bar. The inner bar is clearly visible by its elevated $[\text{M}/\text{H}]$ and low $[\alpha/\text{Fe}]$ enhancements, and shows regions with young stellar populations at its ends. We refer the reader to de Lorenzo-Cáceres et al. (2019b) for a detailed discussion of the double-barred structure of this galaxy. The nuclear disc shows the typical aforementioned properties.
- NGC 6902:** The galaxy NGC 6902 is a peculiar object. Combining the results from this study and G20, it is unclear whether the galaxy hosts a nuclear disc. A weak bar with slightly elevated metallicities and low $[\alpha/\text{Fe}]$ abundances is found, encompassed by a star-forming inner ring at the bar radius. Within this inner ring, spatially coinciding with the bar, a kinematically hot spheroid is detected. Due to these peculiarities, this galaxy is not considered in any of the discussions in this paper.
- NGC 7140:** This galaxy hosts a rather typical nuclear disc, which appearance is slightly contaminated by a singular star-forming spot in the nuclear ring. The moderate $\text{H}\alpha$ emission in the nuclear region is rather smoothly distributed over the nuclear disc, but it nonetheless shows some concentration in a nuclear ring.
- NGC 7552:** A heavily starbursting nuclear ring is evident in the galaxy. This is not only highlighted in the $\text{H}\alpha$ emission-line maps, but also clearly visible in the radial population profiles as extrema of low metallicities and high $[\alpha/\text{Fe}]$ enhancements. Within the nuclear ring, a typical nuclear disc is seen with young ages, elevated metallicities, and low $[\alpha/\text{Fe}]$ enhancements. However, contrary to most nuclear discs, this nuclear disc shows a flat age profile.

NGC 7755: This galaxy hosts a typical nuclear disc with a ring of H α emission at its outermost edge, embedded in a region of older stellar populations. It further highlights the typical population properties found in bars. In particular, the bar is visible by its high metallicities and low $[\alpha/\text{Fe}]$ abundances. The reader is referred to Neumann et al. (2020) for further details on the bar properties.

B.2 Maps of Dust-corrected H α Fluxes

In Fig. B.1 we present maps of dust-corrected H α fluxes for all TIMER galaxies. We note that similar versions of the maps of IC 1438, NGC 4304, NGC 4371, NGC 4643, NGC 4981, NGC 4984, NGC 5248, NGC 6902, and NGC 7755 have already been presented in Neumann et al. (2020), but in order to facilitate the comparison with the maps of the stellar population properties we present these here again. We only display spaxels in which the amplitude-over-noise ratio of the H α line exceeds 5. Fluxes are given in units of $10^{-12} \text{ erg s}^{-1} \text{ cm}^{-2} \text{ arcsec}^{-2}$ and the respective limits of the colour bar are stated in the lower-right corner of each panel. Based on reconstructed intensities from the MUSE cube, we display isophotes in steps of 0.5 mag, identical to the ones displayed in the maps of the stellar population properties.

B.3 Maps and Radial Profiles of Stellar Population Properties

In the left columns of Figs. B.2, B.3, and B.4 we present maps of the light-weighted (upper panels) and mass-weighted (lower panels) mean stellar population properties of the non-star-forming and star-forming subsamples, as well as those with peculiar nuclear regions. All maps have been generated with pPXF and include the modelling of $[\alpha/\text{Fe}]$ enhancements. The figures display age, metallicity, and $[\alpha/\text{Fe}]$ abundances in the left-hand, central, and right-hand panels, respectively, while different galaxies are separated by horizontal lines. The limits of the colour bar are stated in the lower-right corner of each panel. Based on reconstructed intensities from the MUSE cube, we display isophotes in steps of 0.5 mag. North is up; east is to the left.

In the right-hand side of the figures we plot light-weighted stellar ages (first panels), metallicities (second panels), $[\alpha/\text{Fe}]$ enhancements (third panels), and velocity dispersions (fourth panels) as a function of the galactocentric radius of all spatial bins in the field of view. The profiles have been deprojected using inclinations and position angles derived in S⁴G (Muñoz-Mateos et al. 2015), as presented in Table 4.1. The vertical dashed lines represent the kinematic radii of the nuclear discs, which was defined in G20 as the radius at which V/σ reaches its maximum in the region dominated by the nuclear disc.

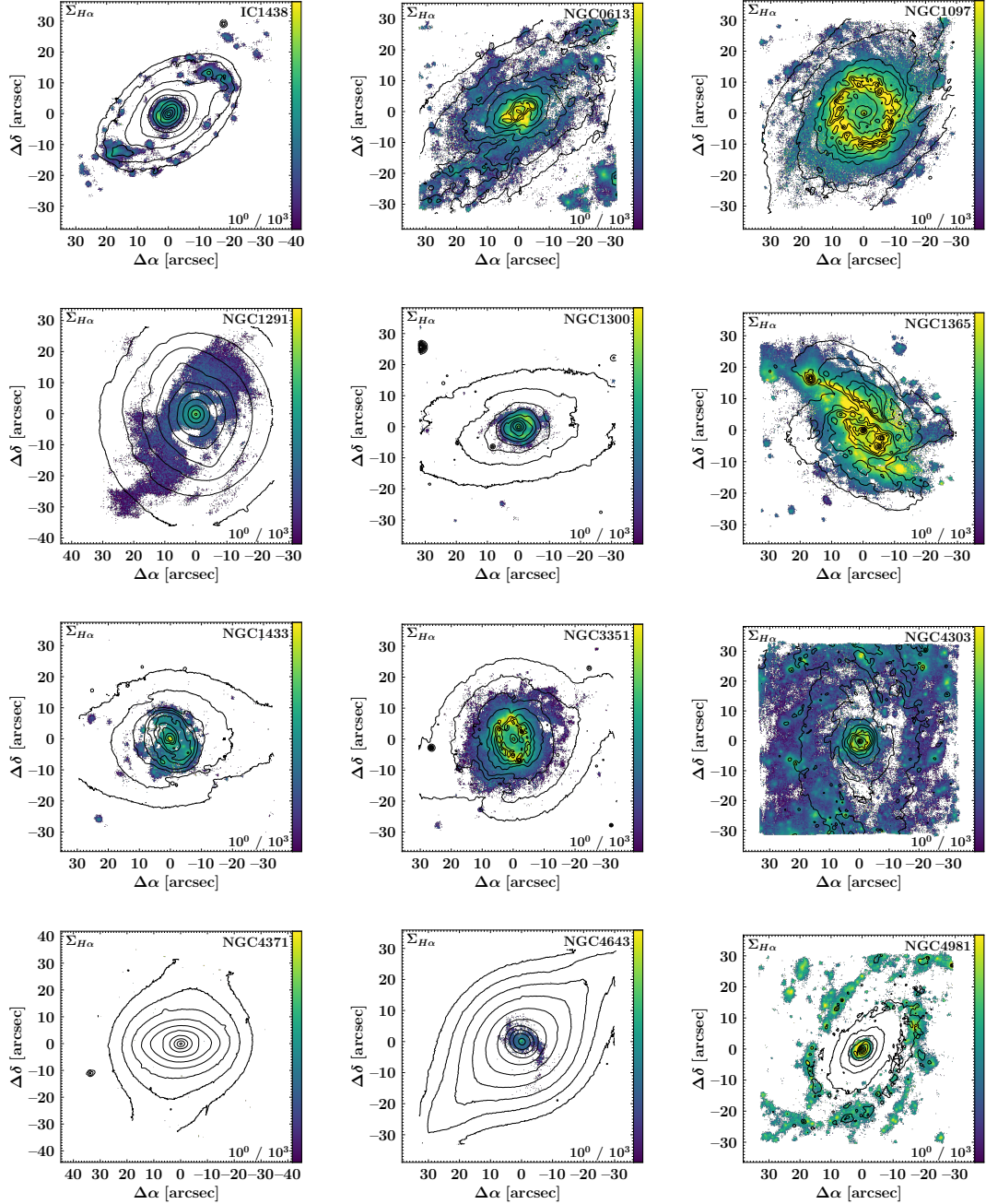


Figure B.1: Maps of dust-corrected $H\alpha$ fluxes for all TIMER galaxies. We note that only spaxels with an $H\alpha$ amplitude-over-noise ratio above 5 are displayed. Fluxes are given in units of $10^{-12} \text{ erg s}^{-1} \text{ cm}^{-2} \text{ arcsec}^{-2}$ and the respective limits of the colour bar are stated in the lower-right corner of each panel. Based on reconstructed intensities from the MUSE cube, we display isophotes in steps of 0.5 mag, identical to the ones displayed in the maps of the stellar population properties. North is up; east is to the left.

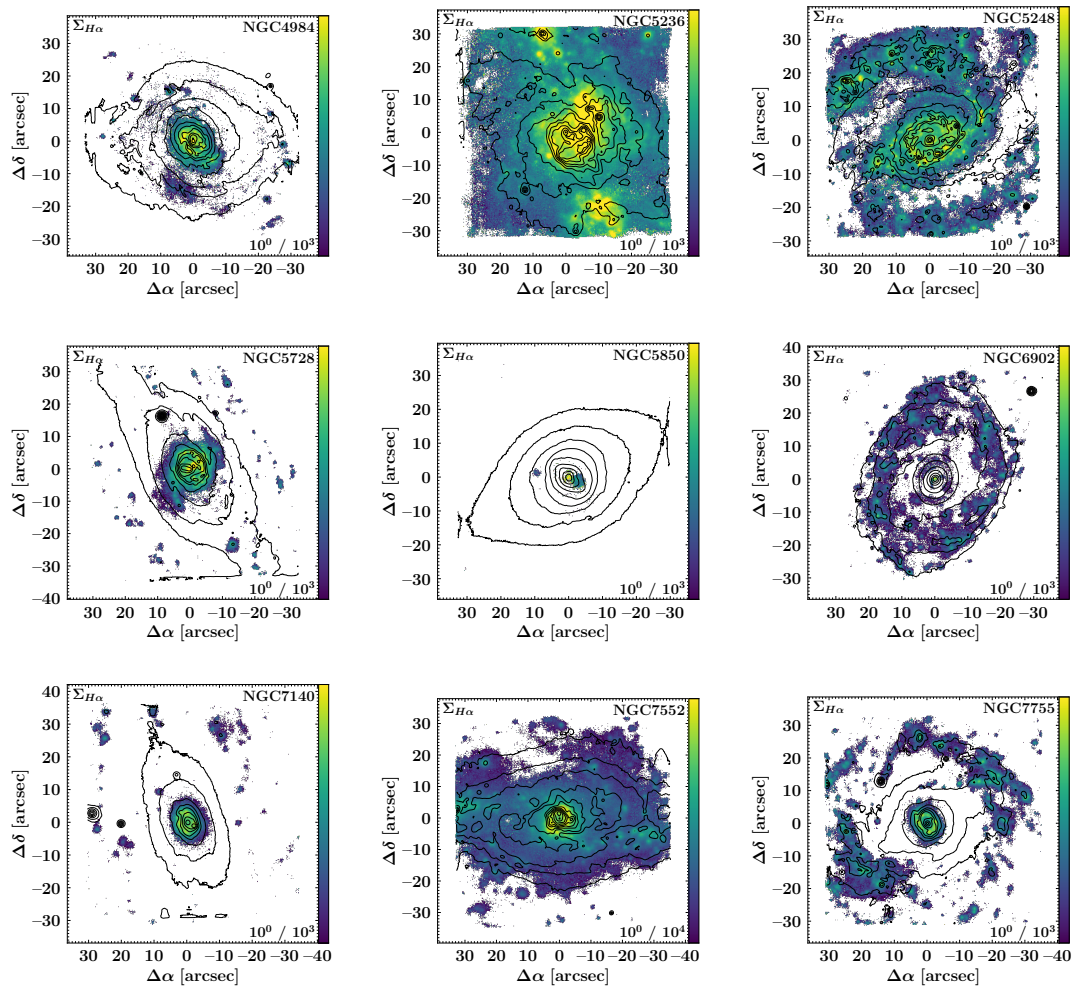


Figure B.1: Continued.

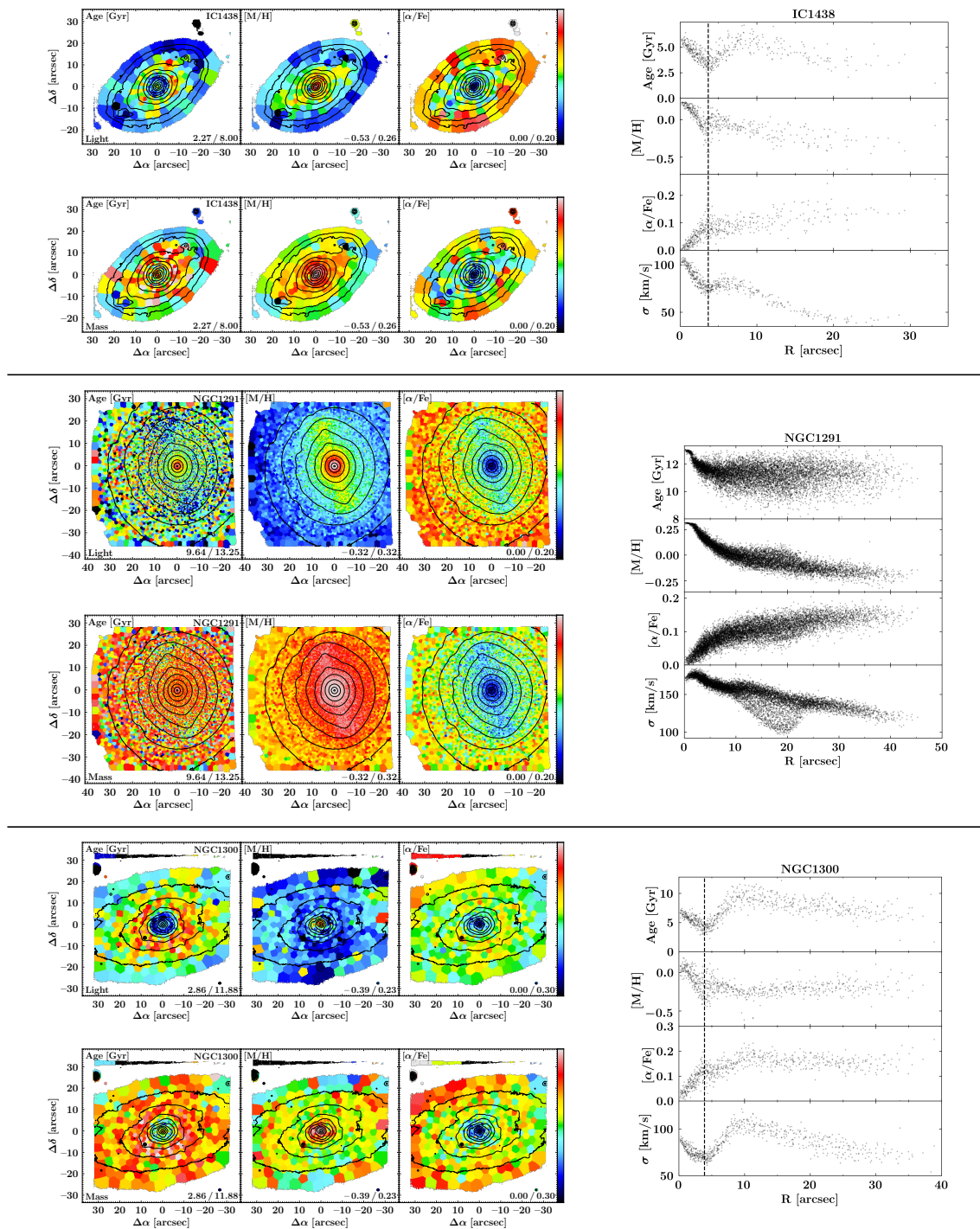


Figure B.2: *Left:* Maps of light-weighted (upper panels) and mass-weighted (lower panels) mean stellar population properties of the subsample without significant star formation in the nuclear ring. All maps have been generated with pPXF and include the modelling of $[\alpha/\text{Fe}]$ enhancements. The figures display age, $[\text{M}/\text{H}]$, and $[\alpha/\text{Fe}]$ enhancements in the left-hand, centre, and right-hand panels, respectively, while different galaxies are separated by horizontal lines. The limits of the colour bar are stated in the lower-right corner of each panel. Based on reconstructed intensities from the MUSE cube, we display isophotes in steps of 0.5 mag. North is up; east is to the left. *Right:* Radial profiles of light-weighted stellar ages (first panels), metallicities (second panels), $[\alpha/\text{Fe}]$ enhancements (third panels), and velocity dispersions (fourth panels) as a function of the galactocentric radius of all spatial bins in the field of view. The profiles have been deprojected using inclinations and position angles derived in S⁴G (Muñoz-Mateos et al. 2015), as presented in Table 4.1. The vertical dashed lines represent the kinematic radii of the nuclear discs, which was defined in G20 as the radius at which V/σ reaches its maximum in the region dominated by the nuclear disc. We note that for NGC 1291 no kinematic radius could be determined, as this galaxy is oriented almost perfectly face-on.

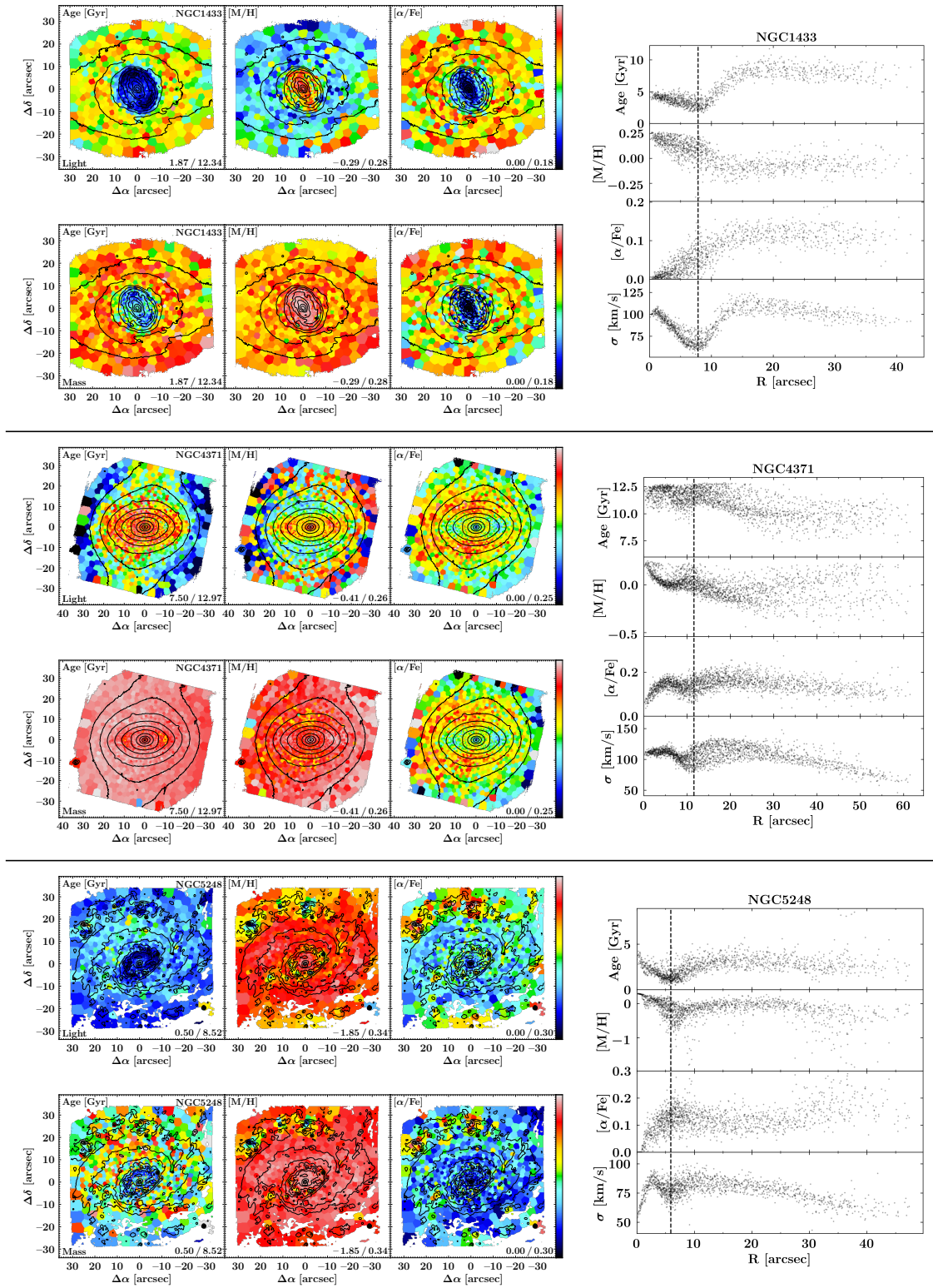


Figure B.2: Continued.

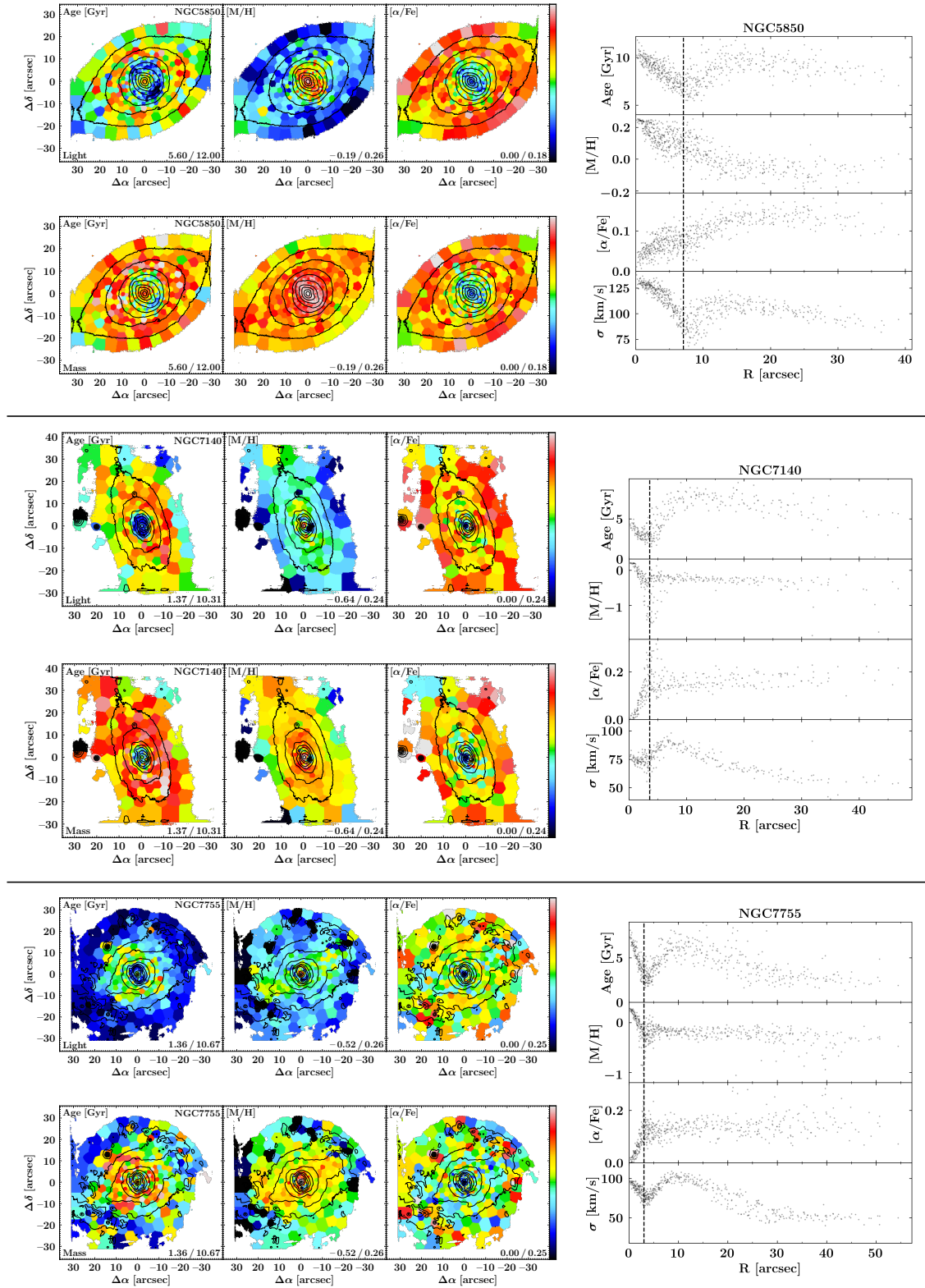


Figure B.2: Continued.

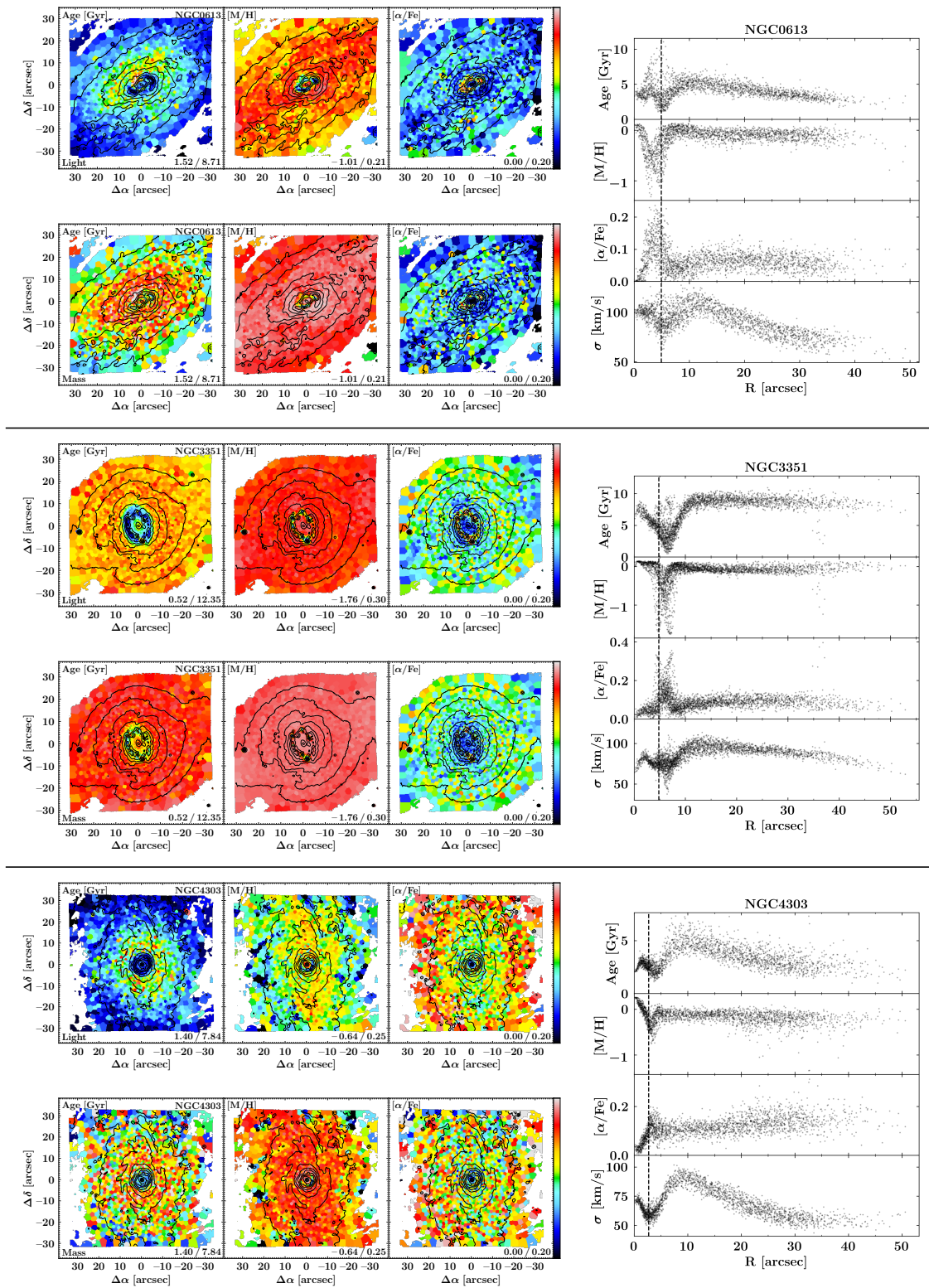


Figure B.3: Same as Fig. B.2, but for the subsample with significant star formation in the nuclear ring.

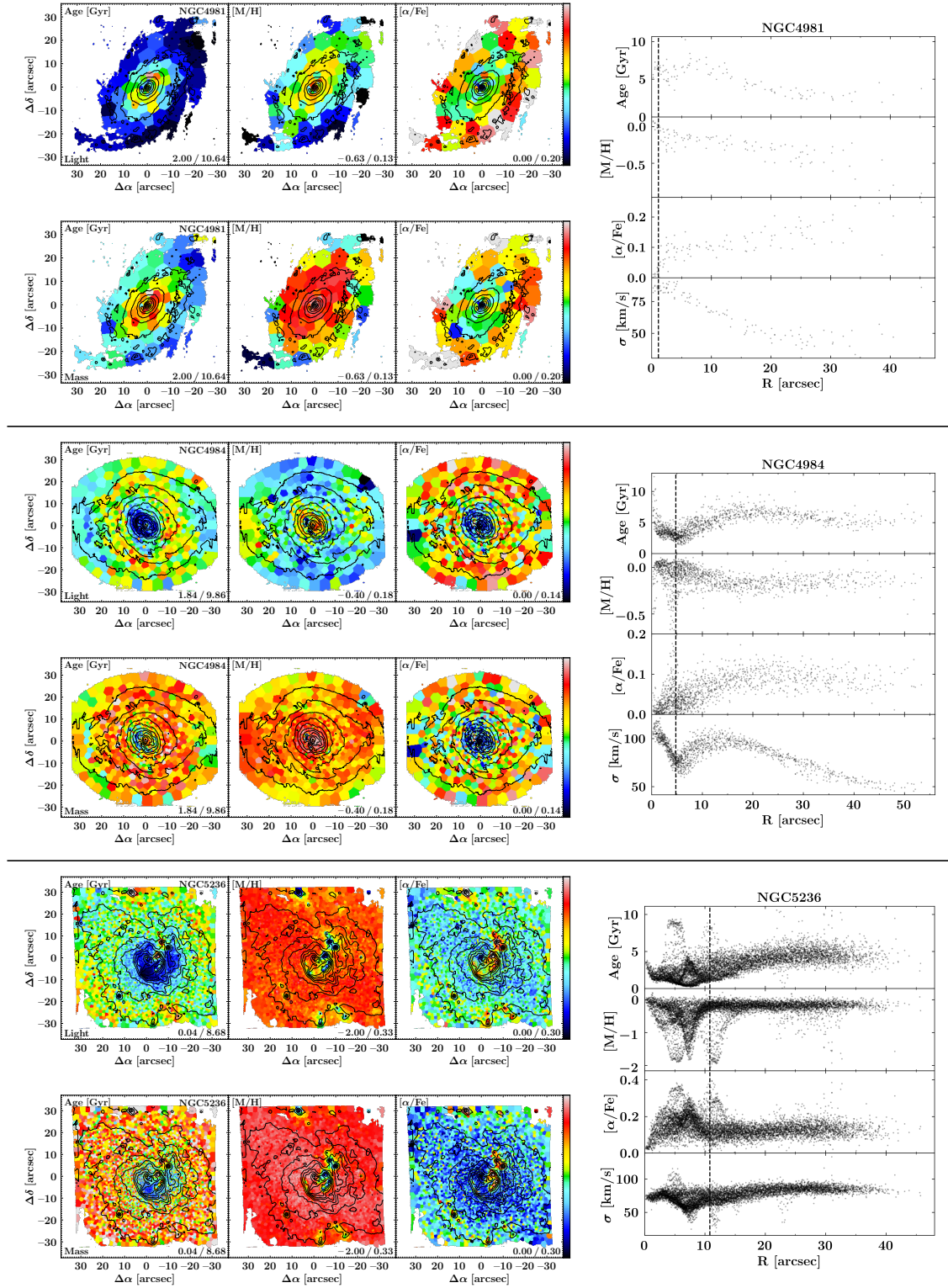


Figure B.3: Continued.

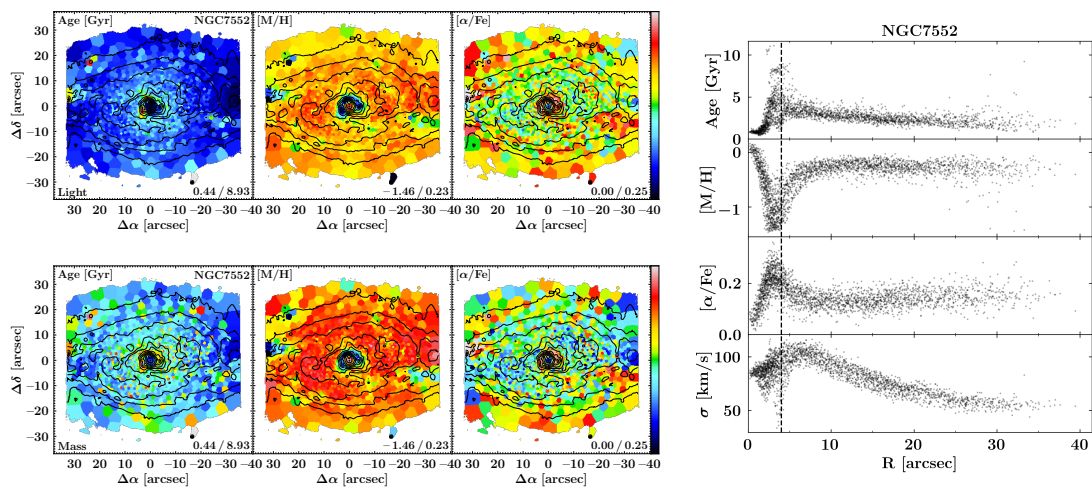


Figure B.3: Continued.

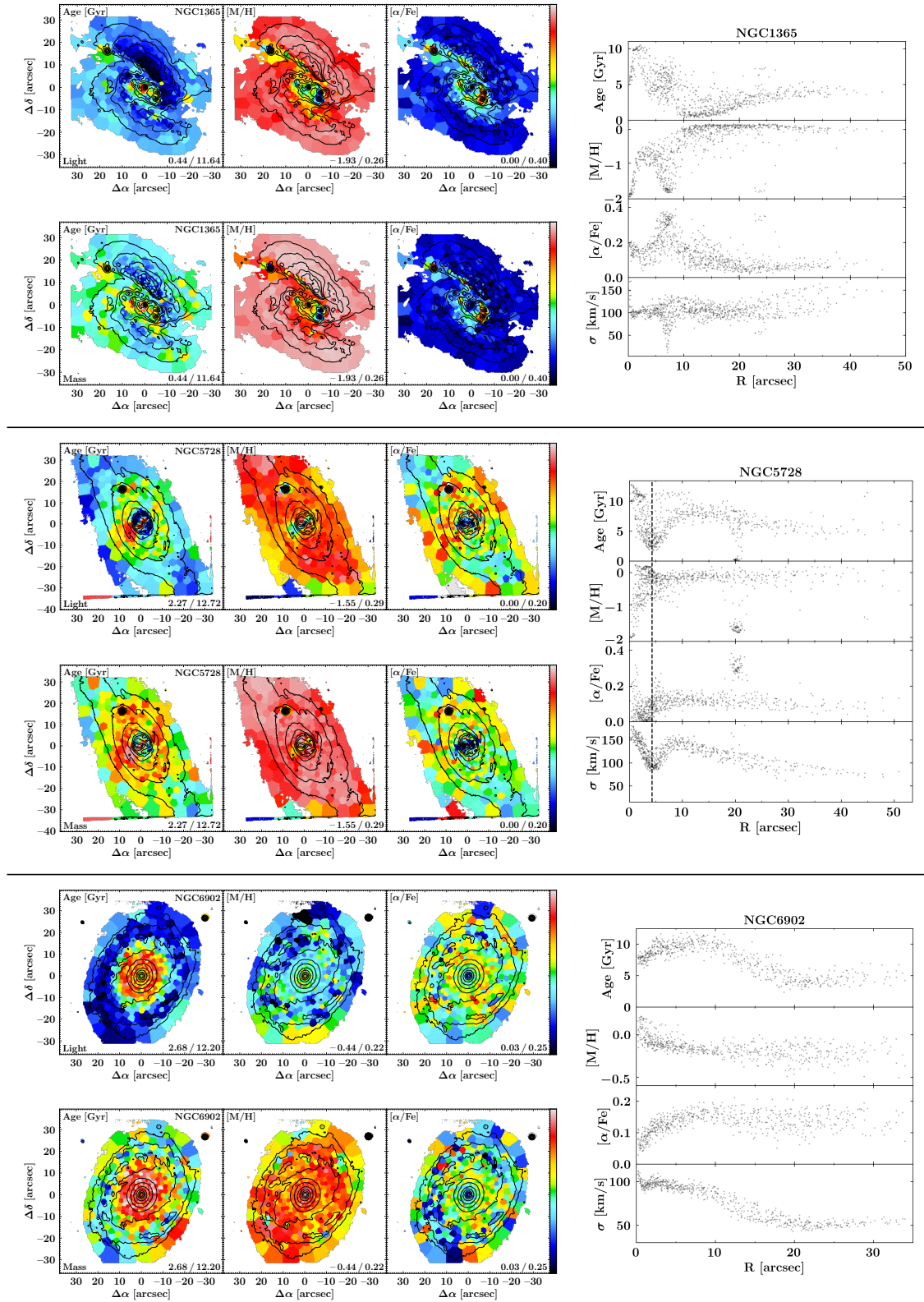


Figure B.4: Same as Fig. B.2, but for the subsample with peculiar nuclear regions. Due to the strong dust extinction, violent star formation, and significant contribution from an AGN, no kinematic radius is measured for NGC 1365. We note that no kinematic radius is provided for NGC 6902, as there are no clear kinematic signatures of a nuclear disc in this galaxy.

Appendix

Bibliography

- Aguerri, J. A. L. 2012, *Advances in Astronomy*, 2012, 382674
- Aguerri, J. A. L., Méndez-Abreu, J., & Corsini, E. M. 2009, *A&A*, 495, 491
- Allard, E. L., Knapen, J. H., Peletier, R. F., & Sarzi, M. 2006, *MNRAS*, 371, 1087
- Alonso, S., Coldwell, G., Duplancic, F., Mesa, V., & Lambas, D. G. 2018, *A&A*, 618, A149
- Alonso-Herrero, A. & Knapen, J. H. 2001, *AJ*, 122, 1350
- Alpher, R. A. & Herman, R. 1948, *Nature*, 162, 774
- Anscombe, F. J. & Glynn, W. J. 1983, *Biometrika*, 70, 227
- Athanassoula, E. 1992a, *MNRAS*, 259, 328
- Athanassoula, E. 1992b, *MNRAS*, 259, 345
- Athanassoula, E. 2002, *ApJ*, 569, L83
- Athanassoula, E. 2003, *MNRAS*, 341, 1179
- Athanassoula, E. 2005, *MNRAS*, 358, 1477
- Athanassoula, E. 2013, Bars and secular evolution in disk galaxies: Theoretical input, 305
- Athanassoula, E. & Beaton, R. L. 2006, *MNRAS*, 370, 1499
- Athanassoula, E., Bienayme, O., Martinet, L., & Pfenniger, D. 1983, *A&A*, 127, 349
- Athanassoula, E., Lambert, J. C., & Dehnen, W. 2005, *MNRAS*, 363, 496
- Athanassoula, E., Laurikainen, E., Salo, H., & Bosma, A. 2015, *MNRAS*, 454, 3843
- Athanassoula, E., Machado, R. E. G., & Rodionov, S. A. 2013, *MNRAS*, 429, 1949
- Athanassoula, E. & Misiriotis, A. 2002, *MNRAS*, 330, 35
- Athanassoula, E., Rodionov, S. A., & Prantzos, N. 2017, *MNRAS*, 467, L46
- Athanassoula, E. & Sellwood, J. A. 1986, *MNRAS*, 221, 213
- Bacon, R., Accardo, M., Adjali, L., et al. 2010, in *Society of Photo-Optical Instrumentation Engineers (SPIE) Conference Series*, Vol. 7735, Proc. SPIE, 773508
- Bacon, R., Adam, G., Baranne, A., et al. 1995, *Astronomy and Astrophysics Supplement Series*, 113, 347
- Bacon, R., Conseil, S., Mary, D., et al. 2017, *A&A*, 608, A1
- Bacon, R., Copin, Y., Monnet, G., et al. 2001, *MNRAS*, 326, 23
- Bagnasco, G., Kolm, M., Ferruit, P., et al. 2007, in *Society of Photo-Optical Instrumentation Engineers (SPIE) Conference Series*, Vol. 6692, *Cryogenic Optical Systems and Instruments XII*, ed. J. B. Heaney & L. G. Burriesci, 66920M
- Baldwin, J. A., Phillips, M. M., & Terlevich, R. 1981, *PASP*, 93, 5
- Barazza, F. D., Jogee, S., & Marinova, I. 2008, *ApJ*, 675, 1194
- Barnes, J. E. 1988, *ApJ*, 331, 699

- Beaton, R. L., Majewski, S. R., Guhathakurta, P., et al. 2007, *ApJ*, 658, L91
- Bender, R. 1990, *A&A*, 229, 441
- Bender, R., Saglia, R. P., & Gerhard, O. E. 1994, *MNRAS*, 269, 785
- Bennett, C. L., Halpern, M., Hinshaw, G., et al. 2003, *ApJS*, 148, 1
- Berentzen, I., Athanassoula, E., Heller, C. H., & Fricke, K. J. 2003, *MNRAS*, 341, 343
- Berentzen, I., Athanassoula, E., Heller, C. H., & Fricke, K. J. 2004, *MNRAS*, 347, 220
- Berentzen, I., Shlosman, I., Martinez-Valpuesta, I., & Heller, C. H. 2007, *ApJ*, 666, 189
- Berrier, J. C. & Sellwood, J. A. 2016, *ApJ*, 831, 65
- Binney, J. 2005, *MNRAS*, 363, 937
- Binney, J., Gerhard, O. E., Stark, A. A., Bally, J., & Uchida, K. I. 1991, *MNRAS*, 252, 210
- Binney, J. & Tremaine, S. 1987, *Galactic dynamics* (Princeton University Press)
- Bittner, A., Falcón-Barroso, J., Nedelchev, B., et al. 2019, *A&A*, 628, A117
- Bittner, A., Gadotti, D. A., Elmegreen, B. G., et al. 2017, *MNRAS*, 471, 1070
- Bittner, A., Sánchez-Blázquez, P., Gadotti, D. A., et al. 2020, *A&A*, 643, A65
- Bland-Hawthorn, J. & Gerhard, O. 2016, *ARA&A*, 54, 529
- Bosma, A. 1978, PhD thesis, -
- Bosma, A. 1981, *AJ*, 86, 1825
- Bosma, A., Gadotti, D. A., de Blok, W. J. G., & Athanassoula, E. 2010, in *Astronomical Society of the Pacific Conference Series*, Vol. 421, *Galaxies in Isolation: Exploring Nature Versus Nurture*, ed. L. Verdes-Montenegro, A. Del Olmo, & J. Sulentic, 53
- Bosma, A. & van der Kruit, P. C. 1979, *A&A*, 79, 281
- Bournaud, F. 2016, *Bulge Growth Through Disc Instabilities in High-Redshift Galaxies*, Vol. 418 (Springer International Publishing Switzerland), 355
- Bournaud, F., Combes, F., & Semelin, B. 2005a, *MNRAS*, 364, L18
- Bournaud, F., Jog, C. J., & Combes, F. 2005b, *A&A*, 437, 69
- Breda, I., Papaderos, P., Gomes, J. M., et al. 2020, *A&A*, 635, A177
- Brook, C. B., Governato, F., Roškar, R., et al. 2011, *MNRAS*, 415, 1051
- Brook, C. B., Stinson, G., Gibson, B. K., et al. 2012, *MNRAS*, 419, 771
- Brooks, A. & Christensen, C. 2016, *Bulge Formation via Mergers in Cosmological Simulations*, Vol. 418 (Springer International Publishing Switzerland), 317
- Bryant, J. J., Owers, M. S., Robotham, A. S. G., et al. 2015, *MNRAS*, 447, 2857
- Bullock, J. S. & Boylan-Kolchin, M. 2017, *ARA&A*, 55, 343
- Bundy, K., Bershady, M. A., Law, D. R., et al. 2015, *ApJ*, 798, 7
- Bureau, M., Aronica, G., Athanassoula, E., et al. 2006, *MNRAS*, 370, 753
- Bureau, M. & Athanassoula, E. 2005, *ApJ*, 626, 159
- Bureau, M. & Freeman, K. C. 1999, *AJ*, 118, 126
- Burstein, D., Faber, S. M., Gaskell, C. M., & Krumm, N. 1984, *ApJ*, 287, 586
- Buta, R. 1986a, *ApJS*, 61, 609
- Buta, R. 1986b, *ApJS*, 61, 631
- Buta, R. & Combes, F. 1996, *Fund. Cosmic Phys.*, 17, 95

- Buta, R. J. 2017, MNRAS, 470, 3819
- Buta, R. J., Sheth, K., Athanassoula, E., et al. 2015, ApJS, 217, 32
- Calzetti, D., Armus, L., Bohlin, R. C., et al. 2000, ApJ, 533, 682
- Cappellari, M. 2017, MNRAS, 466, 798
- Cappellari, M. & Copin, Y. 2003, MNRAS, 342, 345
- Cappellari, M. & Emsellem, E. 2004, PASP, 116, 138
- Cappellari, M., Emsellem, E., Bacon, R., et al. 2007, MNRAS, 379, 418
- Cappellari, M., Emsellem, E., Krajnović, D., et al. 2011a, MNRAS, 413, 813
- Cappellari, M., Emsellem, E., Krajnović, D., et al. 2011b, MNRAS, 416, 1680
- Cervantes, J. L. & Vazdekis, A. 2009, MNRAS, 392, 691
- Chapon, D., Mayer, L., & Teyssier, R. 2013, MNRAS, 429, 3114
- Cheng, J. Y., Rockosi, C. M., Morrison, H. L., et al. 2012, ApJ, 752, 51
- Cheung, E., Trump, J. R., Athanassoula, E., et al. 2015, MNRAS, 447, 506
- Chung, A. & Bureau, M. 2004, AJ, 127, 3192
- Cid Fernandes, R., Mateus, A., Sodré, L., Stasińska, G., & Gomes, J. M. 2005, MNRAS, 358, 363
- Cisternas, M., Gadotti, D. A., Knapen, J. H., et al. 2013, ApJ, 776, 50
- Coccatto, L., Fabricius, M. H., Saglia, R. P., et al. 2018, MNRAS, 477, 1958
- Coccatto, L., Iodice, E., & Arnaboldi, M. 2014, A&A, 569, A83
- Coccatto, L., Morelli, L., Corsini, E. M., et al. 2011, MNRAS, 412, L113
- Coelho, P. & Gadotti, D. A. 2011, ApJ, 743, L13
- Cole, D. R., Debattista, V. P., Erwin, P., Earp, S. W. F., & Roškar, R. 2014, MNRAS, 445, 3352
- Cole, S., Lacey, C. G., Baugh, C. M., & Frenk, C. S. 2000, MNRAS, 319, 168
- Combes, F., Debbasch, F., Friedli, D., & Pfenniger, D. 1990, A&A, 233, 82
- Combes, F. & Gerin, M. 1985, A&A, 150, 327
- Combes, F. & Sanders, R. H. 1981, A&A, 96, 164
- Comerón, S., Elmegreen, B. G., Salo, H., et al. 2012, ApJ, 759, 98
- Comerón, S., Knapen, J. H., Beckman, J. E., et al. 2010, MNRAS, 402, 2462
- Comerón, S., Salo, H., Laurikainen, E., et al. 2014, A&A, 562, A121
- Contopoulos, G. 1980, A&A, 81, 198
- Contopoulos, G. & Grosbol, P. 1989, A&A Rev., 1, 261
- Contopoulos, G. & Papayannopoulos, T. 1980, A&A, 92, 33
- Costantin, L., Corsini, E. M., Méndez-Abreu, J., et al. 2018a, MNRAS, 481, 3623
- Costantin, L., Méndez-Abreu, J., Corsini, E. M., et al. 2018b, A&A, 609, A132
- Cowie, L. L., Songaila, A., Hu, E. M., & Cohen, J. G. 1996, AJ, 112, 839
- Croom, S. M., Lawrence, J. S., Bland-Hawthorn, J., et al. 2012, MNRAS, 421, 872
- D'Agostino, R. B., Belanger, A. J., & D'Agostino, Jr., R. B. 1990, American Statistician, 44, 316
- Dalton, G., Trager, S. C., Abrams, D. C., et al. 2012, in Society of Photo-Optical Instrumentation Engineers (SPIE) Conference Series, Vol. 8446, Ground-based and Airborne Instrumentation for Astronomy IV, 84460P
- Davies, R. I., Müller Sánchez, F., Genzel, R., et al. 2007, ApJ, 671, 1388

- Davies, R. L., Burstein, D., Dressler, A., et al. 1987, *ApJS*, 64, 581
- de Jong, R. S. 1996, *A&A*, 313, 377
- de Lorenzo-Cáceres, A., Falcón-Barroso, J., & Vazdekis, A. 2013, *MNRAS*, 431, 2397
- de Lorenzo-Cáceres, A., Falcón-Barroso, J., Vazdekis, A., & Martínez-Valpuesta, I. 2008, *ApJ*, 684, L83
- de Lorenzo-Cáceres, A., Méndez-Abreu, J., Thorne, B., & Costantin, L. 2019a, *MNRAS*, 484, 665
- de Lorenzo-Cáceres, A., Méndez-Abreu, J., Thorne, B., & Costantin, L. 2020, *MNRAS*, 494, 1826
- de Lorenzo-Cáceres, A., Sánchez-Blázquez, P., Méndez-Abreu, J., et al. 2019b, *MNRAS*, 484, 5296
- de Lorenzo-Cáceres, A., Vazdekis, A., Aguerri, J. A. L., Corsini, E. M., & Debattista, V. P. 2012, *MNRAS*, 420, 1092
- de Souza, R. E. & Dos Anjos, S. 1987, *A&AS*, 70, 465
- de Souza, R. E., Gadotti, D. A., & dos Anjos, S. 2004, *ApJS*, 153, 411
- de Vaucouleurs, G. 1948, *Annales d'Astrophysique*, 11, 247
- de Vaucouleurs, G. 1959, *Handbuch der Physik*, 53, 275
- de Vaucouleurs, G. 1974, in *IAU Symposium*, Vol. 58, *The Formation and Dynamics of Galaxies*, ed. J. R. Shakeshaft, 335
- de Vaucouleurs, G. 1975, *ApJS*, 29, 193
- de Zeeuw, P. T., Bureau, M., Emsellem, E., et al. 2002, *MNRAS*, 329, 513
- Debattista, V. P., Carollo, C. M., Mayer, L., & Moore, B. 2005, *ApJ*, 628, 678
- Debattista, V. P., Mayer, L., Carollo, C. M., et al. 2006, *ApJ*, 645, 209
- Debattista, V. P., Ness, M., Gonzalez, O. A., et al. 2017, *MNRAS*, 469, 1587
- Debattista, V. P. & Shen, J. 2007, *ApJ*, 654, L127
- Díaz-García, S., Moyano, F. D., Comerón, S., et al. 2020, *A&A*, 644, A38
- Díaz-García, S., Salo, H., Laurikainen, E., & Herrera-Endoqui, M. 2016, *A&A*, 587, A160
- Donohoe-Keys, C. E., Martig, M., James, P. A., & Kraljic, K. 2019, *MNRAS*, 489, 4992
- Dopita, M., Hart, J., McGregor, P., et al. 2007, *Ap&SS*, 310, 255
- Dopita, M., Rhee, J., Farage, C., et al. 2010, *Ap&SS*, 327, 245
- Du, M., Shen, J., & Debattista, V. P. 2015, *ApJ*, 804, 139
- Du, M., Shen, J., Debattista, V. P., & de Lorenzo-Cáceres, A. 2017, *ApJ*, 836, 181
- Dumas, G., Mundell, C. G., Emsellem, E., & Nagar, N. M. 2007, *MNRAS*, 379, 1249
- Durré, M. & Mould, J. 2018, *ApJ*, 867, 149
- Einasto, J., Kaasik, A., & Saar, E. 1974, *Nature*, 250, 309
- Eisenhauer, F., Abuter, R., Bickert, K., et al. 2003, in *Society of Photo-Optical Instrumentation Engineers (SPIE) Conference Series*, Vol. 4841, *Instrument Design and Performance for Optical/Infrared Ground-based Telescopes*, ed. M. Iye & A. F. M. Moorwood, 1548–1561
- Eliche-Moral, M. C., González-García, A. C., Balcells, M., et al. 2011, *A&A*, 533, A104
- Ellison, S. L., Nair, P., Patton, D. R., et al. 2011, *MNRAS*, 416, 2182
- Elmegreen, B. G., Bournaud, F., & Elmegreen, D. M. 2008, *ApJ*, 688, 67
- Elmegreen, B. G. & Elmegreen, D. M. 1985, *ApJ*, 288, 438
- Elmegreen, B. G. & Hunter, D. A. 2006, *ApJ*, 636, 712
- Elmegreen, B. G. & Parravano, A. 1994, *ApJ*, 435, L121

- Elmegreen, D. M., Elmegreen, B. G., & Bellin, A. D. 1990, *ApJ*, 364, 415
- Emsellem, E., Cappellari, M., Krajnović, D., et al. 2011, *MNRAS*, 414, 888
- Emsellem, E., Cappellari, M., Krajnović, D., et al. 2007, *MNRAS*, 379, 401
- Emsellem, E., Cappellari, M., Peletier, R. F., et al. 2004, *MNRAS*, 352, 721
- Emsellem, E., Renaud, F., Bournaud, F., et al. 2015, *MNRAS*, 446, 2468
- Englmaier, P. & Shlosman, I. 2004, *ApJ*, 617, L115
- Erwin, P. 2004, *A&A*, 415, 941
- Erwin, P. 2005, *MNRAS*, 364, 283
- Erwin, P. 2015, *ApJ*, 799, 226
- Erwin, P., Beckman, J. E., & Pohlen, M. 2005, *ApJ*, 626, L81
- Erwin, P. & Debattista, V. P. 2013, *MNRAS*, 431, 3060
- Erwin, P. & Debattista, V. P. 2017, *MNRAS*, 468, 2058
- Erwin, P., Pohlen, M., & Beckman, J. E. 2008, *AJ*, 135, 20
- Erwin, P., Saglia, R. P., Fabricius, M., et al. 2015, *MNRAS*, 446, 4039
- Erwin, P. & Sparke, L. S. 2002, *AJ*, 124, 65
- Eskridge, P. B., Frogel, J. A., Pogge, R. W., et al. 2000, *AJ*, 119, 536
- Fabbiano, G., Gioia, I. M., & Trinchieri, G. 1989, *ApJ*, 347, 127
- Faber, S. M., Friel, E. D., Burstein, D., & Gaskell, C. M. 1985, *ApJS*, 57, 711
- Fabricius, M. H., Coccato, L., Bender, R., et al. 2014, *MNRAS*, 441, 2212
- Fakhouri, O., Ma, C.-P., & Boylan-Kolchin, M. 2010, *MNRAS*, 406, 2267
- Falcón-Barroso, J. 2016, *Astrophysics and Space Science Library*, Vol. 418, *The Stellar Kinematics of Extragalactic Bulges* (Springer International Publishing Switzerland), 161
- Falcón-Barroso, J., Bacon, R., Bureau, M., et al. 2006, *MNRAS*, 369, 529
- Falcón-Barroso, J. & Martig, M. 2021, *A&A*, 646, A31
- Falcón-Barroso, J., Peletier, R. F., Emsellem, E., et al. 2004, *MNRAS*, 350, 35
- Falcón-Barroso, J., Ramos Almeida, C., Böker, T., et al. 2014, *MNRAS*, 438, 329
- Falcón-Barroso, J., Sánchez-Blázquez, P., Vazdekis, A., et al. 2011, *A&A*, 532, A95
- Fall, S. M. & Efstathiou, G. 1980, *MNRAS*, 193, 189
- Fisher, D. B. & Drory, N. 2008, *AJ*, 136, 773
- Fisher, D. B. & Drory, N. 2011, *ApJ*, 733, L47
- Fisher, D. B. & Drory, N. 2016, *An Observational Guide to Identifying Pseudobulges and Classical Bulges in Disc Galaxies*, Vol. 418 (Springer International Publishing Switzerland), 41
- Foreman-Mackey, D., Hogg, D. W., Lang, D., & Goodman, J. 2013, *Publications of the Astronomical Society of the Pacific*, 125, 306
- Foyle, K., Courteau, S., & Thacker, R. J. 2008, *MNRAS*, 386, 1821
- Fragkoudi, F., Athanassoula, E., & Bosma, A. 2016, *MNRAS*, 462, L41
- Fragkoudi, F., Athanassoula, E., & Bosma, A. 2017a, *MNRAS*, 466, 474
- Fragkoudi, F., Di Matteo, P., Haywood, M., et al. 2017b, *A&A*, 606, A47
- Fragkoudi, F., Di Matteo, P., Haywood, M., et al. 2018, *A&A*, 616, A180
- Fragkoudi, F., Grand, R. J. J., Pakmor, R., et al. 2020, *MNRAS*, 494, 5936

- Franx, M., Illingworth, G., & Heckman, T. 1989, *ApJ*, 344, 613
- Fraser-McKelvie, A., Aragón-Salamanca, A., Merrifield, M., et al. 2020, *MNRAS*, 495, 4158
- Fraser-McKelvie, A., Merrifield, M., Aragón-Salamanca, A., et al. 2019, *MNRAS*, 488, L6
- Freeman, K. C. 1970, *ApJ*, 160, 811
- Friedli, D. & Martinet, L. 1993, *A&A*, 277, 27
- Gadotti, D. A. 2008, *MNRAS*, 384, 420
- Gadotti, D. A. 2009, *MNRAS*, 393, 1531
- Gadotti, D. A. 2011, *MNRAS*, 415, 3308
- Gadotti, D. A. 2012, arXiv e-prints, arXiv:1208.2295
- Gadotti, D. A., Athanassoula, E., Carrasco, L., et al. 2007, *MNRAS*, 381, 943
- Gadotti, D. A., Baes, M., & Falony, S. 2010, *MNRAS*, 403, 2053
- Gadotti, D. A., Bittner, A., Falcón-Barroso, J., et al. 2020, *A&A*, 643, A14
- Gadotti, D. A. & de Souza, R. E. 2003, *ApJ*, 583, L75
- Gadotti, D. A. & de Souza, R. E. 2005, *ApJ*, 629, 797
- Gadotti, D. A. & dos Anjos, S. 2001, *AJ*, 122, 1298
- Gadotti, D. A., Sánchez-Blázquez, P., Falcón-Barroso, J., et al. 2019, *MNRAS*, 482, 506
- Gadotti, D. A., Seidel, M. K., Sánchez-Blázquez, P., et al. 2015, *A&A*, 584, A90
- Galilei, G. 1610, *Sidereus nuncius magna, longeque admirabilia spectacula pandens lunae facie, fixis innumeris, lacteo circulo, stellis nebulosis, ... Galileo Galileo : nuper a se reperti beneficio sunt observata in apprime vero in quatuor planetis circa Iovis stellam disparibus intervallis, atque periodis, celeritate mirabili circumvolutis ... atque Medicea sidera nuncupandos decrevit*
- Galloway, M. A., Willett, K. W., Fortson, L. F., et al. 2015, *MNRAS*, 448, 3442
- Gamow, G. 1946, *Physical Review*, 70, 572
- Ganda, K., Falcón-Barroso, J., Peletier, R. F., et al. 2006, *MNRAS*, 367, 46
- Garcia, A. M. 1993, *A&AS*, 100, 47
- García-Benito, R., Zibetti, S., Sánchez, S. F., et al. 2015, *A&A*, 576, A135
- Gardner, J. P., Mather, J. C., Clampin, M., et al. 2006, *Space Sci. Rev.*, 123, 485
- Gargiulo, I. D., Monachesi, A., Gómez, F. A., et al. 2019, *MNRAS*, 489, 5742
- Gebhardt, K., Richstone, D., Kormendy, J., et al. 2000, *AJ*, 119, 1157
- Gerhard, O. & Martinez-Valpuesta, I. 2012, *ApJ*, 744, L8
- Gerhard, O. E. 1993, *MNRAS*, 265, 213
- Gerin, M., Combes, F., & Athanassoula, E. 1990, *A&A*, 230, 37
- Gilmozzi, R. & Spyromilio, J. 2007, *The Messenger*, 127, 11
- Gomes, J. M. & Papaderos, P. 2017, *A&A*, 603, A63
- Gonçalves, G., Coelho, P., Schiavon, R., & Usher, C. 2020, *MNRAS*, 499, 2327
- Gonzalez, O. A. & Gadotti, D. 2016, in *Astrophysics and Space Science Library*, Vol. 418, *Galactic Bulges*, ed. E. Laurikainen, R. Peletier, & D. Gadotti, 199
- Gunn, J. E. & Gott, J. Richard, I. 1972, *ApJ*, 176, 1
- Gutiérrez, L., Erwin, P., Aladro, R., & Beckman, J. E. 2011, *AJ*, 142, 145
- Haywood, M., Lehnert, M. D., Di Matteo, P., et al. 2016, *A&A*, 589, A66

- Heavens, A. F., Jimenez, R., & Lahav, O. 2000, MNRAS, 317, 965
- Heckman, T. M. 1980, A&A, 88, 365
- Heller, C., Shlosman, I., & Englmaier, P. 2001, ApJ, 553, 661
- Hernquist, L. 1992, ApJ, 400, 460
- Herrera-Endoqui, M., Díaz-García, S., Laurikainen, E., & Salo, H. 2015, A&A, 582, A86
- Hildebrandt, A., de Lorenzo-Cáceres, A., Méndez-Abreu, J., & Falcón-Barroso, J. 2020, submitted to MNRAS Letters
- Ho, I. T., Medling, A. M., Groves, B., et al. 2016, Ap&SS, 361, 280
- Ho, L. C., Filippenko, A. V., & Sargent, W. L. W. 1997, ApJ, 487, 591
- Hoag, A. A. 1950, AJ, 55, 170
- Hohl, F. 1971, ApJ, 168, 343
- Hopkins, P. F., Cox, T. J., Younger, J. D., & Hernquist, L. 2009a, ApJ, 691, 1168
- Hopkins, P. F., Somerville, R. S., Cox, T. J., et al. 2009b, MNRAS, 397, 802
- Hubble, E. P. 1925, Popular Astronomy, 33, 252
- Hubble, E. P. 1926, ApJ, 64, 321
- Hubble, E. P. 1936, Realm of the Nebulae
- Hunter, D. A. & Elmegreen, B. G. 2006, ApJS, 162, 49
- Husemann, B., Bennert, V. N., Scharwächter, J., Woo, J. H., & Choudhury, O. S. 2016, MNRAS, 455, 1905
- Iannuzzi, F. & Athanassoula, E. 2015, MNRAS, 450, 2514
- Iodice, E., Sarzi, M., Bittner, A., et al. 2019, A&A, 627, A136
- Isobe, T., Feigelson, E. D., Akritas, M. G., & Babu, G. J. 1990, ApJ, 364, 104
- Jalali, M. A. 2007, ApJ, 669, 218
- James, P. A., Bretherton, C. F., & Knapen, J. H. 2009, A&A, 501, 207
- James, P. A. & Percival, S. M. 2016, MNRAS, 457, 917
- James, P. A. & Percival, S. M. 2018, MNRAS, 474, 3101
- Jungwiert, B., Combes, F., & Axon, D. J. 1997, A&AS, 125, 479
- Kalnajs, A. J. 1972, ApJ, 175, 63
- Kalnajs, A. J. 1978, in Structure and Properties of Nearby Galaxies, ed. E. M. Berkhuijsen & R. Wielebinski, Vol. 77, 113
- Kant, I. 1755, Allgemeine Naturgeschichte und Theorie des Himmels
- Kennicutt, Robert C., J. 1989, ApJ, 344, 685
- Kepler, J. 1609, Astronomia nova ..., seu physica coelestis, tradita commentariis de motibus stellae martis
- Kim, T., Gadotti, D. A., Athanassoula, E., et al. 2016, MNRAS, 462, 3430
- Kim, T., Gadotti, D. A., Sheth, K., et al. 2014, ApJ, 782, 64
- Kim, W.-T., Seo, W.-Y., & Kim, Y. 2012a, ApJ, 758, 14
- Kim, W.-T., Seo, W.-Y., Stone, J. M., Yoon, D., & Teuben, P. J. 2012b, ApJ, 747, 60
- Kissler-Patig, M., Pirard, J. F., Casali, M., et al. 2008, A&A, 491, 941
- Knapen, J. H. 2005, A&A, 429, 141

- Knapen, J. H. 2007, *Astrophysics and Space Science Proceedings*, 3, 175
- Knapen, J. H., Beckman, J. E., Heller, C. H., Shlosman, I., & de Jong, R. S. 1995, *ApJ*, 454, 623
- Knapen, J. H., Pérez-Ramírez, D., & Laine, S. 2002, *MNRAS*, 337, 808
- Knapen, J. H., Shlosman, I., & Peletier, R. F. 2000, *ApJ*, 529, 93
- Koleva, M., Prugniel, P., Bouchard, A., & Wu, Y. 2009, *A&A*, 501, 1269
- Kormendy, J. 1982, *ApJ*, 257, 75
- Kormendy, J. 2013, *Secular Evolution in Disk Galaxies* (Cambridge University Press), 1
- Kormendy, J. 2016, *Astrophysics and Space Science Library*, Vol. 418, *Elliptical Galaxies and Bulges of Disc Galaxies: Summary of Progress and Outstanding Issues* (Springer International Publishing Switzerland), 431
- Kormendy, J., Drory, N., Bender, R., & Cornell, M. E. 2010, *ApJ*, 723, 54
- Kormendy, J. & Kennicutt, Robert C., J. 2004, *ARA&A*, 42, 603
- Krajnović, D., Emsellem, E., Cappellari, M., et al. 2011, *MNRAS*, 414, 2923
- Kraljic, K., Bournaud, F., & Martig, M. 2012, *ApJ*, 757, 60
- Kroupa, P. 2001, *MNRAS*, 322, 231
- Kruk, S. J., Erwin, P., Debattista, V. P., & Lintott, C. 2019, *MNRAS*, 490, 4721
- Kruk, S. J., Lintott, C. J., Bamford, S. P., et al. 2018, *MNRAS*, 473, 4731
- Kuijken, K. & Merrifield, M. R. 1993, *MNRAS*, 264, 712
- Kuijken, K. & Merrifield, M. R. 1995, *ApJ*, 443, L13
- Kuntschner, H., Emsellem, E., Bacon, R., et al. 2006, *MNRAS*, 369, 497
- Kuntschner, H., Emsellem, E., Bacon, R., et al. 2010, *MNRAS*, 408, 97
- Laine, S., Shlosman, I., Knapen, J. H., & Peletier, R. F. 2002, *ApJ*, 567, 97
- Laurikainen, E., Peletier, R., & Gadotti, D. 2016, *Galactic Bulges*, Vol. 418 (Springer International Publishing Switzerland)
- Laurikainen, E. & Salo, H. 2016, in *Astrophysics and Space Science Library*, Vol. 418, *Galactic Bulges*, ed. E. Laurikainen, R. Peletier, & D. Gadotti, 77
- Laurikainen, E. & Salo, H. 2017, *A&A*, 598, A10
- Laurikainen, E., Salo, H., & Buta, R. 2005, *MNRAS*, 362, 1319
- Laurikainen, E., Salo, H., Buta, R., & Knapen, J. H. 2007, *MNRAS*, 381, 401
- Laurikainen, E., Salo, H., Buta, R., & Knapen, J. H. 2011, *MNRAS*, 418, 1452
- Leaman, R., Fragkoudi, F., Querejeta, M., et al. 2019, *MNRAS*, 488, 3904
- Li, C., Gadotti, D. A., Mao, S., & Kauffmann, G. 2009, *MNRAS*, 397, 726
- Li, Z., Shen, J., & Kim, W.-T. 2015, *ApJ*, 806, 150
- Li, Z.-Y. & Shen, J. 2012, *ApJ*, 757, L7
- Li, Z.-Y., Shen, J., Bureau, M., et al. 2018, *ApJ*, 854, 65
- Lin, L., Li, C., He, Y., Xiao, T., & Wang, E. 2017, *ApJ*, 838, 105
- Lin, Y., Cervantes Sodi, B., Li, C., Wang, L., & Wang, E. 2014, *ApJ*, 796, 98
- Łokas, E. L. 2019, *A&A*, 629, A52
- Louis, P. D. & Gerhard, O. E. 1988, *MNRAS*, 233, 337
- Lütticke, R., Dettmar, R. J., & Pohlen, M. 2000, *A&AS*, 145, 405

- Lynden-Bell, D. & Kalnajs, A. J. 1972, MNRAS, 157, 1
- Lynden-Bell, D. & Pringle, J. E. 1974, MNRAS, 168, 603
- Lynds, R. & Toomre, A. 1976, ApJ, 209, 382
- Madore, B. F. 2016, *Bulges: Seen from a Philosophically-Informed Historical Perspective*, Vol. 418 (Springer International Publishing Switzerland), 1
- Maller, A. H., Katz, N., Kereš, D., Davé, R., & Weinberg, D. H. 2006, ApJ, 647, 763
- Martín-Navarro, I., Vazdekis, A., Falcón-Barroso, J., et al. 2018, MNRAS, 475, 3700
- Martinez-Valpuesta, I., Knapen, J. H., & Buta, R. 2007, AJ, 134, 1863
- Martinez-Valpuesta, I., Shlosman, I., & Heller, C. 2006, ApJ, 637, 214
- Masters, K. L., Nichol, R. C., Hoyle, B., et al. 2011, MNRAS, 411, 2026
- Mayer, L., Kazantzidis, S., & Escala, A. 2008, Mem. Soc. Astron. Italiana, 79, 1284
- McDermid, R. M., Alatalo, K., Blitz, L., et al. 2015, MNRAS, 448, 3484
- Melvin, T., Masters, K., Lintott, C., et al. 2014, MNRAS, 438, 2882
- Méndez-Abreu, J., Aguerri, J. A. L., Corsini, E. M., & Simonneau, E. 2008a, A&A, 478, 353
- Méndez-Abreu, J., Aguerri, J. A. L., Falcón-Barroso, J., et al. 2018, MNRAS, 474, 1307
- Méndez-Abreu, J., Corsini, E. M., Debattista, V. P., et al. 2008b, ApJ, 679, L73
- Méndez-Abreu, J., de Lorenzo-Cáceres, A., Gadotti, D. A., et al. 2019, MNRAS, 482, L118
- Méndez-Abreu, J., Debattista, V. P., Corsini, E. M., & Aguerri, J. A. L. 2014, A&A, 572, A25
- Méndez-Abreu, J., Sánchez-Janssen, R., & Aguerri, J. A. L. 2010, ApJ, 711, L61
- Menéndez-Delmestre, K., Sheth, K., Schinnerer, E., Jarrett, T. H., & Scoville, N. Z. 2007, ApJ, 657, 790
- Merrifield, M. R. & Kuijken, K. 1999, A&A, 345, L47
- Merritt, D. 1997, AJ, 114, 228
- Milgrom, M. 1983, ApJ, 270, 365
- Miwa, T. & Noguchi, M. 1998, ApJ, 499, 149
- Mo, H., van den Bosch, F. C., & White, S. 2010, *Galaxy Formation and Evolution* (Cambridge University Press)
- Mo, H. J., Mao, S., & White, S. D. M. 1998, MNRAS, 295, 319
- Moffat, A. F. J. 1969, A&A, 3, 455
- Moore, B., Katz, N., Lake, G., Dressler, A., & Oemler, A. 1996, Nature, 379, 613
- Muñoz-Mateos, J. C., Sheth, K., Gil de Paz, A., et al. 2013, ApJ, 771, 59
- Muñoz-Mateos, J. C., Sheth, K., Regan, M., et al. 2015, ApJS, 219, 3
- Neumann, J., Fragkoudi, F., Pérez, I., et al. 2020, A&A, 637, A56
- Neumann, J., Gadotti, D. A., Wisotzki, L., et al. 2019, A&A, 627, A26
- Neumann, J., Wisotzki, L., Choudhury, O. S., et al. 2017, A&A, 604, A30
- Newnham, L., Hess, K. M., Masters, K. L., et al. 2020, MNRAS, 492, 4697
- Newton, I. 1687, *Philosophiae Naturalis Principia Mathematica*. Auctore Js. Newton
- Noguchi, M. 1996, ApJ, 469, 605
- Noguchi, M. 1999, ApJ, 514, 77
- Ocvirk, P., Pichon, C., Lançon, A., & Thiébaud, E. 2006a, MNRAS, 365, 74

- Ocvirk, P., Pichon, C., Lançon, A., & Thiébaud, E. 2006b, *MNRAS*, 365, 46
- Oh, K., Sarzi, M., Schawinski, K., & Yi, S. K. 2011, *The Astrophysical Journal Supplement Series*, 195, 13
- Ondrechen, M. P., van der Hulst, J. M., & Hummel, E. 1989, *ApJ*, 342, 39
- Oser, L., Naab, T., Ostriker, J. P., & Johansson, P. H. 2012, *ApJ*, 744, 63
- Ostriker, J. P. & Peebles, P. J. E. 1973, *ApJ*, 186, 467
- Ostriker, J. P., Peebles, P. J. E., & Yahil, A. 1974, *ApJ*, 193, L1
- Pastrav, B. A., Popescu, C. C., Tuffs, R. J., & Sansom, A. E. 2013, *A&A*, 557, A137
- Paufique, J., Bruton, A., Glindemann, A., et al. 2010, in *Society of Photo-Optical Instrumentation Engineers (SPIE) Conference Series*, Vol. 7736, *Adaptive Optics Systems II*, ed. B. L. Ellerbroek, M. Hart, N. Hubin, & P. L. Wizinowich, 77361P
- Peletier, R. F., Falcón-Barroso, J., Bacon, R., et al. 2007, *MNRAS*, 379, 445
- Peng, C. Y., Ho, L. C., Impey, C. D., & Rix, H.-W. 2002, *AJ*, 124, 266
- Peng, C. Y., Ho, L. C., Impey, C. D., & Rix, H.-W. 2010, *AJ*, 139, 2097
- Penzias, A. A. & Wilson, R. W. 1965, *ApJ*, 142, 419
- Pérez, I., Martínez-Valpuesta, I., Ruiz-Lara, T., et al. 2017, *MNRAS*, 470, L122
- Pérez, I., Sánchez-Blázquez, P., & Zurita, A. 2007, *A&A*, 465, L9
- Pérez, I., Sánchez-Blázquez, P., & Zurita, A. 2009, *A&A*, 495, 775
- Perlmutter, S., Aldering, G., Goldhaber, G., et al. 1999, *ApJ*, 517, 565
- Peschken, N. & Łokas, E. L. 2019, *MNRAS*, 483, 2721
- Pfenniger, D. & Friedli, D. 1991, *A&A*, 252, 75
- Pietrinferni, A., Cassisi, S., Salaris, M., & Castelli, F. 2004, *ApJ*, 612, 168
- Pietrinferni, A., Cassisi, S., Salaris, M., & Castelli, F. 2006, *ApJ*, 642, 797
- Pietrinferni, A., Cassisi, S., Salaris, M., & Hidalgo, S. 2013, *A&A*, 558, A46
- Pietrinferni, A., Cassisi, S., Salaris, M., Percival, S., & Ferguson, J. W. 2009, *ApJ*, 697, 275
- Piner, B. G., Stone, J. M., & Teuben, P. J. 1995, *ApJ*, 449, 508
- Pinna, F., Falcón-Barroso, J., Martig, M., et al. 2019, *A&A*, 623, A19
- Planck Collaboration, Ade, P. A. R., Aghanim, N., et al. 2011, *A&A*, 536, A1
- Planck Collaboration, Ade, P. A. R., Aghanim, N., et al. 2016, *A&A*, 594, A13
- Pohlen, M., Dettmar, R. J., Lütticke, R., & Aronica, G. 2002, *A&A*, 392, 807
- Pohlen, M. & Trujillo, I. 2006, *A&A*, 454, 759
- Porter, L. A., Somerville, R. S., Primack, J. R., & Johansson, P. H. 2014, *MNRAS*, 444, 942
- Prendergast, K. H. 1983, in *IAU Symposium*, Vol. 100, *Internal Kinematics and Dynamics of Galaxies*, ed. E. Athanassoula, 215–220
- Press, W. H., Teukolsky, S. A., Vetterling, W. T., & Flannery, B. P. 1992, *Numerical recipes in FORTRAN. The art of scientific computing* (Cambridge University Press)
- Prieto, M. A., Fernandez-Ontiveros, J. A., Bruzual, G., et al. 2019, *MNRAS*, 485, 3264
- Prochaska, J. X., Naumov, S. O., Carney, B. W., McWilliam, A., & Wolfe, A. M. 2000, *AJ*, 120, 2513
- Querejeta, M., Eliche-Moral, M. C., Tapia, T., et al. 2015, *A&A*, 573, A78
- Raha, N., Sellwood, J. A., James, R. A., & Kahn, F. D. 1991, *Nature*, 352, 411

- Rautiainen, P. & Salo, H. 2000, *A&A*, 362, 465
- Rautiainen, P., Salo, H., & Laurikainen, E. 2002, *MNRAS*, 337, 1233
- Regan, M. W., Thornley, M. D., Vogel, S. N., et al. 2006, *ApJ*, 652, 1112
- Reynaud, D. & Downes, D. 1998, *A&A*, 337, 671
- Riess, A. G., Filippenko, A. V., Challis, P., et al. 1998, *AJ*, 116, 1009
- Rix, H.-W. & White, S. D. M. 1992, *MNRAS*, 254, 389
- Roberts, M. S., Hogg, D. E., Bregman, J. N., Forman, W. R., & Jones, C. 1991, *ApJS*, 75, 751
- Roberts, M. S. & Rots, A. H. 1973, *A&A*, 26, 483
- Romeo, A. B. & Fathi, K. 2015, *MNRAS*, 451, 3107
- Romeo, A. B. & Fathi, K. 2016, *MNRAS*, 460, 2360
- Rousseeuw, J. P. & Leroy, A. M. 1987, *Robust Regression and Outlier Detection* (New York: John Wiley)
- Rousseeuw, P. J. 1984, *J. Am. Statist. Assoc.*, 79, 871
- Rubin, V. C., Ford, W. K., J., & Thonnard, N. 1978, *ApJ*, 225, L107
- Rubin, V. C., Ford, W. K., J., & Thonnard, N. 1980, *ApJ*, 238, 471
- Ruiz-Lara, T., Pérez, I., Gallart, C., et al. 2015, *A&A*, 583, A60
- Sachdeva, S. & Saha, K. 2016, *ApJ*, 820, L4
- Saha, P. & Williams, T. B. 1994, *AJ*, 107, 1295
- Sakamoto, K., Okumura, S. K., Ishizuki, S., & Scoville, N. Z. 1999, *ApJ*, 525, 691
- Saló, H., Laurikainen, E., Laine, J., et al. 2015, *ApJS*, 219, 4
- Sánchez, S. F., Kennicutt, R. C., Gil de Paz, A., et al. 2012, *A&A*, 538, A8
- Sánchez, S. F., Pérez, E., Sánchez-Blázquez, P., et al. 2016, *Rev. Mexicana Astron. Astrofis.*, 52, 171
- Sánchez-Blázquez, P., Ocvirk, P., Gibson, B. K., Pérez, I., & Peletier, R. F. 2011, *MNRAS*, 415, 709
- Sánchez-Blázquez, P., Rosales-Ortega, F. F., Méndez-Abreu, J., et al. 2014, *A&A*, 570, A6
- Sandage, A. 1961, *The Hubble Atlas of Galaxies*
- Sanders, R. H. & Tubbs, A. D. 1980, *ApJ*, 235, 803
- Sargent, W. L. W., Schechter, P. L., Boksenberg, A., & Shorridge, K. 1977, *ApJ*, 212, 326
- Sarzi, M., Falcón-Barroso, J., Davies, R. L., et al. 2006, *MNRAS*, 366, 1151
- Sarzi, M., Iodice, E., Coccato, L., et al. 2018, *A&A*, 616, A121
- Sauvaget, T., Hammer, F., Puech, M., et al. 2018, *MNRAS*, 473, 2521
- Schaye, J. 2004, *ApJ*, 609, 667
- Schlegel, D. J., Finkbeiner, D. P., & Davis, M. 1998, *ApJ*, 500, 525
- Schweizer, F., Whitmore, B. C., & Rubin, V. C. 1983, *AJ*, 88, 909
- Seidel, M. K., Cacho, R., Ruiz-Lara, T., et al. 2015a, *MNRAS*, 446, 2837
- Seidel, M. K., Falcón-Barroso, J., Martínez-Valpuesta, I., et al. 2015b, *MNRAS*, 451, 936
- Seidel, M. K., Falcón-Barroso, J., Martínez-Valpuesta, I., et al. 2016, *MNRAS*, 460, 3784
- Sellwood, J. A. 2014, *Reviews of Modern Physics*, 86, 1
- Sellwood, J. A. & Evans, N. W. 2001, *ApJ*, 546, 176

- Sellwood, J. A., Shen, J., & Li, Z. 2019, *MNRAS*, 486, 4710
- Seo, W.-Y., Kim, W.-T., Kwak, S., et al. 2019, *ApJ*, 872, 5
- Serra, P. & Trager, S. C. 2007, *MNRAS*, 374, 769
- Sérsic, J. L. 1963, *Boletín de la Asociación Argentina de Astronomía La Plata Argentina*, 6, 41
- Sérsic, J. L. 1968, *Atlas de galaxias australes* (Cordoba, Argentina: Observatorio Astronomico, 1968)
- Shapley, H. & Curtis, H. D. 1921, *Bulletin of the National Research Council*, 2, 171
- Shaw, M. A. 1987, *MNRAS*, 229, 691
- Shen, J. & Debattista, V. P. 2009, *ApJ*, 690, 758
- Shen, J., Rich, R. M., Kormendy, J., et al. 2010, *ApJ*, 720, L72
- Sheth, K., Elmegreen, D. M., Elmegreen, B. G., et al. 2008, *ApJ*, 675, 1141
- Sheth, K., Melbourne, J., Elmegreen, D. M., et al. 2012, *ApJ*, 758, 136
- Sheth, K., Regan, M., Hinz, J. L., et al. 2010, *PASP*, 122, 1397
- Sheth, K., Vogel, S. N., Regan, M. W., et al. 2002, *AJ*, 124, 2581
- Sheth, K., Vogel, S. N., Regan, M. W., Thornley, M. D., & Teuben, P. J. 2005, *ApJ*, 632, 217
- Shimizu, T. T., Davies, R. I., Lutz, D., et al. 2019, *MNRAS*, 490, 5860
- Shlosman, I., Begelman, M. C., & Frank, J. 1990, *Nature*, 345, 679
- Shlosman, I., Frank, J., & Begelman, M. C. 1989, *Nature*, 338, 45
- Shlosman, I. & Heller, C. H. 2002, *ApJ*, 565, 921
- Shlosman, I. & Noguchi, M. 1993, *ApJ*, 414, 474
- Simkin, S. M. 1974, *A&A*, 31, 129
- Simkin, S. M., Su, H. J., & Schwarz, M. P. 1980, *ApJ*, 237, 404
- Simmons, B. D., Melvin, T., Lintott, C., et al. 2014, *MNRAS*, 445, 3466
- Skibba, R. A., Masters, K. L., Nichol, R. C., et al. 2012, *MNRAS*, 423, 1485
- Smoot, G. F., Bennett, C. L., Kogut, A., et al. 1992, *ApJ*, 396, L1
- Sormani, M. C., Binney, J., & Magorrian, J. 2015, *MNRAS*, 449, 2421
- Sormani, M. C. & Li, Z. 2020, *MNRAS*, 494, 6030
- Sormani, M. C., Sobacchi, E., Fragkoudi, F., et al. 2018, *MNRAS*, 481, 2
- Sparke, L. S., van Moorsel, G., Erwin, P., & Wehner, E. M. H. 2008, *AJ*, 135, 99
- Statler, T. 1995, *AJ*, 109, 1371
- Stewart, K. R., Bullock, J. S., Wechsler, R. H., Maller, A. H., & Zentner, A. R. 2008, *ApJ*, 683, 597
- Thatte, N., Tecza, M., Clarke, F., et al. 2010a, in *Society of Photo-Optical Instrumentation Engineers (SPIE) Conference Series*, Vol. 7735, *Ground-based and Airborne Instrumentation for Astronomy III*, 77352I
- Thatte, N., Tecza, M., Clarke, F., et al. 2010b, in *Society of Photo-Optical Instrumentation Engineers (SPIE) Conference Series*, Vol. 7735, *Ground-based and Airborne Instrumentation for Astronomy III*, ed. I. S. McLean, S. K. Ramsay, & H. Takami, 77352I
- Thomas, D., Maraston, C., Schawinski, K., Sarzi, M., & Silk, J. 2010, *MNRAS*, 404, 1775
- Tojeiro, R., Heavens, A. F., Jimenez, R., & Panter, B. 2007, *MNRAS*, 381, 1252
- Tonry, J. & Davis, M. 1979, *AJ*, 84, 1511

- Toomre, A. 1964, *ApJ*, 139, 1217
- Toomre, A. 1981, in *Structure and Evolution of Normal Galaxies*, ed. S. M. Fall & D. Lynden-Bell, 111–136
- Toomre, A. & Toomre, J. 1972, *ApJ*, 178, 623
- Trager, S. C. & Somerville, R. S. 2009, *MNRAS*, 395, 608
- Trager, S. C., Worthey, G., Faber, S. M., Burstein, D., & González, J. J. 1998, *The Astrophysical Journal Supplement Series*, 116, 1
- Tremaine, S. 1989, in *Dynamics of Astrophysical Discs*, ed. J. A. Sellwood, 231–238
- van der Kruit, P. C. 1979, *A&AS*, 38, 15
- van der Kruit, P. C. 1987, *A&A*, 173, 59
- van der Marel, R. P. & Franx, M. 1993, *ApJ*, 407, 525
- Vásquez, S., Zoccali, M., Hill, V., et al. 2013, *A&A*, 555, A91
- Vazdekis, A., Coelho, P., Cassisi, S., et al. 2015, *MNRAS*, 449, 1177
- Vazdekis, A., Sánchez-Blázquez, P., Falcón-Barroso, J., et al. 2010, *MNRAS*, 404, 1639
- Venturi, G., Nardini, E., Marconi, A., et al. 2018, *A&A*, 619, A74
- Verley, S., Combes, F., Verdes-Montenegro, L., Bergond, G., & Leon, S. 2007, *A&A*, 474, 43
- Walcher, C. J., Coelho, P. R. T., Gallazzi, A., et al. 2015, *A&A*, 582, A46
- Walsh, D., Carswell, R. F., & Weymann, R. J. 1979, *Nature*, 279, 381
- Wang, J., Hammer, F., Puech, M., Yang, Y., & Flores, H. 2015, *MNRAS*, 452, 3551
- Weilbacher, P. M., Palsa, R., Streicher, O., et al. 2020, *A&A*, 641, A28
- Weilbacher, P. M., Streicher, O., Urrutia, T., et al. 2012, in *Society of Photo-Optical Instrumentation Engineers (SPIE) Conference Series*, Vol. 8451, *Software and Cyberinfrastructure for Astronomy II*, ed. N. M. Radziwill & G. Chiozzi, 84510B
- Weinzirl, T., Jogee, S., Khochfar, S., Burkert, A., & Kormendy, J. 2009, *ApJ*, 696, 411
- Weiss, A., Peletier, R. F., & Matteucci, F. 1995, *A&A*, 296, 73
- Westfall, K. B., Cappellari, M., Bershady, M. A., et al. 2019, arXiv e-prints, arXiv:1901.00856
- White, S. D. M. & Rees, M. J. 1978, *MNRAS*, 183, 341
- Wilkinson, D. M., Maraston, C., Goddard, D., Thomas, D., & Parikh, T. 2017, *MNRAS*, 472, 4297
- Williams, M. J., Bureau, M., & Kuntschner, H. 2012, *MNRAS*, 427, L99
- Wisnioski, E., Förster Schreiber, N. M., Wuyts, S., et al. 2015, *ApJ*, 799, 209
- Worthey, G., Faber, S. M., & Gonzalez, J. J. 1992, *ApJ*, 398, 69
- Worthey, G., Faber, S. M., Gonzalez, J. J., & Burstein, D. 1994, *The Astrophysical Journal Supplement Series*, 94, 687
- Wozniak, H. 2007, *A&A*, 465, L1
- Wozniak, H. 2015, *A&A*, 575, A7
- Zurita, A., Florido, E., Bresolin, F., Pérez, I., & Pérez-Montero, E. 2020, *MNRAS*, 500, 2380
- Zwicky, F. 1933, *Helvetica Physica Acta*, 6, 110

Acknowledgements

First and foremost, a huge thank you to my supervisor Dimitri! Thanks a lot for all your help, support, and guidance over the years, not only during my time as a PhD student but ever since our first research project in Chile. Without you I would not be where I am today and without any doubt this PhD adventure would not have come to such a successful conclusion. I always deeply enjoyed our discussions about Astrophysics (or other adventures somewhere on this planet) and I genuinely hope to continue these in the future. Thanks a lot for everything!

A big thank you also to the rest of the TIMER team! Thanks for the tremendous support with my papers, many intense discussions, and making TIMER such a nice, helpful, and relaxed group. Thanks also to Klaus Dolag for being my official supervisor and Jörg Schreiber, Joseph Mohr, and Barbara Ercolano for taking the time to be part of my thesis committee.

My time as a PhD student at ESO would have never been so enjoyable without the fantastic community in the institute. It might be challenging to name everyone I met during these amazing years and I am not going to try at this point. However, special thanks to Alex for our countless painful climbing and hiking sessions (we really did minimise the fun!), the infamous lunch walks with Aish, and all of Katja's support over the years.

Stephan, from the first semester with all the awful homework assignments to our almost perfectly timed PhD defences we have had a good amount of adventures together: from relaxed days in the English Garden and at the Flaucher, over long climbs in the Alps, to the arctic wilderness of Greenland – I do hope there are many more adventures to come!

Finally, I would like to thank my family and especially my parents for always supporting me throughout my life, even with my sometimes slightly weird plans of studying Astrophysics and travelling the world.

